Physical Modelling of Turbulent Single- and Multi-phase, Impinging Jets using Particle Image Velocimetry (PIV)

by

Donna McKendrick

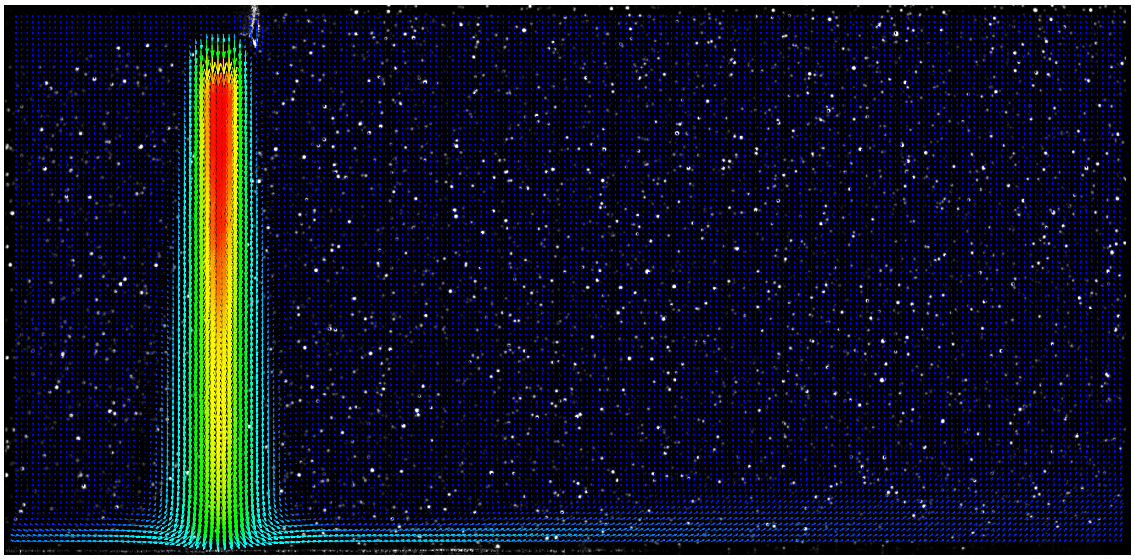

Submitted in accordance with the requirements for the degree of
Doctor of Philosophy

The University of Leeds
Institute of Particle Science and Engineering
School of Process, Environmental and Materials Engineering

March, 2015

The candidate confirms that the work submitted is her own and that the appropriate credit has been given where references has been made to the work of others.

The candidate confirms that the work submitted is her own and that appropriate credit has been given where reference has been made to the work of others.

This copy has been supplied on the understanding that it is copyright material and that no quotation from the thesis may be published without proper acknowledgement.

Assertion of moral rights:

The right of Donna McKendrick to be identified as Author of this work has been asserted by her in accordance with the Copyright, Designs and Patents Act 1988.

© 2015 The University of Leeds and Donna McKendrick

Acknowledgements

I would like to take the opportunity to thank all of the people who have helped me towards the completion of this Ph.D. thesis.

First, thanks go to my supervisors, Professor Mike Fairweather and Professor Simon Biggs. Simon and Mike for their guidance in many aspects of my work. My appreciation is also extended to Dr James Young for his support.

I would like to thank a number of persons within the Faculty of Engineering at the University of Leeds, who without their help my experimental system would not have been successfully designed, constructed, modified, and modified again (and again!): Mr Neil Smith, Mr Robert Harris, the Mechanical Workshop Team, Mr Tarsem Hunjan and his Electric Workshop Team, and Mr Peter Dawson.

Thanks also goes to Professor Mohammed Pourkashanian, Dr Kevin Hughes and Mr Paul Crosby for allowing me to use their PIV to development my understanding of the measurement technique, before my group took receipt of the new PIV system. Paul not only helped me with things directly related to the PIV, he also helped with so many other aspects to do with the development of my experimental rig, that without I do not think I could have completed this work.

I would also like to thank the members of my research group for their support and company at the local watering hole when a cold pint of local ale was hard earned.

And finally, my deepest gratitude goes to my family and friends. They have helped me keep focussed when I needed it and also helped me relax and have fun when it was equally needed. And then to my wonderful fiancé Ed Curl who has shown me more understanding and patience than I thought possible.

Abstract

Two-component velocity vector maps of single- and multi-phase turbulent impinging jets were acquired using particle image velocimetry (PIV). Mean and turbulent characteristics were explored with the impingement surface located at three strategic positions; 2 (within the potential core), 6 (just outside the core) and 10 h/d (fully developed jet).

Single-phase trials present the first extensive exploration of all three regions of an impinging jet. As jet height increased, the more advanced the jet expansion, and the centreline mean axial velocity decreased as the jet spread radially with increasing mean radial velocity. An increase in turbulence levels was seen from 2 to 6 h/d as the end of the potential core was exceeded where turbulence from the mixing layer penetrated to the centre, followed by a decrease at 10 h/d as the jet continued to grow before impingement.

A liquid impinging jet laden with 69μm sized glass particles was explored, the particles were found to not follow the turbulent flow. Particle axial velocities were generally smaller than their single-phase counterparts. As the jet height increased the stagnation region broadened, similarly for the single-phase trials. The particles exhibited considerably lower turbulent velocities. The near-field radial wall jet saw the deflection and acceleration to a greater extent for the smallest jet height (2 h/d) than the larger two (6 and 10 h/d). Particle turbulence intensities in the near-field radial wall jet increased as the jet height increased. The particle turbulence was smaller than that of the single-phase, the greatest difference seen for the middle jet height of 6 h/d.

A sensitivity study of particle size effect on a particle-laden turbulent impinging jet with jet-to-plate separation of six diameters has been completed, three particle sizes used; 20, 46 and 69μm. Within the impingement region, the particles do not decelerate as rapidly as the single-phase due to the particle inertia. Turbulent velocities of the particle phases were considerably lower than the single-phase, the turbulent velocity normal to the impingement surface larger than the radial component.

And finally, a preliminary assessment of the feasibility of using fluorescent particle image velocimetry (fPIV) for the purpose of studying turbulence modulation in impinging liquid jets has been undertaken.

Table of Contents

List of Tables

List of Figures

Nomenclature and Abbreviations

c_s	Solids loading / concentration, %vol
d	Jet line / Nozzle diameter, mm
D	Tank diameter / width, m
d_{IA}	Width / height of Interrogation Area (DynamicStudio software), pixels or mm
d_m	Local time-averaged jet diameter, mm
d_p	Particle diameter, µm
$d_p(Mode)$	Particle diameter (peak of the size distribution), µm
$d_p(Span)$	Particle diameter (statistical description of distribution, non-dimensional, $\left(d_p(90) - d_p(10)\right)/d_p(50)$)
$d_p(10)$	Particle diameter (10^{th} percentile), µm
$d_p(50)$	Particle diameter (50^{th} percentile), µm
$d_p(90)$	Particle diameter (90^{th} percentile), µm
E_c	Electrolyte species
E_s	Electrolyte concentration
h	Height above impingement surface, mm
h/d	Jet-to-plate separation, non-dimensional
L	Liquid height, m
L_e	Pipe entrance length, mm
L_j	Jet line length, mm
Nu	Nusselt number, non-dimensional
Q	Volumetric flowrate, g cm^{-3}
r	Radial distance, mm
Re	Reynolds number, non-dimensional
r_o	Nozzle radius, mm
R1, R2, R3	Steady state rig running durations, mins
r/d	Non-dimensional radial distance, vertical profile locations
s	Distance between the object plane and the imaging optics, m
S_t	Stokes number, non-dimensional
s’	Distance between the image plane and the imaging optics, m
t	Time, s
t_{jf}	Jet firing duration, s
t_s	Settling / consolidation time, s
T_1, T_2, T_3, T_4	Time-averaging time periods, s

Δt	Time step / pulse time, μs
u	Axial fluctuating velocity, m s^{-1}
U	Axial instantaneous velocity, m s^{-1}
U_b	Bulk exit velocity, m s^{-1}
U_c	Jet outlet centreline velocity, m s^{-1}
u_m	Axial velocity local maxima, m s^{-1}
U_o	Jet outlet velocity, m s^{-1}
u'	Axial normal stress (root mean square (RMS) of the fluctuating velocity [$\sqrt{\overline{u^2}}$]), m s^{-1}
$\overline{U}$	Axial mean velocity, m s^{-1}
$\overline{uv}$	Shear stress, m^2 s^{-2}
$(\overline{uv})_m$	Shear stress local maxima, m^2 s^{-2}
v	Radial fluctuating velocity, m s^{-1}
V	Radial instantaneous velocity, m s^{-1}
v_m	Radial velocity local maxima, m s^{-1}
v'	Radial normal stress (root mean square (RMS) of the fluctuating velocity [$\sqrt{\overline{v^2}}$]), m s^{-1}
$\overline{V}$	Radial mean velocity, m s^{-1}
x	Axial distance, mm
x/d	Non-dimensional axial distance, horizontal profile locations

Greek Symbols

δ	Jet velocity half-width, mm
ζ	Zeta potential, mV
η	Amplitude ratio of the particle and fluid velocities, non-dimensional
μ	Dynamic viscosity, Pa s
μ_l	Fluid dynamic viscosity, Pa s
π	Pi, mathematical constant
ρ	Density, kg m^{-3}
ρ_p	Particle density, kg m^{-3}
τ_p	Particle response time, μs

Subscripts

1, 2, 3	Denotes each particle simulant used within Chapter 7
f	Denotes the carrier-phase of a multi-phase system, Chapter 2
g	Denotes the gas-phase of a multi-phase system, Chapter 2
l	Denotes the liquid-phase of a multi-phase system, Chapter 7
p	Denotes the particle dispersed-phase of a multi-phase system, Chapter 7

Abbreviations

CCD	Charge-coupled device
CMC	Critical micelle concentration
F	Impinging jet test rig flowmeter
fPIV	Fluorescent Particle Image Velocimetry
HAST	Highly Active liquor Storage Tank
IA	Interrogation area (PIV image/data processing)
IPSE	Institute of Particle Science and Engineering
JB	Jet ballast
JTT	Jet test tank
LDA	Laser Doppler anemometry
LDV	Laser Doppler velocimetry
NIF	Near- and intermediate-field regions of a free jet
P1	Impinging jet test rig feed pump
P2	Impinging jet test rig return pump
PDA	Phase-Doppler anemometry
PIV	Particle Image velocimetry
PSP	Polyamide seeding particles
RMS	Root-mean-square
ROI	Region of interest (PIV image/data processing)
SDS	Sodium dodecyl sulphate solution

Chapter 1
Introduction

1.1 Research Motivation

Turbulent jet flows are an important class of turbulent free shear flow and are of considerable theoretical interest, as well as having extensive industrial applications. The impingement of fluid jets onto a surface has broad applications across many industries. Heat transfer operations are a popular application of impinging jets due to their very high convection coefficients, particularly within the impingement zone. The pharmaceutical, chemical, water and nuclear industries also use impinging jets in spraying and coating applications; fluidised beds; chemical reactors; and mixing applications. In the nuclear industry, impinging jets are also utilised to mobilise settled sludge material within storage tanks and ponds in preparation for transfer and ultimate immobilisation. Within a radioactive environment, the employment of impinging jets are advantageous as no moving-parts are present; in the event of failure of plant machinery such as impellers, the enclosed unit operation would need to be accessed to perform repairs, which is not desirable. The plant liquor itself is used to form the impinging jet through the application of compressed air to the jet ballast tank (as shown below, Figure 1-1); not adding to the quantity of radioactive material which is environmentally very beneficial, but also allowing operators a greater degree of control of operating conditions through manipulation of the compressed air application. It is this industrial application and others like it that is of particular focus within this thesis.

The nuclear fuel reprocessing cycle is very complex involving many stages (Wilson, 1996) including the treatment of a highly active waste stream. Prior to final immobilisation within a glass matrix through vitrification, the waste stream is stored in agitated tanks to allow additional cooling, to reduce the volume of waste through surface evaporation, and for the preparation of the feed stream to the vitrification plant. Figures 1-1 and 1-2 show a simplified diagram of the agitation and re-suspension jet ballast system used in the Highly Active Storage Tanks (HASTs) at Sellafield (McArthur et al., 2005).

Each tank contains seven jet ballasts (one central jet ballast perpendicular to the base and six peripherals equally spaced around the tanks circumference) for re-suspension in the event of solids settling on the base of the tank, and four airlift circulars for agitation (McArthur et al., 2005), Figure 1-2. The jet ballasts repeatedly scour the tank base, re-suspending any solids that may have settled out. The peripheral jet ballast nozzles are directed toward the tank walls, whereas the central jet ballast nozzle is directed straight down toward the centre of the base of the tank.

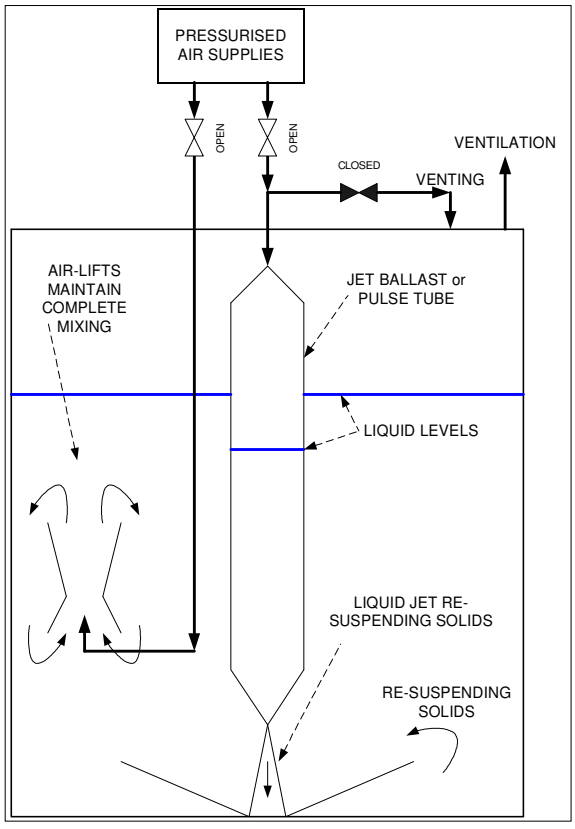

Figure 1-1 Schematic of jet ballast system within Highly Active Storage Tanks (HASTs) at Sellafield.

The jet ballasts are operated by feeding a set pressure of compressed air into the ballast tank. The peripheral jet ballasts are fired sequentially from 1 to 6, and the central jet ballast fires at the same time as the sixth peripheral jet ballast. As the air expands it forces liquor out through the nozzle as a jet which impinges onto the base of the tank at velocities up to 20 ms^{-1} inducing re-suspension of settled solids.

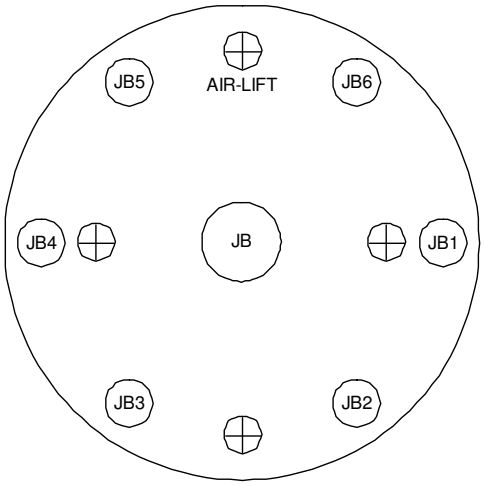

Figure 1-2 Jet ballasts (JB) and air-lifts layout within Highly Active Storage Tanks (HASTs) at Sellafield.

Developing a greater understanding of the flow phenomena of these turbulent impinging jets will enable the optimisation of plant operations and the extension of the plant operating envelope. The benefits can range from health, safety and environmental, to operational lifetime, product quality and yield, and cost. Not surprisingly these are attractive prospects.

The UK nuclear industry published the Sellafield waste strategy (IWS) progress report in September 2011[1], highlighting the UK's continuing efforts and commitment to deal with an inventory of nuclear waste across a number of nuclear sites, with particular focus on the Sellafield site. A new waste plant at Sellafield Ltd in the north-west of England, the Sellafield Sludge Packaging Plant 1 (SPP1), is currently under construction. Legacy waste at the site is currently stored within ponds and silos. Future applications of impinging jets within the industry may be the mobilisation of sludge wastes, some of which have remained relatively undisturbed for many years, as well as within the plant itself.

[1] Report published by the National Decommissioning Authority (NDA) in September 2011 – www.cumbria.gov.uk

1.2 Thesis Objectives

The study of two-phase, solid particle-laden jets has been primarily focussed on computational modelling, although to date very few papers have appeared in the literature. Accurate physical modelling of any engineering system, including free and impinging jets, can serve to aid computer model formulation and validation, the determination of operating requirements, the evaluation of plant throughput requirements, and the optimisation of process operations as well as providing support in design. The primary application requirement of the physical modelling programme discussed within this thesis will be in the formulation and validation of computational models, although the data generated are of value in their own right and improve our understanding of such jets. This programme of study will investigate the influence of process and material properties on the flow phenomena of turbulent single- and multi-phase, impinging jets to address this void.

The key objectives of this work are as follows;

- Develop experimental facilities capable of measuring single- and multi-phase impinging jet flow phenomena with the flexibility to vary, and control, process and material properties.
- Acquire single-phase impinging jet data to prove the experimental system through comparison to the small amount of data available on liquid flows; and to generate liquid data covering all three regions of the impinging jet from the developing jet and impingement region, through to the near- and far-field radial wall jet. All previous workers have focussed on only one or two regions.
- Presentation of particle-laden impinging liquid jet data at three different jet height separations.
- Exploration of particle size effect on the turbulent flow phenomena.

1.3 Thesis Structure

A literature review of turbulent impinging jets has been undertaken and is discussed in Chapter 2. Much experimental work has been done on heat transfer with impinging jets where high Nusselt numbers are found, however only three flow field sources of data for multi-phase impinging jets can be found within the literature and these are reviewed as well as key single-phase data within the literature.

Chapter 3 details the physical modelling experimental programme development. The experimental design considered the range of process and material variables that could be investigated, which was very large due to the fact that very little data exists in the literature. The experimental design produced a hierarchy of variables, settling on the seven variables of most importance with regards to developing our fundamental understanding of turbulent multi-phase impinging jets, model validation and their application within the HASTs. Three of these variables have been explored and data presented. The rig design had to consider many issues relating to the range of experimental process variables being considered; health, safety and environment issues, as well as the practicalities of construction, commissioning, performing the trials, and ultimate decommissioning and dismantling. The final design of the rig will enable the investigation of process and material variables beyond the seven chosen within this programme of study. The third and final stage of the experimental programme development was to consider the measurement technique to be deployed onto the impinging jet test rig. The development efforts necessary to achieve successful acquisition of high quality velocity field data for both liquid and particle-laden liquid impinging jets are detailed. To ensure high quality data acquisition from such a complex measurement system, a robust series of checks were developed.

Chapter 4 presents single-phase impinging liquid jet data at three jet height to impingement plate separations (h/d). Each jet is mapped out, followed by discussion of differences between the jet heights, for all regions of the jet. Comparison is also made to the small amount of data available in the literature to assess the quality of data output from the experimental system. These data also provide a benchmark for comparison in later results chapters.

The particle-laden impinging liquid jet is presented in Chapter 5. The particle-phase flow is presented and compared to the single-phase data, at all three jet heights.

Chapter 6 presents particle-laden liquid jet data for three particle sizes to explore the particle size effect on the fluid flow.

An initial exploration into the use of fluorescent particle image velocimetry (fPIV) to acquire the carrier phase velocity data simultaneously with particle information, and to thereby allow an assessment of turbulence modulation effects in the carrier fluid due to the presence of particles, is described in Chapter 7.

Lastly, Chapter 8 highlights the conclusions drawn from this project of experimental work and suggests areas of future work.

1.4 Co-ordinate System and Nomenclature Used

1.4.1 Introducing the Impinging Jet

The impinging jet of interest in this work is a submerged axisymmetric turbulent jet emerging from a nozzle of diameter d (=$2r_o$) at a normal distance of h above a smooth plate.

There is some variation in the co-ordinate systems employed by other workers. The flow co-ordinate system used throughout this work is that defined by the statistical centreline of the developing jet, with the origin of the r,x co-ordinate system located at the impingement point on the surface (Figure 1-3), i.e. the stagnation point. The x-axis is then directed upwards from the impingement surface along the stagnation line, with the r-axis extending radially parallel to the surface and away from the stagnation point.

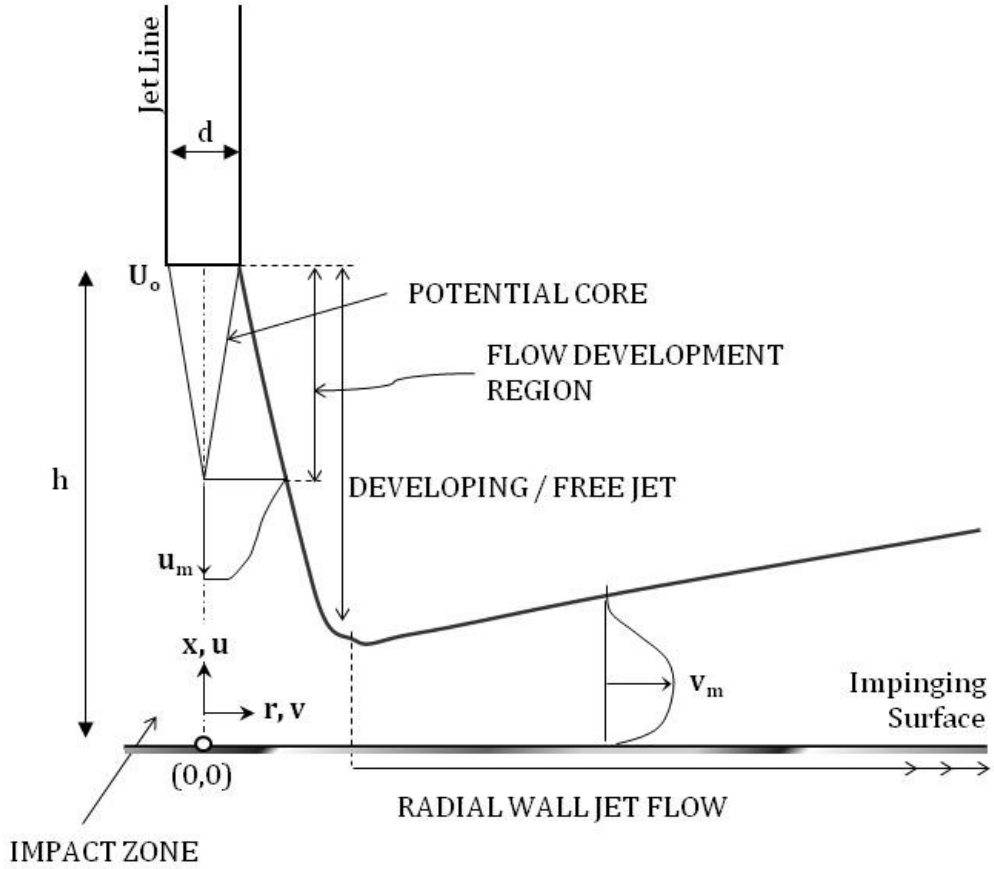

Figure 1-3 Round impinging jet schematic showing regions of the jet and flow co-ordinate system

Figure 1-3 illustrates three distinct regions observed in an impinging jet. The first region, the free jet flow does not feel the presence of the wall and the surrounding fluid is entrained into the jet. When the axisymmetric, round jet is initially formed, typically extending to around 5d (Rajaratnam, 1976) if allowed

to develop, and as fluid exits the jet outlet the centreline axial mean velocity, U_c, remains that of the pipe flow immediately upstream of the outlet. From the end of the potential core (> 5d), the flow proceeds through a period of development, before achieving dynamic equilibrium in the fully developed free jet. The axial mean velocity, $\overline{U}$, continuously decreases from a local maximum of u_m to zero for large values of r.

In the impingement or stagnation region, also known as the impact zone, the wall exerts pressure gradients that change the direction of flow from axial to radial.

In the radial wall region the jet has completely deflected, characterised by strong shear and velocity fluctuations, much higher than seen in an ordinary boundary layer (Fairweather and Grant, 2002).

The regions of the free and impinging jet are discussed in greater detail within the Literature Review in Chapter 3.

1.4.2 Turbulence Statistics

For the purposes of model formulation and validation, and for understanding the flows investigated, the main properties of the flow required are the mean and fluctuating velocities, and the normal and shear stresses. The fluctuating velocity, also known as a random turbulent velocity, is a random (statistically irregular) component added to the mean flow. For a given fluid the instantaneous velocity (U), as a function of time and position, may therefore be considered as the sum of the mean fluid velocity ($\overline{U}$) and the fluctuating velocity (u), see Equations (1-3) and (1-4).

For general annular or pipe flow the direction of flow is primarily in the x direction so that the x velocity component is expected to be much greater than the y and z velocity components. If the fluid flow is laminar then the y and z components may be zero, and if turbulent small non-zero values for the y and z velocity components might be expected, depending on the precise flow configuration. The chaotic nature of turbulent fluid motion means that instantaneously all the velocity components may be positive or negative. From one velocity measurement at t_1 to the next at t_2 the velocity will likely not be the same. Over a long period of time we would, however, expect the x component to gather around some high value, while the y and z components would gather around, or close to, zero so that the average over time would be non-zero for the x component, $\overline{U}$, and zero or near-zero for the y and z

components, $\overline{V}$ and $\overline{W}$ respectively. In the case of the impinging jet system the fluid flow will change in two dimensions so that both the x and y components will change.

Turbulent fluctuations generally follow a Gaussian distribution and the normal stress, u' and v', is described by the root mean square (RMS) of the fluctuating velocity (Hinze, 1975). The normal stresses for the u and v components can therefore be described by $\sqrt{\overline{u^2}}$ and $\sqrt{\overline{v^2}}$, respectively. The fluctuating turbulent velocities (u, v and w), seen as turbulent eddies, are responsible for the transfer of momentum which is the basis of turbulent diffusion. The product uv is related to the amount of momentum convected. The rate of change of momentum averaged over time represents the shear stress $\overline{uv}$.

Axial and radial mean velocities are given by the following equations:

$$\overline{U} = \frac{\sum_{i-1}^{n} U}{n} \tag{1-1}$$

$$\overline{V} = \frac{\sum_{i-1}^{n} V}{n} \tag{1-2}$$

The axial and radial instantaneous velocities are:

$$U = \overline{U} + u \tag{1-3}$$

$$V = \overline{V} + v \tag{1-4}$$

The RMS of the axial and radial fluctuating velocity is given by the following equations:

$$u' = \sqrt{\overline{u^2}} = \sqrt{\frac{\sum_{i=1}^{n}\left(U - \overline{U}\right)^2}{n}} \tag{1-5}$$

$$v' = \sqrt{\overline{v^2}} = \sqrt{\frac{\sum_{i=1}^{n}\left(V - \overline{V}\right)^2}{n}} \tag{1-6}$$

Shear stress is then given by the following equation:

$$\overline{uv} = \overline{UV} - \overline{U}\,\overline{V} \tag{1-7}$$

Chapter 2
Literature Review

Turbulent jet flows are an important class of turbulent free shear flow and are of considerable theoretical interest, as well as having extensive industrial applications. The impingement of fluid jets onto a surface has broad applications across many industries. The pharmaceutical, chemical, water and nuclear industries use impinging jets in spraying and coating applications; fluidised beds; chemical reactors; and mixing applications. In the nuclear industry, impinging jets are also utilised to mobilise settled sludge material within storage tanks and ponds in preparation for transfer and ultimate immobilisation (see Chapter 1). It is this industrial application and others like it that is the focus of this work. Despite their broad application, little literature has been published of particle-laden impinging jets. The employment of impinging jets for applications such as agitation as is the focus of this body of work, are less common, hence the limited availability of data, particularly for multi-phase impinging jets.

Heat transfer operations are a popular application of impinging jets due to very high convection coefficients, among the highest levels of Nusselt number encountered in single-phase convection (Cooper et al., 1993), particularly within the impingement zone. The dimensionless Nusselt number, Nu, is the ratio of convective to conductive heat transfer across a boundary, providing a measure of the rate of heat transfer. This work has been only selectively considered in this chapter where they add to our understanding of the flow fields of turbulent, axisymmetric impinging jets, as they mainly concern heat

transfer characteristics of impinging flows, with little or no flow field measurements being available. Should the reader be interested, a number of comprehensive reviews are available. A comprehensive review of jet impingement boiling including all modes of boiling, jet configuration and nozzle geometry can be found in Wolf et al. (1993). The popularity of the application of this phenomenon has driven considerable interest in this field for many years and is reflected in the vast research reported within the literature. A review of experimental data looking at jet flow and heat transfer characteristics, causes of scatter in the data, and effect of temperature recovery can be found in Jambunathan et al. (1992). More recently, Carlomagno and Ianiro (2014) provided an in-depth review of the thermo-fluid-dynamics of submerged impinging jets at small jet-to-plate separations (h/d).

This chapter provides an overview of the published work relevant to the understanding of single- and multi-phase impinging flows. The review is based on work in which the carrier-phase is in a turbulent state and the particle phase is flowing, submerged and bound by nonturbulent fluid, as is the subject matter of the body of work presented within this thesis. The turbulent, axisymmetric impinging jet can be categorised by several regions; the free jet, the impingement region, and the radial wall jet. The structure of this review will follow each of these regions starting from the jet outlet, through the impingement, out to the far-field of the radial wall jet, presenting and discussing relevant literature. Turbulence statistics required to enable the description of turbulent flows were introduced in Chapter 1, and are used throughout this review. The main properties of turbulent flow are the mean and fluctuating velocities, and the normal and shear stresses.

2.1 The Single-phase Free Jet

Turbulent free jet flows are important shear flows used for turbulence modelling, as well as having extensive heating, cooling, drying, combustion and mixing industrial applications. Although not the focus of the research reported within this thesis, the turbulent free jet makes up one of the regions of the impinging jet prior to the influence of the impingement surface being felt. As such, a summary of free jet work is given highlighting factors of relevance to the axisymmetric turbulent impinging jets studied, as well as those workers who studied the free jet region of impinging jets. This section does not represent a comprehensive review of the experimental study of free jets, a recent review by Ball and co-workers is recommended (Ball et al., 2012). The key experimental parameters of published data discussed within this thesis have been tabulated for your perusal; workers reporting data for the jet outlet and near-field region may be seen in Table 2-1 on page 16, and Table 2-2 on page 20 for the intermediate- and far-field regions of the free jet.

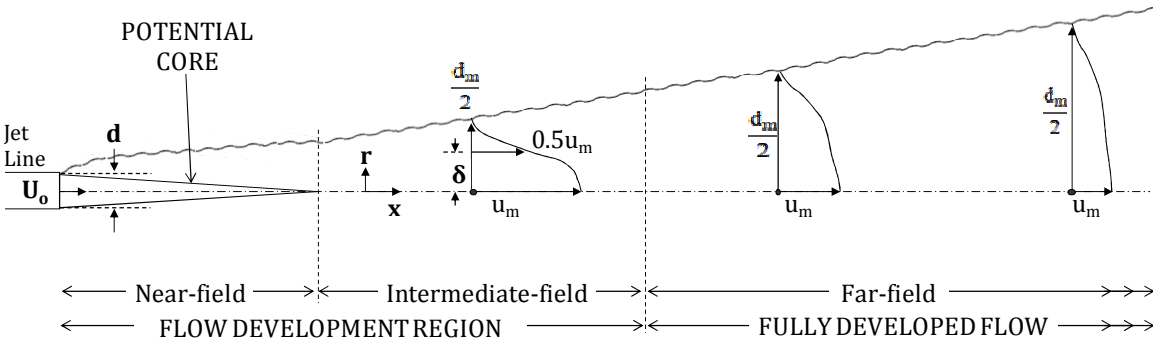

Figure 2-1 Schematic of the turbulent axisymmetric free jet, 3 axial regions.

Axial regions: (1) the near-field, (2) the intermediate-field, and (3) the far-field.

The turbulent axisymmetric free jet is described by three regions in the axial direction (Rajaratnum, 1976), as depicted in Figure 2-1: the near-field, the intermediate-field and the far-field.

As the jet emerges, the velocity profile and turbulence characteristics are dependent on the upstream flow conditions within the jet line and the nozzle shape, the axial velocity dominating the flow structure of the jet. For hydrodynamically fully developed flow issuing from a long pipe, which collapse when normalised for all Reynolds numbers (Hammad and Milanovic, 2011), as employed within the work reported in this thesis (Section 3.2.1), the flow is typically consistent with the power-law equation (2-1). For fully developed

turbulent pipe flow, the simplest and best known velocity profile is known as the power law,

$$\overline{U} = U_c \left(\frac{x}{r}\right)^{1/n} \quad (2\text{-}1)$$

where n is a constant whose value is dependent on the Reynolds number, increasing with increasing Reynolds number. Typical values of n taken for fully developed, turbulent pipe flow are around 6 (Hammad and Milanovic, 2011) and 7 (Fairweather and Hargrave, 2002). An alternative estimation of n was proposed by Hargrave et al. (2006) through equation (2-2), giving an n value of 6.16 for their Reynolds number, Re, of 23,400. For the experimental programme presented in this thesis, an n value of 5.50 is estimated for a Reynolds number, Re, of 10,000.

$$n = -1.7 + \log(Re) \quad (2\text{-}2)$$

Turbulence model evaluation is aided by the use of data acquired from a smooth pipe nozzle as above where fully developed flow was achieved prior to the jet outlet (Cooper et al., 1993). Few workers who have reported data in the impingement region and radial wall jet have also published jet outlet conditions, limiting their usefulness for model validation. Unfortunately they are also of limited value in contributing to the development of our understanding of the physics present within impinging jets as the upstream flow conditions are not known. Cooper et al. (1993) commented flow conditions at the jet outlet have generally been undefined or insufficiently prescribed, confirmed by the review presented here. Of the workers tabulated in Table 2-1 and Table 2-3 only seven (marked by ♦) provide well-defined jet exit profile conditions.

Immediately downstream from the jet outlet, the flow characteristics match the nozzle, initially unaffected by momentum transfer due to the shear-driven interaction between the issuing jet and the ambient surrounding fluid resulting in entrainment of mass, momentum and energy (Carlomagno and Ianiro, 2014). A potential core of approximately uniform flow exists (seen in Figure 2-1), where the flow maintains the flow velocity ($\overline{U}/U_o \geq 0.95$) and total pressure of the pipe flow, the width diminishing with increasing distance as the shear layer and turbulence level grows. The region of the free jet containing the potential core is often referred to as the near-field region (Figure 2-1). Within the potential core, the local maxima, u_m, is equal to the jet outlet conditions. Radial turbulence intensity, v', is generally low with little variation across the jet, while the axial component, u', experiences substantial change (Hammad and Milanovic, 2011). Development of the turbulence shear layer manifests as two

peaks in axial turbulence, u', at radial distance of ±0.45d about the jet axis (centre of the annular shear layer), where velocity fluctuations are strong relative to the jet core.

The length of the potential core has a significant impact on downstream turbulence development of the free and impinging jet, generally accepted to be around 5 to 6d (Gauntner et al., 1970; Rajaratnum, 1976; Cooper et al., 1993; Milanovic and Hammad, 2010). Establishing the length of the potential core can aid the design of heat transfer applications of impinging jets as the maximum heat transfer occurs when the impingement surface is placed just beyond the end of the potential core (Ashforth-Frost and Jambunathan, 1996). Development of the potential core is influenced by upstream conditions and nozzle shape, affecting the boundary layer thickness. The boundary layer thickness in turn controlling the rate of spread of the issuing jet. Comparison of nozzle shape by Ashforth-Frost and Jambunthan (1996), yields interesting results. Differences are, unsurprisingly, seen from the immediate issue of the jet for two different nozzle shapes of the same exit diameter (10mm); fully developed jet exit velocity profile from long nozzle, and flat jet exit velocity profile from orifice nozzle. At the jet outlet the axial normal stress, u', for the fully developed exit profile (long nozzle) was twice the magnitude of the flat exit profile (orifice nozzle). The location of the local maxima, u'_m, were unaffected by the nozzle shape. The potential core length, defined by $\overline{U}/U_o \geq 0.95$, of the fully developed velocity profile was around 7% longer. The flat velocity profile experiences higher shear at the outer edge of the jet compared to its fully developed counterpart, resulting in enhanced entrainment thereby the mixing layer penetrating to the jet axis closer to the jet outlet, shortening the potential core. This is also reflected in the axial turbulence, u', rate of growth of the potential core, up to 2d from the jet outlet, where the fully developed exit jet growth rate is slower.

For reasons as evident by the differences demonstrated above between jet exit velocity profile conditions, only fully developed axisymmetric exit velocity profiles are considered within this thesis. There are however a few exceptions as they can provide useful information relevant to the impinging jets of subject within this body of work:

- Fully developed channel velocity profile using a slot nozzle by Yoshida et al., (1990) is one of the very few solid-laden impinging jet data sets available (Table 2-5).
- Nearly uniform 'top-hat' velocity profile using round, smoothly contracting (contoured) nozzles by Longmire and Anderson (2003) is

one of the very few solid-laden impinging jet papers available (Table 2-5), they also compare free versus impinging jets.

- Neither fully-developed nor uniform velocity profile, but still developing, using round nozzle aspect ratio (length to diameter) of one by Fitzgerald and Garimella (1998) provides insight into the effect of semi-confinement of an impinging jet, similar to the experimental set-up of Yoshida et al. (1990).
- Under-developed channel velocity profile using slot nozzle (Virdung and Rasmuson, 2007) is a solid-laden free jet with jet outlet profile conditions presented.

Authors	[1]*Config*	[2]*Phases*	[3]d_p *(μm)*	c_s *(vol%)*	[4]*h/d*	[5]*Re*	[6]*Method*
Ashforth-Frost & Jambunathan, 1996	A/S (orifice)	Air	-	-	-	22,500	LDA [1a♦ & 1d]
Longmire & Anderson, 2003*	Free	Air – Glass	50-60 (f)	1.63	-	20,000	PIV [1a & 2]
Milanovic & Hammad, 2010	Free	Water	-	-	-	14,602 19,135 24,685	PIV [1a♦, 1b & 1d]
Impinging Jets with Free jet regions							
Yoshida et al., 1990 ‡	Plane (conf)	Air – Glass	48.9	0.1	8 □	10,000	LDA [1a, 1b, 2 & 3a]
Fitzgerald & Garimella, 1998	A/S (conf)	Dielectric FC-77 liquid	-	-	2 △ 3 △ 4 △	8500 13,000 23,000	LDA [2 & 3a]
Ushijima et al., 2001	A/S	Water – Ethylene	1050	0.13	10 ◇	2000 (s) 1600 (m)	PIV LDA [1d & 2]
Fairweather & Hargrave, 2002	A/S	Air	-	-	2 △	18,800	PIV [1a♦, 2 & 3b]
Longmire & Anderson, 2003*	A/S	Air – Glass	25-35 (i) 15-25 (i) 35-45 (i)	1.63	5 △	20,000	PIV [1a & 2]
Hargrave et al., 2006	A/S	Water	-	-	2 △	23,400	PIV [1a♦, 1d, 2 & 3a]
Hammad & Milanovic, 2011	A/S	Water	-	-	2 △	5,000 10,030 15,050	fPIV [1a♦ & 1d]

Table 2-1 Summary of reported experimental data at the jet outlet and in near-field region of the single-phase free jet.

[1] Jet nozzle configuration key: Free – round free jet, A/S – axisymmetric jet, Plane – two-dimensional slot impinging jet, Pipe – pipe flow, (orifice) denotes an orifice nozzle free jet, (conf) denotes confined jet flow, (t-hat) denotes nearly uniform 'top-hat' velocity profile from contoured nozzle.

[2] Where two phases are present, the continuous phase is stated first, following by the dispersed phase, i.e., Liquid – Solid denotes a solid-laden, liquid jet flow.

[3] (f) denotes particle size used for free jet trials, and (i) for particles used in impinging jet trials.

[4] Jet-to-plate separation (h/d) column key for location of the impingement surface: △ within the potential core of the flow development region, □ out with potential core of the flow development region, and ◇ fully developed free jet flow.

[5] (s) denotes Reynolds number employed during single-phase trials, and (m) for multi-phase trials.

[6] Regions of measurement; [1a] Near-field of developing free jet containing potential core, ♦ Jet outlet profile conditions, [1b] Intermediate-field of developing free jet, [1c] Far-field of free jet, [1d] Jet centreline or stagnation line, [2] Impingement/ impact region, [3a] Near-field of radial wall jet, and [3b] Far-field of radial wall jet. Additionally [n/a] denotes pipe flow so this region identification is not applicable.

* Note that Longmire and Anderson, 2003, present data for both free and impinging jets.

† Slot/plane jet nozzle.

‡ Yoshida et al. (1990) jet-to-plate spacing is h/b rather than h/d, where b is the width of the slot jet.

Beyond the potential core, the free jet enters a region of developing flow, the intermediate-field, Figure 2-1. The jet velocity profile progressively widens in the radial direction, and the magnitude along the jet axis decreases, as it loses kinetic energy (Rajaratnam, 1976). Experimental study of a liquid free jet by Milanovic and Hammad (2010) found the centreline axial velocity ($\overline{U}$) fell to approximately 68% of the potential core value at 8d from the jet outlet. The shear layer (Figure 2-2), as a result of the velocity gradient between the issuing jet and the near-static surrounding fluid, progresses through to the jet centreline, this shearing promoting turbulence (Fellouah et al., 2009; Carlomagno and Ianiro, 2014).

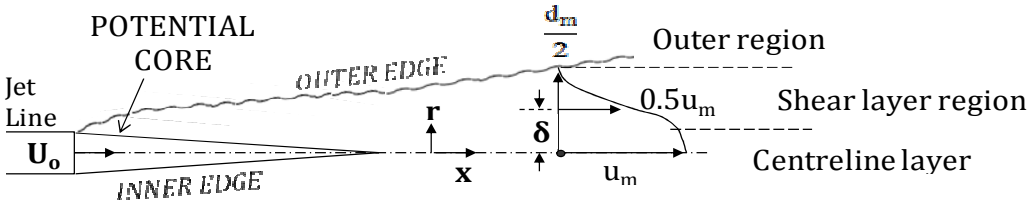

Figure 2-2 Schematic of the developing turbulent axisymmetric free jet, 3 radial regions.

Radial regions: (1) the centreline layer, (2) the shear layer region, and (3) the outer region layer.

The shear layer region exhibits a large velocity gradient in the radial direction resulting in large eddies. These eddies break down to form smaller eddies,

energy transferring from the large to the smaller scales (Longmire and Anderson, 2003). The outer edge is the boundary between the high vorticity jet flow and the near stagnant surrounding fluid, velocities typically around 10% of the jet centreline, U_c, value (Fellouah et al, 2009; Ball et al., 2010). Irrotational (nonturbulent) fluid is entrained into the turbulent flow across this turbulent-nonturbulent boundary (Westerweel et al., 2005). Vortex formation occurs along the outer edge of the free axisymmetric jet. This is caused by Kelvin-Helmholtz instability from the shear force between the high velocity jet and the surrounding stagnant fluid. Small vortices are created close to the nozzle and grow in size as they are carried along the flow until they are big enough to fully interrupt the jet. The vortices then collapse creating a fully turbulent flow.

The near- and intermediate-fields (NIF) make up the flow development region, as seen in (Figure 2-1). The downstream application of jets are significantly influenced by this region, and subsequently the development of turbulence in the developing free jet is critical in influencing the flow arrival conditions on the impingement surface. The axial evolution of the free jet, from jet outlet through the near- and intermediate-fields (NIF), experiences energy exchange between the mean flow and turbulence due to varying size coherent structures.

Jet growth manifests as a result of entrainment from the quiescent surrounding fluid, setting up a large recirculation region (Fairweather and Hargrave, 2002a and 2002b). Axial mean velocity profiles presented by Rajaratnam et al. (2010) for an air impinging jet with jet-to-plate separation (h/d) of 18.5 were not presented to show the negative values of the entrainment zone. However, following the profiles of the free jet prior to the impact zone effects being felt by the flow, we may postulate following each profile as it moves away from the jet axis, the gradient as the velocity axis is crossed, the radial distance from the jet axis where the velocity goes from positive to negative moves away from the axis and the gradient decreases at the jet grows, as would be expected. Upstream of the impingement region, the flow is as free jet (Beltaos and Rajaratnam, 1974; Rajaratnam et al, 2010).

A study of Reynolds number, Re, effect on the near- and intermediate-fields of a round water jet (Milanovic and Hammad, 2010) for the Re values of 14,602, 19,135 and 24,685, the entrainment rate hit a maximum around Reynolds number of 20,000 up to 7d from the jet outlet. This axial distance from the jet outlet of this maximum coincides with the often favourable jet height for impingement to maximise heat transfer (Ashforth-Frost and Jambunathan, 1996). The lower Re initially showed a lower entrainment, but had caught up

by 5d from the outlet. The largest Re however exhibited a substantially lower entrainment rate. For free jets, a transition in the jet flow characteristics takes place at Reynolds number of around 20,000 (Dimotakis, 2000; Fellouah et al., 2009) to a more chaotic and well-mixed state of developed turbulence. This transition is likely the cause of the drop in entrainment at this higher Reynolds number. Across this range of Reynolds numbers studied experimentally, the radial normal stress, v', was found to be independent of Re, while the axial normal stress, u', increased with a rise in Re (Milanovic and Hammad, 2010).

In the far-field region (Figure 2-1) the flow is fully developed and has reached dynamic equilibrium. There is some disagreement as to the axial distance where this self-similarity is achieved but it is generally accepted to occur from 25 to 30 diameters from the jet outlet (Fellouah et al., 2009; Milanovic and Hammad, 2010). Experimental results fit a Gaussian profile (Hinze, 1975), where the round jet broadens linearly and the axial velocity ($\overline{U}$) decay is governed by the hyperbolic law (Carlomagno and Ianiro, 2014). By the far-field, complex three-dimensional flow fields are achieved resulting in a self-similar state (Fellouah et al., 2009).

Two characteristic length scales can be used to describe jet flow (Fellouah et al., 2009), as depicted in Figure 2-1 and Figure 2-2. The local time-averaged diameter, d_m, (depicted as $d_m/2$ but is symmetrical about the jet centreline) is used to characterise the growth of the free jet as the diameter taken from the outer edge boundary, defined by $\overline{U}/U_o \leq 0.1$. This length scale does not find application for impinging jets so was not used within this body of work. The jet velocity half-width, δ, taken from the jet centreline, is used to characterise the growth of the free jet defined as the distance from the local maxima, u_m, to where the mean velocity equals half the local maxima, $0.5u_m$. The jet velocity half-width is also used to define the radial wall jet growth following impingement as discussed later within this literature review.

Authors	*[1]Config*	*[2]Phases*	*[3]d_p (μm)*	*c_s (vol%)*	*[4]h/d*	*[5]Re*	*[6]Method*
Ashforth-Frost & Jambunathan, 1996	A/S (orifice)	Air	-	-	-	22,500	LDA [1a♦ & 1d]
Milanovic & Hammad, 2010	Free	Water	-	-	-	14,602 19,135 24,685	PIV [1a♦, 1b & 1d]
Impinging Jets with Free jet regions							
Yoshida et al., 1990 ‡	Plane (conf)	Air – Glass	48.9	0.1	8 □	10,000	LDA [1a, 1b, 2 & 3a]
Ushijima et al., 2001	A/S	Water – Ethylene	1050	0.13	10 ◇	2000 (s) 1600 (m)	PIV LDA [1d & 2]
Hargrave et al., 2006	A/S	Water	-	-	2 △	23,400	PIV [1a♦, 1d, 2 & 3a]
Rajaratnum et al., 2010	A/S	Air	-	-	18.5 □	100,000	Hot-wire [1c & 2]
Hammad & Milanovic, 2011	A/S	Water	-	-	2 △	5,000 10,030 15,050	fPIV [1a♦ & 1d]

Table 2-2 Summary of reported experimental data in the intermediate- and far-field region of the free jet.

See key / notes for Table 2-1, page 16.

The presence of each region of the free jet as seen in Figure 2-1, is dependent on the distance between the nozzle and the impingement surface, h/d. As the jet height, h, is decreased some of these regions are no longer present. The evolution of the free jet having a significant impact on the impingement region and resultant radial wall jet.

2.2 The Particle-laden Free Jet

Despite the popularity of particle-laden jet flows within industry, and their importance as a shear flow for the development of computational models, they have not been studied as extensively as their single-phase counterparts, as is reflected within this literature review. However, the behaviour of solid particles in turbulent impinging liquid jets has broad applications across many industries including the nuclear applications introduced in Chapter 1, the focus of this work. Multi-phase flow refers to any fluid flow consisting of more than one phase, i.e., a surrounding liquid or gas (the continuous or primary phase) laden with discrete solid, liquid or gas particles (the dispersed or secondary phase). Although the application of multi-phase jets are wide spread, the availability of multi-phase data within the literature is sparse compared to single-phase jets. Particulate multi-phase flows offer problems of far greater complexity than found in single-phase equivalents from a modelling and experimental perspective, going somewhat to explain the dearth of experimental data in particular. Available data within the literature for multi-phase free jets, and multi-phase impinging jets with free jet regions are tabulated in Table 2-3 on page 26. The ability to predict the behaviour of such flows is central to the efficiency and effectiveness of any process where multi-phase flows are encountered, which is vast. Interactions between the phases present are of great importance.

In fluid dynamics, the Stokes number (S_t) provides a measure of a particle's responsiveness to turbulent fluctuations within a flow. It is defined as the ratio of the particle response time to a characteristic fluid time scale,

$$S_t = \frac{\tau_p U_b}{d} \tag{2-3}$$

where U_b is the bulk exit velocity of the jet, d is the jet line diameter, and τ_p is the particle response time (time constant in the exponential decay of particle velocity due to drag) estimated using the following equation.

$$\tau_p = \frac{\rho_p {d_p}^2}{18\mu_l} \tag{2-4}$$

Particles typically fall into one of three categories. Particle motion coupled to the fluid motion, where particle inertia is small compared to the fluid turbulence scales, follows the fluid turbulent fluctuations and has small Stokes numbers, $S_t < 1$. In contrast, if the Stokes number is large, $S_t > 1$, particle inertia is also large and as such they are not influenced by the fluid, with their response time longer than the fluid timescale. Particle dispersion is at its greatest when the Stokes number is near unity, $S_t \approx 1$, where the particle

motion is coupled to the large vortices, migrating to the margins of the eddies and dispersing further than the fluid (Hishida et al, 1992; Tang et al, 1992; Raju and Meiburg, 1995). A schematic representation of the three Stokes number classifications is shown in Figure 2-3.

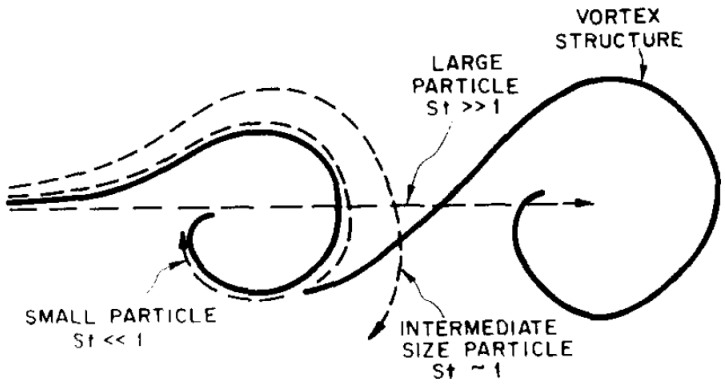

Figure 2-3 Pictorial representation of the effect of Stokes number on particle dispersion in large-scale turbulent structures (Crowe et al, 1988).

Where the dispersed phase is more dense than the carrier fluid (liquid or gas), the dispersed phase will have more inertia than the fluid elements moving at similar velocities (Longmire and Anderson, 2003), detaching from the flow. The dispersed particles will generally be unable to follow every scale of fluctuation in the flow, resulting in faster particles increasing local carrier velocities, and vice versa. The particles may damp or enhance fluctuation levels, the degree of which characterised by Stokes number.

At the jet outlet, particle axial mean velocities, $\overline{U}_p$, have been found to be lower than the single-phase for particle-laden free jets (d_p of 170μm, Tsuji et al., 1988; d_p of 110μm, Gillandt et al., 2001) and particle-laden pipe flow (d_p of 45μm and 136μm, Rizk and Elghobashi, 1989). An increase in particle size, d_p, from 210μm to 780μm resulted in a reduction in the particle axial mean velocity (Sheen et al., 1994). Solids loading (up to 0.0043 vol%) for a solid-laden air free jet having little effect on $\overline{U}_p$.

Turbulence intensity, u' and v', near the jet outlet exhibits different behaviour dependent on the particle size and solids loading of the system. Increasing particle size from 210μm to 460 or 780μm (Sheen et al., 1994) saw a change from the carrier-phase axial turbulence intensity being less than the single-phase ($u'_f < u'$), to the opposite occurring ($u'_f > u'$) for the larger particles. The smaller particles dissipating the turbulent kinetic energy of the fluid, while the larger particles create vortex shedding to enhance the fluid turbulent kinetic energy. Levels of particle phase turbulence intensity, u'_p, are largest near the jet outlet, increasing with increasing solids loading (d_p of 1500μm and solids

loading up to 1.9%, Virdung and Rasmuson, 2007). The radial turbulence intensity of the carrier-phase, v_f', for particles of 210 to 780μm, is lower than the single-phase ($v_f' < v'$). Both components of turbulence intensity, u_f' and v_f', decreasing further with higher solids loading (up to 0.0043 vol%).

Small particles are unable to completely respond to eddy fluctuations in the flow, the presence of small particles and low Stokes numbers, S_t, weakens turbulence (Hinze, 1975; Gore and Crowe, 1989). Particles diameters, d_p, of up to around 200μm suppress turbulence and is reflected in the axial turbulence intensity of the carrier-phase, u_f', for particle-laden free jets (d_p of 13μm, Hetsroni and Sokolov, 1971; d_p of 50 and 200μm respectively, Modarress et al., 1984a and 1984b; d_p of 110μm, Gillandt et al., 2001; d_p of 170μm, Tsuji et al., 1988; d_p of 210μm, Sheen et al., 1994) and pipe flow (d_p of 200μm Tsuji and Morikawa, 1982) being lower than their single-phase counterparts. On the other hand, large particles have large mean slip velocities (between the particles and the fluid phase) resulting in small eddies being generated, enhancing turbulence. Particles of 243 and 460μm generated a carrier-phase turbulence intensity only marginally larger than the single-phase (Tsuji et al., 1988 and Sheen et al., 1994, respectively). Turbulence enhancement has been seen for particles larger than 780μm for free jets (d_p of 780μm Sheen et al., 1994; d_p of 1400μm, Tsuji et al., 1988) and pipe flow (d_p of 800μm, Lee and Durst, 1982; d_p of 3400μm, Tsuji and Morikawa, 1982). The experimental parameters for each of these trials can be found in Table 2-3. This data would indicate there is a general criterion for the effect of particle size on the turbulent intensity of the carrier-phase, for particles of diameter, d_p, 200μm and smaller having a dampening effect, while particles of 780μm, increasing the turbulence intensity. However, significantly more work would be required before a consensus was reached.

Radial growth of the free jet, or the jet spreading rate, of the carrier-phase of a solid-laden free jet, is augmented by the presence of the particles unless they have a Stokes number near unity where they follow the fluid flow. Particles of diameters from 13 to 1400μm reduce the spreading rate of the carrier-phase compared to an equivalent single-phase free jet (d_p of 13μm, Hetsroni and Sokolov, 1971; d_p of 50μm, Popper et al., 1975; d_p of 200μm, Modarress et al., 1984a; d_p of 110μm, Gillandt et al., 2001). The rate of spreading decreases as particle size decreases (d_p of 170, 243, 500 and 1400μm, Tsuji et al., 1988; d_p of 210, 460 and 780μm, Sheen et al., 1994). While it is enhanced with an increase in the volume concentration, c_s, of solids in the system (c_s of 0.3, 1.2 and 1.9vol%, Virdung and Rasmuson, 2007). Large particles produce turbulence in

their wake resulting in increased radial growth (Gore and Crowe, 1989), an increase in volume fraction enhancing the production of turbulence. At the jet outer edge, particles encounter outwardly flow sooner than particles near the jet centreline. The resultant particle distribution varies with particle size; the smaller particles studied by Longmire and Anderson (2003) of around 20μm distributing throughout the jet while the larger, up to 60μm, remained around the centreline of the jet.

While the radial component mean velocity, $\overline{V}$, growth rate of a particle-laden gas jet is slower than for the single-phase jet (d_p of 48.9μm, Yoshida et al., 1990). Turbulence modification of the gas caused by the particles attributed to transfer from the particles to the gas. Around the jet axis, turbulence intensities are larger for the carrier-phase which may be attributed to the particle Stokes number, S_t, of 1.6 (near unity) denoting particles migrating to the margins of eddies and 'un-mixing' as they disperse.

For particles with large Stokes numbers, $S_t>1$, particles tend to concentrate in zones of deceleration as they respond relatively slowly to the change in the velocity flow field (S_t of 7.6 and 13.6, Longmire and Anderson, 2003). The concentration effect increasing with larger Stokes numbers, and this clustering becoming stronger moving downstream until the particles are dispersed. Particle dispersion occurs quicker for the lower particle Stokes numbers, S_t, particles accelerated outward by outwardly moving fluid.

Increasing the solids loading of a free jet means the ratio of particle to fluid momentum will increase as the jet relinquishes momentum in order to accelerate the particles (Longmire and Anderson, 2003). The peaks in carrier-phase axial turbulence intensity, u_f', seen in the shear layer region (Figure 2-2), increases in magnitude as more solids are added (Virdung and Rasmuson, 1989).

Authors	[1]*Config*	[2]*Phases*	[3]d_p (μm)	c_s (vol%)	[4]*h/d*	[5]*Re*	[6]*Method*
			Free jet and pipe flows				
Hetsroni & Sokoloz, 1971	A/S	Air – Oil	13	0.00025	-	83,300	Hot-wire [1c]
Popper et al., 1975	A/S	Air-Oil	50	0.0005	-	10,000	LDV [1b, 1c & 1d]
Lee & Durst, 1982	Pipe	Air – Glass	800	0.12	-	8000	LDA [n/a]
Tsuji & Morikawa, 1982	Pipe	Air - Polystyrene	200 3400	0.4	-	20,000	LDV [n/a]
Modarress et al., 1984a	A/S	Air – Glass	200	0.00035	-	17,000	LDV [1a♦ & 1d]
Modarress et al., 1984b	A/S	Air – Glass	50	0.0002	-	13,000	LDV [1a♦ & 1d]
Tsuji et al., 1988	A/S	Air - Polystyrene	170 243 500 1400	0.5	-	22,500	LDV Pitot [1a♦, 1c & 1d]
Sheen et al., 1994	Free	Air - Polystyrene	210 460 780	≤0.0043	-	20,000	LDA [1a, 1c & 1d]
Gillandt et al., 2001	A/S	Air - Glass	110	0.04	-	5700	PDA [1a♦, 1b, 1c & 1d]
Longmire & Anderson, 2003*	Free	Air – Glass	50-60 (f)	1.63	-	20,000	PIV [1a & 2]
Virdung & Rasmuson, 2007	Free † (conf)	Alcohol – Glass	1500	0.3 1.2 1.9	-	5000	PIV [1a♦ & 1b]
Fan et al., 2010	Free	Water - Glass	70	0.02	-	4300	PDA [1d]
			Impinging jets with free jet regions				
Yoshida et al., 1990 ‡	Plane (conf)	Air – Glass	48.9	0.1	8 □	10,000	LDA [1a, 1b, 1d, 2 & 3a]
Ushijima et al., 2001	A/S	Water – Ethylene	1050	0.13	10 ◇	2000 (s) 1600 (m)	PIV LDA [1d & 2]

Fairweather & Hargrave, 2002	A/S	Air	-	-	2 △	18,800	PIV [1a♦, 2 & 3b]
Longmire & Anderson, 2003*	A/S	Air – Glass	25-35 (i) 15-25 (i) 35-45 (i)	1.63	5 △	20,000	PIV [1a & 2]

Table 2-3 Summary of reported experimental data for particle-laden free jet and pipe flows, and particle-laden impinging flow jets with free jet regions.

See key / notes for Table 2-1, page 16.

2.3 The Single-phase Impingement Region / Impact Zone

The characteristics of the impingement region of a turbulent axisymmetric impinging jet is dependent on the approaching free jet. The physics of the free jet, as discussed in Section 2.1, only persisting until the presence of the impingement surface is felt. A tabulated collection of the experimental data in the impingement region discussed can be seen in Table 2-4 on page 31.

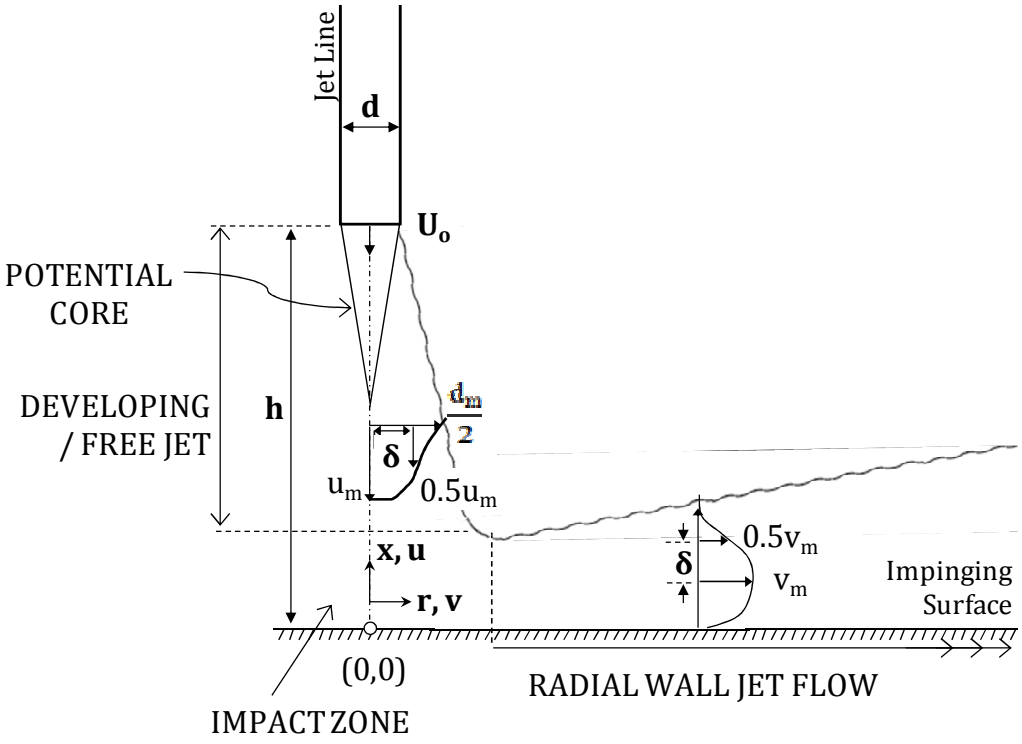

Figure 2-4 Schematic of the turbulent axisymmetric impinging jet

Impinging jet region: (1) the free jet, (2) the impingement region / impact zone, and (3) the radial wall jet.

Approaching the impingement surface (Figure 2-4), flow is deflected due to pressure gradients within the flow field (Dianat et al., 1995; Hargrave et al., 2006; Hammad and Milanovic, 2011). Pressure reflections from the solid surface alter the shear layer, turning and stretching large-scale structures. Deceleration in the vicinity of the impingement surface generates normal and shear stresses. Turbulence energy is created by the normal straining as opposed to being created by shear for parallel flows such as the free jet (Cooper et al., 1993). Axial turbulence levels having larger magnitude than their radial counterparts. Dependent on the upstream free jet, large eddies may persist until they break-up into smaller eddies at impingement, or the pressure field stretches and distorts them until they arrive at the impingement surface. Turbulence in the radial direction increases due to instability in the impact zone as the wall is approached, turbulence increasing until the wall is reached.

The axial velocity component drops and is transformed into accelerated radial velocity due to the forced sudden change in direction. Static pressure abruptly increases due to the axial velocity drop, and then decreases as the flow accelerates along the impingement surface.

High normal and shear stresses are found in the areas of deceleration and acceleration (Carlomagno and Ianiro, 2014), having a strong effect on local transport properties such as heat transfer. If the flow entering the impingement region has developed turbulence through to the jet centreline, single-phase heat transfer is enhanced, achieving an optimum heat transfer if the jet-to-plate (h/d) separation is approximately 110% of the potential core length (Ashford-frost and Jambunathan, 1996). For the slot impinging jet, as opposed the round jets which are the subject of the work, heat transfer reaches a maximum with the impingement surface positioned around 8d from the jet outlet (Yoshida et al., 1990). Increasing the jet height, h, results in a decrease in velocity and turbulence, reducing heat transfer.

How far the impinging / impact zone extends from the impingement surface, where the approaching jet is influenced by the presence of the impingement surface, has not met general agreement. Several workers have focussed on the small jet heights (h/d) of 2 due to their relative convenience for turbulence modelling. Cooper et al. (1993) and Craft et al. (1993), showed for an approaching air impinging jet, within 0.7d of the impingement surface, axial turbulence levels increased in the mixing region as result of the sudden deceleration due to the impingement surface. From around 0.3d above the base then followed an abrupt drop in turbulence due to the wall dampening effect.

Tracking axial mean velocity, $\overline{U}$, along the jet axis, or stagnation line, Hammad and Milanovic (2011) found the wall influence was felt within 0.8d of the impingement surface. Varying Reynolds number, Re, from 5,000 to 15,050 saw no measureable difference in the axial dimension of the impingement region but was somewhat narrower in the radial direction with increasing Re. For the large jet height of 18.5d, Rajaratnam et al. (2010) found the impingement region extended 1d above the impingement surface. Within 0.8d of the base, normal (u', v' and w') and shear stresses ($\overline{uv}$) decrease rapidly.

The other workers who have studied the impingement region of an impinging jet (see Table 2-4) have generally presented data either experiencing the influence of the impingement surface, i.e., within the impact region, or locations with the free jet, rather than making study of identifying the upper edge of the region. For example, data presented by Fairweather and Hargrave (2002) in the approaching jet at the jet outlet (1.9d above the impingement surface,

equivalent to 0.1d from the jet outlet) with the next subsequent profile taken 1.4d downstream (0.5d above the impingement surface); an increase in centreline turbulence evident. From 0.5d to 0.25d above the base little difference is seen, the turbulence then drops within 0.25d of the impingement surface, in agreement with Cooper et al. (1993). The resolution of radial profiles within the stagnation region is low so no information is given between these positions, an axial profile taken through the jet axis as taken by Cooper et al. (1993) could improve this. So the data sets discussed suggests the impact region extends to around 0.7 to 0.8d above the base, but there is not enough data to draw any firm conclusions.

A final abrupt escalation of turbulence within 0.1d of the impingement surface was seen by Cooper et al. (1993). However, this final increase so close to the base is thought to be attributed to known sensitivities of hot-wire probes in areas of high turbulent fluctuations generally under predicting turbulence levels, and difficulty in separating the velocity components. As technology and computational capabilities have advanced, more recent workers have used non-intrusive measurement techniques (see Data Tables on pages 16, 20, 31 and 36) such as Laser Doppler Anemometry (LDA) and Particle Image Velocimetry (PIV). Such non-intrusive techniques do not suffer the errors and directional ambiguities associated with intrusive probes such as hot-wire or pitot tubes. Hot-wire probes and LDA are single-point measurement techniques so can give a high spatial resolution, but are restricted in terms of the extent of the data sets that may be acquired. One of the key aims of the current study within this thesis is the exploration of all three regions of an impinging jet, at three different jet heights (h/d) so the application of Particle Image Velocimetry, PIV, was developed (Section 3.3, page 60).

Turbulence in the approaching free jet has a great impact on the downstream regions. Vortices in the free jet shear layer (primary vortices), can penetrate the wall boundary layer. The primary vortices dynamically scrubbing away the boundary layer whilst travelling against and along the impingement surface (Carlomagno and Ianiro, 2014). Secondary vortices may be formed by the turbulent flow field. Progressing along the impingement surface from the impingement region, towards the radial wall jet, turbulence fluctuations in velocity and pressure gradients can result in local flow reversals producing secondary vortices. The radial local maxima mean velocity, v_m, steadily decays as the shear layer region (Figure 2-5) mixes with the ambient surrounding fluid (Hargrave et al., 2006), the location of this maxima shifts away from the impingement surface as flow moves into the radial wall jet region, Section 2.5.

Jet-to-plate spacing ratio (h/d) plays a part in the development of turbulence within the free, approaching jet. When confinement of the jet through placement of an impingement surface is made within the potential core, turbulence levels along the jet centreline are generally relatively small as momentum has not yet penetrated to the axis. Cooper et al. (1993) saw a marked difference between the near-wall axial turbulence, u', peak values for different jet heights; 2 (within the potential core), 6 (out-with the potential core / developing flow) and 10 h/d (fully developed free jet). Impingement made within the potential core, h/d ratio of 2, peak values were barely half of that for the larger h/d ratios, 6 and 10 respectively. Turbulence intensity levels near the stagnation point grew from 2 to 6 h/d. Radial turbulent intensity, v', achieved a maximum at 2 diameters radial distance (2 r/d) from the jet centreline for the smallest jet height studied (2 h/d), while turbulence levels at the same profile location for the larger two jet heights were similar in value to their respective stagnation areas. Varying developments in turbulence are seen between the radial profile locations of 1.5 and 2 r/d; the smallest jet height saw a marked rise in turbulence, the median jet height remained uniform, while turbulence dropped across this area for the largest jet height. These turbulence developments coincide with changes in Nusselt number within the same area; an increase for 2 h/d, slight fall at 6 h/d, and a steep decline for 10 h/d (Baughn and Shimizu, 1989). Providing a strong demonstration of the popularity of impinging jets for the purpose of heat transfer applications at small jet-to-plate spacings.

Reynolds number (Re), ratio of inertial forces to viscous forces, also plays a part in the development of turbulence. A rise of Re from 23,000 to 70,00 for an air impinging jet saw an increase in the normalised radial peak mean velocities, v_m, (of 5 to 12%), and radial turbulence intensity near the stagnation point (Cooper et al., 1993).

Authors	[1]*Config*	[2]*Phases*	[3]d_p (μm)	c_s (vol%)	[4]*h/d*	[5]*Re*	[6]*Method*
Yoshida et al., 1990 ‡	Plane (conf)	Air – Glass	48.9	0.1	8 □	10,000	LDA [1a, 1b, 2 & 3a]
Cooper et al., 1993	A/S	Air	-	-	2 △ 6 □ 10 ◇	23,000 70,000	Hot-wire [2 & 3a]
Fitzgerald & Garimella, 1998	A/S (conf)	Dielectric FC-77 liquid	-	-	2 3 4	8500 13,000 23,000	LDA [2 & 3a]
Fairweather & Hargrave, 2002	A/S	Air	-	-	2 △	18,800	PIV [1a♦, 2 & 3b]
Longmire & Anderson, 2003*	Free A/S (t-hat)	Air – Glass	25-35 (i) 15-25 (i) 35-45 (i) 50-60 (f)	1.63	5 △	20,000	PIV [1a & 2]
Hargrave et al., 2006	A/S	Water	-	-	2 △	23,400	PIV [1a♦, 1d, 2 & 3a]
Rajaratnum et al., 2010	A/S	Air	-	-	18.5 □	100,000	Hot-wire [1c & 2]
Hammad & Milanovic, 2011	A/S	Water	-	-	2 △	5,000 10,030 15,050	fPIV [1a & 1d]

Table 2-4 Summary of reported experimental data in the impingement region of a turbulent axisymmetric impinging jet.

See key / notes for Table 2-1, page 16.

2.4 The Particle-laden Impingement Region / Impact Zone

The impingement region for particle-laden impinging jets have been found to extend up to 1d above the base (Yoshida et al., 1990; Ushijima et al., 2001; Longmire and Anderson, 2003), similar range as the single-phase jets already discussed. The small amount of multi-phase experimental data in the impingement region discussed can be seen in Table 2-5 on page 34, reflected in the size of this table compared to those that have come before.

It is worth noting that each of the three particle-laden impinging jet papers discussed here were focussed on particular aspects of the impinging jet and as such provide data for only small sections of the flow field, shown in Table 2-5. Unfortunately none provide a well prescribed jet outlet profile, required to enable turbulence model validation, the importance of the jet outlet conditions (nozzle conditions) already discussed. Yoshida et al. (1990) provides data for the largest proportion of the impinging jet, by far. Data profiles of axial mean velocity within the approaching free jet, $\overline{U}$, for the single- and carrier-phases, plus the addition of particle-phase data to vertical profiles taken at radial distances up to 4d of the near-filed radial wall jet. However, the configuration of their impinging jet differs from the one employed within the body of work presented within this thesis. Yoshida et al. (1990) used a two-dimensional slot jet with fully developed channel flow at the jet exit. Additionally, their jet was confined by the positioning of a plate parallel to the impingement surface at the height of the jet outlet (8 h/b).

Such a confined (single-phase) impinging jet results in a more complex flow structure (Fitzgerald and Garimella, 1998) than an unconfined impinging jet. The impinging jet is highly influenced by a difference in the recirculation field, entrainment previously shown to be crucial to the development of the turbulent flow field. The recirculation zone is toroidal in nature, limiting levels of entrainment compared to their un-confined impinging jet cousins. Heat transfer applications for example experience a reduction in the stagnation zone heat transfer, believed to be due to the re-circulated fluid being already heated by the base, resulting in less of a temperature gradient to help drive the heat transfer. Confinement manifests lower levels of turbulence, in turn reducing stagnation heat transfer by up to 10%. The length of the potential core has been found to increase by up to 20% due to confinement for a gas free jet (Re of 22,500, Ashforth-Frost and Jambunathan, 1996). Levels of turbulence decrease for confined flow geometries, the effects of confinement becoming less significant as distance from the jet outlet increases.

Ushijima et al. (2001) and Longmire and Anderson (2003) do add something to our understanding of particle-laden impinging jets however each present only a very small amount of data or information. Ushijima et al. (2001) provide mean axial velocity, $\overline{U}$, and axial turbulence intensity, u', along the stagnation line and one radial profile taken within the free jet region, for large particles (d_p of 1050μm) and low Reynolds number (Re of 2000) from an axisymmetric, fully developed jet outlet. Longmire and Anderson (2003) used periodic forcing to generate vortices, unfortunately no velocity data is published, only images and vorticity contours. For the purposes of being able to compare these data to data generated and presented in this thesis, it is important to note these differences.

The velocity profiles approaching the impingement plate for the gas-only and particle-laden gas jets studied by Yoshida et al. (1990) were significantly different. The axial gas-phase velocity decreases as we approach the impinging plate however the solid-phase velocity does not due to large inertia of particles resulting in particles rebounding off the plate, rebounding up to 2.5d upstream into the approaching jet. The rebounding particles generate reverse gas flow. Unfortunately, Yoshida et al. (1990) did not provide sufficient information to calculate the Stokes number, S_t, for their particles however from the behaviour reported we can deduce a $S_t > 1$. Within the stagnation region, particles with large Stokes numbers tend to accumulate in zones of deceleration. As the fluid flow decelerates approaching the impingement surface, particles can only decelerate by drag interactions. As a result, particles of high Stokes numbers tend to rebound off the base, travelling back up in to the oncoming flow. Longmire and Anderson (2003) found for particles with Stokes numbers, S_t, of 7.6 and 13.6, rebound heights and residence times in the impact zone increase with increasing Stokes number.

An intensification of the gas-phase radial turbulence intensity, v', for the solid-laden impinging jet (d_p of 48.9μm, Yoshida et al., 1990), in comparison to the single-phase jet, was seen near the stagnation point due to the interaction between the gas and rebounding particle, different to the reduction of gas turbulence seen for particle-laden free jets (d_p of 210 to 780μm, Sheen et al., 1994). Turbulence is generated by the wake of the particles because of the difference in the gas and particle velocities. Interestingly the axial gas turbulence intensity, u' components of both the multi- and single-phase jets were found to be more similar. The same was seen for the Reynolds shear stresses, $\overline{uv}$. Anisotropy between the axial and radial turbulence intensity components of the multi-phase jet is amplified by gas-solid interactions as a result of the large difference between the gas and particle inertia.

Authors	[1]*Config.*	[2]*Phases*	[3]d_p *(μm)*	c_s *(vol%)*	[4]*h/d*	[5]*Re*	[6]*Method*
Yoshida et al., 1990 ‡	Plane (conf)	Air – Glass	48.9	0.1	8 □	10,000	LDA [1a, 1b, 2 & 3a]
Ushijima et al., 2001	A/S	Water – Ethylene	1050	0.13	10 ◇	2000 (s) 1600 (m)	PIV LDA [1d & 2]
Longmire & Anderson, 2003*	A/S	Air – Glass	25-35 (i) 15-25 (i) 35-45 (i)	1.63	5 △	20,000	PIV [1a & 2]

Table 2-5 Summary of reported experimental data for particle-laden impinging jets, in the impingement region.

See key / notes for Table 2-1, page 16.

2.5 The Single-phase Radial Wall Jet

The radial wall jet (Figure 2-5), following impingement, is generally split into two regions; the near-field where the radial wall jet is developing, and the fully developed far-field where self-similarity has been achieved. Each will be taken in turn, tabulated data found in Table 2-6 on page 36.

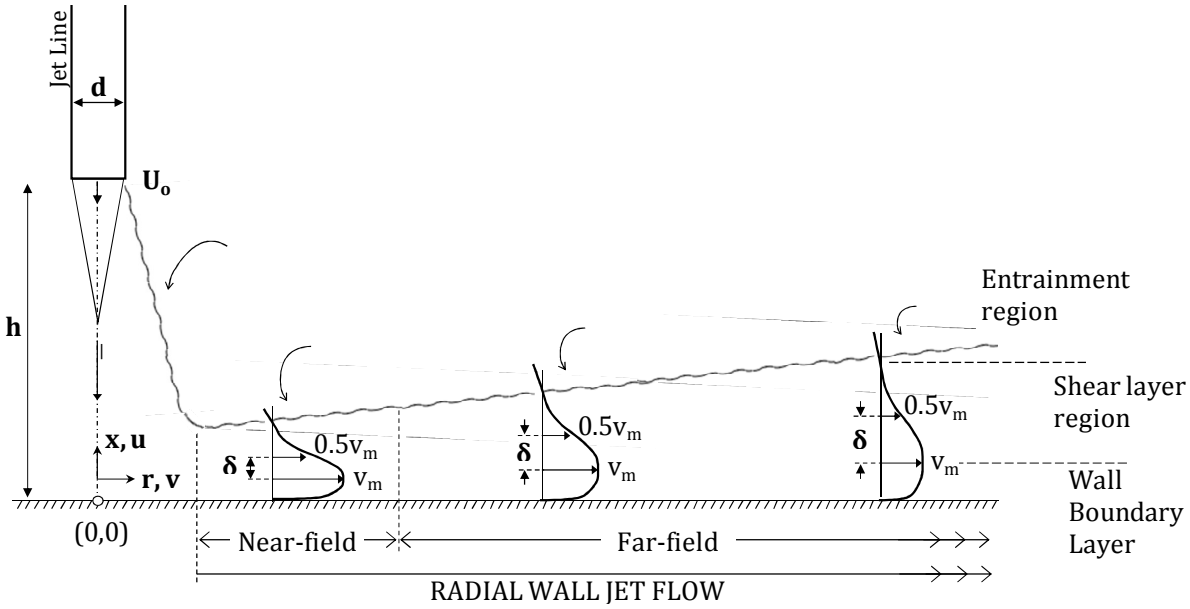

Figure 2-5 Schematic of the turbulent axisymmetric impinging jet, radial wall jet regions.

Wall jet regions: (1) the near-field radial wall jet, and (2) the far-field radial wall jet.

The near-field wall jet, characterised by strong shear and velocity fluctuations (much higher than an ordinary boundary layer), immediately follows impingement. The wall jet spreads radially outward developing into a semi-confined flow, growly linearly with increasing radial distance from the jet axis. The slope of wall jet growth increasing itself with raising the jet height from 2 to 10 h/d (Cooper et al., 1993), as more mixing occurs before impingement the turbulence levels are able to grow. Just beyond the impingement region, the flow structure will be significantly affected by strong curvature of streamlines.

Momentum exchange with the near-stagnant surrounding fluid, through entrainment, the impinging flow evolves into a wall jet flow. The axial mean velocity, $\overline{U}$, becomes negative at the outer edge of the radial wall jet due to entrainment (Hargrave et al., 2006) as depicted in the entrainment region on Figure 2-5. The entrainment region is at its strongest on the outer edge nearest the stagnation point (Dianat et al., 1996) where the negative values of the local radial mean velocity, v_m, are at their largest. The radial velocity component linearly accelerates from zero at the stagnation point (where the jet centreline

intersects the impingement surface) to a maximum value. Glauert (1956) states the maximum radial velocity occurs around one diameter from the jet centreline (1 r/d). At this radial distance from the jet centreline, the high axial direction flow of the expanding free jet is present in the outer shear layer (Hargrave et al., 2006).

The height of the local radial velocity maxima (Figure 2-4), v_m, above the impingement surface denotes the wall boundary layer which grows as the radial wall jet develops outward. Entraining the quiescent surrounding fluid, the wall jet grows in thickness and the location of v_m moving farther from the impingement surface, while the magnitude of v_m falls (Hargrave et al., 2006). The shear layer being influenced by the velocity gradient at the wall (where there is no-slip condition) and the velocity gradient across the outer edge between the wall jet and the surrounding fluid.

Authors	[1]*Config*	[2]*Phases*	[3]d_p *(μm)*	c_s *(vol%)*	[4]*h/d*	[5]*Re*	[6]*Method*
Yoshida et al., 1990 ‡	Plane (conf)	Air – Glass	48.9	0.1	8 □	10,000	LDA [1a, 1b, 2 & 3a]
Cooper et al., 1993	A/S	Air	-	-	2 △ 6 □ 10 ◇	23,000 70,000	Hot-wire [2 & 3a]
Fitzgerald & Garimella, 1998	A/S (conf)	Dielectric FC-77 liquid	-	-	2 3 4	8500 13,000 23,000	LDA [2 & 3a]
Fairweather & Hargrave, 2002	A/S	Air	-	-	2 △	18,800	PIV [1a♦, 2 & 3b]
Hargrave et al., 2006	A/S	Water	-	-	2 △	23,400	PIV [1a♦, 1d, 2 & 3a]

Table 2-6 Summary of reported experimental data in the radial wall region of a turbulent axisymmetric impinging jet.

See key / notes for Table 2-1, page 16.

2.6 The Particle-laden Radial Wall Jet

For particle-laden gas impinging jets, of particles with large Stokes number (i.e., particles are slow to respond to turbulent fluctuations) turbulence intensity for the multi-phase flow was around 50% larger than the single-phase near the stagnation region (1r/d), Yoshida et al. (1990). Attributed to interaction between the radially flowing gas and the particles mainly moving normal to the impingement surface, the particles initially having no radial momentum. As the radial wall jet develops (4r/d - 4d radially from jet axis), differences between the single-phase and the gas-phase of the particle-laden flow are lessened near the base, with the solid-phase lagging behind. As the near-field wall jet develops, the gas-phase turbulence intensity, v_g', decays, approaching the single-phase flow. In the upper shear layer, the gas-phase velocity is larger than the single-phase as rebounding particles accelerate through this region.

By the far-field radial wall jet, the local radial velocity maxima, v_m, steadily decays as the jet mixes with the surrounding fluid. The position of this maxima moving away from the impingement surface as the wall jet develops (Fairweather and Hargrave, 2002).

Beyond the outer edge of the wall jet, negative radial velocities occur as a result of recirculation within the so-called near-stagnant surrounding fluid. A large, low velocity recirculation zone was found by Fairweather and Hargrave (2002), seen to extend 8d above the impingement surface at radial distance of 10 r/d from the jet axis, characterised by entrainment streamlines approximately 45^0 normal to the base.

This fully developed flow is confirmed through the manifestation of self-similarity, achieved from 10d along the impingement surface (10 r/d) from the jet axis (Poreh et al., 1967; Dianat et al., 1996; Fairweather and Hargrave, 2002).

Authors	[1]*Config.*	[2]*Phases*	[3]d_p *(μm)*	c_s *(vol%)*	[3]*h/d*	[4]*Re*	[5]*Method*
Yoshida et al., 1990 ‡	Plane (conf)	Air – Glass	48.9	0.1	8 □	10,000	LDA [1a, 1b, 2 & 3a]

Table 2-7 Summary of reported experimental data for particle-laden impinging jets, in the radial wall jet region.

See key / notes for Table 2-1, page 16.

2.7 Summary / Comments

The number of entries in the data tables (on pages 16, 20, 26, 31, 34, 36 and 37) as the literature review progresses through each of the three regions of the impinging jet drops quite dramatically. It is clear to see from this reduction in the number of available sources of data, as we progress through the jet as well as, by the addition of particulates for particle-laden flows. Even the single-phase impinging jet data sets, no worker has explored all 3 regions of the impinging jet, especially including jet outlet conditions, so crucial to the understanding of the development of the turbulent impinging jet. The work contained within this thesis attempts to address this void in a systematic way. Firstly, through providing a single-phase benchmark. Secondly, exploring the effect of jet-to-plate spacing on a particle-laden turbulent impinging jet. Thirdly, studying particle size effect, and finally, introducing initial testing using fluorescent particle image velocimetry (fPIV) to measure the turbulence modulation effect of particles on the carrier fluid.

Chapter 3
Physical Modelling

Impinging jets are extensively used across many industries. However, the study of two-phase, solid-laden jets has been primarily focussed on computational modelling, although few papers have appeared in the literature. Accurate physical modelling of any engineering system, including free and impinging jets, can serve to aid computer model formulation and validation, the determination of operating requirements, the evaluation of plant throughput requirements, and the optimisation of process operations as well as providing support in design. The primary application requirement of the physical modelling programme discussed here will be in the formulation and validation of computational models.

Physical modelling of turbulent solid-liquid and liquid only jets will be performed to explore the effects of process and material variables on flow phenomena. Particle size effects will be explored, as will the jet height above the impingement surface. The experimental design, the first phase in the development of the physical modelling programme, is discussed in Section 3.1.

The next phase of programme development is the experimental rig design. This design process must not only take into account the experimental variables to be explored but must also consider health, safety and environment issues as well as the practicalities of construction, commissioning, performing the trials, and ultimate decommissioning and dismantling. The design of the impinging jet rig is discussed in Section 3.2.

For any physical modelling activity, in order to gain appropriate insight into the work, measurements must be made. These may range from simple observations by operators, to highly sophisticated, non-intrusive techniques where very detailed data can be generated. The measurement technique, particle image velocimetry (PIV), employed on the test jet rig is discussed in Section 3.3. An exploration of the application of PIV for the acquisition of instantaneous velocity vector data of turbulent impinging jets was undertaken, and limitations or areas of difficulty identified, discussed in Section 3.4. Test particle selection and characterisation is discussed in Sections 3.5 and 3.6.

3.1 Experimental Design

A reasonable amount of physical modelling of the flow phenomena of single-phase impinging jets has been published to date, although this is significantly less than that available for free jets. Much has been done previously investigating heat transfer within the impinging region of both gas and liquid jets where high Nusselt numbers are found, although papers reporting flow data are less common. In contrast, data on two-phase impinging flows are very rare (refer to the Literature Review in Chapter 2). The experimental design discussed here aims to address this void in a systematic fashion to investigate the effect of both process and material variables.

Developing a good experimental design is key to successful experimental research. In order to achieve this it is necessary to clearly identify the desired output which in this instance is the development of datasets for the formulation and validation of computational models. Measurements of the turbulence properties of each phase are required: the liquid properties from single-phase trials, and both the continuous and dispersed phases from the multi-phase trials. The data of particular interest, in both the axial and radial directions, are the mean velocities, $\overline{U}$ and $\overline{V}$, the root-mean square (RMS) of the fluctuating velocities, u' ($=\sqrt{\overline{u^2}}$) and v' ($=\sqrt{\overline{v^2}}$), and the shear stress ($\overline{uv}$).

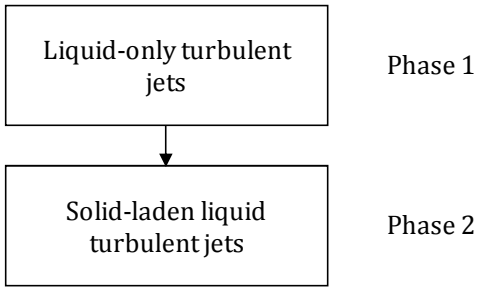

Figure 3-1 Schematic of the two phases of the experimental programme.

The ultimate, long-term, goal of the experimental programme discussed here is to characterise the onset conditions for the mobilisation of a settled / consolidated sludge bed by the application of a turbulent impinging fluid jet.

Before trials on multi-phase jets are performed, a series of trials of liquid-only jets will be undertaken, see Figure 3-1. This set of trials will test both the experimental rig and the measurement techniques to be employed. The second phase of trials on solid-laden jets will examine the influence that the presence of solids in the jet flow has by comparing with the results from Phase 1.

3.1.1 Process Variables

No comprehensive investigation into process variable effects on the flow phenomena of impinging solid-liquid jets has been done previously. Hence, the array of variables still to be examined is extensive. In the context of heat transfer data, process variables such as jet nozzle diameter and type, height of jet from the impingement surface and jet Reynolds number have been investigated for both gas and liquid impinging jets (Jambunathan et al., 1992; Goldstein & Franchett, 1988).

The mathematical description of a turbulent jet requires the nozzle diameter d (or $2r_o$), axial distance x, and the jet outlet velocity U_o (Rajaratnam, 1976). As such, these variables are of immediate interest. There are also a great many other potential process variables which could be examined to further develop our understanding of solid-liquid turbulent impinging jet flows; these are introduced in Table 3-1.

Table 3-1 Tabulated range of process variables.

Potential Process Variables	Comments	
Jet line diameter d	$d = 2r_o$	Fundamental parameters used to describe turbulent jets as discussed in Chapter 1.
Jet outlet velocity U_o		
Jet volumetric flow rate Q	$Q = U_o \pi r_o^2$	Measured directly during the trials.
Jet Reynolds number Re	$Re = \frac{\rho U_o d}{\mu}$	Derived from the jet diameter d and outlet velocity U_o. Allows non-dimensional comparison.
Jet height above impingement surface h	The purpose of this work is to investigate impinging jets so varying the height of the jet above the impingement surface is of great importance.	
Tank diameter D	Only the impingement surface is to confine the flow, therefore these parameters must be sufficiently large to ensure they are not causing an obstruction to the flow.	
Liquid height H		
Jet firing duration t_{jf}	The development of most predictive methods to characterise jet flow assumes steady state, however, there is also interest in the initial development of the jet flow as well as the mobilisation of a settled sludge bed. Existing agitation systems such as those applied within the nuclear industry employ impinging jets through firing cycles so this parameter is of great interest.	
Settling / consolidation time t_s	The formation of any settled bed is dependent on the time the system is allowed to settle and consolidate – the longer the settling period to form the bed, the greater the consolidation of that bed until a maximum packing is achieved.	

3.1.2 Material Variables

For an engineering system where the process parameters are maintained constant, changes in the material physical properties will result in different flow phenomena. For multi-phase systems this effect is more complex than that of single-phase. Not only can each phase exhibit different physical properties but each of these properties may have a different influence on the other phases present, hence the interactions between these phases are also important. Table 3-2 shows the range of material variables considered for this programme of work.

Table 3-2 Tabulated range of material variables.

Potential Material Variables	Comments
Particle size d_p	These are key fundamental properties for any solid-liquid system.
Solids concentration c_s	
Particle density ρ_p	
Fluid viscosity μ_l	
Zeta potential ζ	For colloidal systems, ζ is a measure of the surface charge of the particles which can be manipulated by varying the pH, E_s and E_c. Such manipulations will either stabilise or destabilise a suspension as is described by the DVLO theory (Shaw, 1993).
pH	
Electrolyte species E_s	
Electrolyte concentration E_c	
Settling behaviour	$f(d_p, c_s, \rho_p, \mu_l, pH, \zeta, E_s, E_c)$ i.e., for a given ρ_p and μ_l, if d_p is very small and c_s is high we can expect hindered settling so that the settling is very slow. While if d_p is very large and c_s is low then there would be free settling and the particles would settle very quickly. Similarly if ρ_p is increased we would expect the particle to settle increasingly more quickly, and if μ_l was increased the resultant settling would be slower.
Solids packing fraction	$f(d_p, c_s, \rho_p, \mu_l, pH, \zeta, E_s, E_c)$ These variables are essentially different ways of describing a solid bed structure, i.e., for any cohesive material, the greater the solids packing fraction, the greater the shear / compressive yield stress until a maximum packing fraction is achieved when the gel point is met.
Shear / compressive yield stress	
Gel point	

3.1.3 Experimental Design Protocol - Variable Selection

As already seen there are a wide range of potential process and material variables. Thorough investigation of each of these variables would require an enormous experimental programme probably extending over many years. A programme of this magnitude would also be excessively expensive. To study all the variables noted would far exceed the time scale and scope of the current programme.

For the purposes of model formulation and validation, as is the primary purpose of this thesis, this level of detail is not necessary. A hierarchy of variables, both process and material, has been constructed (Table 3-3) to allow identification of the most important and interesting variables to focus our efforts. The hierarchy and assigned priority of variables tabulated below incorporates the top seven variables from Table 3-1 and Table 3-2.

Table 3-3 Hierarchy of variables and applicable experimental programme phase.

Process / Material Variable	Assigned Priority
Jet height above impinging surface h	1
Particle size d_p	2
Particle density ρ_p	3
Solids concentration c_s	4
Jet Reynolds number Re	5
Jet line diameter d	6
Settling / consolidation time t_s	7
Jet firing duration t_{jf}	8

By the end of this programme of work we will have developed our understanding of three impinging jets with h/d ratios of 2, 6 and 10, respectively. We will also explore the turbulence modulation in these jets due to the presence of particles with three mean sizes of 20, 46 and 69μm. In addition, any effects caused by particle density are also investigated.

The selection of h/d ratio brings us back to what we know about impinging jets, as outlined in Chapter 1 of this thesis. The axisymmetric impinging jet is characterized by three regions (Rajaratnam, 1976) as depicted in Figure 1-3; (1) the free jet, (2) the impingement zone, also known as the stagnation region/point, and (3) the radial wall jet. The free jet is the fluid flow from the nozzle, where it is allowed to expand freely. The potential core is within the free jet and is that part of the jet where the flow maintains its exit velocity, and is surrounded by a mixing layer which experiences shear, including turbulence, typically up to 5d from the nozzle outlet (Rajaratnam, 1976). A better

understanding of axisymmetric, multi-phase jets can be achieved through the study of positioning the impingement surface in strategic regions; h/d ratio of 2 is within the potential core, h/d ratio of 6 is just outside the core, and for an h/d ratio of 10 the jet flow has developed further before impingement. The h/d ratios of 2 and 10 are the outer limits of the measurement capabilities of the PIV used on the jet test rig, as is discussed further in Section (Section 3.3.3, page 64). And the ratio of 6 has been selected over 5 to allow comparison to the small quantity of data so far published (Cooper et al., 1993; Nishino et al., 1996; Zhou et al., 2007).

The choice of particle sizes investigated here is discussed in Section 3.5.1 of this thesis. The rig design, as discussed in Section 3.2, has been developed with sufficient flexibility built-in to allow the initiation of further physical modelling of those variables omitted as well as the variables selected for investigation within the scope of this work.

3.2 Rig Design

The development of an appropriate and effective rig design is vital to the success of this work. The design of the rig must allow sufficient flexibility to enable characterisation of the impinging jet while varying both process and material properties, as discussed in Section 3.1. Consideration of the advanced fluid dynamic measurement techniques to be employed and the locations where rig operations are to take place must also be made at the design stage, and incorporated.

3.2.1 The Jet Test Tank

The impinging jet tank is the centre-piece of the jet test rig, and hence the starting point for the rig design. The design of the tank had four main considerations to be taken into account: the variables to be studied, rig location, test materials, and measurement techniques to be used.

Rig operations were required to take place in a number of laboratories within the Institute of Particle Science and Engineering (IPSE). Rig construction and commissioning were to take place in the same wet laboratory as all future cleaning efforts required between periods of data acquisition. The development of the measurement technique and its deployment, and the single-phase trials (Phase 1) of the experimental programme, were to take place in one laser laboratory, while the data acquisition for the multi-phase trials (Phase 2) was to be undertaken in another laser laboratory. During periods of non-operation the rig had to be stored at another location within the faculty. To allow the manoeuvring of the rig between each of these facilities, the rig overall size was restricted to 1150mm by 500mm by 1750mm.

During laser measurements, as discussed in greater detail in Section 3.3, the jet test tank had to be shielded to comply with laser health and safety requirements. This shielding had to totally enclose the measurement area being studied and, as such, the tank was not accessible while performing measurements. In order to minimise the proportion of the rig not accessible during data acquisition the rig was designed in two sections: one part of the rig frame to house the jet test tank, with all other components housed outside the enclosed, or shielded, part. To allow sufficient space for all other components of the rig, other than the jet test tank, the overall rig volume was effectively split in two sections: the shielded section containing the jet test tank which was 500 by 500 by 1750mm, and the rest of the rig which was housed within the

remaining 650 by 500 by 1750mm part of the overall rig volume. This meant that the jet test tank maximum footprint could not exceed 500mm by 500mm.

Only the impingement surface, perpendicular to the jet line, was to confine the jet flow. Hence, the diameter or width, and height of the tank must be such that they do not contribute an obstruction. With the maximum diameter of the tank being set, a balance had to be struck between the jet diameter d and the tank diameter/width D so that the tank walls did not confine the jet flow. A 50d distance between the jet centreline and the tank walls was selected to ensure that within the measurement region of interest, i.e., up to 15d from the jet centreline, wall effects were negligible, verified by data acquired at the outer region of the radial wall jet in Section 4.4.3. This set a maximum d of 5mm to comply with the maximum footprint of 500mm by 500mm. Figure 3-2 shows the dimensional design for the jet test tank for a jet line diameter of 5mm, and also for a d of 4mm. The use of a jet line with an even smaller diameter was not considered as it was deemed to be too small and restricted the possible flow Reynolds numbers and particle sizes.

When investigating single- and multi-phase flows, unless it is the focus of the study, it is important that the turbulent pipe flow within the jet line, but before the nozzle is reached, is allowed to develop fully. The smaller the pipe diameter used, the smaller any particles must be to allow this. Again, a balance must be struck between using tracer particles small enough to follow the flow fluctuations for the single-phase tests while still being large enough for the measurement technique to detect. The particles to be used in the multi-phase trials are to be larger still, while avoiding introducing the further complication of wall effects.

As can be seen, the non-dimensional specifications for both configurations provide 50d from the jet centreline to the inside of the tank walls, 110d from the impingement surface to the fluid surface, and an additional 30d of ullage. It is important to note that these are internal dimensions and the tank wall thickness has not yet been taken into account; this will be discussed below.

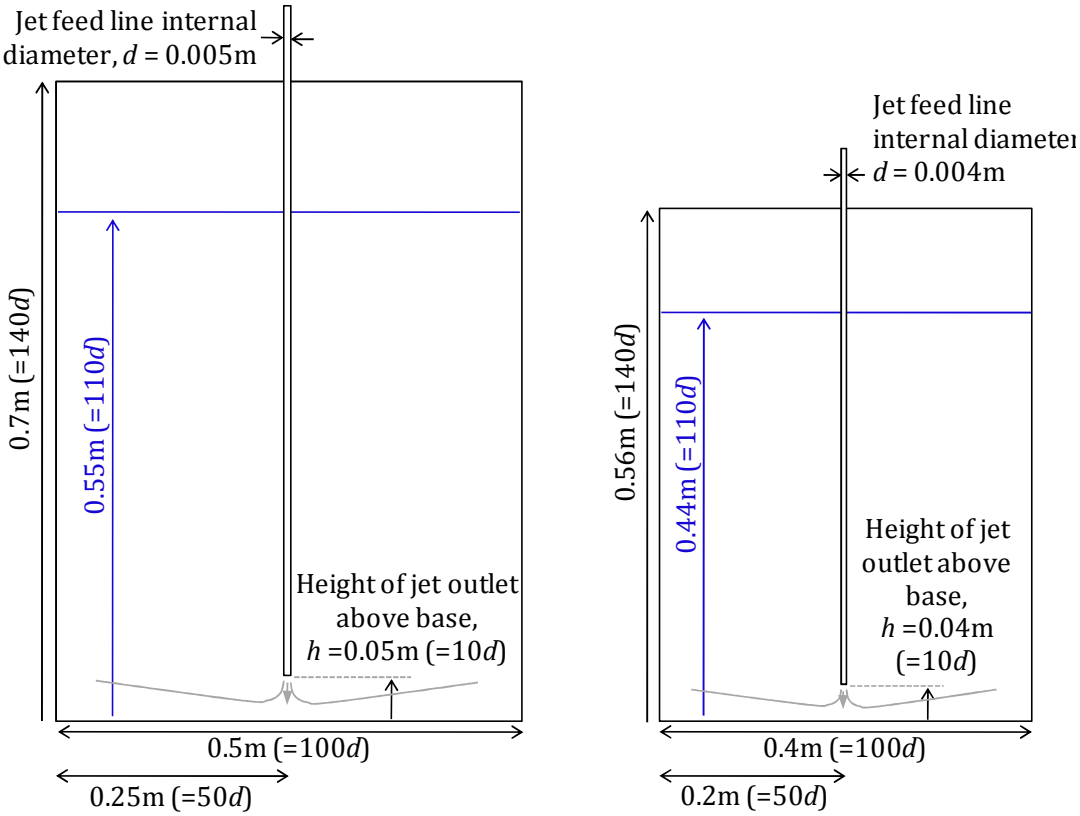

Figure 3-2 Jet test tank dimensional design options for jet line diameters of 5 and 4mm.

The experimental design also required the height of the jet above the tank base to be altered, as discussed in Section 3.1.3, and set at h/d ratios of 10, 6 and 2. The headroom above the tank also had to allow for the variation in height of the jet line, which was suspended perpendicularly above the centre of the tank base.

Many different nozzle configurations are available, the one most commonly reported in the literature for impinging jets (see Chapter 2), a long pipe generating a hydrodynamically fully developed jet, was used.

The region of turbulent pipe flow downstream of a point beyond which the flow is invariant is considered to be fully developed. The length of pipe, known as the entrance length (L_e), before fully developed flow is achieved for turbulent conditions typically ranges from 18d to 95d (Munson et al., 2002). The entrance length is a function of Reynolds number,

$$\frac{L_e}{d} \approx 4.4\,Re^{1/6} \qquad (3\text{-}1)$$

For a Reynolds number of 10,000 as used within this body of work, the entrance length is calculated to be 20.4d. A jet line length (L_j) of 150d was used to ensure that fully developed turbulent flow had been achieved upstream of

the jet flow forming. The jet line was held in position through a framework secured to the top of the tank. The material selected for the jet line was stainless steel due to its resistance to water corrosion.

The operational level within the tank was maintained by locating an overflow port at 110d above the base.

As with the construction of any experimental test system, cost is also a consideration. In addition to designing in the flexibility to examine a range of variables as previously discussed, there are obvious cost implications with the set-up of any experimental system, and in this instance it was not only the cost of the fabrication of the rig itself but the purchase of the test materials that also had to be factored into the total cost. The test materials required to generate data suitable for computational model validation are a significant investment. Colloidal materials with small particle size and shape distributions are also very expensive. Therefore minimising the quantity required had significant cost benefits. The design of the rig flowsheet included this consideration, see Section 3.2.3.

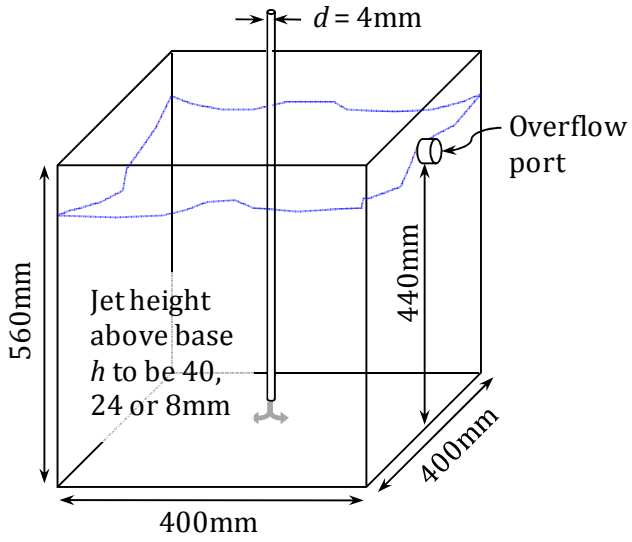

Figure 3-3 Schematic of final jet test tank design, internal dimensions.

The tank design was also guided by the measurement technique to be employed. The non-intrusive PIV technique employed here is discussed fully in Section 3.3. For now, it is only necessary to know that this requires the walls of the tank to be transparent, colourless, scratch-free and with good optical properties such that they do not reflect or deflect the laser sheets the instrumentation uses, or distort the camera images.

Taking all of these issues into consideration, the final design for the jet test tank was based on a jet line diameter d of 4mm, Figure 3-3, of a size given in the figure, and fabricated of 10mm thick Optiwhite[1] glass.

3.2.2 The Feed and Overflow Systems

Many different engineering systems are used across a wide range of industries for the mixing, storage and transportation of solid-liquid systems. The key objectives of the feed and overflow systems on this rig are to firstly supply a well-controlled, well-mixed solid-laden flow. And secondly, as the datasets generated from this rig will be used for the validation of computational models; the particle properties such as size and shape, as well as surface properties, need to be consistent and well characterised. Of primary importance to the overflow / solids recovery system is not surprisingly the recovery and re-use of the solids. The test simulant materials are expensive and are, therefore, re-used wherever possible.

To efficiently and reliably supply the required level of agitation, two key factors were important when considering the feed and overflow systems;

- Mixing/storage – mixing intensity is important to ensure a well mixed feed to the jet test tank, along with the need to minimise any distortion, or destruction, of the particles. Air entrainment must also be avoided as liquid-solid flow is to be measured, not gas-liquid-solid flow.
- Transporting – the method of inducing and maintaining flow must be controllable. Here again the distortion must be minimised.

Pumps need to:

- Satisfy feed rates/velocities, with variable speed.
- Smooth delivery, with no pulsing.
- Handle solids at low concentrations.
- Batch operations (only operated during office hours).

[1] Low iron extra clear float glass with very high light transmission.

3.2.3 Detailed Rig Design, Frame Development and Level Control System

The flowsheet for this experimental rig underwent several revisions. In its most basic form it was simply,

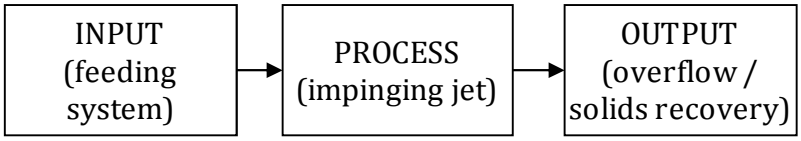

Having reviewed the available options for the input (feed system) and output (overflow / solids recovery system) and concluded that mixer tanks and centrifugal pumps would be most suitable, the simple rig design is schematically shown in Figure 3-4.

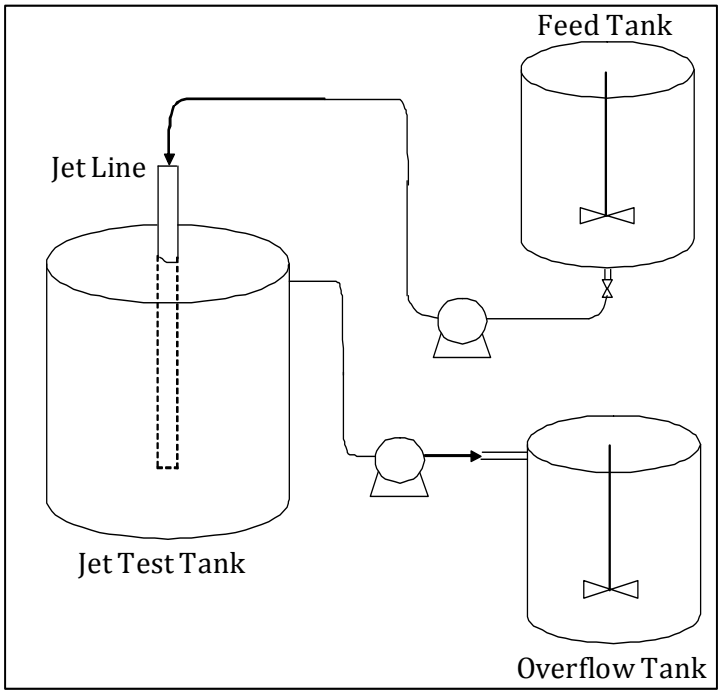

Figure 3-4 Basic schematic of the impinging jet test rig.

A cyclic design was applied, and is detailed in Figure 3-5. As can be seen, starting from the feed tank, test simulant is agitated by a mixer impellor before being pumped through a flowmeter and control valve to the jet test tank (JTT). The control valve is used to set the required flowrate for trials. The level in the JTT was maintained by the use of an overflow line. From the overflow tank the simulant is pumped back to the feed tank. In addition to a pump (noted as P2), this process line has a three way valve for bleeding of air or to be used as a drain line, and a non-return valve to prevent the process liquid from siphoning back into the overflow tank when P2 is not in operation.

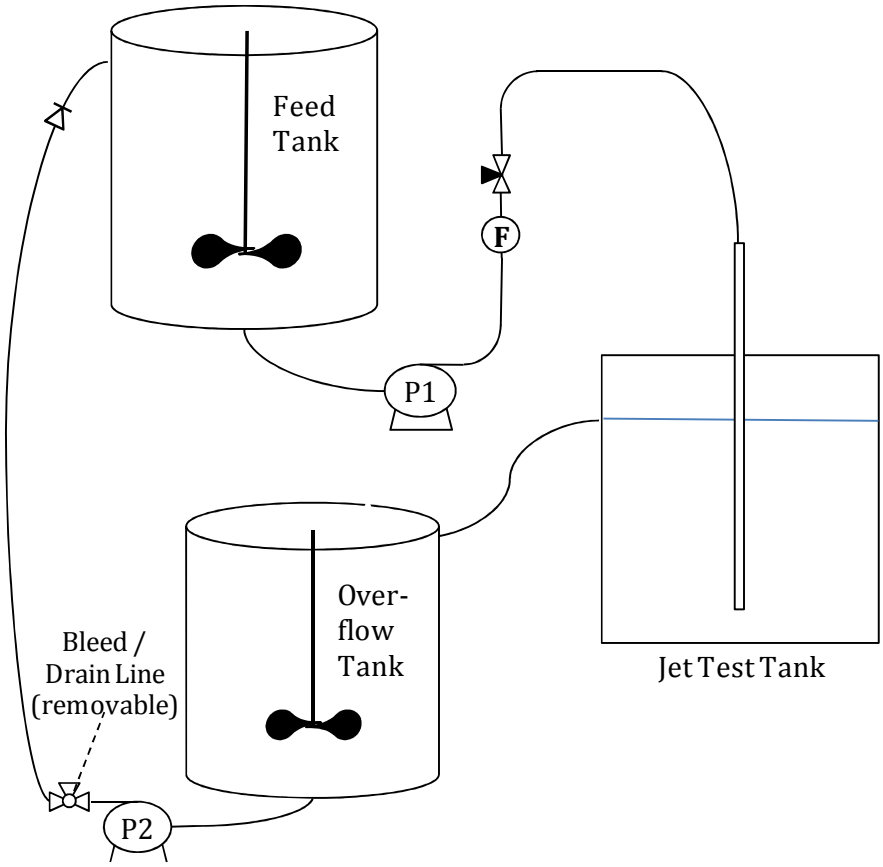

Figure 3-5 Detailed schematic of the impinging jet test rig.

The rig design incorporated solutions to satisfy the necessity to manoeuvre it between different laboratories, and laser safety requirements. As such the development of the rig frame was as important to the success of this research as the rig unit operations.

As previously discussed, the rig frame was divided into two sections; one side housing the jet test tank which must provide shielding to satisfy laser safety requirements, and the other housing all other rig components.

The shielded side of the frame houses the JTT and the jet line support structure. The height of the tank from the floor is determined by the height of the laser bench, a key starting point for the frame design. The pumps which transfer fluid from the feed tank to the jet test tank, and from the overflow tank back to the feed tank, are not self-priming so must be installed such that the static head of liquid in each process line is sufficient to prime their respective pump. Also, the overflow line from the JTT to the overflow tank was gravity fed. A 1" bore line was used to ensure there were no restrictions to the overflow from the jet test tank while it is shielded and inaccessible. As this line is gravity fed the overflow tank inlet port must be below the jet test tank overflow port. Due to the limited volume available in the unshielded side of the frame, these were the key

requirements to satisfy in this design with regards to the positioning of the unit operations. The arms of the frame were used to mount the flowmeter, control valves and feed tank mixer. And the process lines, flexible re-enforced tubing, were secured to the frame. All components of the rig had to be secured to prevent any tripping or catching hazards during all of the manoeuvres the rig made throughout IPSE.

The jet test tank vertical position is adjusted by use of a lifting system incorporated into the rig design. When working with laser systems it is considered best practice to move the position of the measurement area to be studied rather than the laser system. This is true from a laser health and safety perspective as well as a measurement one. Successful acquisition of PIV data is dependent on very sensitive alignment of the laser sheet and CCD camera, contributing a considerable time investment. Therefore minimising the frequency of performing this alignment operation is favourable. The built-in lifting capability, coupled with the manoeuvrability of the rig due to its wheels, allows the jet test tank to be positioned to allow the measurement of flow phenomena at any position within the tank. Although not a prime focus of this programme of research, this would in future allow measurements to be made within the re-circulation region of impinging or free jets if desired. It will also allow the rig to be adjusted to accommodate the use of laser systems within different laboratories with different laser bench heights (which has been an advantage during the progress of this work).

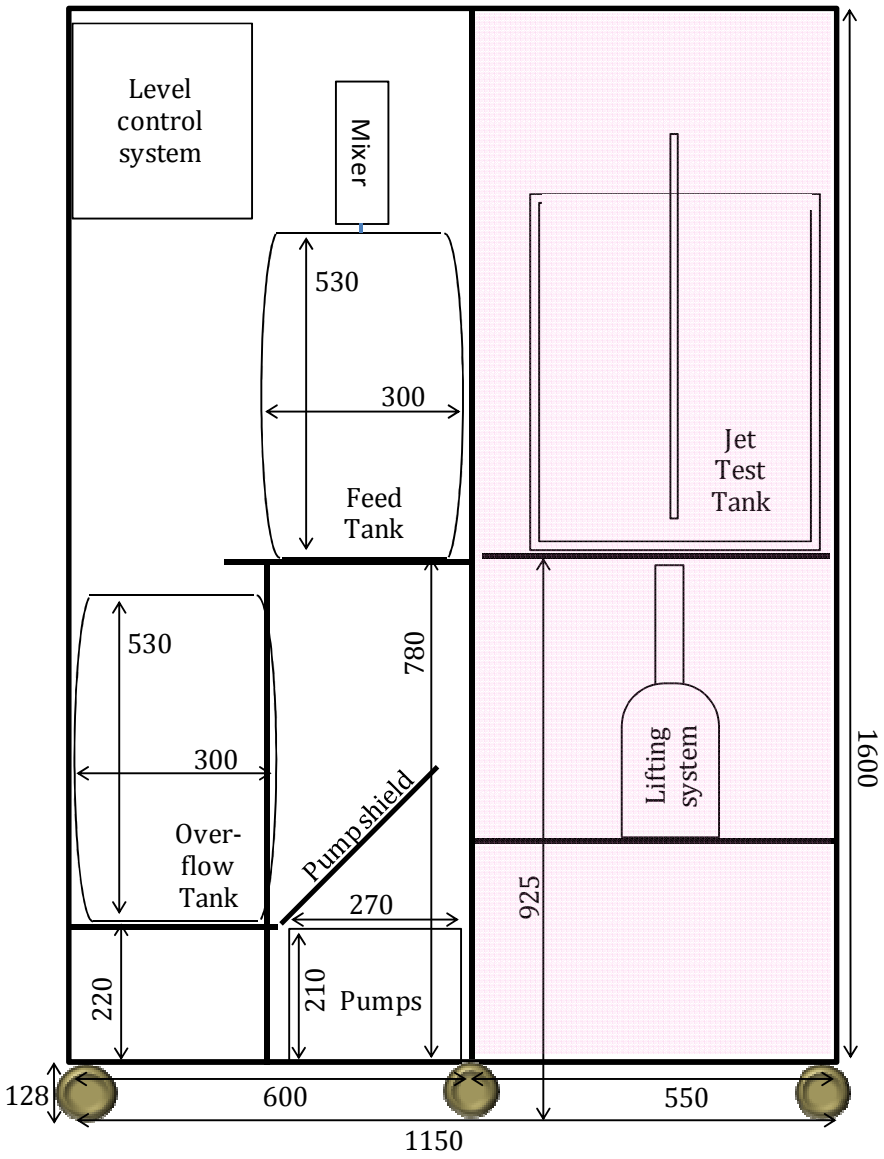

Figure 3-6 Schematic of rig frame design showing positioning of all three tanks, pumps, level control system and lifting system (dimensions in mm).

A detailed schematic of the rig frame is seen in Figure 3-6 showing the location of the main unit operations. The rig frame had to accommodate a number of requirements;

- Manoeuvrable between different laboratories – lockable wheels were installed.
- Jet tank lifting system.
- Laser shielding – The side of the rig housing the test tank must be shielded during laser measurements, shaded section of schematic.
- Control box mounting.

3.2.4 Rig Construction and Operation

The construction of an experimental rig for the purposes of research is always an iterative process. The requirements of such a system seldom lends itself to using off-the-shelf apparatus. As with the nature of research, as more is explored and learned it is often necessary to continue developing the experimental set-up. This project was no different. A lot was learned during construction as well as commissioning of the rig, and even the initial runs undertaken helped develop the rig to that shown in Figure 3-7.

As already described previously within this section, the rig was designed and constructed to be contained within a manoeuvrable framework which can be seen in Figure 3-7(a) and (b). The rig was developed by proportioning the frame into two sections, as previously noted.

Some of the laser shielding, the black sections, can be seen behind, and above, the tank in image (a), while the shielding to the right of the tank can be seen in (b). The shielding was made up of sheets of mild steel painted matt black on the inside where the laser sheet was operational, and blue on the outside to match the rest of the rig. During laser operations on the rig, the jet test tank was completely encased by screwing more of these steel sheets to the frame all around the JTT to prevent any laser light from escaping where it might cause a risk to persons working within the laboratory. The shielding was screwed in place for the laser operations to provide a secure shield from the risk associated with working with lasers. It can, however, also be removed to allow operations such as rig set-up and cleaning, and for the purpose of capturing images for illustration. It is essential, however, to note that during laser operations this shielding had to be in place to satisfy health and safety requirements. Laser operations could not commence without all of the shielding being in place.

The right side of the rig in Figure 3-7 (a) and (b) houses all other components of the rig, with the upper of the blue drums being the feed tank and the lower the overflow tank. Both pumps were secured to the base of the frame and the pump shield was fixed to the overflow tank shelf.

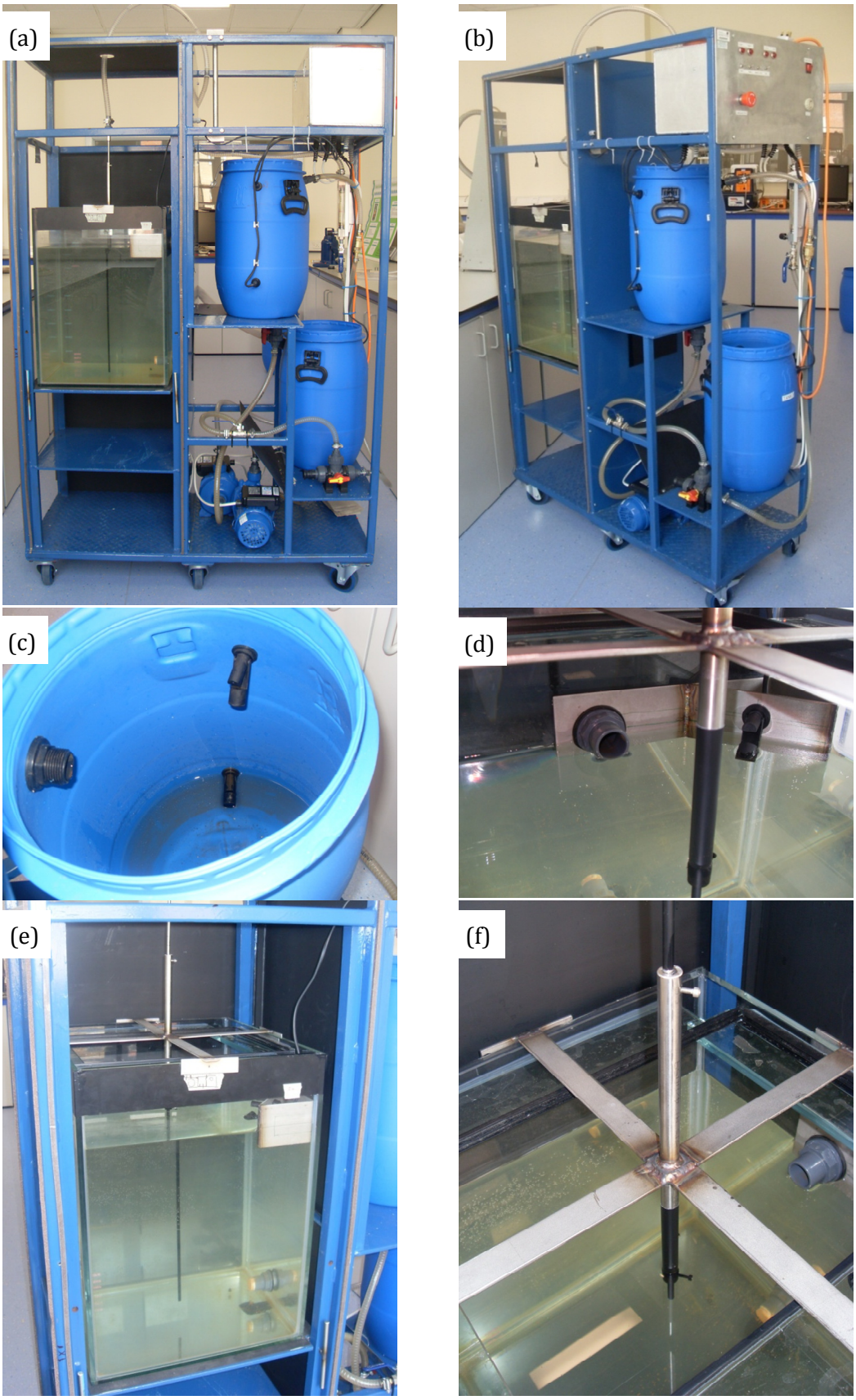

Figure 3-7 Photos of the (a) and (b) jet test rig, (c) level float switches in overflow tank, (d) overflow port and level float switch in jet test tank, (e) jet test tank, and (f) jet line and jet line support.

One of the process variables this rig was developed to allow exploration of the jet Reynolds number, achieved by controlling the flowrate. The flowmeter and needle valve can be seen secured to the far right, vertical arm of the frame. Alongside the flowmeter is the non-return valve on the line between the overflow and feed tanks to prevent liquid siphoning back to the overflow tank when pump 2 is not running. During experiments a mixer was added to the feed tank which was secured to the vertical stainless steel rod seen above and slightly to the left of the feed tank, and plugged into the back of the level control system.

The level control system, more clearly seen in (b), was positioned in the top right of the frame. All electrical components of the rig were controlled by this system, as well as a series of level switches like those seen in Figure 3-7 (c) and (d). Two operational schemes were programmed. Manual mode allowing each pump to be operated as and when required for operations such as rig set-up or cleaning. In this mode the level switches are not activated. Auto mode was engaged on all trials undertaken. The key requirement for the trials was to achieve a well controlled feed to the impinging jet, and to maintain the operational level within the test tank. The latter requirement of maintaining the level within the tank was achieved through the gravity overflow line via the overflow port seen in Figure 3-7 (d). The former requirement was achieved through the auto mode of the control system. The Feed Pump (P1 on Figure 3-5) would continue running unless the level in the feed tank exceeded the upper level switch, or was below the lower level switch, in which case both pumps were switched of and a buzzer sounded to alert the operator. To maintain the operation of P1 and hence the impinging jet supply into the test tank, the Return Pump (P2 on Figure 3-5) switched on and off according to the activation of the level switches in the overflow tank. The overflow tank filled via the overflow line from the JTT until the upper level switch activated, switching on pump 2, and continued to recycle its contents back into the feed tank until the lower level switch was passed and the pump was switched off. During laser trials when the JTT was enclosed within the shielding and not accessible by the operator, a level switch installed on the JTT switched off both pumps and alerted the operator if the level exceeded the location of the overflow port, Figure 3-7 (d).

The jet line support on the top of the jet test tank allowed the jet height above the base to be adjusted, Figure 3-7 (e) and (f). The jet line and part of the support that may have come into contact with the laser sheet were painted matt black. Securing screws hold the jet line at the required height and

alignment to tank base was achieved by adjusting any of the four fixing arms across the top of the tank.

The impinging fluid jets to be considered as part of this work will be used to mobilise settled sludge beds. However it should be understood that when solid-laden jets impinge onto a surface they are likely to have an effect on the solid surface beneath. Slurry erosion-corrosion, due to impacting solid particles during transportation of solid-liquid flows, is a common problem in all slurry handling industries. This phenomenon, called tribo-corrosion, is corrosion in association with mechanical degradation processes such as abrasion and erosion.

Plant machinery such as pumps, valves and agitators can experience significant material loss through erosion-corrosion (Zheng et al., 2000). The rate of material loss is dependent on many factors including the properties of the impacting particles, the surface properties as well as the aqueous environment. Neville and McDougall (2002) showed that material loss substantially increased when the solids loading of the jet was increased, similarly when the temperature was raised from 18 to 50^{o}C. Jana and Stack (2005) produced material performance maps for a number of pure metals for oblique and normal solid impact angles. With increasing pH and electrochemical potential of the aqueous environment Jana found the overall material loss change was dependent on the metal surface being impacted. The erosion-corrosion effects of impinging jets are not within the scope of this work so it not discussed any further. They are however issues that may impact the long-term operation of the Jet Test Rig, in particular the condition of the tank base where impingement occurs, and so routine inspections and maintenance will be required.

3.2.5 Alignment and Calibration

The alignment of the jet line to the tank base was critically important to allow the acquisition of good quality impinging jet data. The jet line support frame on the top of the jet test tank allowed the jet line to be aligned to the base of the tank by adjusting any of the four arms.

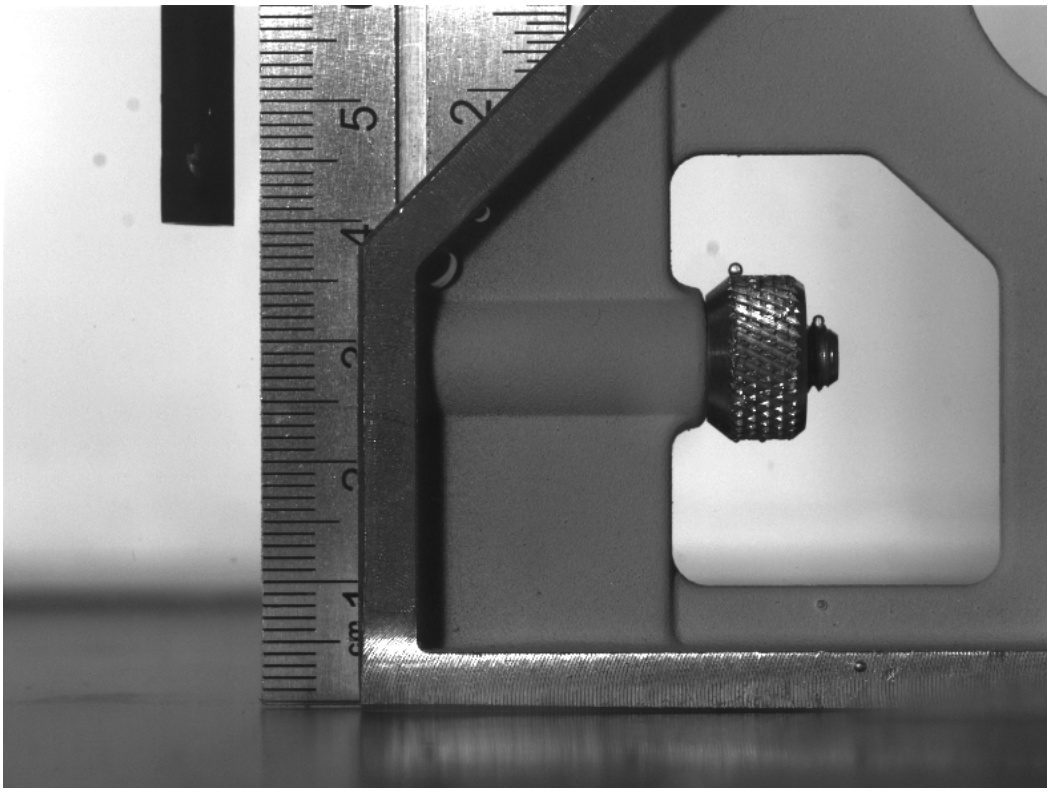

Figure 3-8 Calibration image captured by the PIV CCD camera.

A submerged carpenter's angle was used to align the jet line to the tank base. The jet height above the base was set using the graduated rule of the carpenter's angle. Figure 3-8 is a calibration image taken using the PIV CCD camera during set-up and alignment for the single phase trials at an h/d ratio of 10.

3.3 Particle Image Velocimetry (PIV)

The application of high precision measurement techniques is vital to the formulation and validation of computational models; a key driver for this work. Measurements for physical modelling can be made in many different ways depending on the level of detail and accuracy required, as well as the practicalities of the system under investigation, and can range from intrusive techniques which have a direct effect on flow phenomena to highly sophisticated non-intrusive techniques.

The ideal measurement or characterisation of any physical system will incorporate the application of non-intrusive techniques which do not interrupt or interfere with the dynamics of the system.

3.3.1 What is PIV?

Particle image velocimetry, or PIV, is a non-intrusive, whole-flow-field, laser optical measurement technique. Real-time, instantaneous velocity vectors of micron-sized particles are measured for a cross-section of the flow.

The basic components of a PIV system are a light source to illuminate the area of flow of interest, plus a method of capturing images of the flow. Most applications require the addition of small tracer particles which when illuminated will scatter light. The target cross-section of flow is illuminated by a pulsed laser light sheet, Figure 3-9.

A camera captures an image for each pulse and the image is divided into small interrogation areas (IAs). Each IA is cross-correlated between two subsequent frames, pixel-by-pixel, to produce an accurate measure of particle displacement and therefore particle velocity. Velocity vector maps are then generated by cross-correlating each IA of each frame.

Spatial resolution and dynamic range are important concepts in PIV measurement (Raffel et al., 2007). The size of the IA and the image magnification are balanced against the size of the flow structures to be investigated. Particles travelling further than the size of the interrogation area, with the pulse time Δt, will result in the loss of velocity data setting a limit to the highest measurable velocity. A general rule of thumb[2] is:

[2] Measurement Principles of PIV information sheet from Dantec Dynamics, the distributor of the PIV, website – www.dantecdynamics.com

$$\frac{\frac{s'}{s}v\Delta t}{d_{IA}} < 25\% \qquad (3\text{-}2)$$

where v is the instantaneous fluid velocity, and all other variables are depicted on Figure 3-9 below.

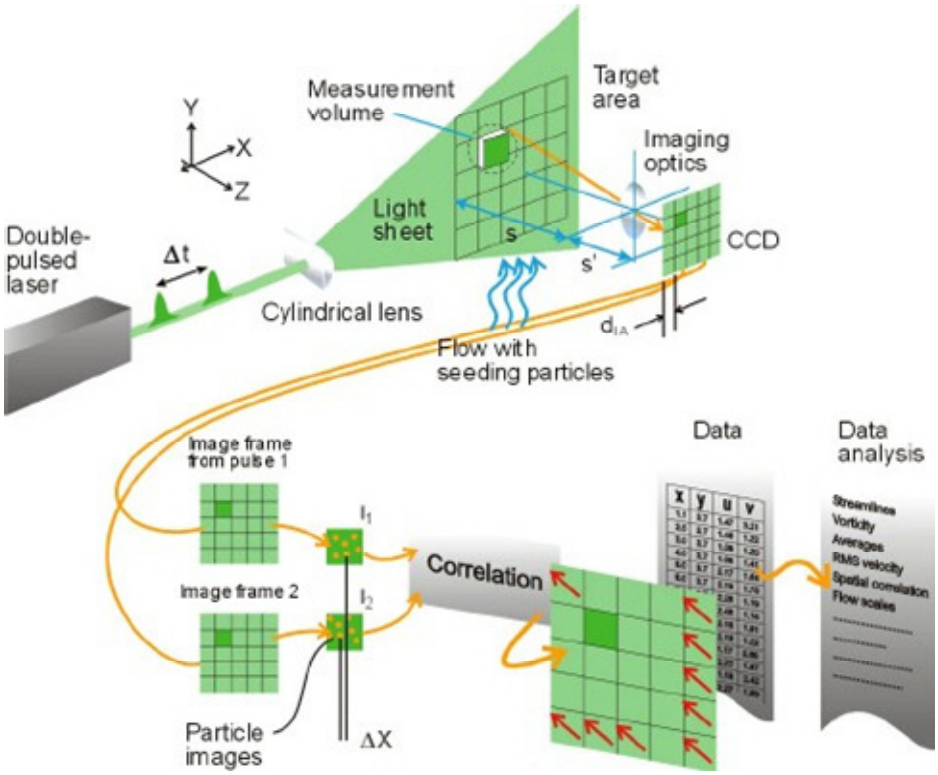

Figure 3-9 Schematic of particle image velocimetry (PIV) system[3].

The PIV is a measurement technique for the measurement of low solids concentration flowing systems, and it can experience difficulties at higher concentrations. The difficulty arises from obscuring the view of the camera by the flow of many particles in the space between the camera and laser sheet. Also, if the cross-section of the flow illuminated by the laser sheet is too concentrated, the image interrogation software may be overwhelmed.

This measurement technique has gained popularity over recent years and as such much has been written on its application. Grant (1997) summarises the scientific developments such as optical measurement techniques, image processing, flow visualisation and speckle metrology, which have allowed the evolution of PIV. Methods for analysing PIV images such as correlation

[3] Image taken from Dantec Dynamics, the distributor of the PIV, website – www.dantecdynamics.com

methods, spatial filtering techniques, and resolution, precision and dynamic range are also discussed, as are developments in PIV itself.

More practical aspects of using PIV have been reported by Stanislas and Monier (1997), with emphasis on set-up using the Nd:YAG laser, from source to recording medium. Issues relating to realising an adequate light sheet are addressed such as thickness of the light sheet, scattered light intensity effect, and depth of field (distance between the object plane and the lens, and image plane lens respectively), with theoretical tools offered to act as guidelines.

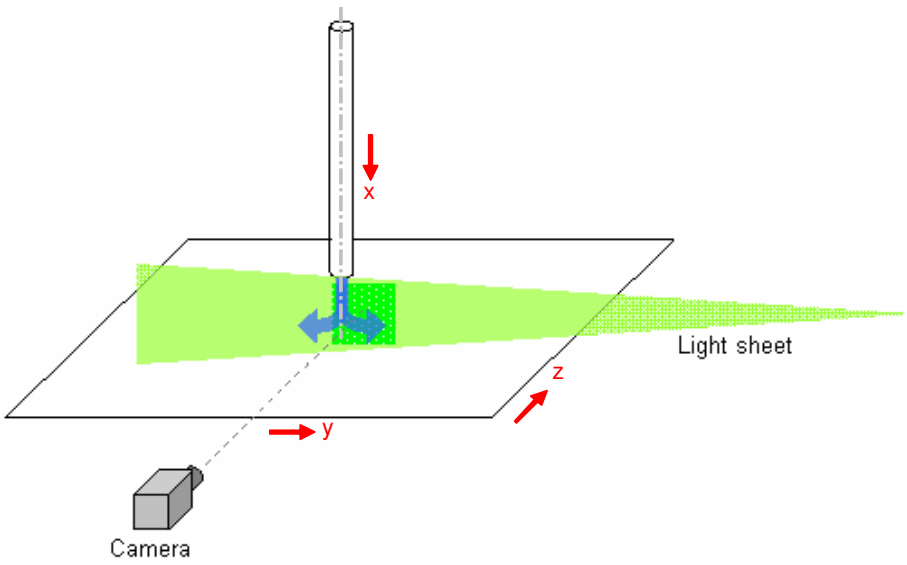

Figure 3-10 Impinging jet test rig PIV configuration.

The impinging jet test rig PIV configuration used within this work is given in Figure 3-10. Illumination from the laser light sheet is normal to the tank base (x-axis), dissecting through the centreline of the jet flow. The camera is set-up perpendicular to the light sheet overlapping the jet centreline.

3.3.2 Seeding, Illumination and Image Capture

PIV measurements, as with laser Doppler anemometry (LDA), rely on particles suspended in the flow to scatter light from the applied laser sheet (or cross volume for LDA) to provide velocity information. The accuracy of the data for measurement of the fluid phase is limited by the ability of the particles to follow the fluid flow. Tracer particles should be sufficiently small to follow the fluid flow yet large enough for the CCD camera to detect. A compromise is made between reducing the particle size, for quick response of the tracer particles in the fluid, and achieving a high signal-to-noise ratio of the particle images by increasing the particle size. The visibility of the particle depends on the 90^0

scattering characteristics of the particles, described by the Mie scattering theory.

To prevent the risk of bias in the measured velocities, the particle number density (number of particles per unit volume) should not vary in the flow (Buchhave et al., 1979; Melling, 1997). The seeding particles should therefore be uniformly distributed throughout the whole measurement area, including the nearly stagnant surrounding fluid. If the ambient fluid is not seeded, the velocity of fluid particles entrained may not be measured. Seeding the jet test rig was accomplished by the addition of test particles to the feed tank, and the rig allowed to run at steady state for a sufficient time (see Section 3.4.2 for rig steady state data) to best ensure the homogenous distribution throughout the entire rig. Melling (1997) reviewed a range of tracer particles for their scattering and tracking characteristics in both gas and liquid flows and found that the laser characteristics and light sheet dimensions indicated the interaction between the choice of particle diameter and scattering light intensity. Melling suggests a criterion for specifying the maximum particle size based on η, the amplitude ratio of the particle and fluid velocities, and $\overline{u_p^2}/\overline{u_l^2}$, the fluctuating energies of the time-averaged particle and fluid. Selection of test particles are discussed in Section 3.5.

The cross-section of flow of interest is illuminated by a monochromatic light sheet with high energy density (Raffel et al., 2007). The illumination source was a double-cavity Nd:YAG laser configured to generate 400 mJ pulses, firing at a rate of 15Hz with pulse width 4ns. A series of spherical and cylindrical lenses formed the divergent light sheet, an optical mirror was then used to re-direct the laser sheet through 90^0. The vertical light sheet, of approximately 1mm thickness, illuminated the measurement area within the tank, dissecting through the centreline of the jet flow, as seen in Figure 3-11.

Kadambi et al. (1998) highlighted the importance of the uniform light intensity of the laser sheet. Through investigating the limitations of using PIV to measure the particle size of calibrated monodispersed and polydispersed static particles, the variation of light sheet intensity was found to cause images of particles in regions away from the centre to appear superficially smaller, while particles found away from the focal point appeared superficially large. The current experimental system was set-up such that a central cross-section of the laser sheet illuminated the measurement area of interest, staying away from the fringes of the light sheet where the intensity is not uniform and the sheet width tails off.

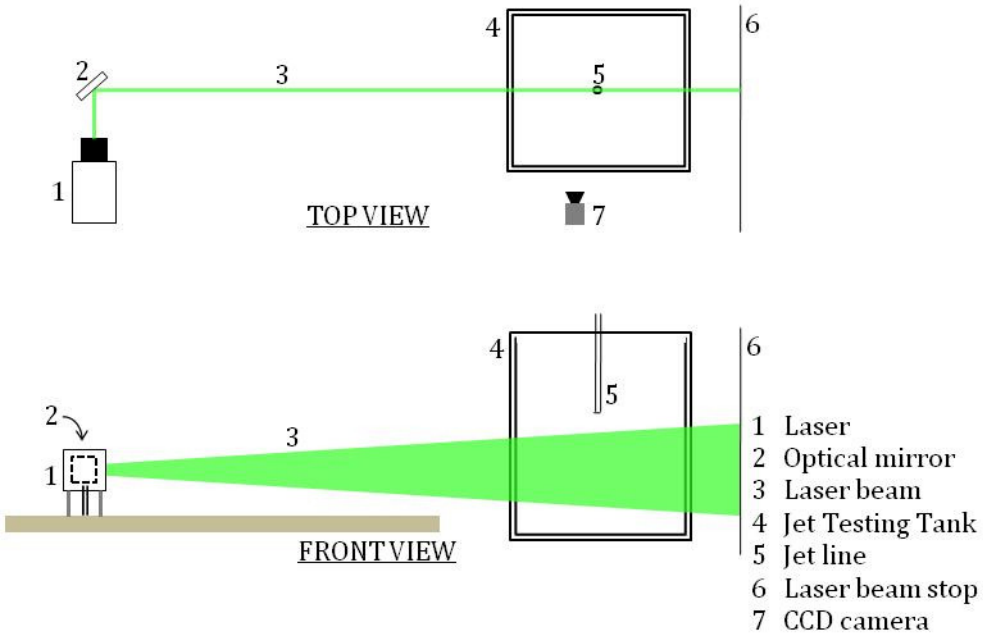

Figure 3-11 Schematic of PIV set-up on jet test rig.

The 12-bit cross-correlation CCD camera (model FlowSense 2M) was placed perpendicular to the laser sheet, with a resolution of 1600 x 1200 pixels, and synchronised to "fire" with each laser pulse.

3.3.3 Measurement Area, Computational Realities and Profile Locations

In studying impinging jets, it was of interest to explore not just a small part of the jet as other workers have focussed (Beltaos and Rajaratnam, 1974; Yoshida et al., 1990; Cooper et al., 1993; Dianat et al., 1996; Ushijima et al., 2001; Fairweather and Hargrave, 2002), but all three regions of the jet, from the potential core out to the far-field of the radial wall jet.

A calibration image gathered for h/d = 10 is shown in Figure 3-12. This was the largest jet-to-plate separation employed throughout this work. A radial distance from the jet axis of up to 15d was required to achieve the aim of measuring out to the far-field radial wall jet.

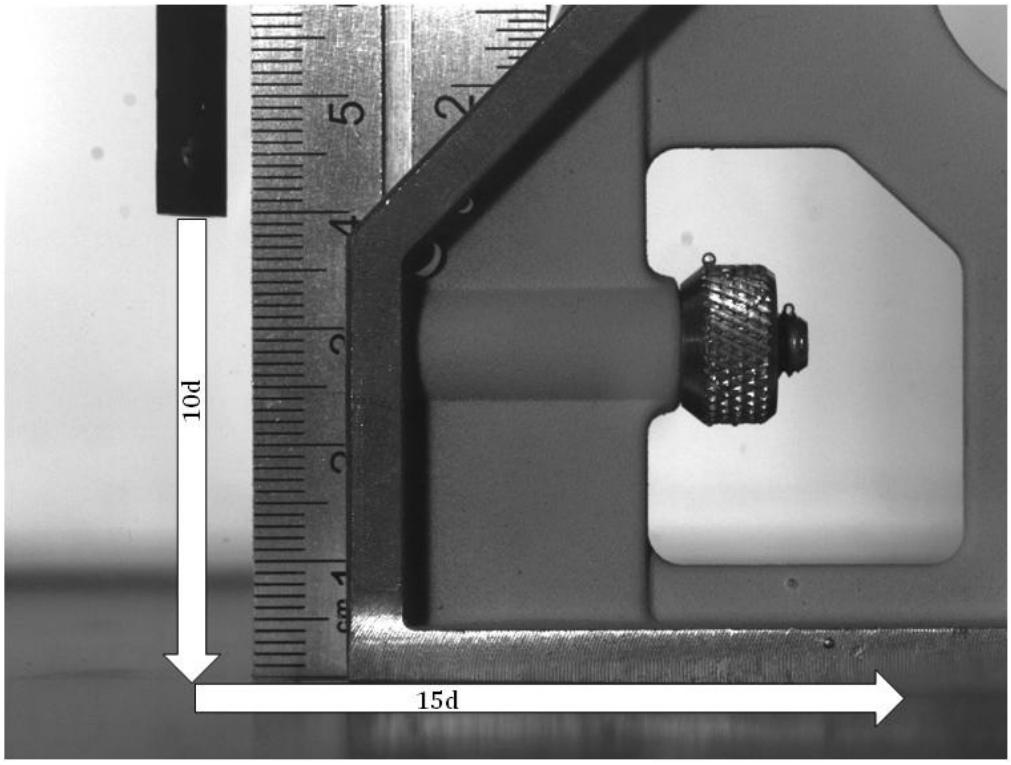

Figure 3-12 PIV measurement area dimensions for impinging jet at jet-to-plate separation of 10d.

Computational realities demand that a selection of velocity profiles be made. Data handling and processing, not to mention the memory requirements of the PIV technique, is extensive. Therefore it was necessary to be selective in terms of the number of profile locations investigated. A range of profile locations were selected, both horizontal and vertical, at strategic positions for each of three regions of the impinging jet, at all three jet-to-plate separation heights; viz. h/d ratios of 2, 6 and 10. Schematics of the horizontal and vertical profile locations are shown for h/d ratios of 2, 6 and 10 (top to bottom) in Figure 3-13. The vertical profile locations are common for each of the jet heights applied. The horizontal profiles have been selected to allow comparison of the stagnation line and radial wall jet region. Axial distances from the impingement surface, as well as the axial distances from the jet outlet, are common to all three jet heights. Additional comparisons are made possible at 2 and 5d from the jet outlet for the 6 and 10 h/d jets.

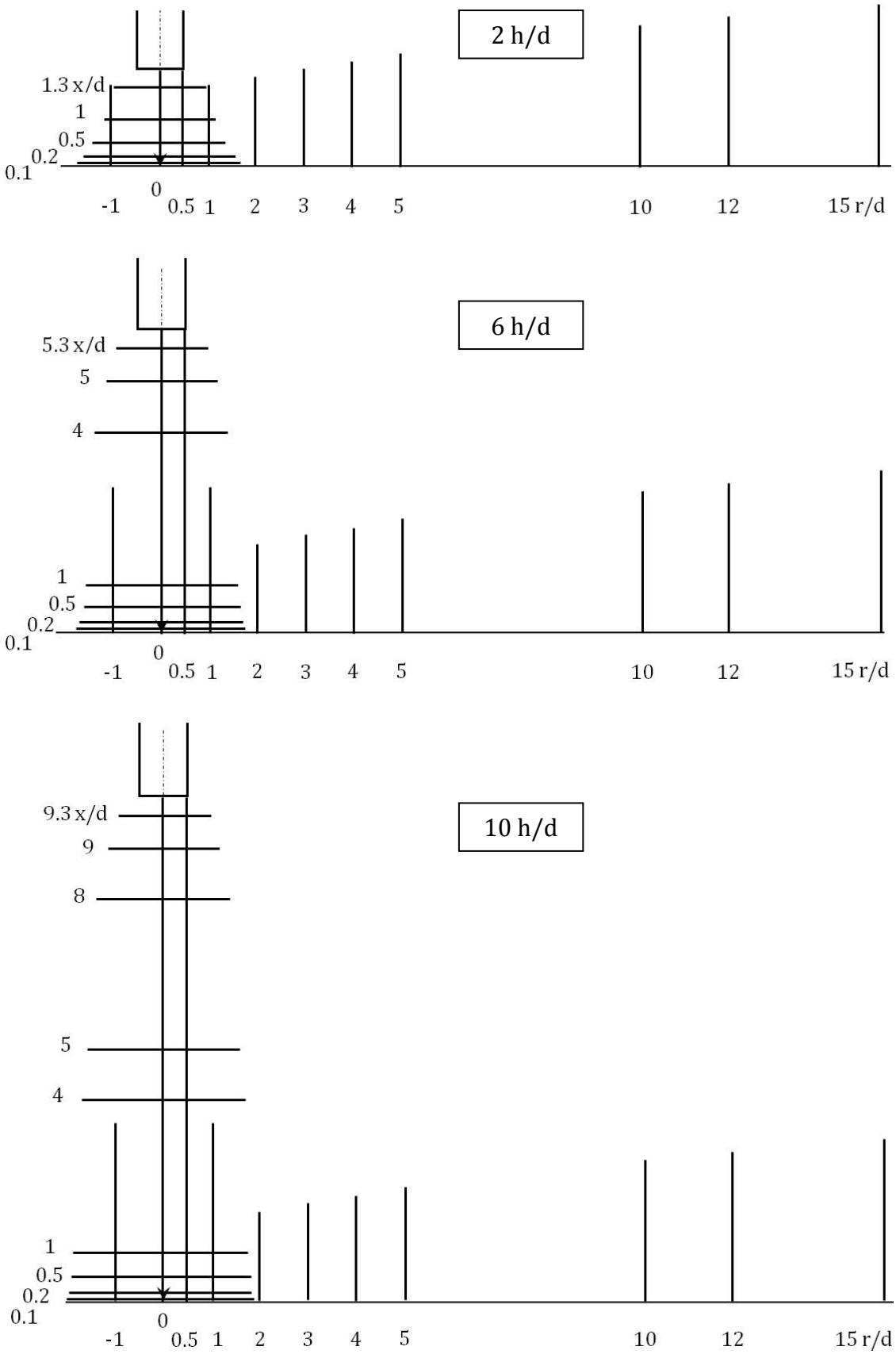

Figure 3-13 Profile locations investigated for an impinging jet with h/d ratios = 2, 6 and 10 (top, middle and bottom respectively).

3.3.4 Data Processing, from Raw Images to Vector Maps

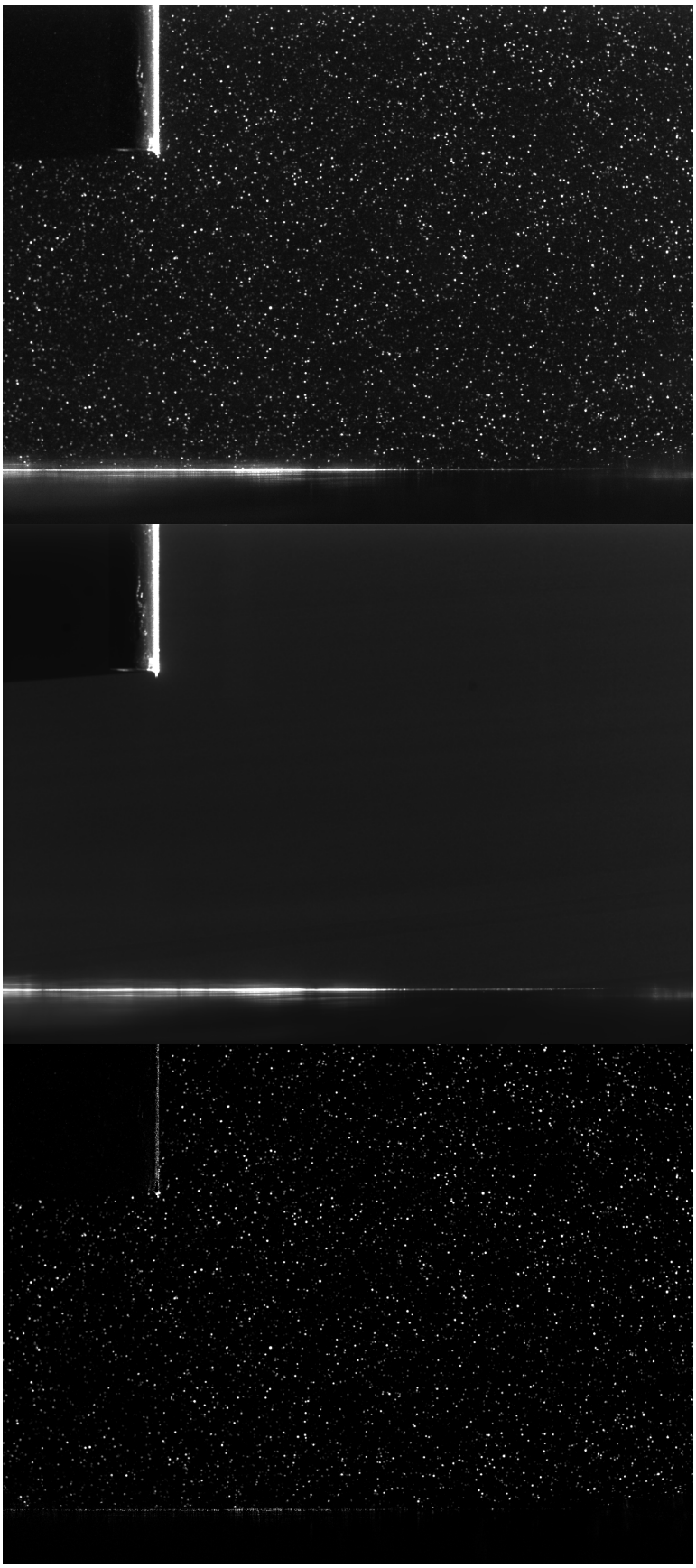

Figure 3-14 PIV data processing stages: Raw image (top), image mean (middle), and image arithmetic (bottom).

From the raw images captured by the CCD camera (Figure 3-14, top image), a series of processing steps were undertaken, the same methodology applied to all data acquired and presented within this thesis.

Captured flow images were pre-processed for background subtraction, in particular light scattering from the jet line and tank base, prior to subsequent processing. The average intensity of each pixel with identical x- and y-coordinates across the time series was calculated, and an image of the common background, referred to as Image Mean, produced as seen in the middle image of Figure 3-14. The jet line and tank base were both coloured matt black to reduce scattering of laser light in order to protect the CCD camera, the resultant mean scattering from these components are seen in this image. This stage would also identify any apparent 'hot pixel' CCD-sensor damage, were it present. Image arithmetic was next applied to subtract the Image Mean from all raw images, an example of which is seen in the bottom image of Figure 3-14.

As already discussed in Section 3.3.3, PIV data handling and processing, not to mention the memory requirements of the PIV technique, is extensive. The DynamicStudio[4] software platform allows a region of interest to be extracted (Figure 3-15, top image), referred to as ROI Extract, reducing the size and processing time of each image file. The ROI of the impinging jets under exploration within this thesis extended from the jet outlet (seen in the top left corner of this image) through to the far-field radial wall jet.

An adaptive cross-correlation technique was applied to each image pair to evaluate the velocity field. The method used, on the DynamicStudio software platform, was an automatic and adaptive method for calculating velocity vectors based on particle images. The method iteratively adjusts the size and shape of the individual interrogation areas (IA) in order to adapt to local seeding densities and flow gradients. The final IA was 16 by 16 pixels with 50% overlap in both the horizontal and vertical directions. The Universal outlier detection algorithm (Westerweel and Scarano, 2005) was applied to remove outliers. A velocity vector map for each image pair was then determined from the particle displacements and pulse time, Δt. The overall measurement field of view was typically 198 x 95 vectors, a total of 18,810 vectors. For the example shown as the middle vector map in Figure 3-15, 311 vectors were substituted (colour coded green). The pixel sizes were 0.053 or 0.054mm giving a spatial

[4] DynamicStudio is an advanced imaging software platform created by Dantec Dynamics Ltd for the acquisition and processing of PIV data.

resolution between data points of 0.0432mm ±0.004mm, resulting in an overall measurement area of approximately 85.50 x 41.02mm.

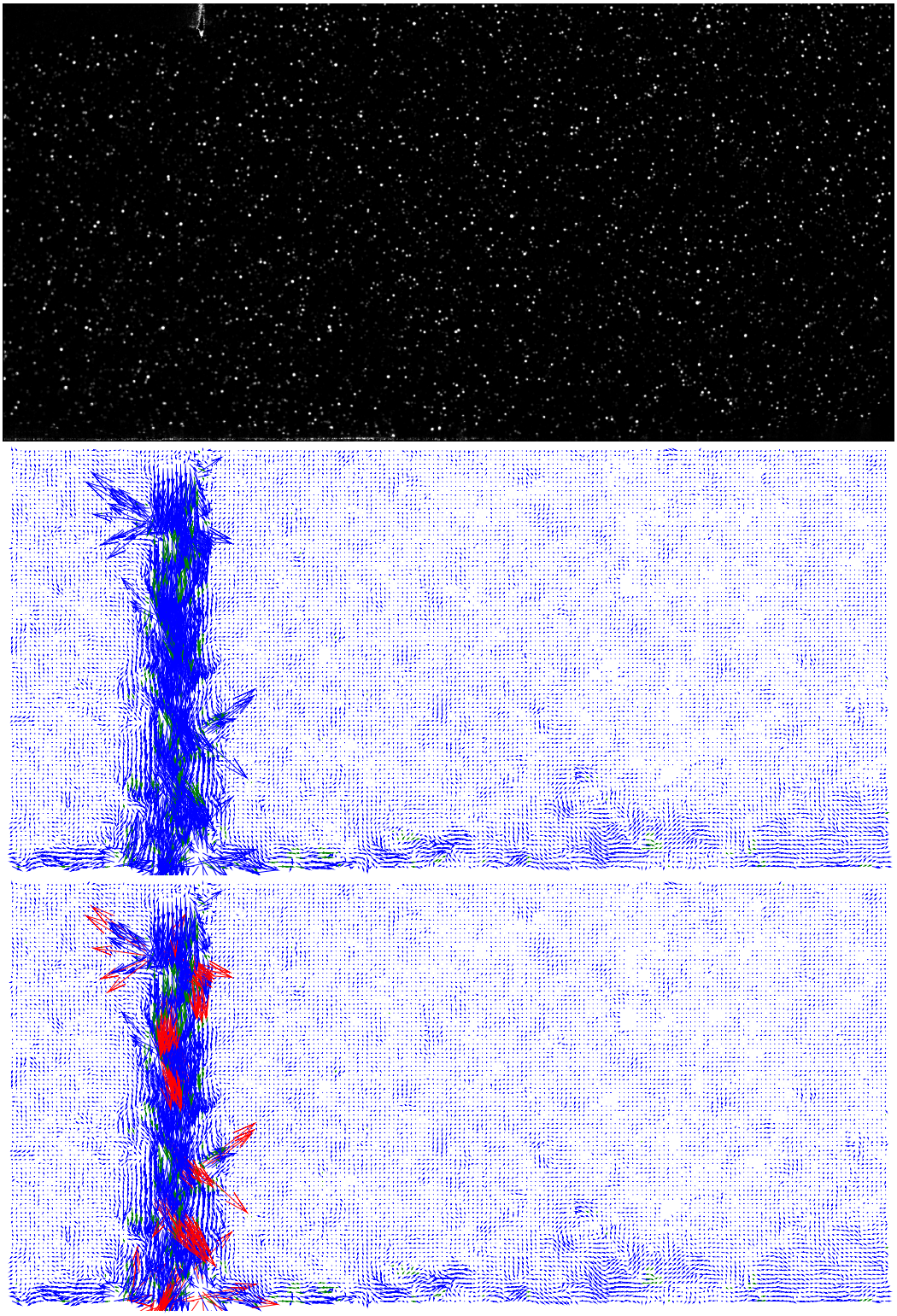

Figure 3-15 PIV data processing stages: ROI extract (top), adaptive PIV correlation (middle), and range validation (bottom).

During the data handling procedure of raw PIV data, a filtering stage to eliminate bad, or erroneous, velocity vectors, referred to as outliers, is necessary. Erroneous vectors can arise from the finite number of tracer particles, the interrogation area size, excessive particle displacements normal to the light sheet, large velocity gradients, or poor image quality. The PIV software platform DynamicStudio has a number of methods for doing this, and these are discussed here. Shinneeb et al. (2004) reports a method which uses a variable threshold by calculating the mean variation between a vector and its eight neighbouring vectors, allowing smaller thresholds to be used without significant loss of good vectors.

The vector map data were validated against an expected range of velocities. For the present measurements, the bulk mean velocity issuing from the jet line was set to 2.5 ms^{-1}, this was a Reynolds number of 10,000. Allowing for the velocity gradient across the diameter of the jet line, the local velocity at any point within the jet test tank could not have exceeded 3.5 ms^{-1}. Any vectors outside the range of ±3.5 ms^{-1} were rejected and colour coded red in the bottom vector map in Figure 3-15. In the present example, 121 vectors were rejected for this vector map at time t. This stage of validation does not substitute invalid vectors with an estimated value, further validation is required to do this.

To remove further spurious vectors, a minimum peak height ratio of 1.2 was selected, forcing more stringent conditions on peak identification for the subsequent determination of vectors. For high particle concentrations it is often satisfactory to use a value of 1.1, or if a very strict validation is required a value as high as 2 can be used[5]. From this validation stage, a further 289 vectors were rejected (total of 410 rejected vectors for this vector map of 18,810 vectors so far), in Figure 3-16 top vector map, again the rejected vectors are colour coded red. For the case of the impinging jets under investigation within this work, the spurious vectors rejected as a result of the data processing outlined are from the areas where fluid flow is detected and not the surrounding near-stagnant fluid.

The final validation compared each vector with the average of the local neighbourhood, 3 by 3. Vectors which deviate too much from their neighbours were replaced by the average of the neighbours as a reasonable estimate of true velocities. The larger the neighbouring area, the smoother the vector field

[5] Information yielded during measurement development efforts with the assistance of Dantec Dynamic Application Specialists.

becomes leading to a loss of resolution. For the given example in Figure 3-16 (middle vector map), 92 vectors were substituted.

The example instantaneous vector map shown in Figure 3-15 and Figure 3-16, at time t, had 410 vectors rejected and 403 vectors substituted, out of the original 18,810.

The final vector map in Figure 3-16 is the vector statistics which is simply a vector map of the mean velocity vectors averaged across the duration of the PIV measurement (see Section 3.4.1) disregarding the rejected vectors, colour coded to provide a visual representation of mean velocities.

Instantaneous velocity data profiles used within this thesis were taken from the moving average instantaneous vector maps, the methodology used is introduced in the following section.

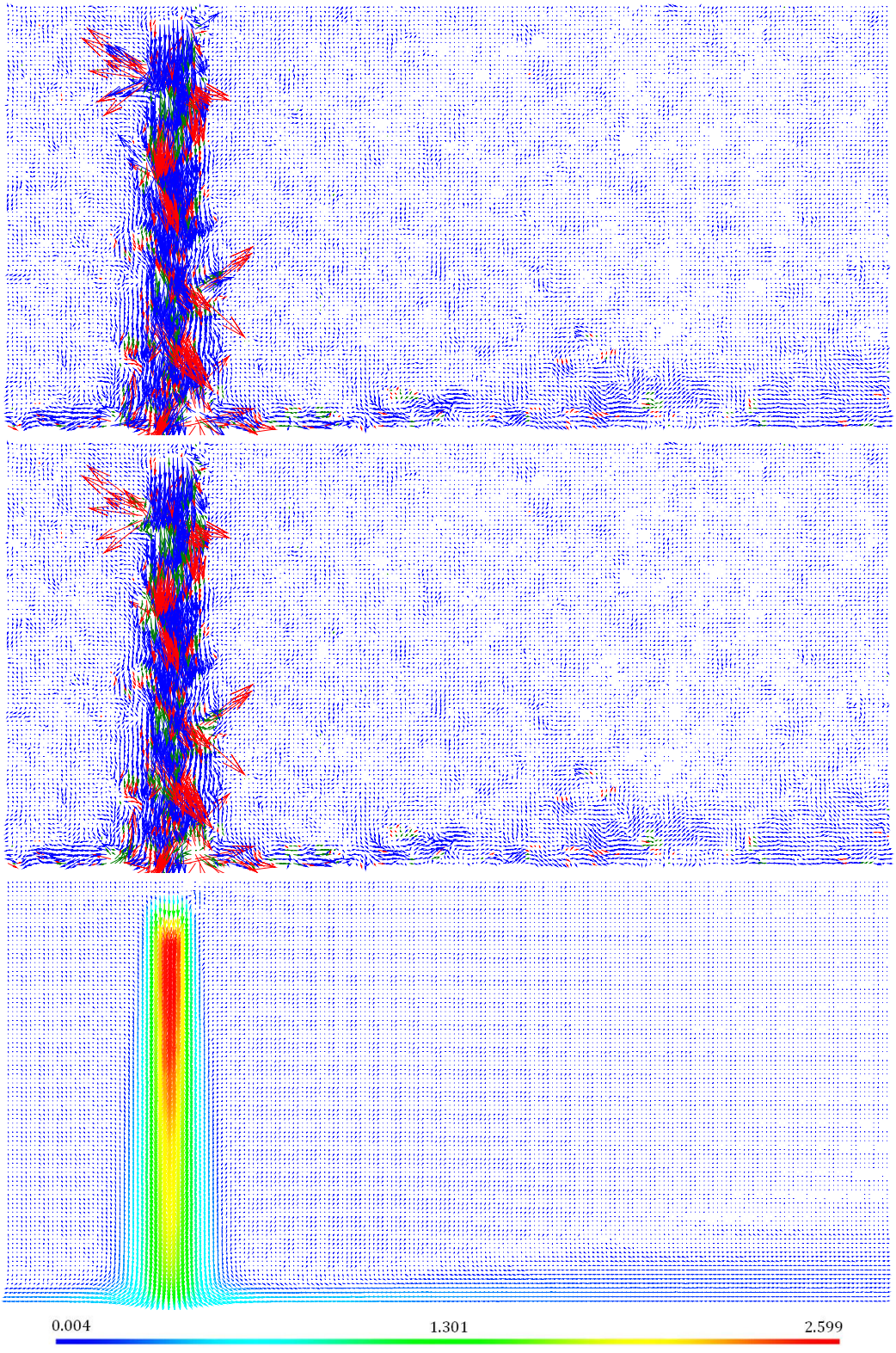

Figure 3-16 PIV data processing stages: Peak validation (top), moving average validation (middle), and vector statistics (bottom).

3.3.5 Exporting Profile Plots

Once the raw images have undergone processing as discussed in the above section, profile plots must be exported to enable calculation of the mean and turbulent statistics of the flow.

The pixel co-ordinates of the profile plots to be examined, as detailed in Figure 3-13, were determined in relation to the position of the impact point on the instantaneous vector map. During the PIV calibration, the origin (0,0) was set to the impact point on the jet axis at the impinging surface. A check can be made by applying the metric rule to the vector map, y=0 should be in line with the base. Plotting the mean axial velocity along the stagnation line provides another check as it is obvious in the data when the wall has been reached. The x-pixel location of the jet centreline was found using a horizontal profile taken near the jet outlet, fitting a Gaussian plot to the data helped identify the maximum velocity should it lie between two data points.

A velocity vector was generated for each IA within the measurement area, with a typical spatial resolution of 0.0432mm. The selection of the co-ordinate for either end of the profile plot line was input into the DynamicStudio software, which "snaps" to the nearest vector. This means the axial or radial location of the profile may be a maximum of 0.0216mm either side of the determined location. It is not possible to assign the location of the IAs so is likely the jet centreline and impact point would likely be between two data points.

The two components of the mean velocity, $\overline{U}$ and $\overline{V}$, as well as the root-mean-square (RMS) of the fluctuating velocities, u' ($= \sqrt{\overline{u^2}}$) and v' ($= \sqrt{\overline{v^2}}$), and shear stress ($\overline{uv}$) were calculated from the instantaneous velocity vector data acquired using PIV and processed as detailed.

3.4 Exploring Impinging Jet Data using Planar PIV – Proving the System

3.4.1 Time averaging

In an ideal world, with limitless processing capabilities, an infinite number of time steps would be used when acquiring turbulent flow data. However, in the real world this is not practical or often possible due to computational limitations. To explore the impact this may have on experimentally studying free shear turbulent flows such as an impinging jet, a study of a variety of time periods was conducted.

Table 3-4 Data set time periods for PIV time averaging testing

Time period	*T1*	*T2*	*T3*	*T4*
Number of time steps	1054	2170	3100	4030
Number of PIV runs	17	35	50	65
Measurement duration	1m 10.3s	2m 24.7s	3m 26.7s	4m 28.7s

Using a data set acquired for 4.48 minutes, we can explore the effect of varying the time periods of measurement. The data set was processed and the turbulent statistics performed on increasingly smaller proportions of this dataset as shown on Table 3-4.

It is important to use a sufficient number of time steps to ensure statistically meaningful time-averaged data are derived. The influence of the number of time steps has been assessed through the determination of mean axial and radial velocity ($\overline{U}$ and $\overline{V}$ respectively), and shear stress ($\overline{uv}$) for profiles taken at two different positions within the impinging and radial wall jet.

A transverse profile of the developing jet was taken one diameter above the impingement surface and the derived time-averaged mean velocities, and shear stress are shown in Figure 3-17. The mean axial velocity ($\overline{U}$) which is dominant in this region of flow, shows no scatter at even the smallest time period T1. Radially, there is an element of scatter at T1, the amount of scatter reduced from T2 (2170 image pairs and above). The shear stress, which is the averaged product of two fluctuating velocities (Chapter 1), illustrates more scatter than the mean velocities. Data determined from T1 (1054 time steps) exhibit a great deal of scatter, Figure 3-17(c). From 3100 time steps, the derived profiles are independent of the number of time steps used.

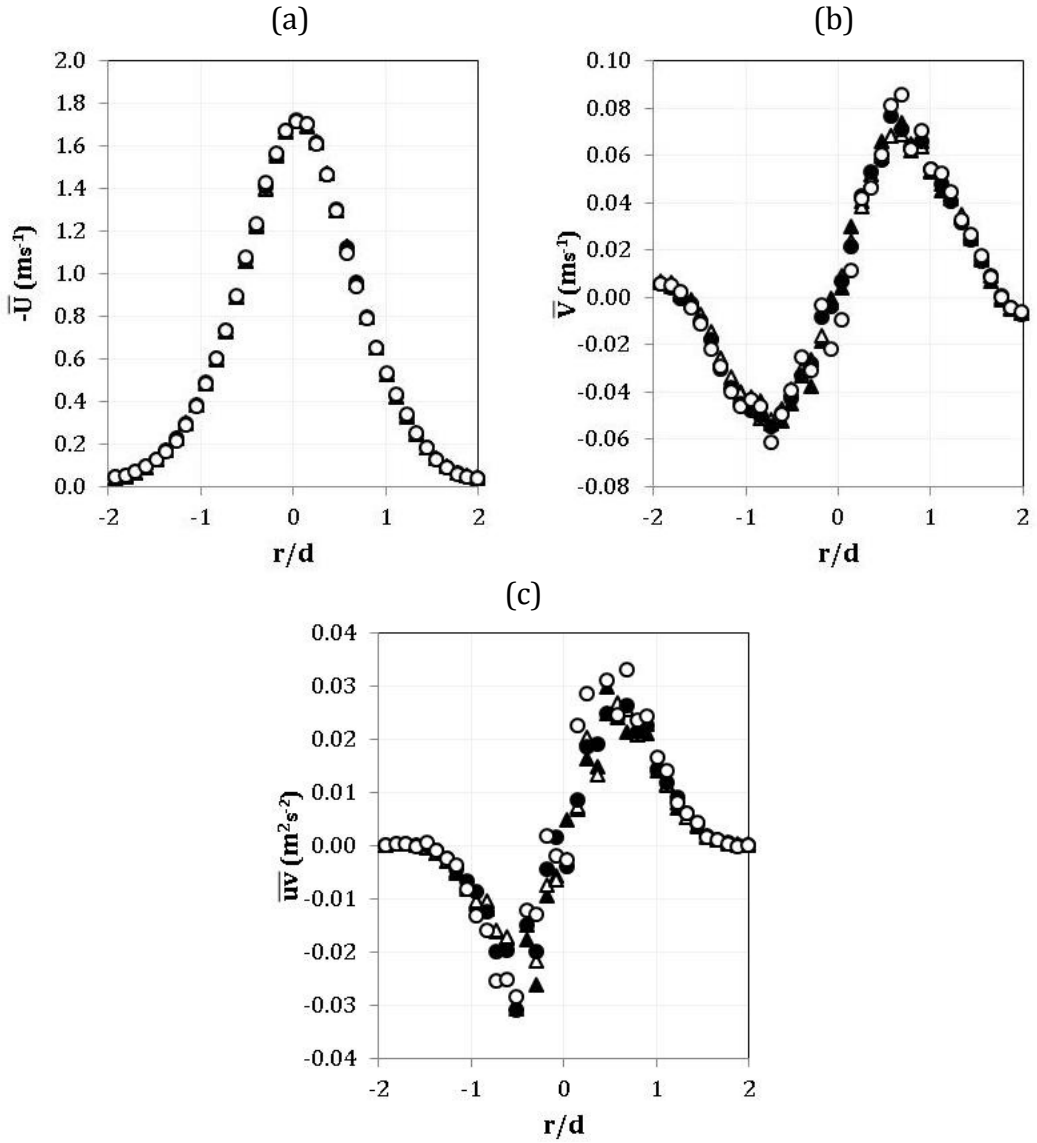

Figure 3-17 Time averaging testing using single-phase data at h/d ratio = 10, horizontal profile taken at 1d above the impingement surface: ○ T1, ● T2, △ T3, and ▲ T4: (a) mean axial velocity, (b) mean radial velocity, and (c) shear stress.

In the near-field radial wall jet, a profile normal to the impingement surface four diameters from the jet axis was taken, mean velocities ($\overline{U}$ and $\overline{V}$) and shear stress ($\overline{uv}$) were derived and are shown in Figure 3-18. Again the dominant mean velocity, which in the radial wall jet is $\overline{V}$, displays no scatter for the time periods under assessment. The axial mean velocity exhibits a small amount of scatter. And again, the shear stress data shows a large amount of scatter for T1, reducing for T2, and finally the derived profiles became independent of the number of time steps for T3 and T4 (3100 and 4030 image pairs respectively).

As a result of this sensitivity study, 3100 time steps (or image pairs) has been acquired for all experimental trials performed. The CCD camera has a buffer

capacity of 62 image pairs, therefore to accomplish this target of 3100 image pairs, the PIV was run 50 times and the data merged.

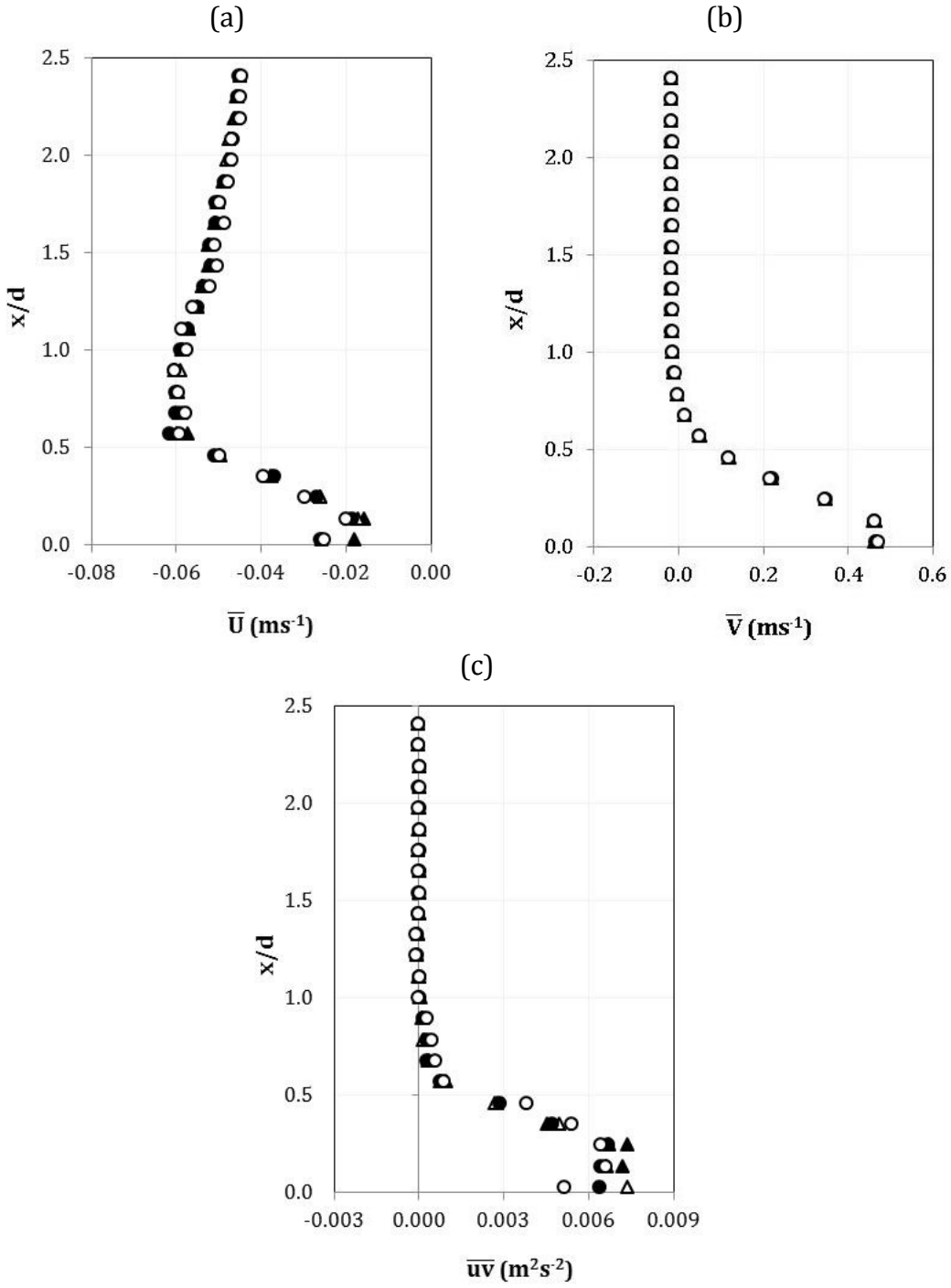

Figure 3-18 Time averaging testing using single-phase data at h/d ratio = 10, vertical profile taken at 4 r/d: ○ T1, ● T2, △ T3, and ▲ T4: (a) mean axial velocity, (b) mean radial velocity, and (c) Reynolds shear stress.

It is important to note that although the data acquisition was not continuous, the impinging jets studied within this programme of study were at steady state. Had the focus of this research been the study of non-steady state conditions, such as sequential jet firing time as is the operational application of impinging

jets currently employed in highly active storage tanks within the nuclear industry (Chapter 1), the experimental approach would require modification.

3.4.2 Steady state testing of the Jet Test Rig

The impinging jets of interest within this program of study are at steady state. As such, all experimental trials were to be performed after allowing the rig to run for a sufficient time to ensure steady state had been reached prior to engagement of the PIV. To confirm the operational methodology incorporated sufficient time for the rig to achieve steady state, a study of start-up durations prior to initiating data acquisition was conducted, see Table 3-5.

Table 3-5 Data acquisition start times for rig steady state testing

Run number	*R1*	*R2*	*R3*
Rig running time before PIV data acquisition	10 mins	30 mins	60mins

The Jet Test Rig was started-up and run for 10 minutes before starting the PIV data acquisition for the first data set, R1. As discussed in Section 3.4.1, in order to acquire a sufficient number of time steps the PIV was run 50 times and the data merged. This equates to a data acquisition duration of 3 minutes and 26.7 seconds.

Between each PIV run, the images captured by the CCD camera was downloaded typically taking around 10 seconds per download, equating to a total PIV run duration of 11.78 minutes. PIV acquisition was then repeated at 30 and 60 minutes, R2 and R3 respectively, from the initial rig start-up. Note the rig was left running between each of these data acquisition periods.

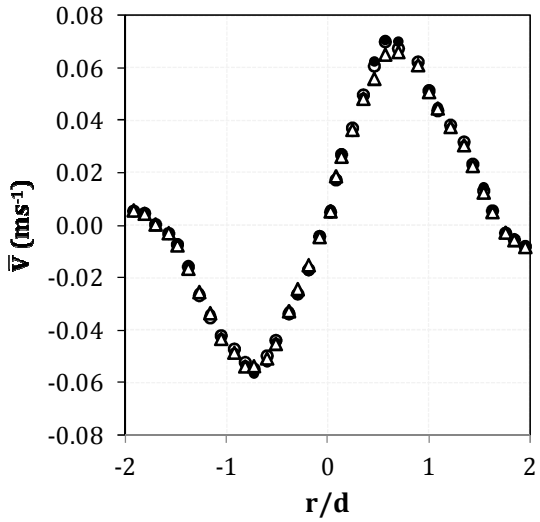

Figure 3-19 Steady state testing using single-phase data at h/d ratio = 10, horizontal profile taken at 1d above the impingement surface: ○ R1, ● R2, and △ R3: mean radial velocity.

The same transverse profile of the developing jet one diameter above the impingement surface, as assessed for the time averaging study above, was taken for R1, R2 and R3. Figure 3-19 shows very good agreement between the different PIV data acquisition start times, confirming 10 minutes start-up time is sufficient to allow the rig to achieve steady state.

3.4.3 PIV Settings to Capture Impinging Jet Regions, Δt selection

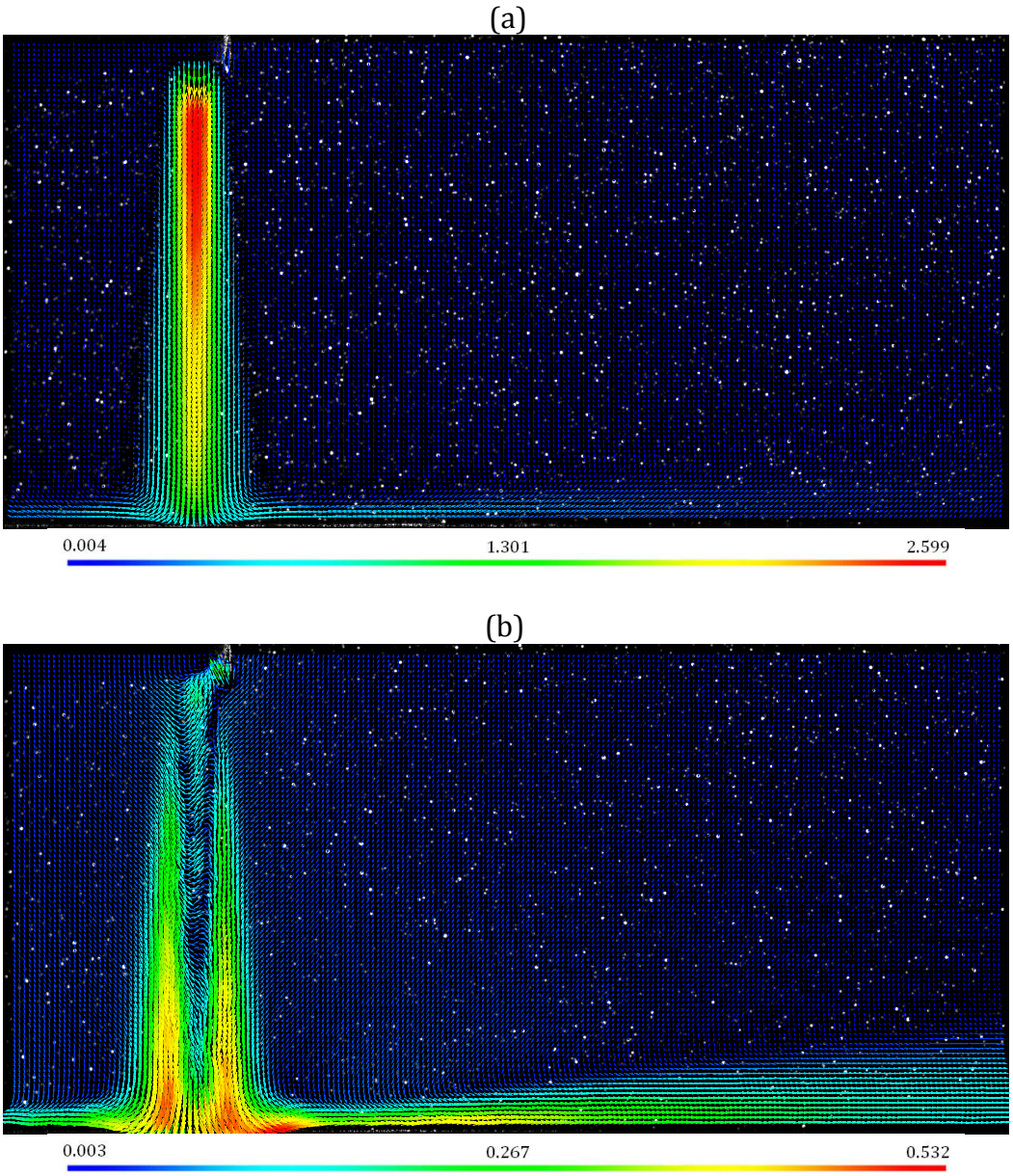

Figure 3-20 Vector map overlain on ROI extract for Δt of (a) 100μs and (b) 500μs.

Large velocity gradients can be found in impinging jets, from the potential core through to the far-field radial wall jet. Experimentally measuring such a large range of velocities is very difficult, particularly if trying to do so using a single measurement technique.

The displacement of particles between light pulses are determined through evaluation of the PIV recordings. The duration of light pulses, 4ns for the impinging jets trials within this thesis, must be short enough to "freeze" the motion of the particles, avoiding blurring of the images. The time interval between the pulses, Δt, are dependent on local velocity and image

magnification, the latter determined through calibration. The time interval, Δt, must be long enough to determine the particle displacement with sufficient resolution, and short enough to avoid the loss of particles from the interrogation area (IA). It is assumed all particles within one interrogation area have moved homogenously between each image pair. The two-component velocity vector of the local flow in each IA, in the plane of the laser sheet, is calculated from the particle displacement and the time interval.

The employment of two different values for Δt was necessary in order to capture the whole impinging jet, from the developing jet region through to the far-field radial wall jet;

- To capture the developing jet, the impingement region, and the near-field radial wall jet, a Δt of 100μs was employed. A time-average velocity vector map for Δt of 100μs is shown in Figure 3-20(a). In the far-field region, for this Δt value the particle displacements are too small to be evaluated and therefore appear, in this figure, as if there is no flow.
- And to capture the far-field radial wall jet a Δt of 500μs was used, see Figure 3-20(b) for time-averaged velocity vector map. Note, near the jet outlet where the velocity vectors are at their largest, particle displacements for the Δt of 500μs exceed the boundaries of the IAs and result in the apparent lack of vectors in this region of the vector map.

3.4.4 PIV Measurement Limitations in Relation to Impinging Jets

The measurement of turbulent fluid flows is a challenge, made increasingly difficult for flows which are essentially three dimensional, such as impinging jets, despite their axisymmetric nature. This is reflected by the limited amount of data within the literature even in light of the importance and interest levels in this flow configuration, although many have studied it from a computational perspective (Craft et al.,1993; Dianat et al., 1996; Kubacki and Dick, 2011). The level of complexity also considerably increases when attempting to add particulates into the measurement domain.

Focussing on the single-phase system for the purpose of illustration, impinging jet flows exhibit large velocity gradients, from the developing jet region, to the stagnation point, through to the radial wall jet (Chapter 1). Each of these regions of flow presents a challenge for measurement using the PIV.

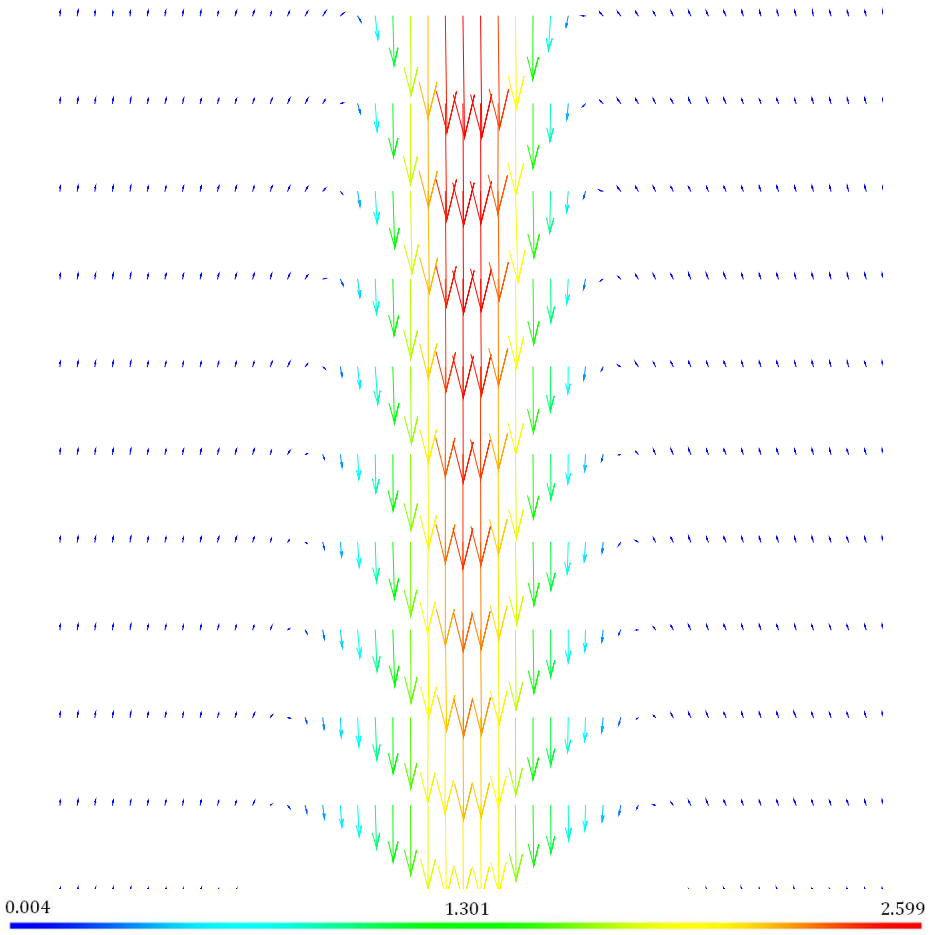

Figure 3-21 Vector map of the developing jet following issue from jet outlet, showing every 5th vector in the vertical plane (h/d ratio = 10)

PIV generates velocity vectors which are subsequently broken down to their axial and radial component. In regions where the flow is heavily dominant in one direction, as in the top several rows of vectors in Figure 3-21, the PIV may be unable to resolve the radial component of instantaneous velocity.

3.4.5 Jet Line and PIV Alignment

Accurately aligning the jet line to the tank base is vitally important, as are aligning the PIV laser sheet with the centre of the issuing jet, and perpendicularly setting up the camera to the laser sheet. The precise location of the centreline in relation to the PIV measurement plane is not a priori known. The scale of the experimental trials presented within this thesis is small. For a jet line internal diameter of d = 4mm, and a laser sheet of approximately 1mm thickness, even a small mis-alignment would render the data unusable. As such, considerable effort was put into developing the alignment activities for each and every experimental trial undertaken.

The alignment of the jet line was achieved through the use of a graduated carpenters angle submerged in the jet test tank, as discussed in Section 3.2.5, checked using the CCD camera and the DynamicStudio software platform run in Free Run mode to allow a 'zoomed-in' inspection, an example calibration image can be seen in Figure 3-8, page 59.

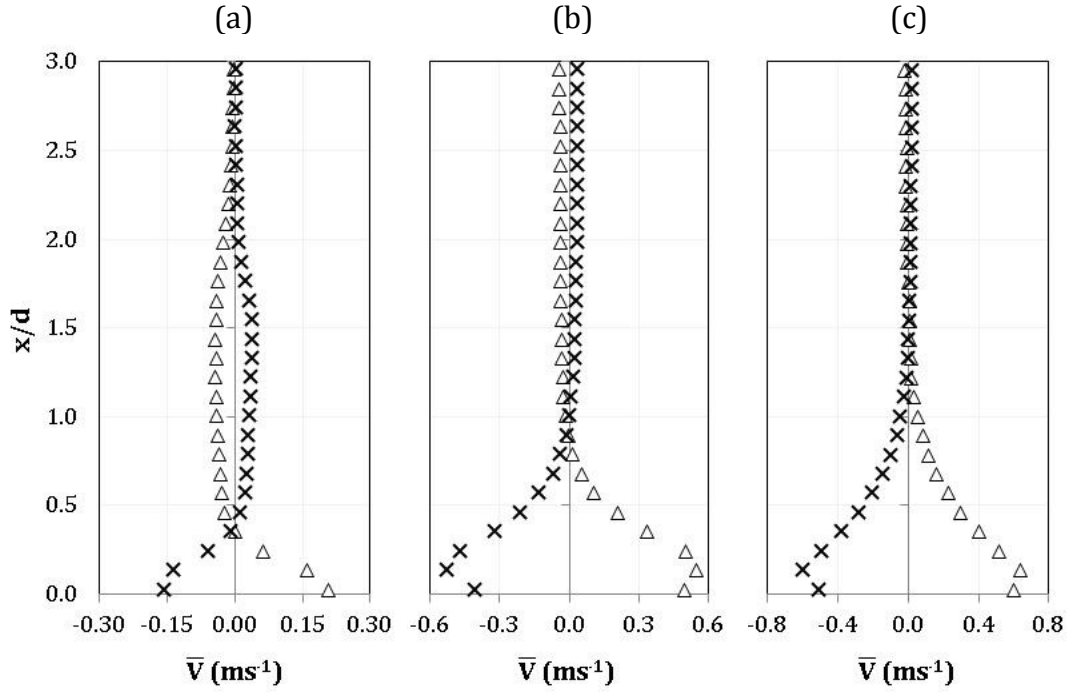

Figure 3-22 Single-phase mean axial velocity data for profiles taken either side of the jet centreline (△ 1 r/d and ✕ -1 r/d), at jet heights, h/d ratios of: (a) 2, (b) 6, and (c) 10.

The alignment of both the jet line and laser sheet were checked through the acquisition of a relatively small number of time steps, typically 100 instead of the 3100 time steps required when performing the full acquisition of data presented within the results chapters of this thesis. This small amount of data would be processed and profile plots taken at one diameter positions either side of the jet centreline (1 x/d and -1 x/d). This was undertaken as part of the experimental set-up procedure before each experiment was performed.

On completion of data acquisition (the 3100 time steps), each dataset was processed following the processing stages discussed in Section 3.3.4. This check was then performed again on the full dataset, taking profile plots at one diameter either side of the jet axis to check alignment. Figure 3-22 presents the profiles taken for this purpose for each of the three single-phase trials presented in Chapter 4. As can be seen, the radial mean velocities are mirrored either side of the jet axis confirming the jet line, laser sheet and CCD camera

were well aligned. This operation was undertaken for all trials performed, the plots in Figure 3-22 shown for illustration.

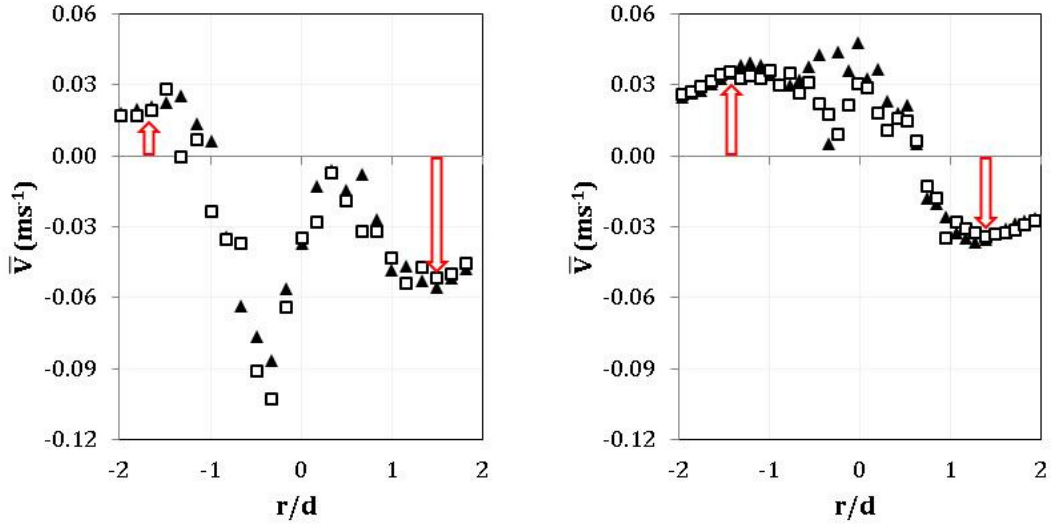

Figure 3-23 Radial velocity profiles to demonstrate consequence of laser mis-alignment at ▲ 5 x/d, and □ 6 x/d, left: poor alignment, and right: good alignment

Another check performed required the exploration of the radial mean velocity profiles within the developing jet. When the laser sheet was well aligned to the jet centreline, the radial velocity profiles are expected to be symmetrical as seen in the Figure 3-23 right plot. The mean radial velocity about the jet centreline, within ±1 r/d, demonstrates the PIV measurement limitation in regions of highly one-directional flow if attempting to resolve the inferior vector component, as discussed in Section 3.4.4. However, for the region outside of the potential core, more than one diameter from the jet centreline, the fluid flow is clearly symmetrical. The radial velocity is of similar magnitude either side of the jet axis at 0 r/d. The sign of the values are negative on one side of the jet axis and positive on the other as the origin was set at the impact point on the impingement surface, see Chapter1. When the laser sheet is poorly aligned it is seen by the lack of symmetry as seen on the left-hand plot in Figure 3-23.

3.4.6 Experimental Uncertainties

No physical quantity can be measured without uncertainty so effort is made to minimise errors where possible. There are two types of experimental errors; systematic errors and random errors.

Systematic errors affect the accuracy[6] of measurement, inherent errors that are not improved by repeated measurements but may be reduced by refining measurement methods or techniques. The development of increasingly sophisticated measurement techniques can help improve the systematic errors.

Random errors affect the precision[7] of measurement, unpredictable variations in the measurement that are improved by repeated measurements as well as refining measurement methods or techniques.

The preceding sections of this chapter were heavily focussed on developing measurement methodologies to improve measurement quality and reduce systematic and random errors. For example, the importance in using a sufficient number of velocity vectors to achieve statistically meaningful results from PIV velocity vector data as discussed earlier in this section (Fairweather and Hargrave, 2002).

In accordance with the work done by Fairweather and Hargrave (2002), whom used PIV in the measurement of an impinging jet, the following errors are estimated:

- ± 5% for the mean velocities in regions of high shear,
- ± 3% for the mean velocities in the radial wall jet,
- ± 5% for axial turbulence intensity in the radial wall jet
- ± 4% for radial turbulence intensity in the radial wall jet
- ± 7% for shear stress in the radial wall jet.

[6] Accuracy provides the extent to which a given measurement agrees with the true or accepted value for that measurement.

[7] Precision, also referred to as repeatability, measures how closely two or more measurements agree with each other.

3.5 Test Simulant Particles

The PIV measurement technique relies on the light scattering properties of particles within the flow. For the single-phase trials this required the addition of tracer particles small enough to follow the fluid flow but large enough to be detected by the camera. The dispersed phase particles were selected according the size range of interest but they also had to have adequate scattering characteristics. The selection of the right test particles is crucial to the acquisition of good quality PIV data.

3.5.1 Particle Selection for Single-phase Trials

The addition of tracer particles were required for the single-phase trials as the PIV technique measures the velocity of a fluid element indirectly by means of the measurement of the velocity of tracer particles within the flow.

Polyamide seeding particles (PSP), produced by polymerisation processes, were used as tracers in the current experimental programme with mean diameter of 20μm. When suspended in water, the PSP particles were somewhat hydrophobic and tended to clump together on the air/water surfaces, including the surfaces of bubbles created during agitation. To counteract this and enable these particles to be used as tracers within an aqueous environment, the particles were pre-treated with the anionic surfactant; sodium dodecyl sulphate (SDS) solution. Commonly used in cleaning and hygiene products, the application of this surfactant gave the particles an amphiphilic coating. A SDS solution at twice the critical micelle concentration (CMC) was prepared and the dry particles added, agitated by means of sonication to prevent the creation of bubbles. The resultant suspension was the feed supply to the jet test rig for the single-phase trials discussed in Chapter 4.

The particle size distribution can be seen in Figure 3-24, and particle size statistical information as well as particle density are presented in Table 3-6 below.

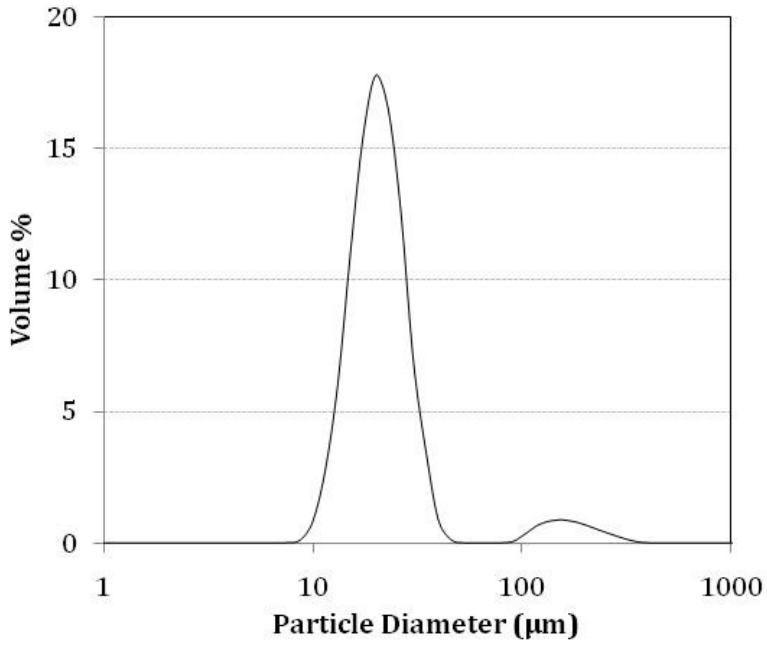

Figure 3-24 Particle size distribution of single-phase tracers.

In fluid dynamics, the Stokes number (S_t) provides a measure of a particle's responsiveness to turbulent fluctuations within a flow. It is defined as the ratio of the particle response time to a characteristic fluid time scale,

$$S_t = \frac{\tau_p U_b}{d} \tag{3-3}$$

where U_b is the bulk exit velocity of the jet, d is the jet line diameter, and τ_p is the particle response time estimated using the following equation.

$$\tau_p = \frac{\rho_p {d_p}^2}{18\mu_l} \tag{3-4}$$

The Stokes number, using the d_p (0.5) particle size, calculated for these tracer particles, was 0.146, indicating they would follow the fluid flow; coupling to the fluid motion where the particle inertia is small compared to the fluid turbulence scales, confirmed within Chapter 4.

Table 3-6 Particle properties of test particles.

Test case		*Tracers*	*Particle 1*	*Particle 2*	*Particle 3*
Particle size data, d_p (µm)	d_p (Mode)	19.95	22.91	45.71	69.18
	d_p (0.1)	13.19	7.59	26.36	50.85
	d_p (0.5)	19.29	19.95	40.28	68.58
	d_p (0.9)	29.86	45.71	56.43	91.73
	d_p (Span)	0.86	1.91	0.75	0.60
Particle density, ρ_p ($g.cm^{-3}$)		1.08	2.50	2.45	2.45

3.5.2 Particle Selection for Multi-phase Trials

A range of particle sizes were tested in the jet test rig to assess the feasibility of their use as test particles in particle-laden impinging liquid jet trials. The largest size tested, particles of mean diameter of around 200μm were found to settle significantly within the duration of the PIV data acquisition, rendering them unsuitable for the current programme of study. Particles supplied to the jet flow were circulated throughout the entire rig. As the PIV acquisition progressed, the solids loading of the jet flow issuing from the jet line fell as particles were settled out of the suspension.

The particles, soda-lime glass beads, used as the dispersed phase and reported within this thesis were of three sizes; [8]Particle 1 was 20μm, [9]Particle 2 was 45μm, and Particle 3 was 70μm. Each test particle was put into suspension before being added to the jet test rig to ensure good wetting of the particles. Silica particles are commonly used for such experimental work as they are non-toxic, non-hazardous, relatively inexpensive, chemically inert, typically spherical and most importantly have desirable scattering characteristics. The particle size distribution can be seen in Figure 3-25, and particle size statistical information as well as particle density are presented in Table 3-6 above.

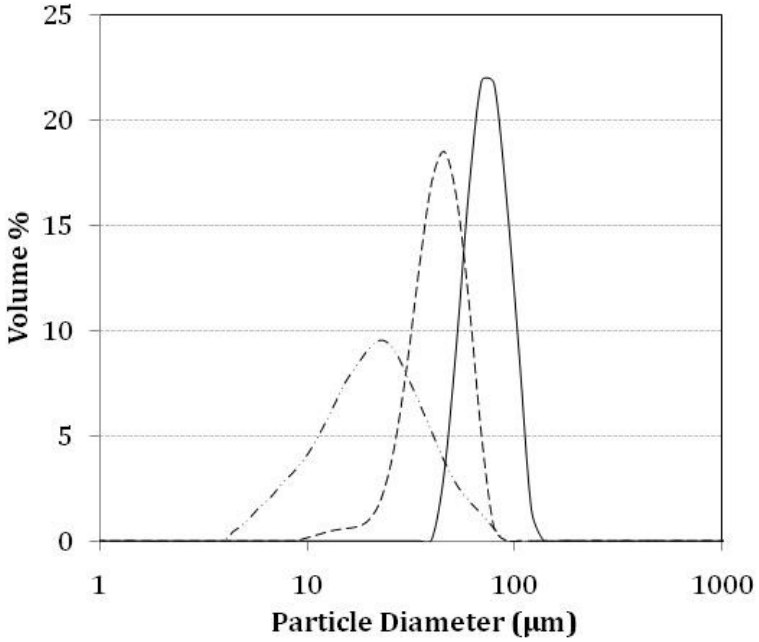

Figure 3-25 Particle size distribution of test particles used in particle-laden trials.

—·· — Particle 1, ---- Particle 2, and — Particle 3.

[8] Product classification Spheriglass 3000 from Potters Industries.

[9] Product classification Honite 22 (45μm), and Honite 18 (70μm) from Guyson International Ltd.

The PIV technique is a low solids concentration measurement technique. The CCD camera must be capable of seeing the measurement area which could become difficult if the system becomes opaque. The experimental rig designed and employed in this programme of research requires the camera to 'look through' 0.198m of the test simulant. The more particles in the system, the more the clarity of the liquor declines, making viewing of the measurement area increasingly difficult. All particle simulants used in the Jet Test Rig were put into suspension before loading them into the rig. At this stage, many fines were evident in the Particle 1 suspension by the milky appearance of the liquor, even after a period of allowing the simulant to settle. The suspension was allowed to settle for approximately an hour and the milky liquor above the settled bed decanted prior to use in the jet test rig and the above particle size distribution taken.

Another restriction of PIV, particularly for multi-phase flows, is the number of particles within each Interrogation Area (IA). Too many particles within an IA can overwhelm the cross-correlation. A solids loading of 0.01 vol% was used for all particle-laden trials reported within this thesis.

3.6 Simulant Characterisation Techniques

All test particles to be used in the impinging jet test rig underwent characterisation to develop a clear understanding of the behaviour of the material at both the particulate and bulk levels to aid interpretation of data collected from the physical modelling programme discussed earlier in this chapter. Each of these characterisation properties, if taken in isolation, is generally of limited value. However, the combined understanding given by the material properties allows greater quality control, optimisation of operations, troubleshooting, and aids design. The techniques employed are described below. Results obtained for each test particle are shown in Table 3-6 on page 86.

3.6.1 Particle Size and Shape - Laser Diffraction - Distribution Malvern Mastersizer 2000 (MS2000)

Particle size and shape analysis is, as its name suggests, a particle property of a particulate system, be it for dry powders or wet suspensions. The statistical representation of particle size is complex. Stating particle size as a unique, single statistic does not give a realistic representation of the majority of particulate systems where the particle shape is anything other than spherical. If all particles within a sample are spherical then a diameter can be stated. However, as shape moves further from spherical, the task becomes increasingly difficult.

In reality very few systems are spherical and instead have a range of sizes and shapes, making it increasingly difficult to be represented statistically. As a strategy to enable the statistical representation of particle size, a number of different definitions are used relating to the equivalent property of a sphere.

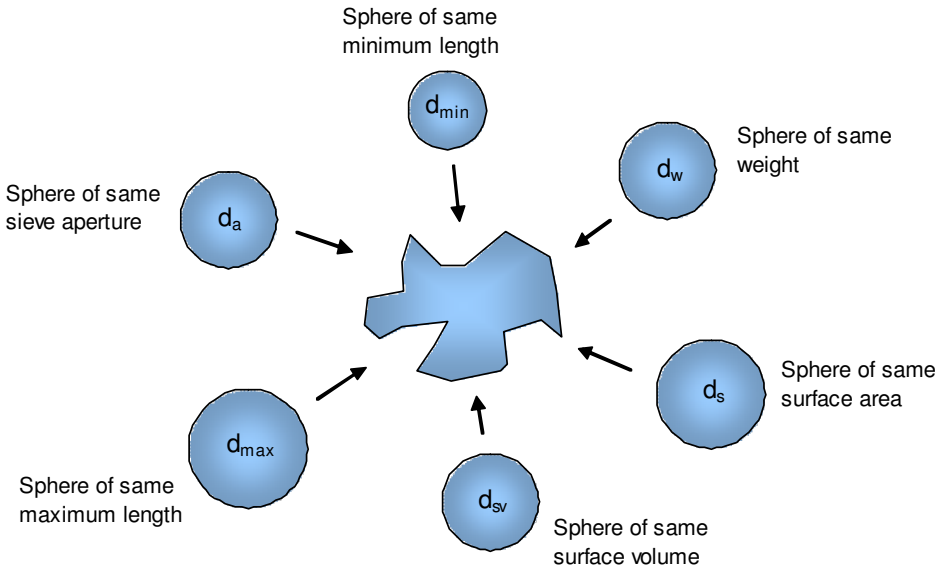

Figure 3-26 Diagram of particle size definitions from size analysis.

Many more particle size definitions are used (Allen, 1997). For example, a catalyst engineer is interested in surface area (d_s), whereas a chemical engineer may be more interested in comparison by weight basis. The greater the irregularity of the particle shape, the greater the variation in these values for a single particle. The laser diffraction technique generates a volume distribution, so if the density is constant it is equivalent to a weight distribution (d_w).

As particles flow through a focussed laser beam they scatter light. The scattering angle is inversely proportional to their size.

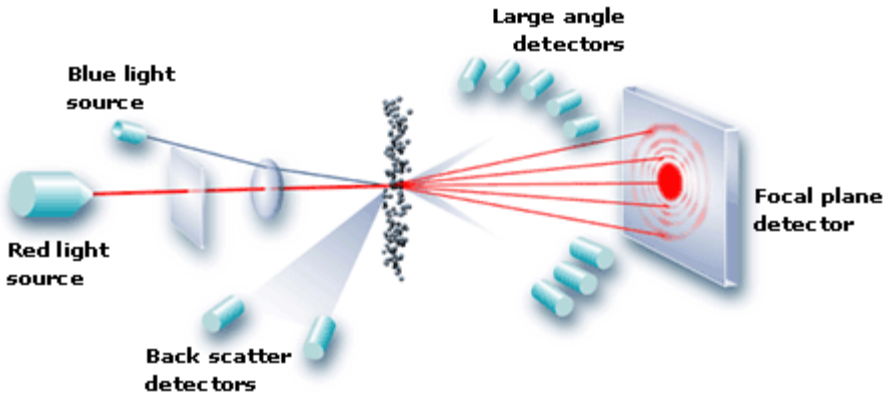

Figure 3-27 Schematic of laser diffraction particle size analysis technique – MS2000[10]

Mapping the scattering intensity and angle allows calculation of the particle size. Matching this data to the theoretical profile predicted by Mie theory,

[10] Image taken from Malvern Instruments, the manufacturer and distributor of the MS2000, website – www.malvern.com

through the application of the real and imaginary components of the refractive index of the system, results in a size distribution representative of the system being analysed. The refractive index values can be adjusted manually if they are not known prior to analysis until the real and theoretical outputs are in agreement. This technique assumes sphericity, and as such the further from spherical the particles being analysed are the larger the error in the results.

3.6.2 Particle Density - AccuPyc

Applying the same principle as Archimedes used to measure the gold in King Hiero II's crown by submerging it in water, the AccuPyc measures the amount of gas displaced by the solid. Pressures observed upon filling and discharging the sample chamber allow calculation of the solid volume, coupled with accurate measurement of the sample mass, enabling the particle density to be calculated.

Chapter 4
Results and Discussion – Single-Phase, Impinging Jets

The orthogonal impingement of a round turbulent jet onto a solid flat surface is an important class of turbulent free shear flow and is of considerable theoretical interest, as well as having extensive industrial applications. Heat transfer operations are a popular application of impinging jets due to very high convection coefficients, particularly within the impact zone. However the physical modelling of the turbulence of such systems has focussed on small regions of the impinging jet, primarily the stagnation and near-field radial wall jet close to the impingement surface.

This chapter presents the first extensive exploration of all three regions of an unconfined, axisymmetric liquid impinging jet, at 3 strategic jet heights of 2, 6 and 10 diameters. Although other configurations of impinging jets are out with the remit of this body of research, a summary of such experimental work can be found in Chapter 2.

Additionally, the datasets provide an evaluation of the experimental system developed by testing against the known flow structure of a single-phase impinging jet, and the small amount of data available (Poreh et al., 1967; Cooper et al., 1993; Fairweather and Hargrave, 2002; Rajaratnam et al., 2010). The single-phase data presented also provide a benchmark for comparison to multi-phase measurements made in the subsequent chapters of this thesis. Particle image Velocimetry (PIV) measurements of the single-phase impinging

jets were made using neutrally buoyant tracer particles of 20μm mean diameter (d_{50}) that follow the fluid flow.

Two components of mean velocity, $\overline{U}$ and $\overline{V}$, as well as the root-mean-square (RMS) of the fluctuating velocities, u' ($=\sqrt{\overline{u^2}}$) and v' ($=\sqrt{\overline{v^2}}$), and shear stress ($\overline{uv}$) were calculated from instantaneous velocity vector data acquired using PIV. Measurement results for the developing jet, impinging region, and the near- and far-field radial wall jet are presented. The origin (0,0) of the co-ordinate system is set to the stagnation point where the jet centreline crosses the impingement surface, discussed in Chapter 1. Profile locations taken upstream of the stagnation point are reported to decrease from the jet outlet towards the impingement surface, i.e., for the largest jet height (10 h/d) examined 9 x/d is close to the jet outlet while 0.1 x/d is the profile taken closest to the impingement surface; the radial wall jet profiles increase radially from the jet axis, i.e., 1 r/d is in the near-field while 10 r/d is in the far-field (Figure 3-13, page 66).

The first three sections of this chapter map the growth of the developing jet, the deflection of the impinging region, through to the radial expansion of the near- and far-field wall jets, taking each jet height in turn. Section 4.1 presents the smallest h/d ratio of 2, within the potential core; h/d ratio of 6, just outside the core in Section 4.2; and the largest h/d ratio of 10 the jet flow has developed further before impingement is presented in Section 4.3.

The effect of the different jet heights on the turbulent flow phenomena of turbulent liquid impinging jets are discussed in Section 4.4.

4.1 Impinging Jet Data – h/d = 2, within potential core

In the following, measurement results for the developing jet, impingement region, and the near- and far-field radial wall jet are presented for a turbulent impinging liquid jet located two diameters above the impingement surface (h/d ratio of 2). Mean velocities $\overline{U}$ and $\overline{V}$ in the axial and radial directions of the jet, respectively, as well as the RMS of the turbulent fluctuating velocities (u' and v') and shear stress ($\overline{uv}$) are shown for all of these regions and discussed in turn.

4.1.1 Mean Velocity Experimental Data

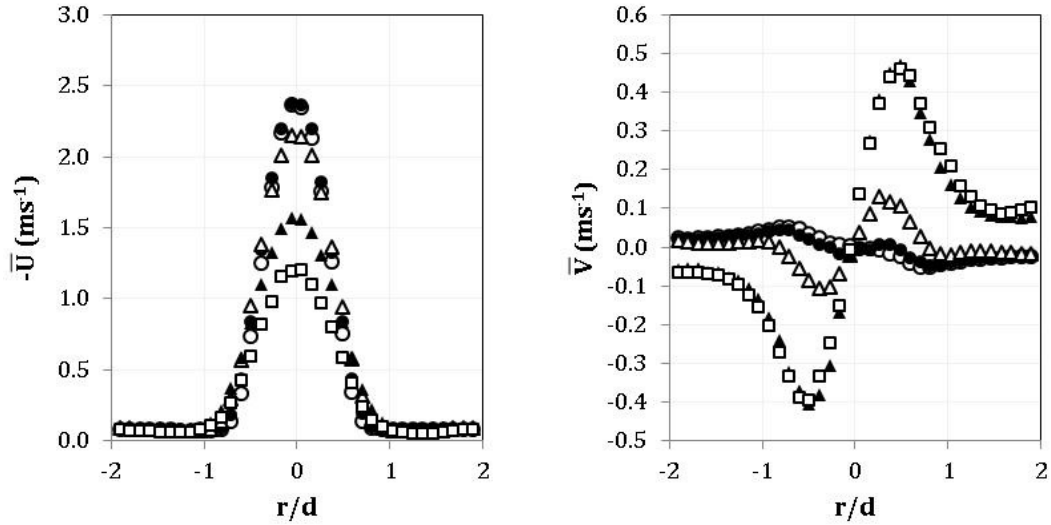

Figure 4-1 Single-phase developing jet data at h/d ratio = 2, axial and radial mean velocity profiles at ○ 1.3 x/d, ● 1 x/d, △ 0.5 x/d, ▲ 0.2 x/d, and □ 0.1 x/d.

Horizontal profiles were taken at a range of axial locations along the height of the developing jet; 0.7, 1, 1.5, 1.8 and 1.9 diameters from the jet outlet. The jet flow co-ordinate system locates the origin (0,0) at the impact point, where the jet centreline intersects the impingement surface; horizontal profiles are therefore reported at 1.3, 1, 0.5, 0.2 and 0.1 x/d respectively. Velocity distributions show good flow symmetry and the axial mean velocity, $\overline{U}$, profile near the jet outlet, when normalised by the maximum jet centreline velocity, U_c ($\overline{U}/U_c$), correlates well with expected fully developed pipe conditions as approximated by the empirical power law profile (Munson et al., 2002).

As expected, the axial mean velocity is seen to decrease as the impingement surface is approached, Figure 4-1. For a free jet where the fluid flow is unaware of the presence of the wall, the potential core of the developing jet typically extends around 5 diameters (Rajaratnam, 1976) from the initial jet formed at

the nozzle, such that the centreline axial mean velocity would remain equal to that of the pipe flow immediately prior to the outlet. For the range of x/d ratios we can explore for this case, if there were no impingement surface present we would therefore expect the axial centreline mean velocity to remain the same as at 1.3 x/d, but this is not the case. From Figure 4-1 we see that within one diameter of the impingement zone the axial velocity begins to decrease at an increased rate than would be seen for a free jet. A pressure gradient exerted by the wall causes a modification to the turbulence field within the stagnation region, resulting in deceleration of the approaching liquid jet. The effect of the wall becomes greater as the jet approaches the impingement surface. From 1 to 0.5 x/d the velocity decreases by just 0.23ms^{-1}, while from 0.5 to 0.1 x/d the velocity decreases by 0.99ms^{-1} to a centreline minimum of 1.19ms^{-1}. The presence of the wall has therefore resulted in a more significant decrease in velocity from 0.5 to 0.1 x/d (nearly 75% more) than the slightly greater distance between 1 and 0.5 x/d. As the jet is expanding and the axial velocity decreasing, the shape of the velocity profile begins to stretch. Outside of the developing jet, seen here at greater than one diameter from the jet centreline, the axial component of velocity is near zero.

As the axial mean velocity decreases, the corresponding radial component increases, Figure 4-1. Where the potential core is present before the wall effect is felt, more than one diameter above the impingement surface, the flow is dominated by the axial component and as such the radial velocities at 1.3 and 1 x/d are close to zero, showing a slight deviation from zero outside the developing jet where we can see initial entrainment from the stagnant surrounding fluid, with a very small peak of ±0.04ms^{-1} at around 0.8 diameters from the jet centreline. As the jet approaches the surface, the radial velocity becomes increasingly interesting. From the centreline where the radial mean velocity is zero, the velocity increases until it reaches a local maxima (V_m) and subsequently begins to reduce. The location and magnitude of the local maxima is dependent on the expansion of the developing jet and the effect of the impingement surface. At 0.5 x/d the local maxima of 0.12ms^{-1} is at 0.3 r/d, while further from the jet outlet (closer to the impingement surface) at 0.2 and 0.1 x/d, the local maxima of 0.45ms^{-1} is located at 0.4 r/d. The radial velocity reaches a maximum for 0.2 and 0.1 x/d. As the jet has approached the wall, the effect of the impingement surface and the expansion of the jet can be seen in the increase in the radial velocity local maxima and in its location moving away from the centreline. The highest rate of change is seen closest to the impingement surface, increasing by 0.45ms^{-1} between 0.5 and 0.2 x/d,

(distance of 0.3 diameters) when the increase between the prior profiles at 1 and 0.5 x/d was only 0.08ms^{-1}.

The deflected jet and the beginning of the radial wall jet can be seen at 0.2 and 0.1 x/d in Figure 4-1 from ±1 r/d. For the profiles at 1.3 to 0.5 x/d the radial velocity tends towards zero due to very small entrainment velocities outside of the developing jet. However at 0.2 and 0.1 x/d the radial velocity decreases from the local maxima (V_m) to around 0.1ms^{-1} at ±2 r/d.

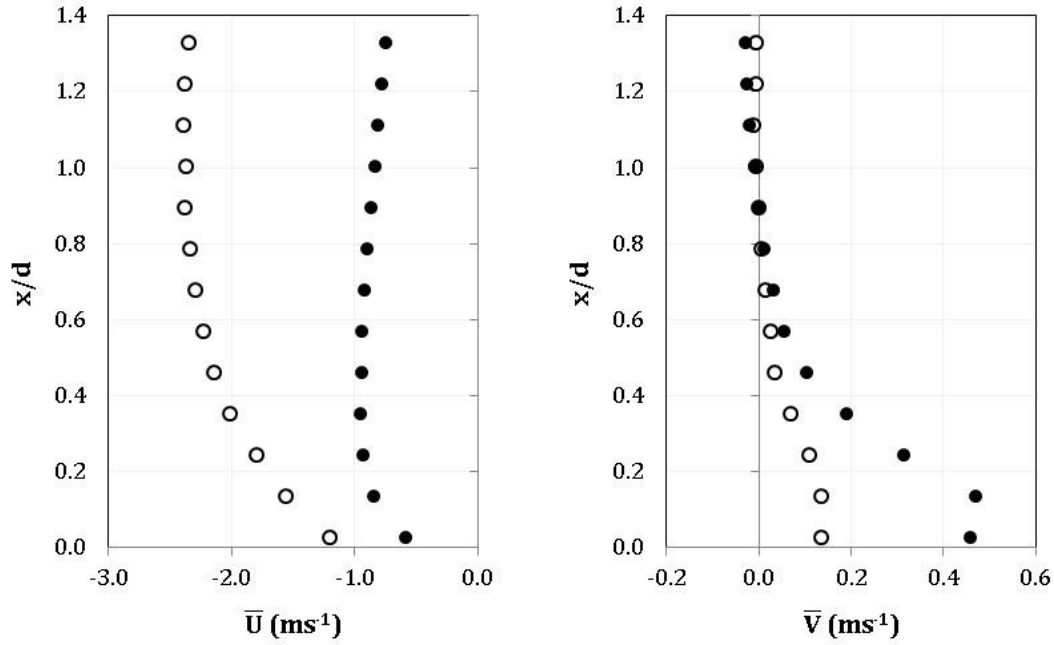

Figure 4-2 Single-phase mean axial and radial velocity data at h/d ratio = 2, vertical profiles within the impinging jet - ○ 0 r/d and ● 0.5 r/d.

Vertical profiles track the development of the flow approaching the impingement surface. The vertical velocity is reported as positive away from the wall and so for the impinging jet the values are shown as negative. The larger the velocity magnitude, the faster the flow is approaching the wall at 0 x/d in Figure 4-2. Along the jet centreline (0 r/d) the axial velocity is at its maximum closest the jet outlet and maintains this magnitude until it decreases due to entrainment and, ultimately, the presence of the wall has an impact. Initially, from 2 to 0.8 x/d, the turbulence generated on the boundaries of the jet has not penetrated to the jet axis and hence the jet outlet velocity is unchanged. As the wall is approached from 0.8 to 0 x/d, the fluid flow begins to decelerate and the axial velocity decreases. Moving to the 0.5 r/d profile, the flow experiences a slight acceleration as the jet expands until around 0.3d of the surface where the presence of the wall decelerates the flow in the axial direction. Here we see the deflected jet where the flow becomes more radial, as is reflected in the radial component of the mean velocity.

More than 1d from the surface the radial mean velocity is slightly negative due to entrainment from the stagnant surrounding fluid, becoming positive and increasing to a maximum of nearly 0.5ms^{-1} at 0.15 x/d before decelerating again closest to the wall. The magnitude of each velocity component at the data points closest the wall are similar, indicating just how deflected the jet flow is in this region.

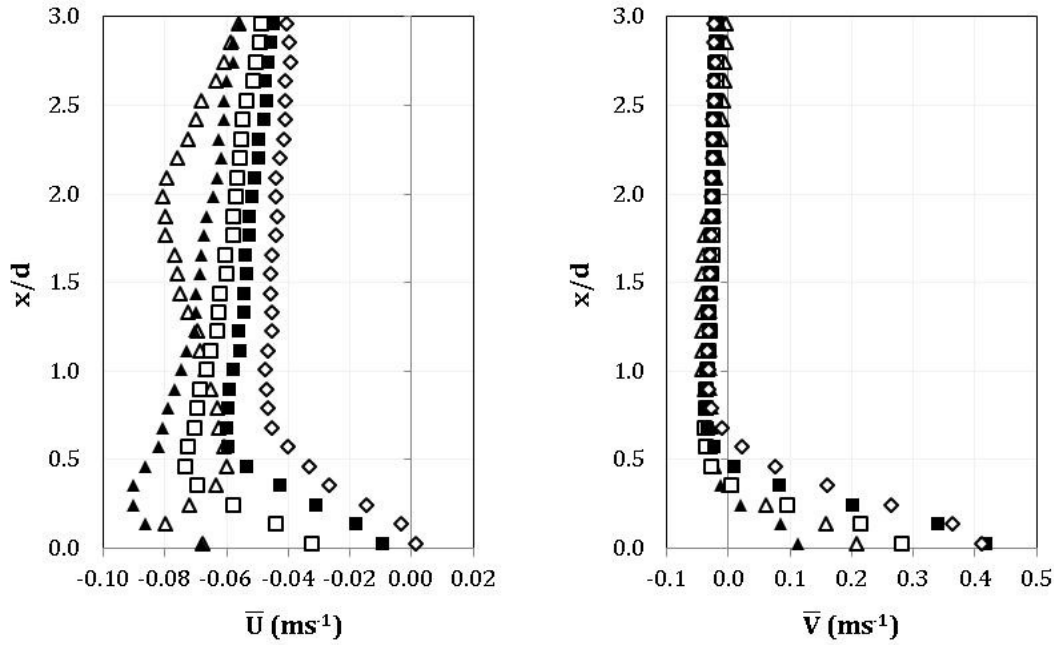

Figure 4-3 Single-phase mean axial and radial velocity data at h/d ratio = 2, vertical profiles within the radial wall jet near-field region - △ 1 r/d, ▲ 2 r/d, □ 3 r/d, ■ 4 r/d, and ◇ 5 r/d.

The impinging jet is deflected radially by the stagnation region, undergoing deflection and acceleration in the near-field wall jet. On a vertical line at 1d from the jet axis (hollow triangles on Figure 4-3), approaching the wall the axial mean velocity increases between 3 and 2 x/d. In this case, the jet outlet is located 2 diameters above the impingement surface so this section of the profile taken at 1 x/d is only 0.25d from the outside of the jet line, running parallel to it. As it approaches the initial jet issuing from the jet nozzle, at 2 x/d, the axial velocity accelerates. We have already seen on Figure 4-1 that the developing jet only expands to a width of around 2d about the jet axis within 0.5d of the impingement surface. Here we see, from 2 to 0.5 x/d, a subtle deceleration until the radial wall jet is reached around 0.5d from the wall. At the same time, the radial velocity component becomes increasingly negative as fluid is being entrained into the radial wall jet.

The radial wall jet axial component of the mean velocity within 0.5d of the wall, normal to the surface, begins to increase again until the data point closest to 0

x/d where it decreases again. Meanwhile the radial component gradually increases.

Moving another diameter out from the jet centreline, solid triangles in Figure 4-3, the near-field radial wall jet has begun to form. On the axial component plot, the velocity towards the wall is increasing, entraining the surrounding fluid until reaching the radial wall jet where the downward velocity decreases from around 0.3 x/d. Meanwhile the radial mean velocity parallel to the impingement surface becomes more negative as it approaches the wall jet, becoming positive and increasing to just over $0.2ms^{-1}$ near the wall. The point where the velocity gradient changes from negative to positive indicates the expansion of the radial wall jet at this radial position. The wall jet decelerates from 1 r/d.

At 3, 4 and 5 diameters the shape of the axial mean velocity profile is the same as at 2d. The difference in gradient above the wall jet moving away from the jet axis indicates a deceleration in the entraining velocity, while the location of the change in direction of the gradient shows that the jet is expanding as we move away from the jet axis, from 0.5 x/d at 3d to around 0.7 x/d at 5d. Within the wall jet, the downward velocity diminishes as the wall is approached, and only at 5d does the velocity at the data point closest the wall become positive showing a small velocity perpendicular to the surface. This suggests that although we were unable to get the resolution close to the wall sufficient to measure the radial velocity as it tends to zero in this region, due to the very small scale, the radial wall jet is developing from a near-field radial wall jet to that of the far-field radial wall jet where the flow is self-similar. The radial velocity component is negative above the wall jet due to downward entrainment of fluid, becoming positive and increasing in magnitude within the wall jet itself. The radial wall jet is also experiencing an acceleration radially outward from the jet centreline, with the mean velocity increasing up to $0.42ms^{-1}$ at 5 r/d.

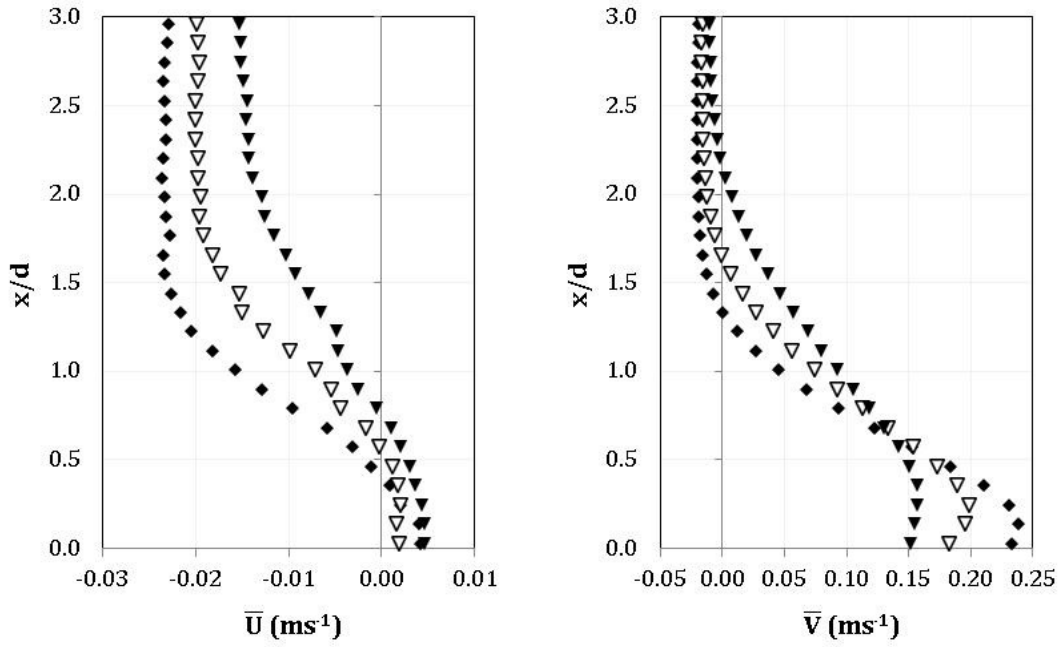

Figure 4-4 Single-phase mean axial and radial velocity data at h/d ratio = 2, vertical profiles within the radial wall jet far-field region - ◆ 10 r/d, ▽ 12 r/d, and ▼ 15 r/d.

Looking at the far-field of the radial wall jet, the radial component of the mean velocity shows the expansion of the jet. The shape of the velocity profiles are the same here, stretching and becoming flatter as the distance from the stagnation region increases. The local maximum V_m decays as the wall jet loses momentum from 10 to 15 r/d while the height of the wall jet increases, as seen by the height above the wall where the velocity tends to zero and becomes negative due to the small entrainment velocities present. The fluid flow, in the lower shear layer close to the wall, is subject to the no-slip condition at the wall, seen by the reduction in radial velocity the closer the wall gets. In the upper shear layer of the wall jet, the wall jet height changes at a greater rate than the near-field region. In the far-field, the wall jet height increases from 1.7 to 2.2d above the wall for 12 and 15 x/d, respectively, where in the near-field the jet height changes from 0.4 to 0.7d above the base for 2 and 5 r/d respectively. And as the radial mean velocity changes, so does the axial component as the wall jet is radially spreading and decelerating. Similar to the near-field, fluid is being entrained from the stagnant surroundings. However this time at increasingly smaller velocities and not showing the acceleration seen in the near-field (Figure 4-3). In fact at 15d from the jet axis, within the height range measured, it appears the entrainment velocity is decelerating towards the wall jet. From the same height where the radial velocity goes from negative to positive, the boundary layer region of the wall jet, the axial velocity decreases towards zero and eventually becoming positive, albeit with small magnitude, as

the wall is approached. These results demonstrate with increasing distance r from the stagnation line, the height of the wall jet is increasing and the maximum velocity values decaying as the wall jet mixes with the ambient fluid. These data are similar to those reported by other workers (Poreh et al., 1967; Fairweather and Hargrave, 2002).

4.1.2 RMS Fluctuating Velocity Experimental Data

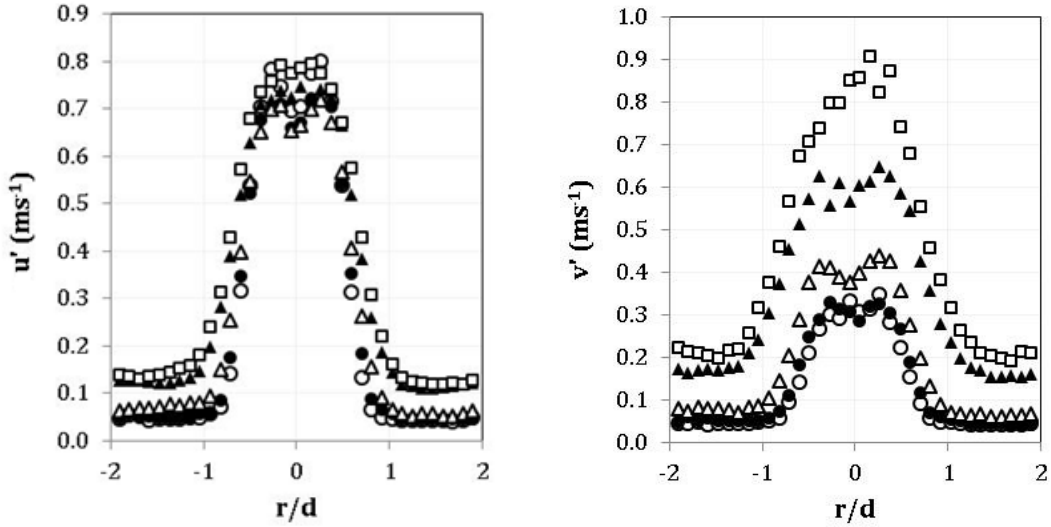

Figure 4-5 Single-phase developing jet data at h/d ratio = 2, axial and radial RMS fluctuating velocity profiles at ○ 1.3 x/d, ● 1 x/d, △ 0.5 x/d, ▲ 0.2 x/d, and □ 0.1 x/d.

The axial profiles of RMS of the fluctuating velocities (normal stress u') within the developing jet, before the pressure gradient exerted by the wall is felt, are substantially greater than the radial component (Figure 4-5). Two peaks are seen at the outer edges of the jet, around 0.3 r/d for 0.7 d (1.3 x/d) and 1d (1 x/d) from the jet outlet, where velocity fluctuations are stronger than within the potential core, hence the decrease towards the jet centreline. The location of the peaks are dictated by the development of the turbulent shear layer and can be considered to be located at the centre of the shear layer. As the jet develops and expands the shear layer grows, moving the position of this centre outwards, as seen when comparing profiles at 1 and 0.5 x/d. Overall, the magnitude of the axial turbulent velocity does not change significantly. The radial turbulent velocity on the other hand undergoes a significant increase as the wall is approached, due to radial deflection from the stagnation region.

The stagnation pressure created by the impingement has a dampening effect on the axial velocity fluctuations, slowing the growth of the jet in that direction. The influence of the wall is evident by the increase in the radial fluctuating

velocity for the profiles within one diameter of the impingement surface. This is in agreement with the findings of other workers (Beltaos and Rajaratam; 1974; Rajaratnam et al., 2010) who observed that for large impingement heights greater than 8.3d, the impinging jet feels the presence of the wall from an x/h distance of 0.86 which is equivalent to 0.8d above the wall for this case. As already seen when reviewing the mean velocity data, the change becomes more pronounced as the wall is approached. By the final profile, taken just 0.1d from the surface, the magnitude of the radial fluctuating velocity exceeds that of the axial component, with no hint of the centre of the shear layer remaining.

Again, the beginning of the radial wall jet is seen more than 1d radially from the axis, where for 0.1 and 0.2d above the surface the fluctuating velocities remain higher than for the region outside of the developing jet.

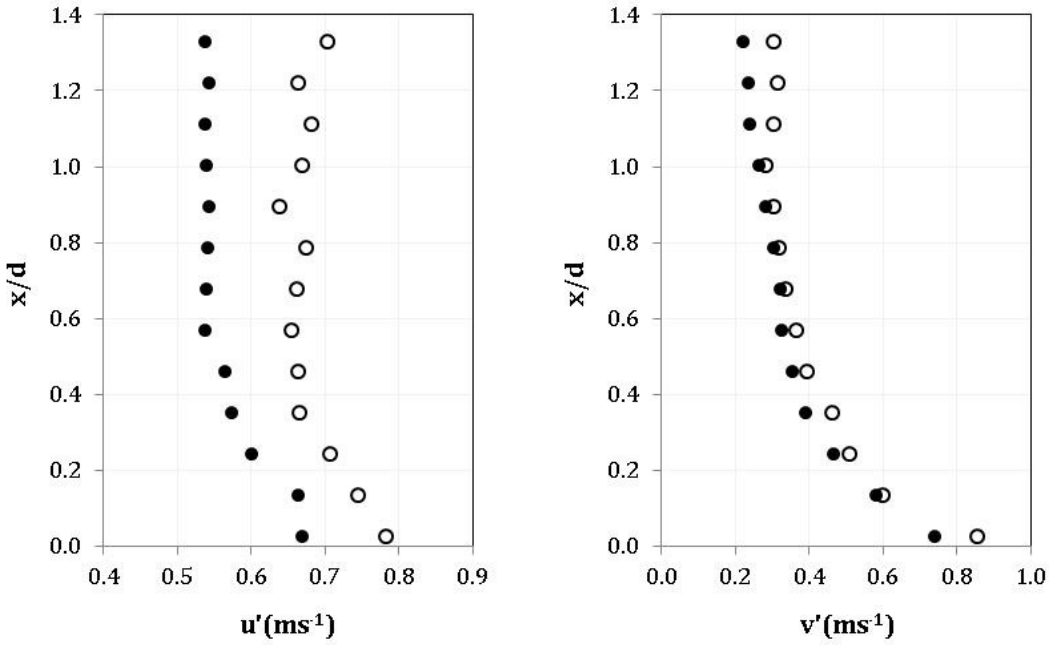

Figure 4-6 Single-phase axial and radial RMS fluctuating velocity data at h/d ratio = 2, vertical profiles within the impinging jet - ○ 0 r/d and ● 0.5 r/d.

Examining the stagnation line data given in Figure 4-6 affords a greater resolution of data points along the axis compared to the horizontal profiles of Figure 4-5, although these data plots of course have their merit. As discussed within Section 3.3.3 (page 64), it was not computationally realistic to export and process data profiles of the jet about the axis (taking horizontal slices) at too many axial locations. Taking a profile along the jet axis and 0.5d away from the centreline allows us to capture any changes measured between the horizontal profile positions.

Following the turbulent velocities along the stagnation line as the impingement surface is approached, the radial component varies more significantly than it's

axial counterpart. The axial fluctuating velocity remains fairly constant (note x-axis scale) within the developing jet, consistent with being within the potential core, until around 0.4d where the wall causes it to increase. Rapid flow deceleration results in shear layer growth. Cooper et al. (1993) found that for the same jet-to-plate separation, at a Reynolds number of 23,000 for a gas jet, the turbulence abruptly decreased from 0.1d due to the dampening effect of the wall. This is not seen within this dataset due to the difference in spatial resolution between the experimental systems. The radial turbulence on the other hand slowly increases from 0.31 to 0.60ms $^{-1}$ to 0.2 x/d, with a more rapid increase until the wall due to energy transfer to the radial direction from the wall normal direction. The study of a water impinging jet at the same jet-to-plate separation with a Reynolds number 23,400 by Hargrave et al. (2006) found the same trend, with the more rapid increase from 0.2d away from the surface. The magnitude of the axial and radial turbulence becoming very similar close to the impinging surface.

At 0.5d from the axis, the turbulence is not wholly different. Turbulence normal to the base follows a very similar trend, but around 0.1ms^{-1} lower. It remains constant until 0.5d, 0.1d earlier than the centreline profile, before increasing as the wall is approached. Radially, the turbulence is marginally different and continuously increases as the wall is approached, the rate of increase growing as x decreases.

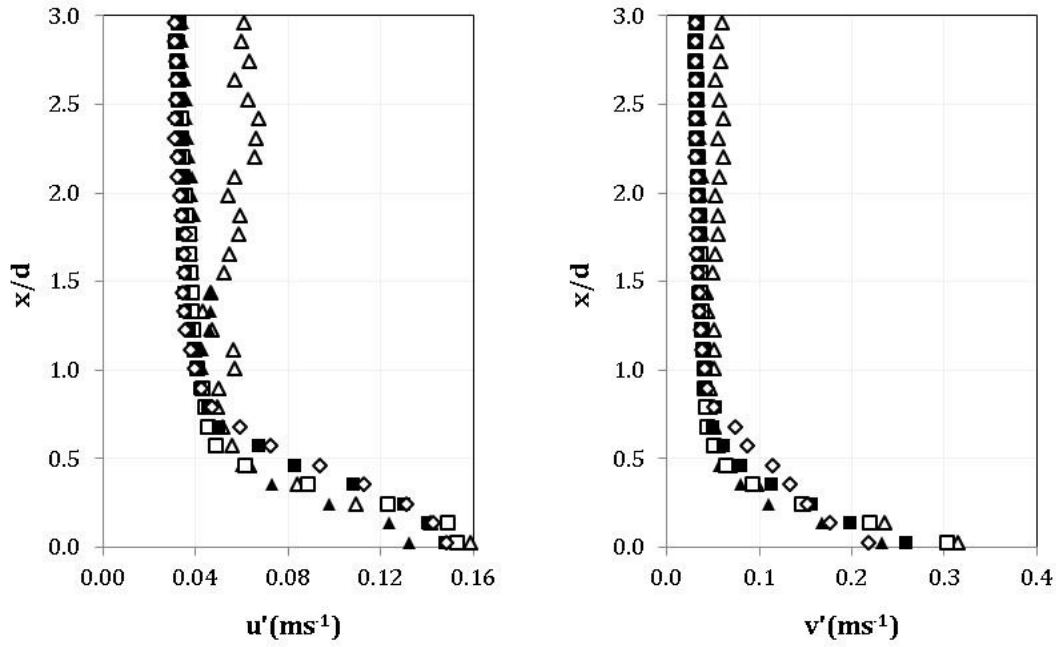

Figure 4-7 Single-phase axial and radial RMS fluctuating velocity data at h/d ratio = 2, vertical profiles within the radial wall jet near-field region - △ 1 r/d, ▲ 2 r/d, □ 3 r/d, ■ 4 r/d, and ◇ 5 r/d.

With increasing radial distance from the jet axis, turbulent velocities drop significantly from the stagnation region as the radial wall jet forms, with more than an order of magnitude drop for the axial component u' (comparing Figure 4-7 to Figure 4-6).

In the otherwise stagnant ambient region above the wall jet, turbulent velocities are small (around 0.04ms^{-1}), very gradually increasing towards the wall jet as fluid is entrained at the turbulent/non-turbulent interface, Figure 4-7. The profile taken at 1 r/d appears somewhat different in this area, although the magnitudes of u' and v' are similar, with the difference magnified for u' due to the scale of the x-axis. The upper portion of the profile runs parallel to the jet line (only 0.25d from the jet line outside wall, a distance of 1mm) and may account for this discrepancy. At this radial distance from the jet centreline, we are close to regions of jet development.

All profiles are of a similar shape in the radial wall jet. Turbulent velocities display a decrease from 1d and 2d, followed by an increase with increasing r. Deflection from the stagnation region accompanied by acceleration in the wall jet can be seen as the outer shear layer grows with increasing distance from 2d.

Cooper et al. (1993) and Hargrave et al. (2006) found a double-peaked radial turbulent velocity (v') profile within the forming wall jet with increasing radial distance from the stagnation point, for the radial distances from 1 to 2d. These peaks are representative of the two shear layers generated in the wall jet. Velocity decays from the peak close to the surface into the stagnant surrounding fluid forming the outer shear layer. Turbulent fluctuations at the outer edge of the shear layer boundary instigate an increase in u'. The inner shear layer forms due to viscous interactions with the impinging surface. The data here does not show this double peak very near the wall. Both these investigators focussed on a small section of the impinging jet, namely the stagnation zone and very near-field. A jet line diameter d of 26mm was used by Cooper et al. (1993), and the accompanying paper by Craft et al. (1993) showed a typical resolution using hot-wire anemometer near the wall to be around 20 data points within 0.1d (= 2.6mm) of the wall. In the experimental system employed for this work, two data points within the same normalised dimension in our experimental system were measured. Hargrave et al. (2006) used a jet diameter d of 13.3mm focussed on a measurement area extending 2.5 diameters radially from the jet centreline and vertically up to 2 diameters from the impingement surface. With a jet diameter of 13.3mm the measurement area was around 47mm (to allow for both sides of the developing jet to be recorded) by 27mm. By focussing on only one region of the impinging jet they achieved a

higher data point density than captured within this work where a measurement area of 85mm by 63mm was employed with a jet diameter of 4mm to allow us to explore all three regions of the impinging jet. The difference in data point spatial resolution is likely why the double-peak of radial turbulent velocity seen by Hargrave et al. (2006) is not evident in the data presented here.

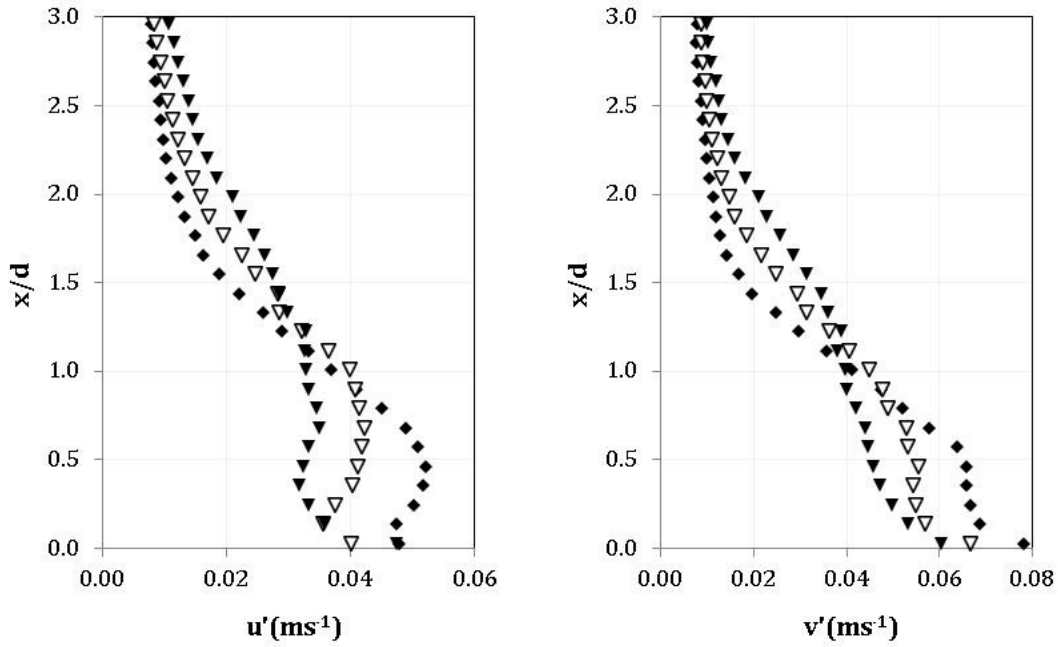

Figure 4-8 Single-phase axial and radial RMS fluctuating velocity data at h/d ratio = 2, vertical profiles within the radial wall jet far-field region - ◆ 10 r/d, ▽ 12 r/d, and ▼ 15 r/d.

The radial wall jet, as it progresses from the near- to far-field, undergoes radial spreading and deceleration, the amount of turbulent fluid growing due to entrainment. Figure 4-8 shows data for the RMS of the fluctuating axial and radial velocities. On the approach to the impingement surface, the turbulent velocities at 10d from the jet axis remain constant at 0.04ms^{-1} until the upper boundary of the radial wall jet is reached. Within the wall jet, u' and v' increase their peak (u'_m and v'_m) at 0.5d above the wall which indicates the centre of the upper shear layer. A second peak is seen at the same height from the impingement surface as the maximum radial velocity V_m (Figure 4-4). Pressure reflections from the wall slowing the growth of the wall jet by dampening the axial fluctuations. The radial turbulent velocity v' within the wall jet is greater in value than u' but does not display such pronounced peaks. The data profiles at 12d and 15d display similar trends with the upper peak, although less pronounced, magnitude decaying as r increases. The vertical position x/d of the upper shear layer centre increasing as the jet expands. The lower peak,

corresponding to where the maximum radial mean velocity V_m is seen, appears more distinct as we move away from the jet axis.

4.1.3 Reynolds Shear Stress Experimental Data

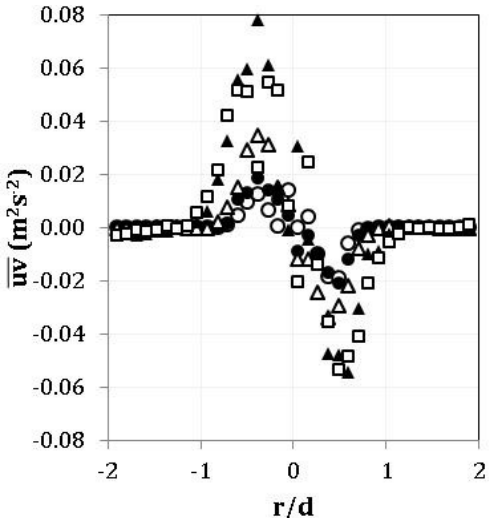

Figure 4-9 Single-phase developing jet data at h/d ratio = 2, shear stress profiles at ○ 1.3 x/d, ● 1 x/d, △ 0.5 x/d, ▲ 0.2 x/d, and □ 0.1 x/d

Shear stress data, Figure 4-9, approaches zero at the axis of symmetry (jet centreline), before decreasing to a peak at the same radial distance as the peak seen in the turbulent velocity data, at the centre of the shear layer, as also found by Rajaratnam et al. (2010). Due to the co-ordinate system applied (Chapter 1) where the origin is situated on the jet axis at the impingement surface, axial velocities approaching the base are denoted as negative and radial flow directed from the axis to the right as positive. Hence, the shear stress is shown as negative to the right of the axis and positive to the left. Turbulence penetrates towards the jet axis and the potential core diminishes as the turbulent shear layer grows towards the jet axis. As the wall is approached, the influence of the wall increases, increasing the local maxima $(\overline{uv})_m$ due to increased turbulence within the impingement region. The shear layer grows in magnitude and width pushing $(\overline{uv})_m$ further from the jet axis.

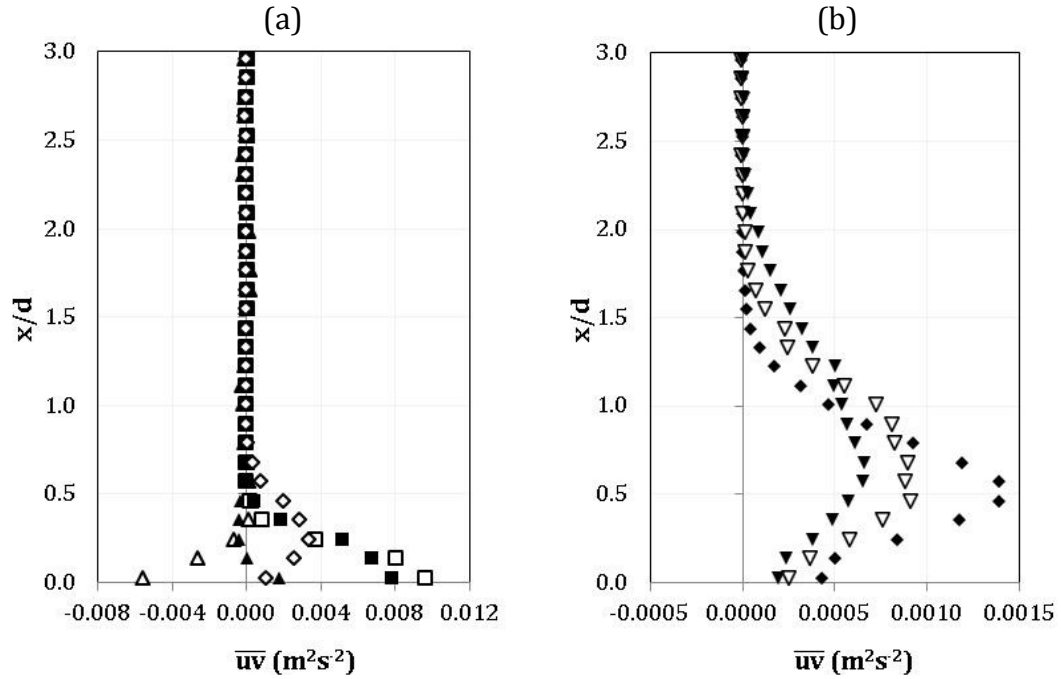

Figure 4-10 Single-phase shear stress data at h/d ratio = 2, vertical profiles within: (a) radial wall jet near-field region - △ 1 r/d, ▲ 2 r/d, □ 3 r/d, ■ 4 r/d, ◇ 5 r/d, (b) radial wall jet far-field region - ◆ 10 r/d, ▽ 12 r/d, ▼ 15 r/d.

The deflecting region of the impinging jet can be seen from the change in shear stress as distance from the jet axis is increased, Figure 4-10. One diameter from the stagnation point the shear stress is negative before becoming positive from 2d radially outwards. At 2, 3 and 4d the rise in the shear stress shows the growth of the upper shear layer as the flow deflects and accelerates after impingement. The lower shear layer which tends to zero at the wall (Cooper et al., 1990), due to the viscous forces at the wall, in the near-field radial wall jet is not evident in these data as it is too small scale for these measurements. At 2 r/d the profile goes slightly negative (-0.0004 m^2s^{-2}) around 0.3d (Cooper et al., (1990) found this maximum at 2 r/d) from the base before turning positive closer to the wall. The largest shear stress in the radial wall jet is recorded at 3 r/d, falling a little at 4 r/d followed by a more significant drop at 5 r/d where the lower shear layer is seen.

Moving towards the far-field both shear layers become clear as the flow radially spreads and decelerates, the shape of the distribution remaining constant but stretching for profiles from 5d. Approaching the wall jet axially from the otherwise stagnant surrounding fluid where the shear stress $\overline{uv}$ asymptotes to zero, the wall jet boundary layer signals the rise in shear stress until the local maxima $(\overline{uv})_m$ is reached around the same height as u'_m (Figure 4-8).

4.1.4 Summary

Two-dimensional measurements of mean and fluctuating velocities (normal stress), and shear stress are presented for all three regions (the developing jet, impingement region, and near- and far-field radial wall jet) of a liquid impinging jet at a jet-to-plate separation of two diameters. The dataset is consistent with expectations and the small amount of data available (Poreh et al., 1967; Cooper et al., 1993; Fairweather and Hargrave, 2002; Rajaratnam et al., 2010), the experimental system developed having been tested against the known flow structure of a single-phase impinging jet.

4.2 Impinging Jet Data – h/d = 6, outside potential core

Measurements were also made for an impinging jet configuration with a jet-to-plate separation (h/d) of 6 diameters, such that the impingement surface was just outside of the potential core of the jet. Mean velocities $\overline{U}$ and $\overline{V}$ in the axial and radial directions of the jet, respectively, as well as the RMS of the turbulent fluctuating velocities (u' and v') and shear stress ($\overline{uv}$) are shown for all of three regions of the jet and discussed in turn.

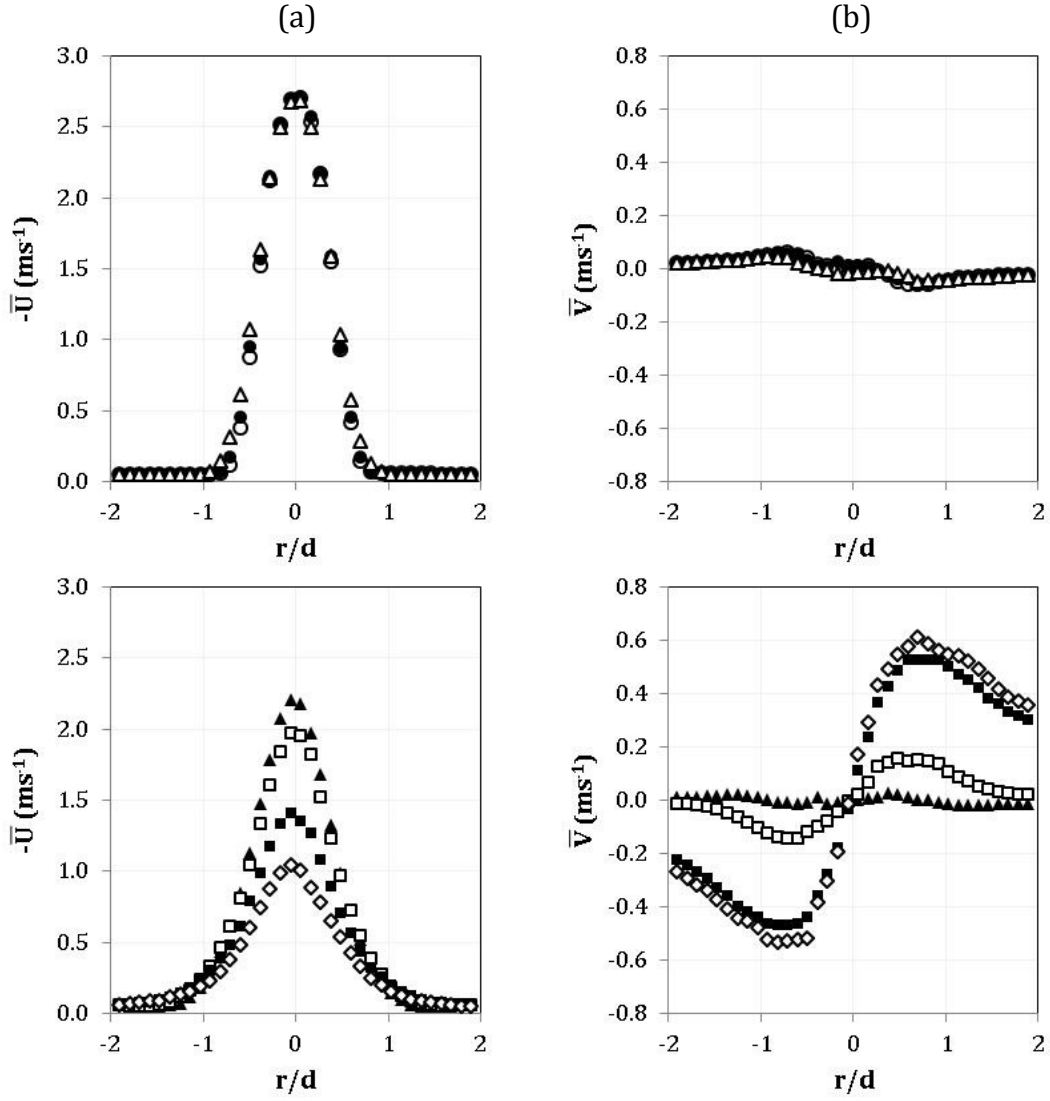

Figure 4-11 Single-phase developing jet data mean velocity data at h/d ratio = 6, horizontal profiles taken at ○ 5.3 x/d, ● 5 x/d, △ 4 x/d, ▲ 1 x/d, □ 1.5 x/d, ■ 0.2 x/d and ◇ 0.1 x/d: (a) mean axial velocity, (b) mean radial velocity.

Mean velocity data acquired from the developing jet region are shown in Figure 4-11. The flow close to the jet outlet is dominated by the axial component, the radial component remaining very close to zero, for the horizontal profiles taken within the first two diameters of the developing jet. This region contains the

potential core of the jet where the velocity does not diminish as the turbulence has not yet penetrated to the jet axis. The basic form of the velocity distributions here are similar to the previous impinging jet at 2 h/d, however, in this case the jet was allowed to develop further before the pressure gradient exerted by the wall caused modification to the turbulence field within the stagnation region, resulting in deceleration of the approaching liquid jet. As the wall is approached, the axial velocity diminishes as the radial component grows.

The potential core typically extends to around 5d from its source (Rajaratnam, 1976), beyond this point for a free jet the flow centreline velocity would begin to decay. An enhanced deceleration is however seen within 1d of the wall, as seen for a jet-to-plate separation of 2d. The magnitude of the jet centreline axial velocity is lower and the radial velocity greater at 1d from the base at this jet-to-wall separation than at 2 h/d.

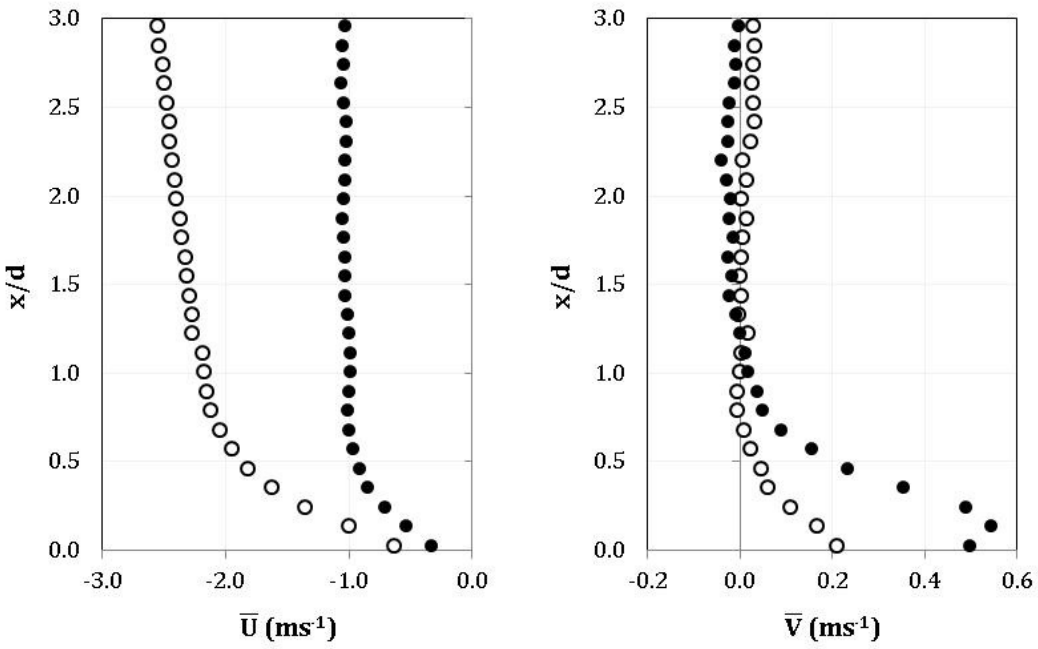

Figure 4-12 Single-phase mean axial and radial velocity data at h/d ratio = 6, vertical profiles within the impinging jet - ○ 0 r/d and ● 0.5 r/d.

The axial velocity profile along the stagnation decays from a maximum of 2.70ms^{-1} near the jet outlet, falling only a fraction within the first 3 diameters to 2.55ms^{-1}. The rate of deceleration is then fairly consistent until around 1d above the floor (Figure 4-12), where it then decays more rapidly as the wall exerts a pressure gradient in the stagnation region. As with the data at an h/d ratio of 2, we would expect the radial velocity to be zero along the stagnation line, but as discussed in the Physical Modelling Chapter (Section 3.3.5, page 73), the centreline profile is taken as close to the jet axis as possible but it is not

always possible to select the exact location of the centreline resulting in this profile potentially being slightly to one side of that line, hence resulting in non-zero velocities. The profiles 0.5d from the jet axis show the jet deflecting from the stagnation region, heading towards the radial wall jet.

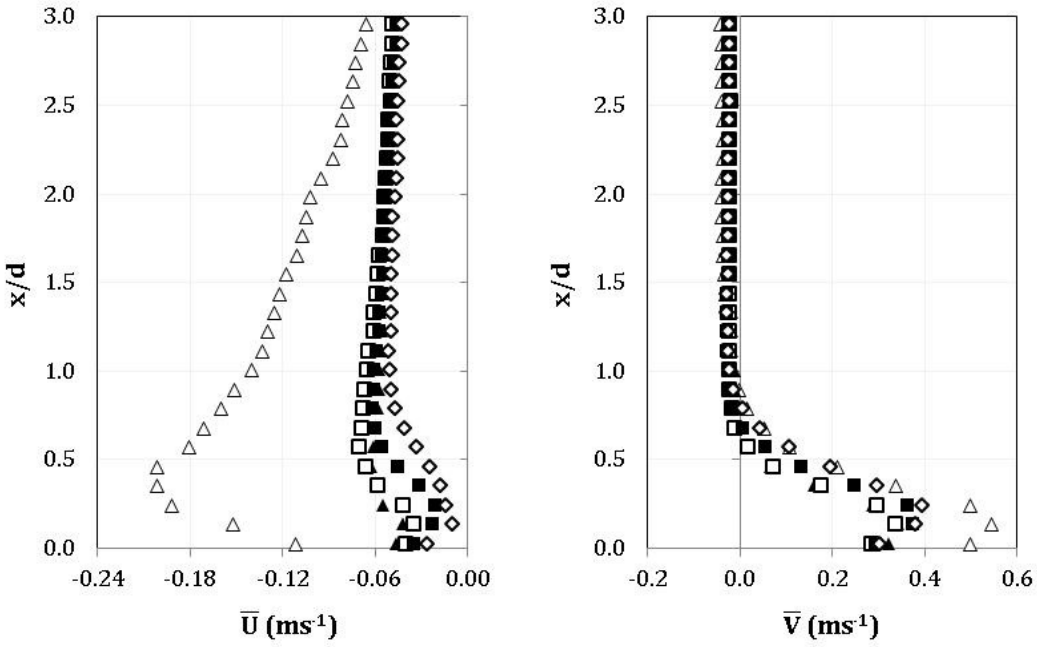

Figure 4-13 Single-phase mean axial and radial velocity data at h/d ratio = 6, vertical profiles within the radial wall jet near-field region - △ 1 r/d, ▲ 2 r/d, □ 3 r/d, ■ 4 r/d, and ◇ 5 r/d.

The profile at 1 r/d shows the growth of the outer regions of the developing jet as it accelerates towards the wall, Figure 4-13. At the jet height of 6d, the developing jet grows radially significantly more than at 2 h/d and appears as acceleration at this radial distance from the jet axis. The magnitude reduces again as the flow is deflected and begins to accelerate radially from 2 diameters. As the radial velocity increases with increasing distance from the jet axis, the axial component decays. Above the radial wall jet, liquid is entrained contributing to its growth. On this occasion, the data display two peaks. The first, as the wall is approached, is at the boundary between the entraining liquid (negative velocity as flow moves towards the base) and the upper shear layer of the developing wall jet, slowing the downward flow. The second peak coincides with a peak in the radial mean velocity, where axially, flow is directed again towards the wall. The magnitude of velocities in this region are around an order of magnitude smaller in the radial direction compared to the initial developing jet, and around two orders of magnitude in the axial direction.

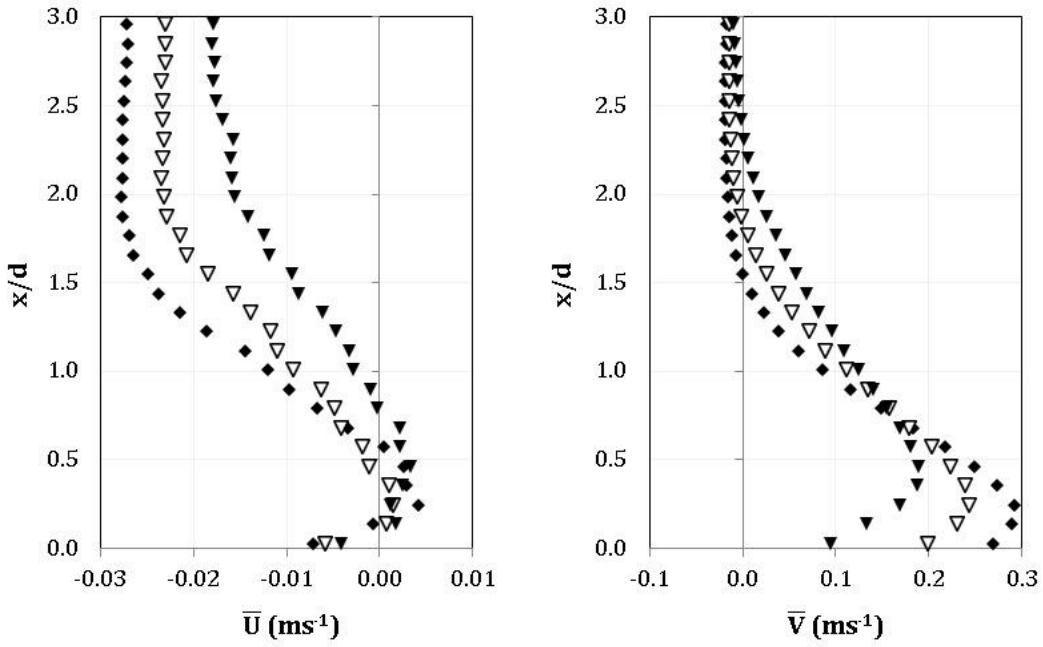

Figure 4-14 Single-phase mean axial velocity data at h/d ratio = 6, vertical profiles within the radial wall jet far-field region - ◆ 10 r/d, ▽ 12 r/d, and ▼ 15 r/d.

By the far-field of the radial wall jet, the velocity profiles are more developed showing the radial growth and deceleration expected within this region (Fairweather and Hargrave, 2002). Two peaks are again evident (Figure 4-14), this time the upper peak at the boundary is less defined and the lower peak with positive velocity. This local maxima U_m shows a region of upward flow, albeit of small magnitude, decaying with increasing r, but still remaining positive. Radial velocities are also decaying and the growth of the height of the wall jet is clear from the axial location of the local maxima V_m and the change in height of where the velocity decreases to a small negative value. Entrainment velocities are also decreasing with greater distance from the jet axis.

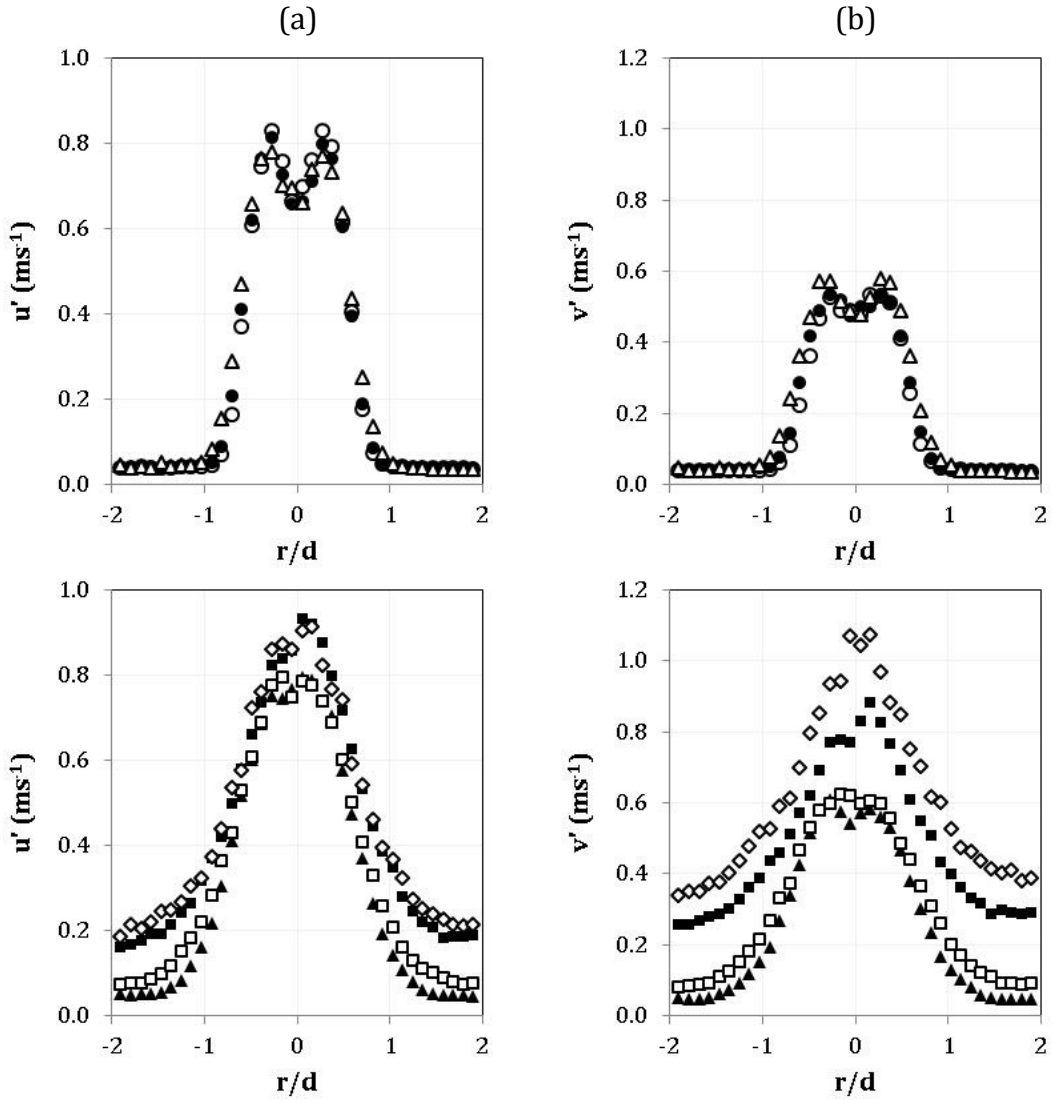

Figure 4-15 Single-phase developing jet data RMS fluctuating velocity data at h/d ratio = 6, horizontal profiles taken at ○ 5.3 x/d, ● 5 x/d, △ 4 x/d, ▲ 1 x/d, □ 1.5 x/d, ■ 0.2 x/d and ◇ 0.1 x/d: (a) axial fluctuating RMS, (b) radial fluctuating RMS.

Fluctuating velocities are presented in Figure 4-15. Within the developing jet, where the effects of the impingement surface are not felt, the turbulent velocity plots display the expected trends found for turbulent free jets (Warda et al., 1999; Fellouah and Pollard, 2009; Milanovic and Hammad, 2010). Two peaks about the jet centreline indicate the centre of the shear layers, with the turbulence intensity being lower at the jet axis. The magnitude of the turbulence intensity in the axial direction is larger than in the radial direction. Turbulence levels in the impinging jet increase as the impinging surface is approached, the effect becoming more significant the closer to the wall. Within this region the twin peak trend is no longer present. Again, as we saw in the radial turbulence velocity for the smaller jet-to-plate separation tested, the profiles taken just above the wall at the beginning of the radial wall jet can be

seen where the turbulence levels do not tend towards zero but instead remaining at up to nearly 0.4ms^{-1} which is close to the initial centreline level of turbulence. Axial turbulence undergoes a less significant change.

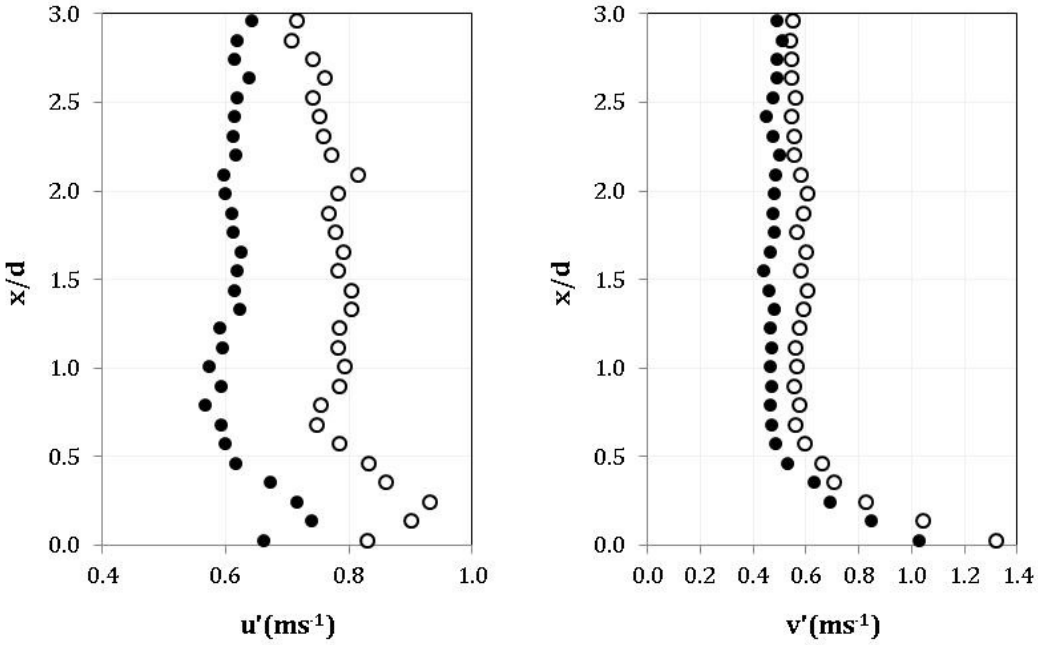

Figure 4-16 Single-phase axial RMS fluctuating velocity data at h/d ratio = 6, vertical profiles within the impinging jet - ○ 0 r/d and ● 0.5 r/d.

There is little difference between the fluctuating velocity profiles at 0 and 0.5d. The axial component trends are very similar, only the magnitude is a little different, around 0.2ms^{-1} greater along the jet axis than its neighbouring profile at 0.5d. Axially there is a subtle increase approaching the wall to a height of 0.5d where a more rapid increase is seen followed by a decrease as the wall is reached. Radially, the turbulence velocity remains constant until the same height above the base where it experiences a sharp increase.

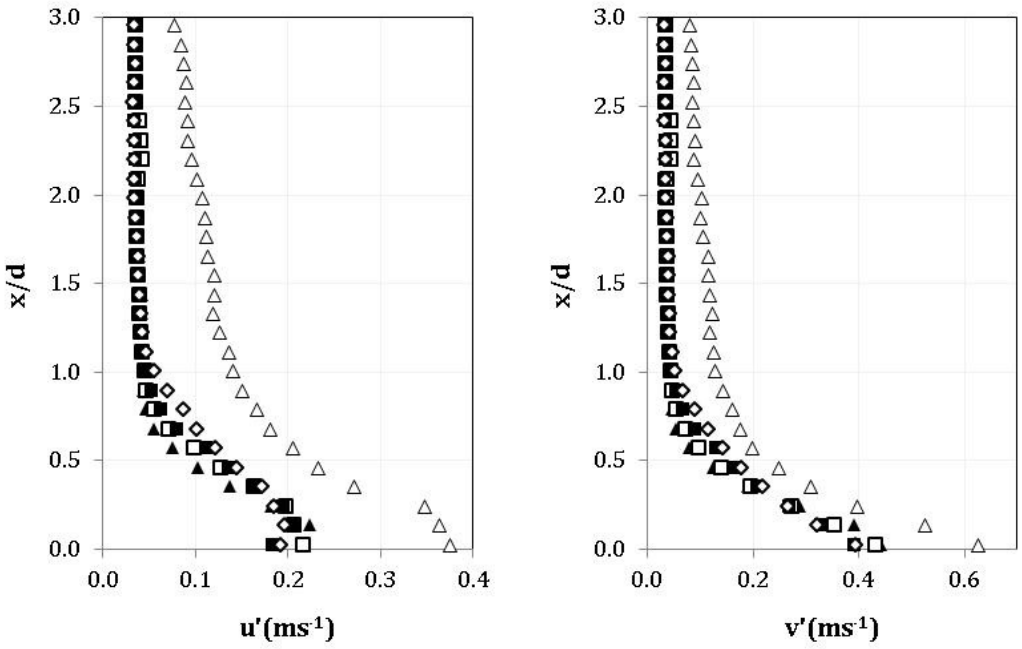

Figure 4-17 Single-phase axial RMS fluctuating velocity data at h/d ratio = 6, vertical profiles within the radial wall jet near-field region - △ 1 r/d, ▲ 2 r/d, □ 3 r/d, ■ 4 r/d, and ◇ 5 r/d.

The near-field radial wall jet, from the deflection of the stagnation region, accelerates until the far-field is reached where the flow becomes self-similar. As seen from the velocity data, Figure 4-13, the profile at 1 r/d shows the radial growth of the outer edges of the developing jet. It has a similar shape to the other profiles here but with higher values, reaching a maximum of $0.38ms^{-1}$ close to the wall.

The highest turbulence velocities are seen at 2 r/d after which the local maxima reduce as we move away from the jet axis. The radial turbulence velocities are approximately 50% greater within the wall jet than the axial component due to the redistribution of turbulence energy attributed to the pressure gradient exerted by the wall.

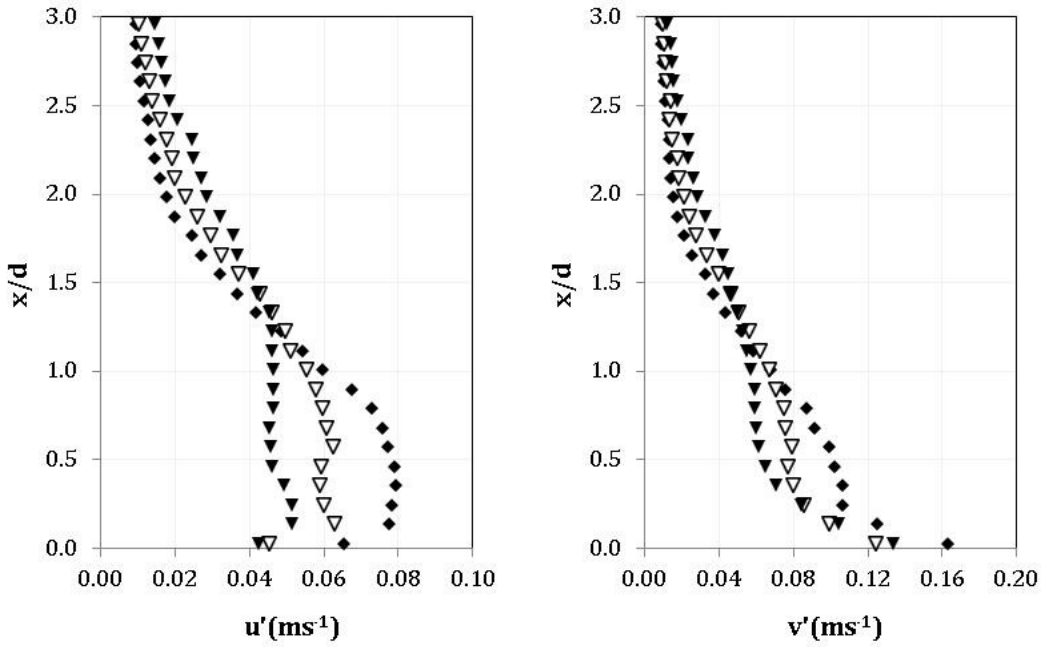

Figure 4-18 Single-phase axial RMS fluctuating velocity data at h/d ratio = 6, vertical profiles within the radial wall jet far-field region - ◆ 10 r/d, ▽ 12 r/d, and ▼ 15 r/d.

RMS fluctuating velocities within the far-field region have reduced quite considerably from the near-field, Figure 4-18, and by nearly an order of magnitude. Like the near-field region, the turbulence velocity at 10 r/d increases through the upper shear layer of the wall jet until a local maximum is reached. The radial turbulence velocity then has a second peak very close to the wall before a final increase before the wall is reached. The profiles at 12 and 15 r/d are somewhat different. At these radial distances, the axial RMS fluctuating velocity varies towards the impingement surface, initialling following a similar trend to 10 r/d above the wall jet. For the axial component, no definite peak can be seen but there is an inversion (slight dip) around the same height as the radial velocity peak, and then another change in gradient as the wall is reached. Radially, the turbulent velocity is continually growing but going through a section of no apparent change which would appear to be within the upper shear layer, before an increase again towards the wall.

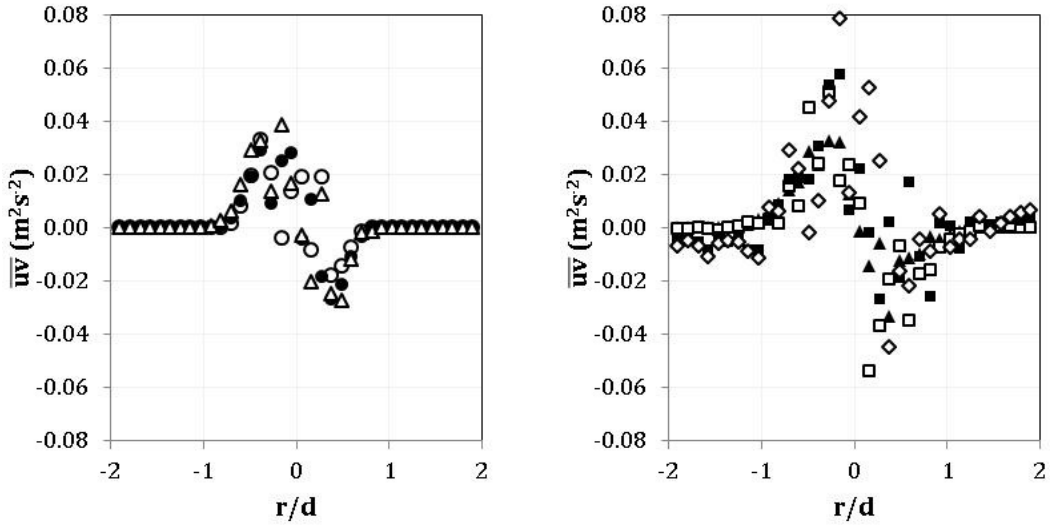

Figure 4-19 Single-phase developing jet shear stress data at h/d ratio = 6, horizontal profiles taken at ○ 5.3 x/d, ● 5 x/d, △ 4 x/d, ▲ 1 x/d, □ 1.5 x/d, ■ 0.2 x/d and ◇ 0.1 x/d.

The fluid flow in the developing jet is dominated by the axial velocity component making the radial component extracted from the velocity vectors produced from the PIV measurements very difficult to resolve. The calculation of shear stress is the product of both the u and v instantaneous velocities so if one component is problematic, this is amplified within these statistics. This can be seen in the results of Figure 4-19. Within the developing jet before and after the wall exerts a pressure gradient, the shear stress data are quite erratic. The general shape is consistent with that of other workers (Rajaratnam and Hammad, 2010). As expected, the shear stress goes through zero at the jet axis and increases radially outwards until it reaches a local maximum at the centre of the shear layer, before diminishing at the outer edge of the jet into the surrounding fluid. Shear stress values increase the closer to the impingement surface due to the turbulence within the stagnation region, the pressure gradient exerted by the wall modifying the turbulence distribution in the vicinity of the impingement surface.

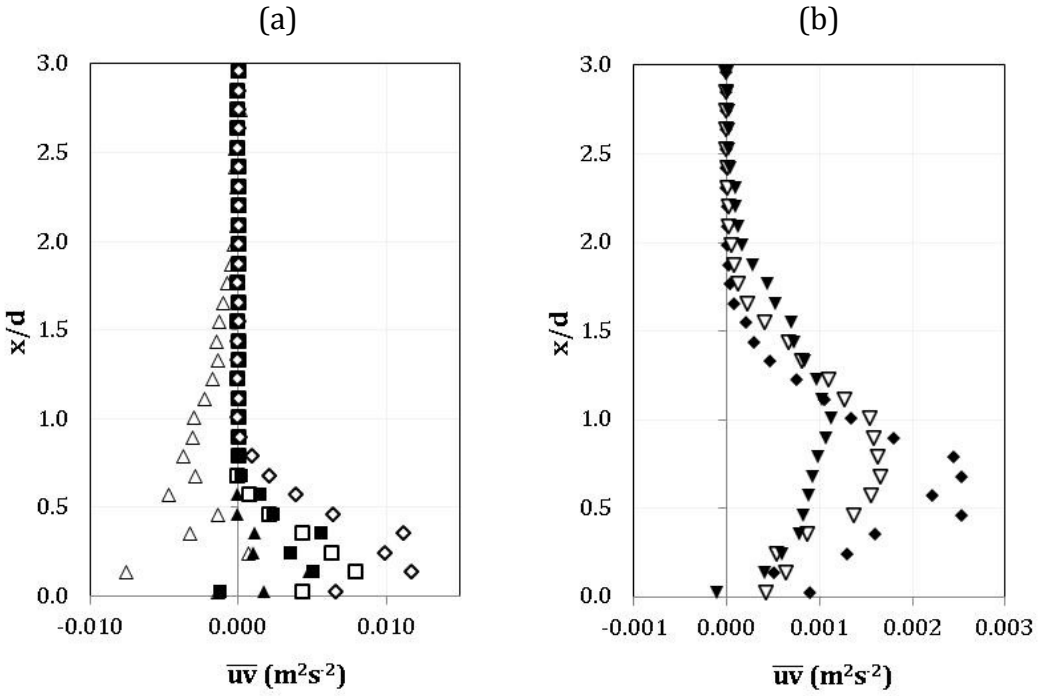

Figure 4-20 Single-phase shear stress data at h/d ratio = 6, vertical profiles within: (a) radial wall jet near-field region - △ 1 r/d, ▲ 2 r/d, □ 3 r/d, ■ 4 r/d, ◇ 5 r/d, (b) radial wall jet far-field region - ◆ 10 r/d, ▽ 12 r/d, ▼ 15 r/d.

At 1 r/d, Figure 4-20, the shear stress is negative, according to the co-ordinate system used here, as already seen in previous figures. The shear stress within the wall jet at first increases as we move away from the jet centreline reaching a maximum at 5d. In the far-field the flow decelerates and the shear stress decays. The shape of all profiles from 2 to 15 r/d is similar, with increases through the upper shear layer, reaching a local maximum around the same height as the corresponding radial velocities. The height of these maxima increase as the jet expands.

4.3 Impinging Jet Data – h/d = 10, developing jet

The largest jet height tested within the work was at 10d. This is representative of a fully developed free jet prior to impingement. Again, mean velocities $\overline{U}$ and $\overline{V}$ in the axial and radial directions of the jet, respectively, as well as the RMS of the turbulent fluctuating velocities (u' and v') and shear stress ($\overline{uv}$) are shown below for all of three regions of the impinging jet, and discussed in turn.

The mean velocity data shown in Figure 4-21 have been taken a axial locations near the jet outlet (9.3, 9 and 8 x/d), the middle of the developing jet where the potential core of the jet typically ends (5 and 4 x/d), and close to the impingement region (1, 0.5, 0.2 and 0.1 x/d). As expected, the profiles near the jet outlet collapse. The axial component corresponds to the power law expected for a fully developed pipe flow, while the radial component remains around zero, with the jet dominated by the axial flow in this region. By 5 and 4 x/d, the centreline velocity has begun to decay with only a small difference between these locations. Here, the turbulence is penetrating to the jet axis.

Until the impingement surface begins to impact on the flow phenomena of the impinging jet, it may be considered a free jet. Milanovic and Hammad (2010) found, for a liquid turbulent round jet, the magnitude of the centreline axial velocity ($\overline{U}$) at 8d from the jet outlet was approximately 68% of the potential core value. For the impinging jet with jet-to-plate separation (h/d) of 10 presented here, taking the potential core value at 8 x/d, Figure 4-21, (2d from the jet outlet) and 2 x/d, Figure 4-22 (8d from the jet outlet, as used by Milanovic and Hammad, 2010), the centreline axial velocity was 70.4% of the potential core value. The strong correlation here confirms for the impinging jet at 10 h/d, the effect of the impingement surface is negligible more than 2d above the surface.

When the impingement surface begins to impact on the approaching flow, within 2d of the surface, we see that the axial velocity decays and the radial velocity increases as the flow is deflected. There is radial spreading of the annular shear layer due to the fully developed turbulent jet interacting with the ambient fluid.

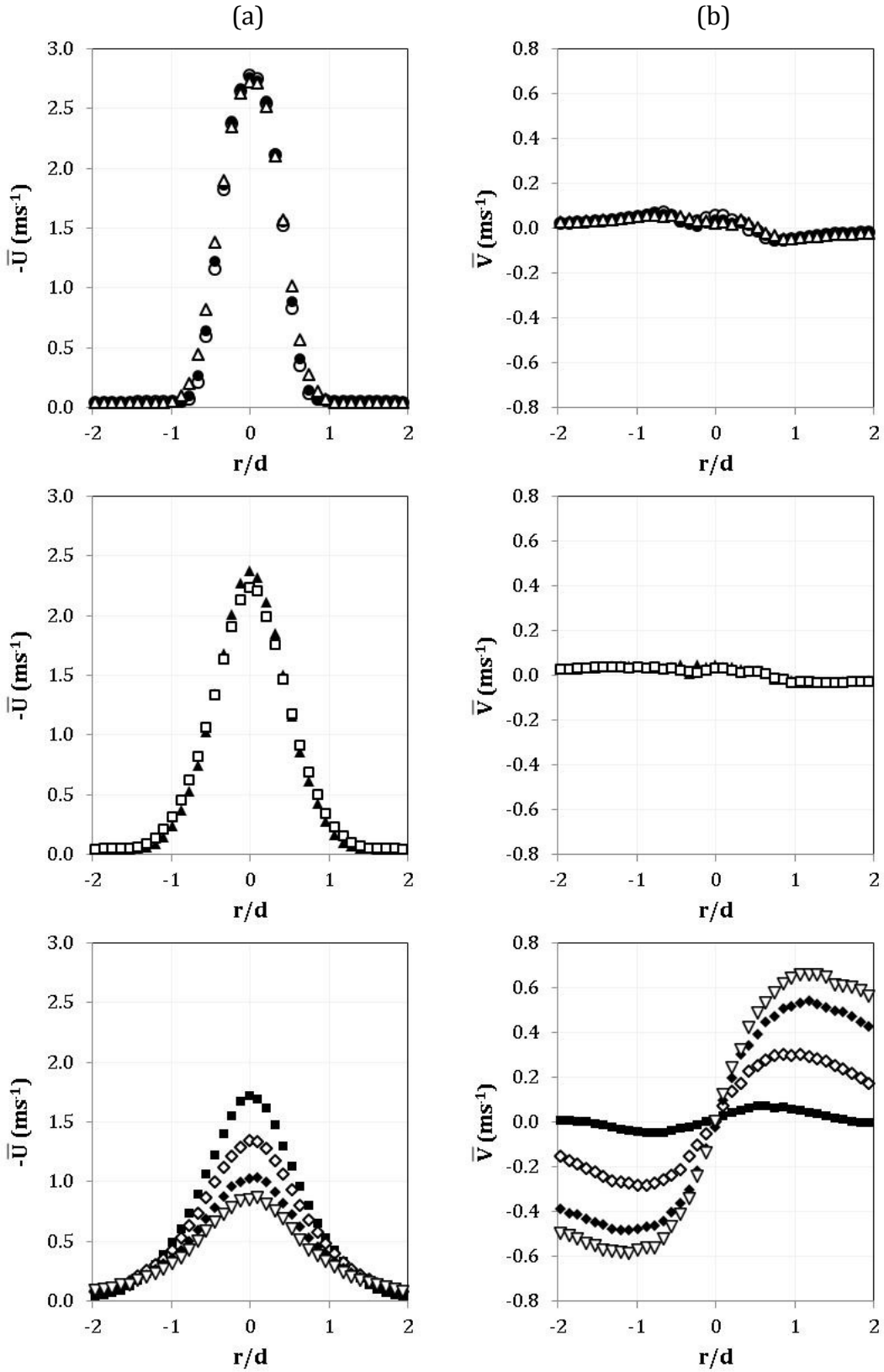

Figure 4-21 Single-phase developing jet mean velocity data at h/d ratio = 10, horizontal profiles taken at ○ 9.3 x/d, ● 9 x/d, △ 8 x/d, ▲ 5 x/d, □ 4 x/d, ■ 1 x/d, ◇ 0.5 x/d, ◆ 0.2 x/d, and ▽ 0.1 x/d: (a) mean axial velocity, and (b) mean radial velocity.

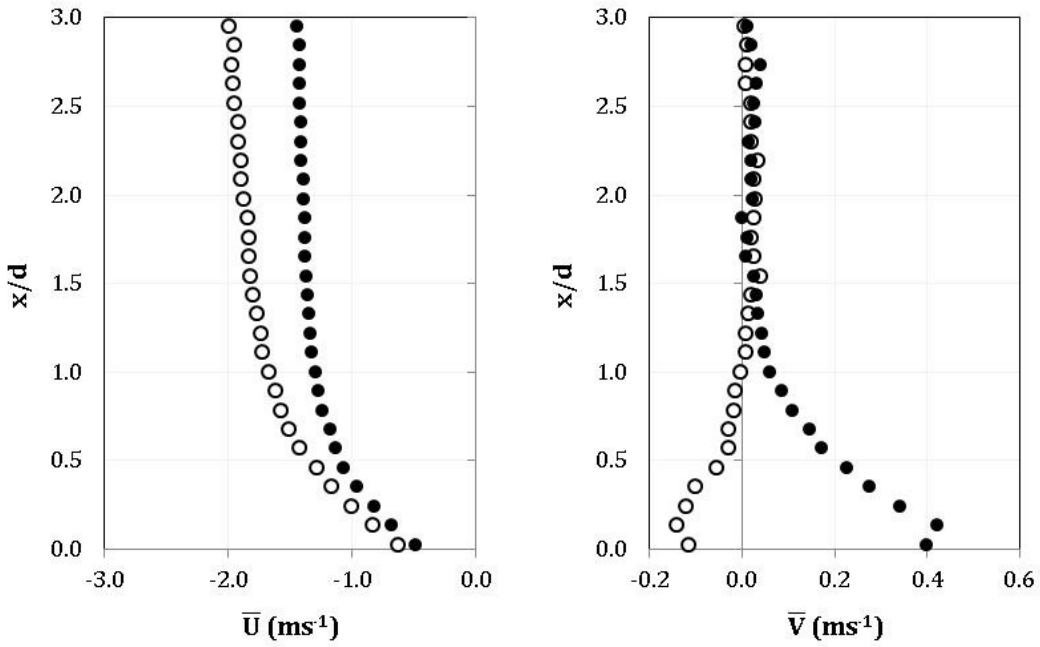

Figure 4-22 Single-phase mean axial and radial velocity data at h/d ratio = 10, vertical profiles within the impinging jet - ○ 0 r/d and ● 0.5 r/d.

Following the mean velocity change along the stagnation line in Figure 4-22 shows the axial component decaying from 2.66ms^{-1} near the outlet until 1 x/d where the deceleration rate increases as it approaches the impingement region. For the profile taken at 0.5d radially from the jet centreline, the axial component remains relatively unchanged until about 1 x/d from the wall, and again the rate of decay increases due to the wall. Meanwhile the radial velocity increases from around the same height as the axial component begins to change.

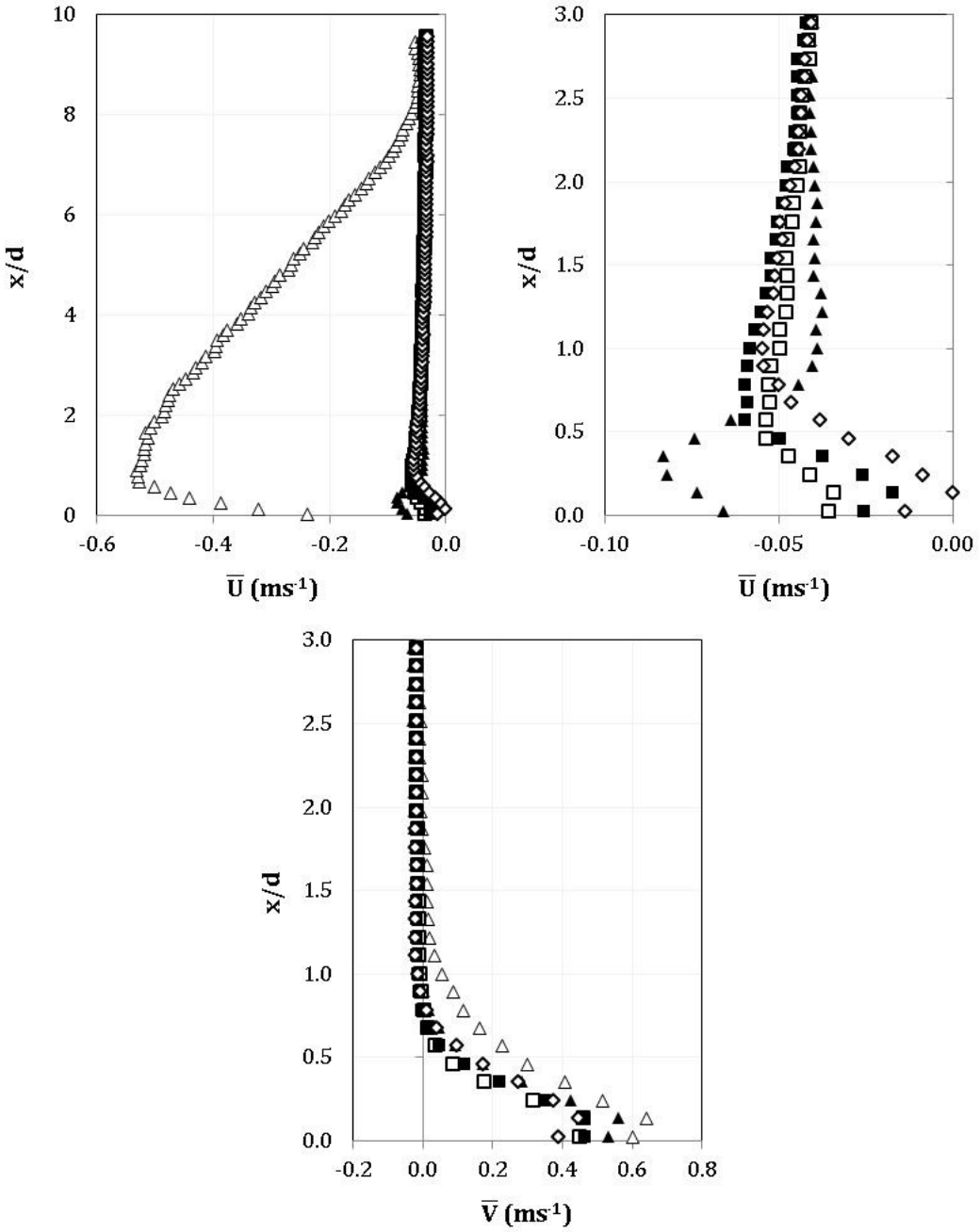

Figure 4-23 Single-phase mean axial and radial velocity data at h/d ratio = 10, vertical profiles within the radial wall jet near-field region - △ 1 r/d, ▲ 2 r/d, □ 3 r/d, ■ 4 r/d, and ◇ 5 r/d.

At this jet-to-plate separation, $\overline{U}$ at 1 r/d has been allowed to increase to a higher local maximum than the other two jet separations tested, it of course tends to zero as the wall is reached, Figure 4-23. Looking at a magnified scale for the near-field axial velocity profiles (top right-hand plot), interestingly 2 r/d has a similar profile shape as that at 1 r/d, albeit the increase in axial velocity does not begin until within 1d of the wall, above which the entraining velocity remains relatively constant. For the other jet heights tested, the data at 2 r/d suggests the beginning of the near-field wall jet. However at this jet height of

10 diameters it would appear that the deflecting part of the jet extends a little further out from the jet axis. From 3 r/d, the data shows the developing jet, with the axial velocity within the wall jet accelerating (although remaining negative) while the radial velocity falls. The local maxima for both velocity components occur at the same height above the base.

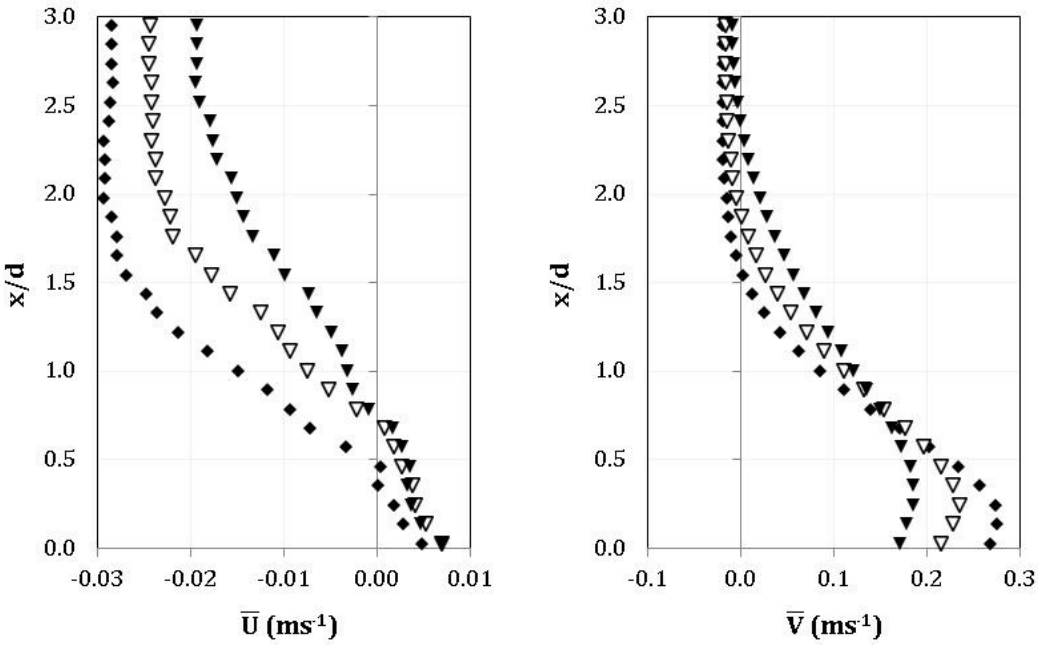

Figure 4-24 Single-phase mean axial and radial velocity data at h/d ratio = 10, vertical profiles within the radial wall jet far-field region - ◆ 10 r/d, ▽ 12 r/d, and ▼ 15 r/d.

Out in the far-field, Figure 4-24, the radial velocity falls further as we move away from the jet axis. As within the near-field the axial velocity continues to increase becoming positive around 0.5 x/d for 10 r/d, and 0.7 for 12 and 15 r/d. The radial component is also continuing the same behaviour as in the near-field and is decreasing with increasing r.

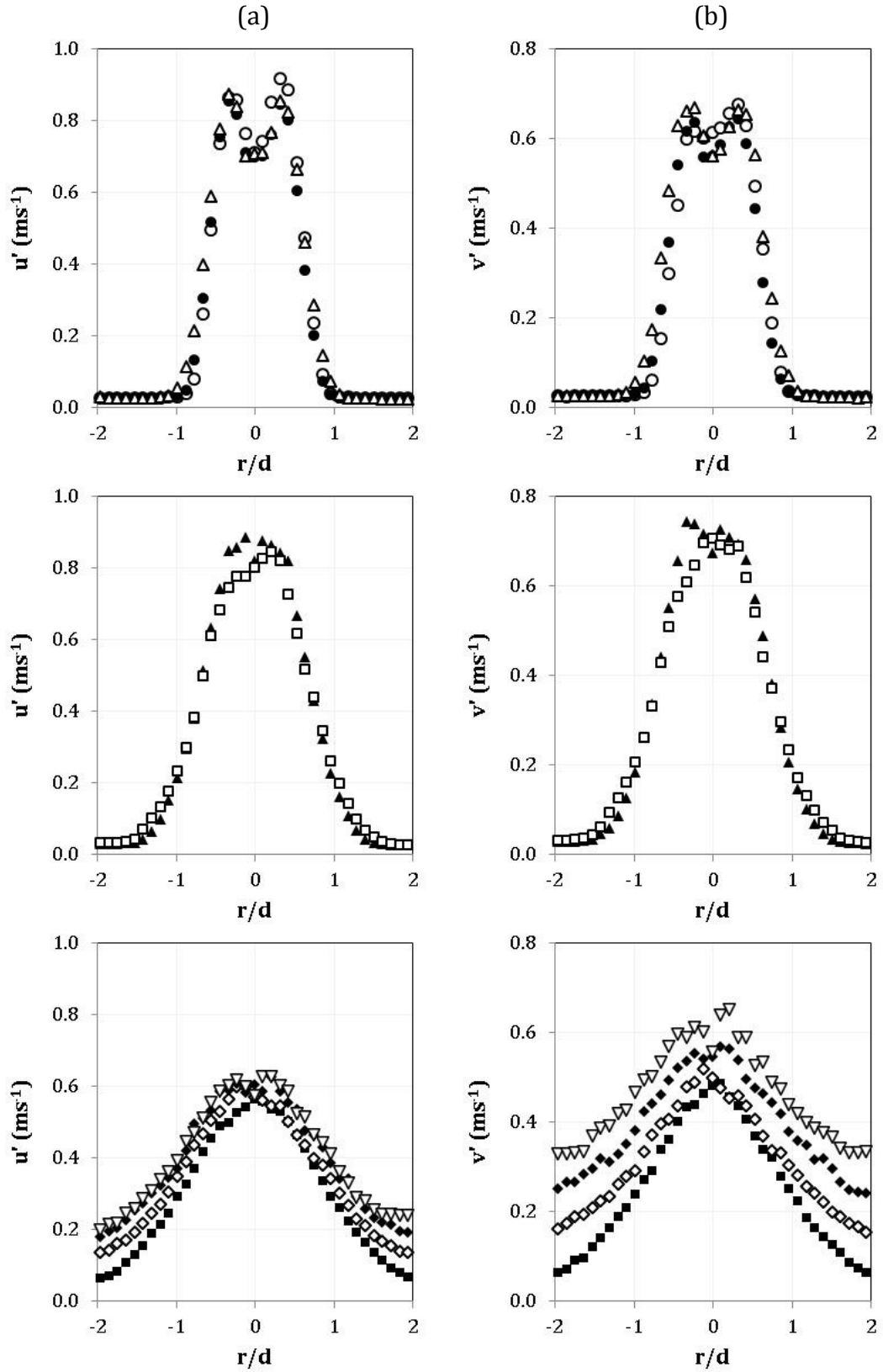

Figure 4-25 Single-phase developing jet data RMS fluctuating velocity data at h/d ratio = 10, horizontal profiles taken at ○ 9.3 x/d, ● 9 x/d, △ 8 x/d, ▲ 5 x/d, □ 4 x/d, ■ 1 x/d, ◇ 0.5 x/d, ◆ 0.2 x/d, and ▽ 0.1 x/d: (a) axial fluctuating RMS, and (b) radial fluctuating RMS.

The values of axial turbulent velocities (Figure 4-25) within the developing jet, up to 6d from the jet outlet, and before the wall is felt, remain relatively unchanged, although at 5 and 4 x/d the twin peaks are no longer present as the turbulence penetrates to the jet centreline. The radial RMS component increases slightly across these profiles, with lower values than their axial counterparts. Within 1d of the wall jet once again turbulence levels increase. For this case however, the spread between the profiles is not as substantial as with the other two smaller jet-to-plate separations studied. Also the twin peaks are more prominent as the jet height is increased as the shear mixing layers around the potential core are increasingly free to develop before the influence of the impingement surface is exerted.

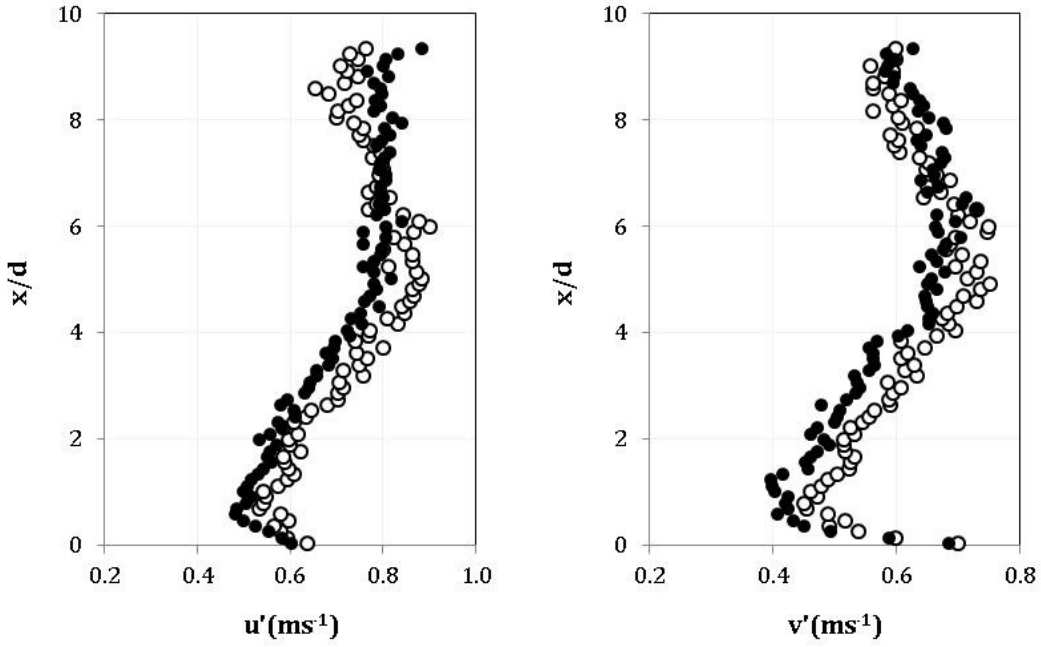

Figure 4-26 Single-phase axial and RMS radial fluctuating velocity data at h/d ratio = 10, vertical profiles within the impinging jet - ○ 0 r/d and ● 0.5 r/d.

Vertical profiles taken at 0 and 0.5d, Figure 4-26, show interesting RMS fluctuating velocity behaviour. The trends are similar for each component and the magnitudes are not dissimilar. From the jet outlet, all profiles have a negative gradient increasing gradually until 5 x/d which is half way between the jet outlet and the impingement surface, the axial components have slightly higher values. This is also the typical length of the potential core. The turbulent velocities then begin to fall at a higher rate than in the previous region, again at similar gradients and values to one another before increasing again on the final approach to the wall (from 0.5d above the floor).

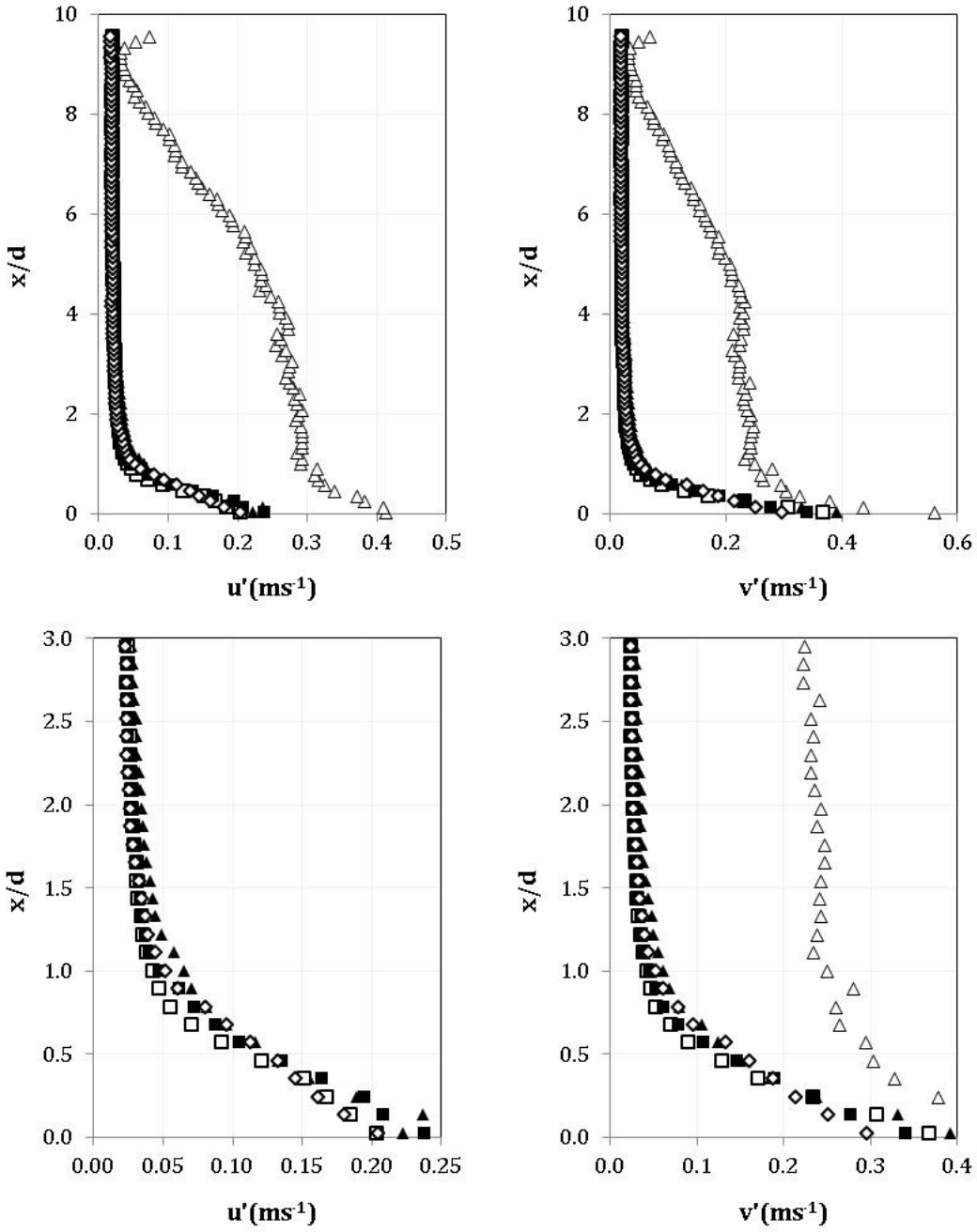

Figure 4-27 Single-phase axial and radial RMS fluctuating velocity data at h/d ratio = 10, vertical profiles within the radial wall jet near-field region - △ 1 r/d, ▲ 2 r/d, □ 3 r/d, ■ 4 r/d, and ◇ 5 r/d.

As the fluid from the impinging jet is deflected after hitting the stagnation region, the near-field radial wall jet forms (Figure 4-27). There is considerable reduction in the RMS of the fluctuating velocity from 1 to 2 r/d. At 1d from the centre of the jet we can see the developing jet expand as it moves away from the jet outlet. From 2 to 5 r/d the change is much more subtle. Radially there is an increase, within the wall jet, with increasing r, while the change in the axial component is even more subtle.

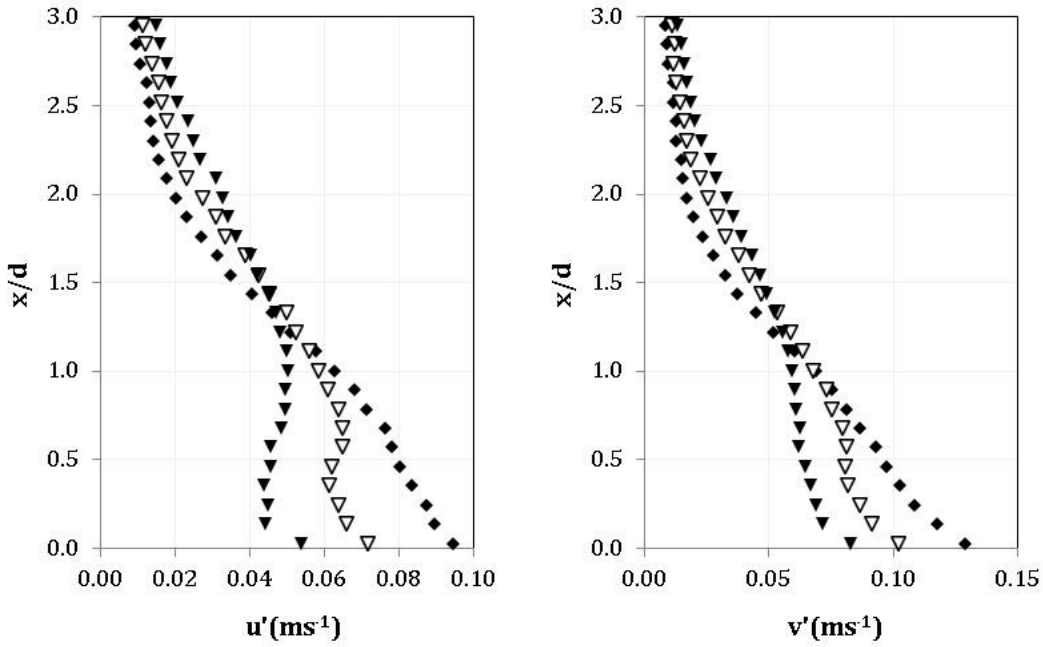

Figure 4-28 Single-phase axial and radial RMS fluctuating data at h/d ratio = 10, vertical profiles within the radial wall jet far-field region - ◆ 10 r/d, ▽ 12 r/d, and ▼ 15 r/d.

With increasing distance from the jet axis, Figure 4-28, the turbulence velocities are decreasing within the wall jet, the magnitude of the radial component being greatest. The inversion in the profile shape near the wall coincides with the position of the local radial mean velocity maximum V_m.

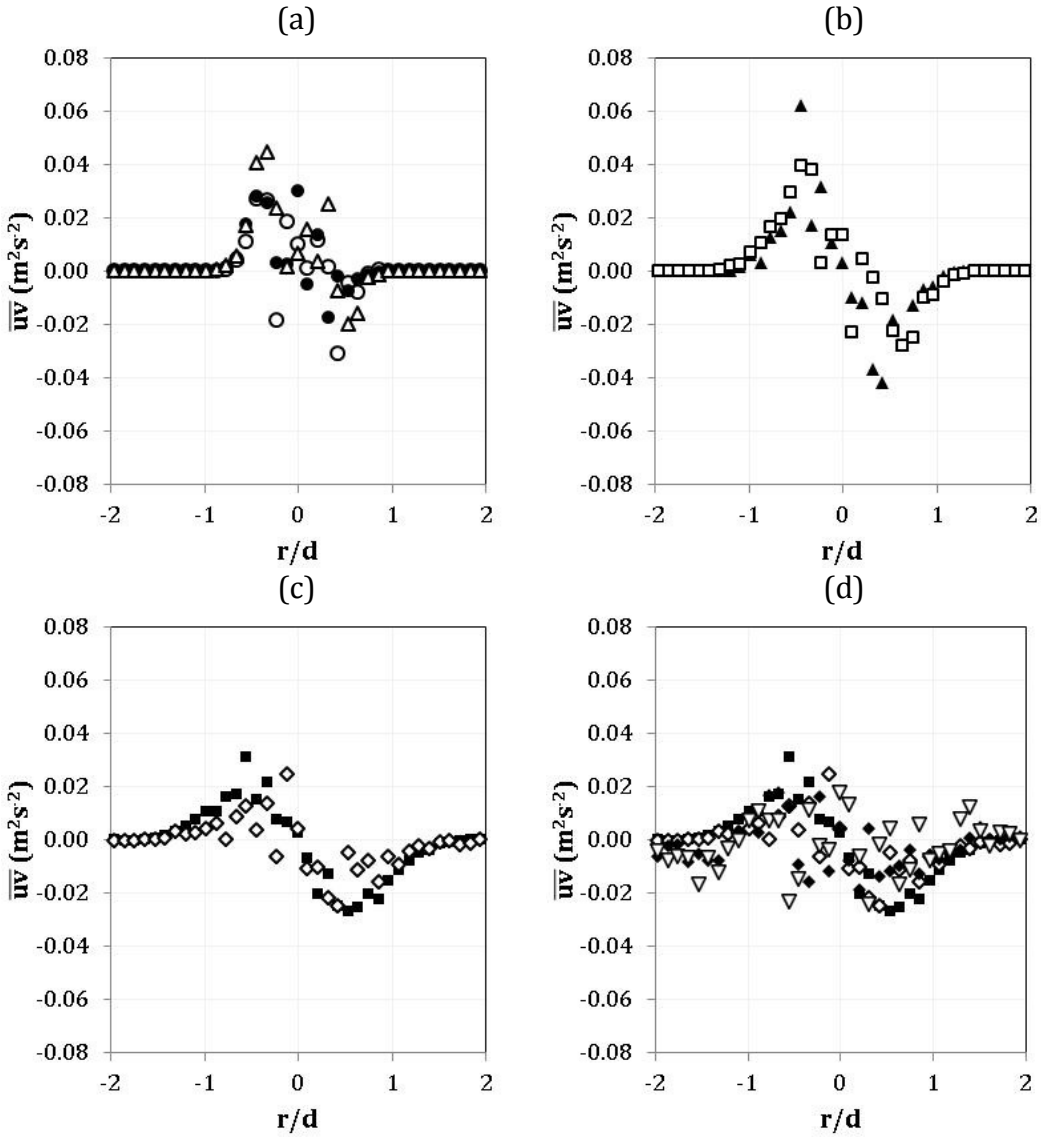

Figure 4-29 Single-phase developing jet shear stress data at h/d ratio = 10, horizontal profiles taken at (a) ○ 9.3 x/d, ● 9 x/d, △ 8 x/d, (b) ▲ 5 x/d, □ 4 x/d, (c) ■ 1 x/d, ◇ 0.5 x/d (d) ■ 1 x/d, ◇ 0.5 x/d, ◆ 0.2 x/d, and ▽ 0.1 x/d

As previously, close to the jet outlet where the flow is dominant in the axial direction, resolving the radial component of velocity is difficult. And without good quality, reliable radial instantaneous velocity data, any calculation of turbulence properties such as shear stresses has its limitations (Section 3.4.4, page 80). This can be clearly seen on Figure 4-29(a) where within the developing region the data shows a hint of the pattern expected but there is significant scatter. Moving to the middle of the developing jet at 5 and 4 x/d the pattern is more clear, with the magnitude also increased now we are beyond the potential core. Closer to the impingement region at 1 and 0.5 x/d, Figure

4-29(c), the shear stress values have decreased and the local maximum $(\overline{uv})_m$ moves to a greater radial distance from the jet axis.

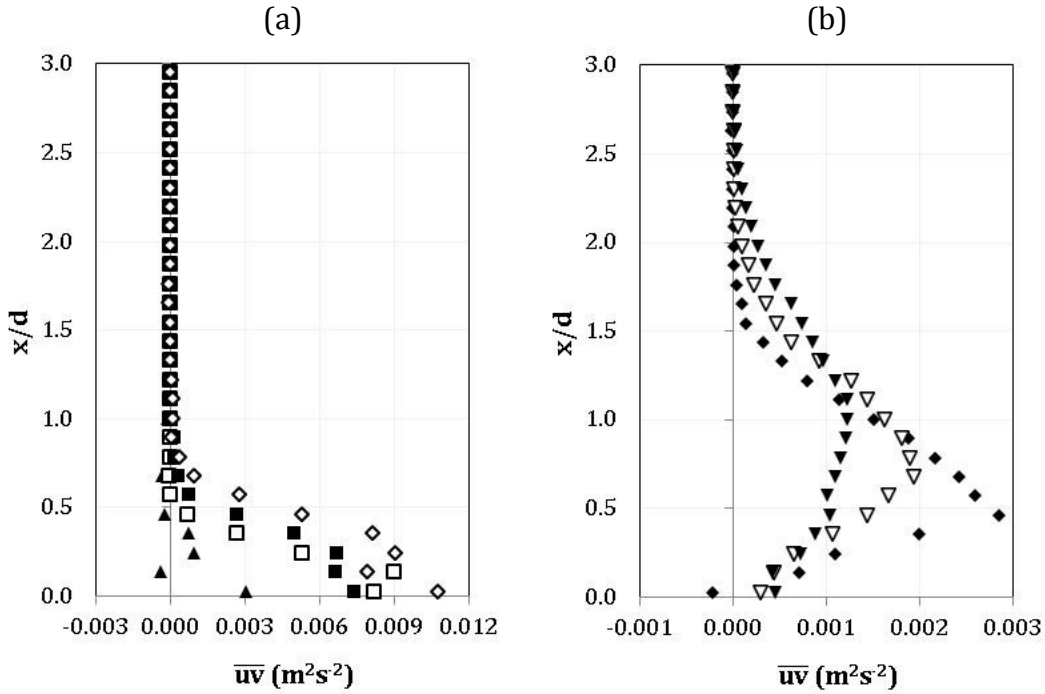

Figure 4-30 Single-phase shear stress data at h/d ratio = 10, vertical profiles within: (a) radial wall jet near-field region - ▲ 2 r/d, □ 3 r/d, ■ 4 r/d, ◇ 5 r/d, (b) radial wall jet far-field region - ◆ 10 r/d, ▽ 12 r/d, ▼ 15 r/d.

The near- and far-field wall jet can be described by the development of the shear layers (Figure 4-30). Within the near-field, the shear stress grows with increasing distance from the jet axis. The shear layers can be clearly seen in the far-field, the upper shear layer by the negative gradient as the shear stress increases as the wall is approached, and the lower layer by the decrease in shear stress closer to the wall.

4.4 Jet Height Effect

The effect of jet height on the turbulent flow phenomena of a turbulent liquid impinging jet is explored. The impingement surface has been positioned in strategic regions; h/d ratio of 2 is within the potential core, h/d ratio of 6 is just outside the core, and for an h/d ratio of 10 the jet flow has developed further before impingement. Profiles from within the developing jet, impinging region, and near- and far-field radial wall jet, have been presented and comparisons made.

4.4.1 Developing jet and impinging region

The developing jet region of an impinging jet contains the potential core where the velocity profile of the fully developed pipe flow gradually diminishes in width.

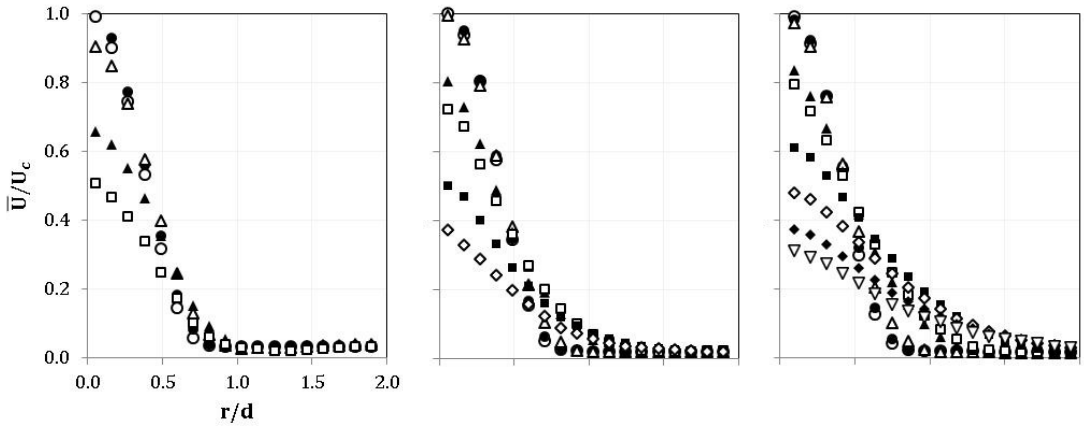

Figure 4-31 Single-phase developing jet normalised axial mean velocity component at h/d ratio of 2 (left), 6 (middle) and 10 (right):

h/d ratio 2: ○ 1.3 x/d, ● 1 x/d, △ 0.5 x/d, ▲ 0.2 x/d and □ 0.1 x/d,

h/d ratio 6: ○ 5.3 x/d, ● 5 x/d, △ 4 x/d, ▲ 1 x/d, □ 0.5 x/d, ■ 0.2 x/d and ◇ 0.1 x/d

h/d ratio 10: ○ 9.3 x/d, ● 9 x/d, △ 8 x/d, ▲ 5 x/d, □ 4 x/d, ■ 1 x/d, ◇ 0.5 x/d, ◆ 0.2 x/d, and ▽ 0.1 x/d.

The axial mean velocity normalised by the jet centreline outlet velocity, U_c, allows us to see the growth of the developing jet as it approaches the wall, Figure 4-31. All three jet heights initially begin with profiles where the mean axial velocity remains that of the pipe flow. The profiles near the jet outlet are comparable to the expected fully developed pipe flow conditions approximated by the power law. The higher the jet line from the impingement surface, from

left to right in Figure 4-31, the more advanced the expansion of the jet. The centreline mean axial velocity decreases as the jet spreads radially.

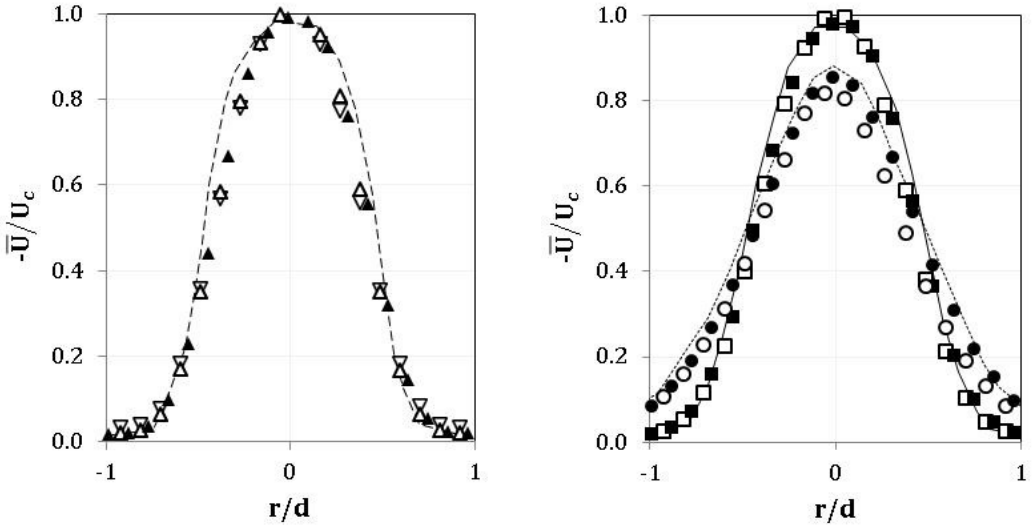

Figure 4-32 Normalised axial mean velocity for single phase impinging jets at each h/d ratio, 1d from jet outlet (right – triangles, long dash), 2 and 5d from jet outlet (left – squares and circles respectively, solid line and short dash respectively)

Data profiles key: 2 h/d (upside triangle), 6 h/d (open symbols) and 10 h/d (closed symbols), and Milanovic et al., 2010 (lines)

Axial mean and RMS fluctuating velocities at 1, 2 and 5d from the jet outlet for each jet-to-plate separation explored are displayed in Figure 4-32 (and Figure 4-33 below). The mean velocity normalised by the jet centreline initial velocity profiles collapse upon one another indicating fully developed pipe conditions and also show good flow symmetry.

There is very good agreement between the profiles taken at 1d from the jet outlet for the trials performed at each of the three h/d ratios where no wall effects should be felt. According to the work of Beltaos and Rajaratnam (1974) and Rajaratnam et al. (2010), for large jet heights (h/d > 8.3) the impingement wall effect is only felt within 0.14 x/h of the surface which equates to 1.4d above the wall for the 10 h/d case. And if their findings were applicable to smaller jet-to-plate separations we would expect the wall effect to be present only within 0.28d of the wall for the 2 h/d case, and 0.84d for 6 h/d.

Further profiles are compared at 2 and 5d from the jet outlet for the larger two jet heights tested and are very similar. Each has been plotted against data from a water free jet at Reynolds number of 14,000 (Milanovic and Hammad, 2010) and show very good agreement indicating, that within the developing jet where the impingement surface is having no impact, the flow behaves as a free jet.

This also gives confirmation that the experimental runs were indeed performed under similar conditions.

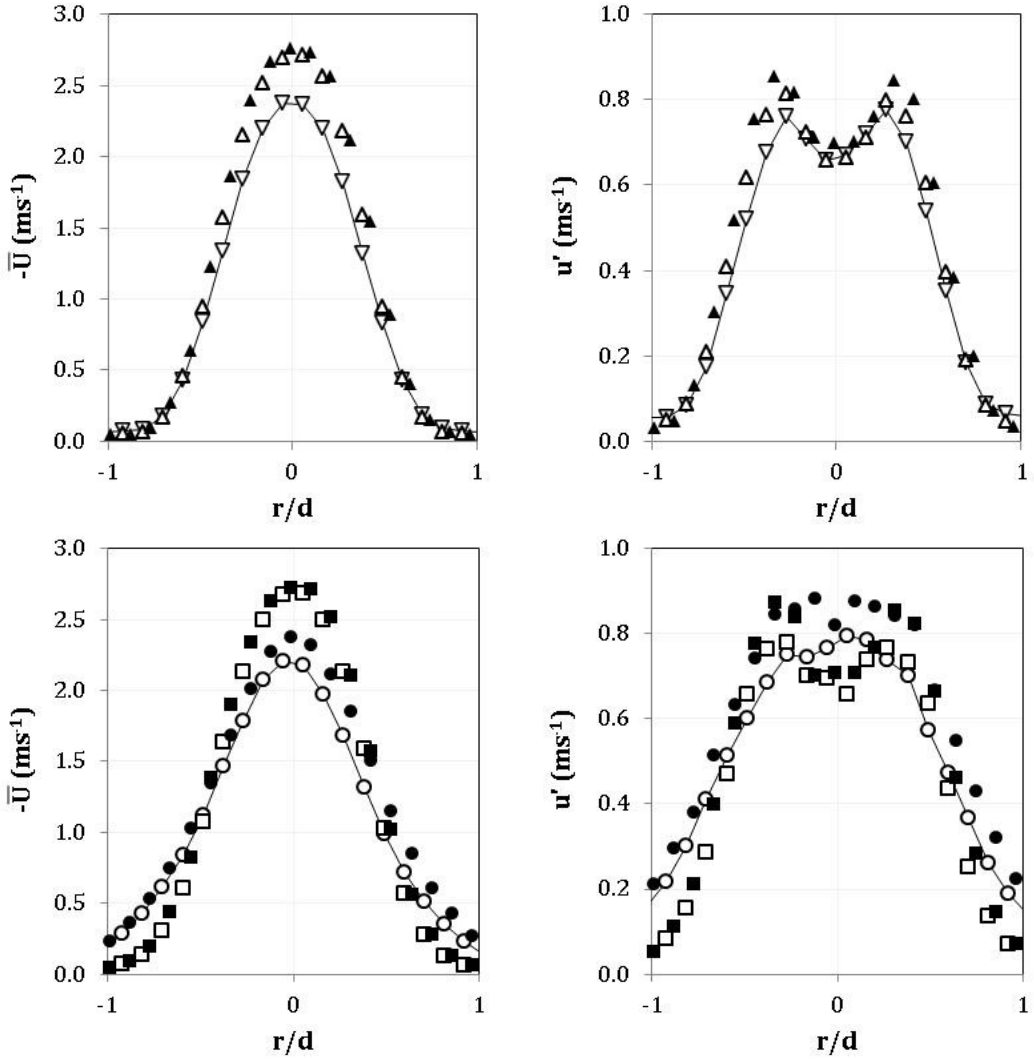

Figure 4-33 Normalised axial mean and RMS fluctuating velocities for single phase impinging jets at each h/d ratio, 1d from jet outlet (right – triangles), 2 and 5d from jet outlet (left – squares and circles respectively)

Data profiles key: 2 h/d (upside triangle), 6 h/d (open symbols) and 10 h/d (closed symbols)

Looking at the data, Figure 4-33, for each jet-to-plate height, we can see differences between the data at each of these locations. On the top left plot, the axial mean velocity at 1 x/d does not collapse as would be expect. In this region there should be no difference between $\overline{U}$ and u' values around the centreline. However, $\overline{U}$ is lower at 2hd (U_m of 2.36ms^{-1}) than for the other two jet heights studied ($U_m$of 2.70 and 2.78ms^{-1} at 6 and 10 h/d respectively). From Figure 4-33, and the experimental protocols employed to best ensure the runs were comparable, we have confidence that the trials were performed at the flowrate appropriate to achieve a Reynolds number of 10,000 consistently across the

programme. However, the mean and fluctuating velocity is lower for h/d of 2, yet the data from the 6 and 10 h/d trials agree.

For the larger two jet separations (6 and 10 h/d), the profiles at 2d from the jet outlet would not be expected to be influenced by the presence of the impingement surface 4 and 8 diameters away, and they do indeed collapse as would be expected if the experiments were performed well, i.e. the flowrate was consistent across all of the trials.

Moving to 5d from the jet outlet, so that the profile is 1d away from the wall for the 6 h/d trial, yet is still far enough away during the 10 h/d trial, allows a comparison to be made. Again for the profile at 1 diameter from the base (the 6 h/d trial) the velocity is lower than that of the highest jet height (10 h/d trial). This would suggest that the influence of the wall is being felt at 1d explaining the drop in $\overline{U}$ and u' values at 1 x/d for both the 2 and 6 h/d cases.

Beltaos and Rajaratam (1974) and Rajaratnam et al. (2010) observed for large impingement heights greater than 8.3d, the impinging jet feels the presence of the wall from an x/h distance of 0.86 which is equivalent to; 0.3, 0.8 and 1.4d above the wall for the 2, 6 and 10 h/d jets respectively. Data has not been acquired for a larger jet height, or indeed an equivalent free jet, so we can not conclusively state that the observation made by these workers applies to the largest jet height (10 h/d) tested here which adheres to their recommendation of jet heights greater than 8.3d. We can however conclude that the observation does not extend to the smaller jet height separations of 2 and 6 h/d as both have been found to be influenced by the presence of the wall at 1d from the impingement surface, both smaller distances than suggested by the parameter of 0.86 x/h.

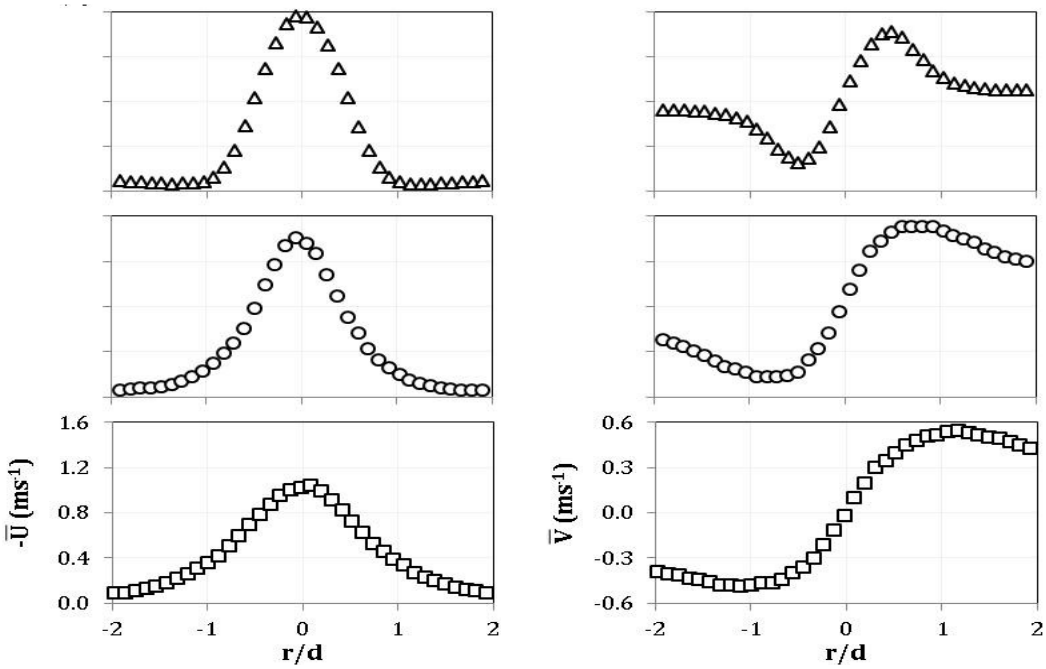

Figure 4-34 Jet height effect on axial and radial mean velocity data at 0.2d above the wall for single phase impinging jets at h/d ratios of 2, 6 and 10 (top to bottom)

Within the impingement region, Figure 4-34, profiles taken within 1d of the impingement surface show the same trends when comparing the three jet-to-plate separations investigated. For the purposes of illustration the profiles taken at 0.2d above the wall are presented, but are representative of the other vertical distances within this region. The centreline axial velocity is lower the greater the jet-to-plate separation h/d since the greater the jet height h, the more the developing jet has been able to grow before reaching the wall, as expected. The shape of the profiles is also consistent, although radially stretched for the axial component with increasing h while the radial velocity has increased diagonal stretching. The radial expansion of the jet is clearly seen in the radial mean velocity profiles.

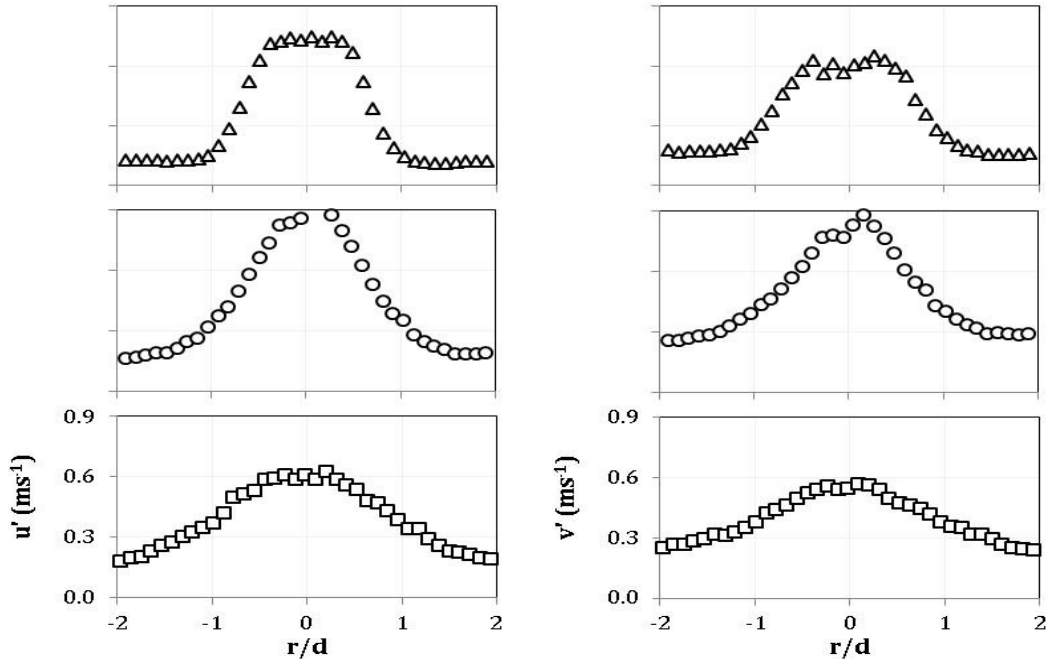

Figure 4-35 Jet height effect on axial and radial RMS fluctuating velocity data at 0.2d above the wall for single phase impinging jets at h/d ratios of 2, 6 and 10 (top to bottom)

Near the impingement surface where the pressure gradients caused by the wall are deflecting the approaching jet radially, the axial and radial RMS fluctuating velocities are similar in value at each h/d tested, Figure 4-35. When comparing across the jet-to-plate heights, the turbulent velocities are greater at 6 h/d than at 2 and 10 h/d, Figure 4-35. Beyond the potential core of a round turbulent jet, turbulence has penetrated to the axis resulting in the increase in turbulence seen from 2 to 6 h/d. The width of the potential core can be seen in the plateau of the top data plots (triangles). As the jet has been allowed to develop further the turbulence level decreases as with the 10 h/d case.

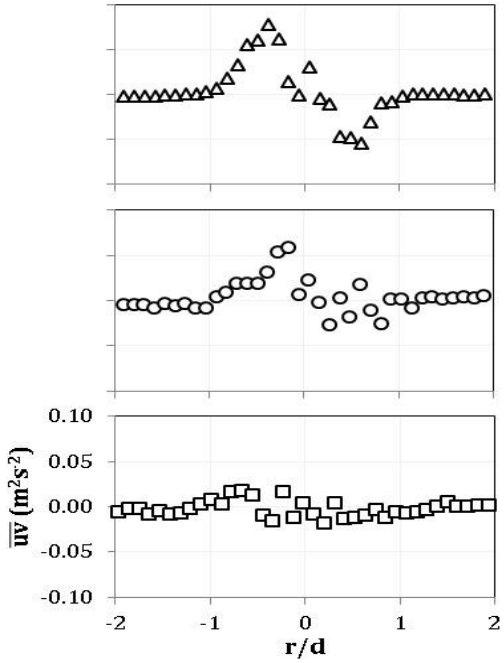

Figure 4-36 Jet height effect on shear stress data at 0.2d above the wall for single phase impinging jets at h/d ratios of 2, 6 and 10

Now although there is an increase in the RMS fluctuating velocity from 2 to 6 h/d, the data in Figure 4-36 show a fairly steady decrease in the shear stress as the jet outlet moves away from the impingement surface.

4.4.2 Near-field radial wall jet region

The development of the near-field radial wall jet is influenced by the jet height. The greater the distance the developing jet has to grow and expand, for a given flowrate and jet outlet diameter, then the larger the differences in the turbulence evolution. As the wall is approached the deflecting radial wall jet will be influenced by the levels of turbulence in and around the stagnation region.

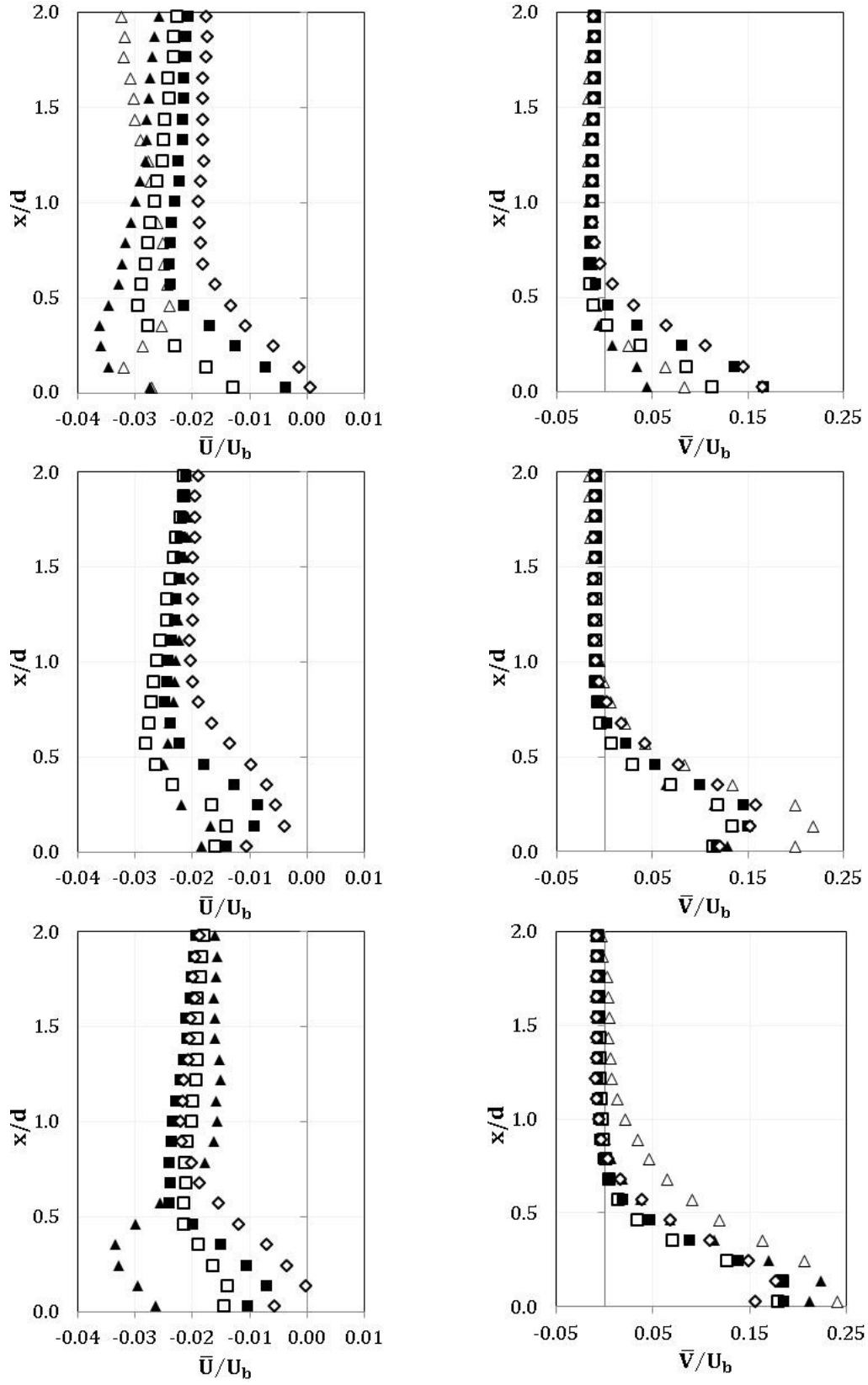

Figure 4-37 Jet height effect on normalised axial and radial mean velocity data in the near-field wall jet for single phase impinging jets at h/d ratios of 2 (top), 6 (middle) and 10 (bottom)

Vertical profiles taken at △ 1 r/d, ▲ 2 r/d, □ 3 r/d, ■ 4 r/d and ◇ 5 r/d

The progression of the near-field wall jet from 2 to 5d is very clear for the 2 h/d case from the normalised mean velocity data in Figure 4-37. The downward velocity at all radial stations is increasing until the wall jet is met where it begins to slow.

The axial velocity profiles from 3 to 5d from the jet axis are the same shape for all jet heights tested here. There is a slight increase in the downward velocity (vertical velocity is negative if heading towards the wall) as fluid is entrained into the wall jet, followed by a region of decay through the upper shear layer and finally a second inversion, corresponding to the local radial maximum velocity V_m, to an increasing downward velocity within the lower shear layer as the wall gets closer. This slight increase is not seen in the 2 h/d data because the shear layer is so thin it was not detectable at the resolution of these experiments. Interestingly, the magnitudes within the wall jet for this region of the flow at 2 and 10 h/d are similar, while they are more negative at 6 h/d. At this middle jet height, the developing jet has evolved beyond the potential core and the turbulence will have penetrated through to the jet axis, but not evolved further where it will expand and lose momentum, hence the higher downward velocities. Simultaneously in the same region, the radial velocity grows as r increases. The local maxima are seen for 6 and 10 h/d but not 2 h/d, again likely due to the thickness of the lower shear layer and resolution of the experiments. The wall jet is accelerating radially from 3 to 5 r/d at 6 h/d, but has begun to decelerate by 5 r/d for the 10 h/d dataset indicating the onset of the far-field wall jet.

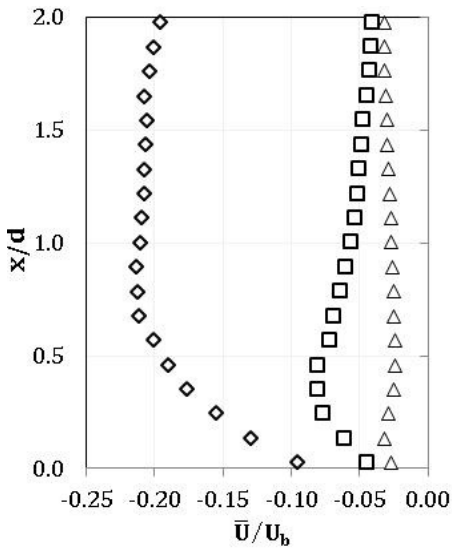

Figure 4-38 Jet height effect on normalised axial mean velocity at 1 r/d at h/d ratios of 2 (△), 6 (□) and 10 (◇)

The profiles taken at 1 d from the jet axis show rather different trends across the jet heights. As the developing jet evolves more for higher h, the jet not only develops axially but radially too and this is seen in the axial velocity profiles at 1d, Figure 4-38. For the lowest jet height tested, the initial jet expansion is minimal before the impingement such that at 1d the relatively small velocity is from entrainment. As the source pipe outlet is raised, and

the developing jet evolves before impinging, it expands radially which is why we see the increase in the normalised axial velocity ($\overline{U}/U_b$) with increasing h. Radially the velocity is increasing as the jet line is raised from 2 through to 10 h/d.

Another difference in the mean velocity distributions is at 2d (not shown). At 2 and 6 h/d these profiles follow the same trend as at 2 to 5 r/d, but for the larger jet height the axial velocity follows the trend of 1 r/d for the same separation suggesting the jet is still being deflected by the stagnation region and has not quite become a radial wall jet. The area of the stagnation region must be broader for 10 h/d as the developing jet has expanded radially to a greater extent.

Turbulent velocities within the near-field do not change significantly within each dataset but they do differ with changing jet-to-plate separation, Figure 4-39.

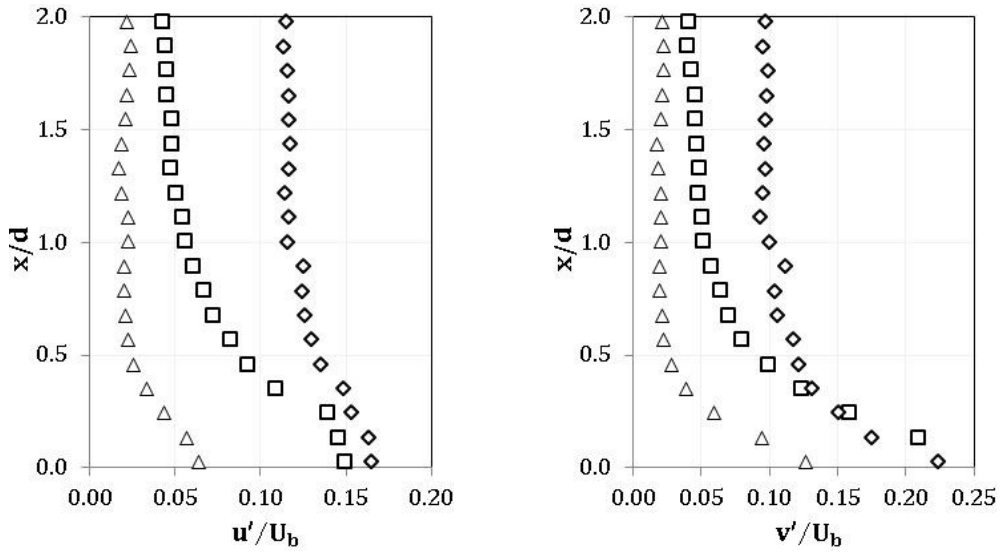

Figure 4-39 Jet height effect on axial and radial RMS fluctuating velocity data at 1d from the jet axis at h/d ratios of 2 (△), 6 (□) and 10 (◇)

Not unexpectedly perhaps, the axial and radial RMS fluctuating velocity profiles are quite different between the various jet heights. Both components have their lowest values for 2 h/d, increasing through 6 to 10 h/d. Similar to the difference seen in the mean velocity data, the difference is due to how much (or little) the developing jet has evolved before impingement.

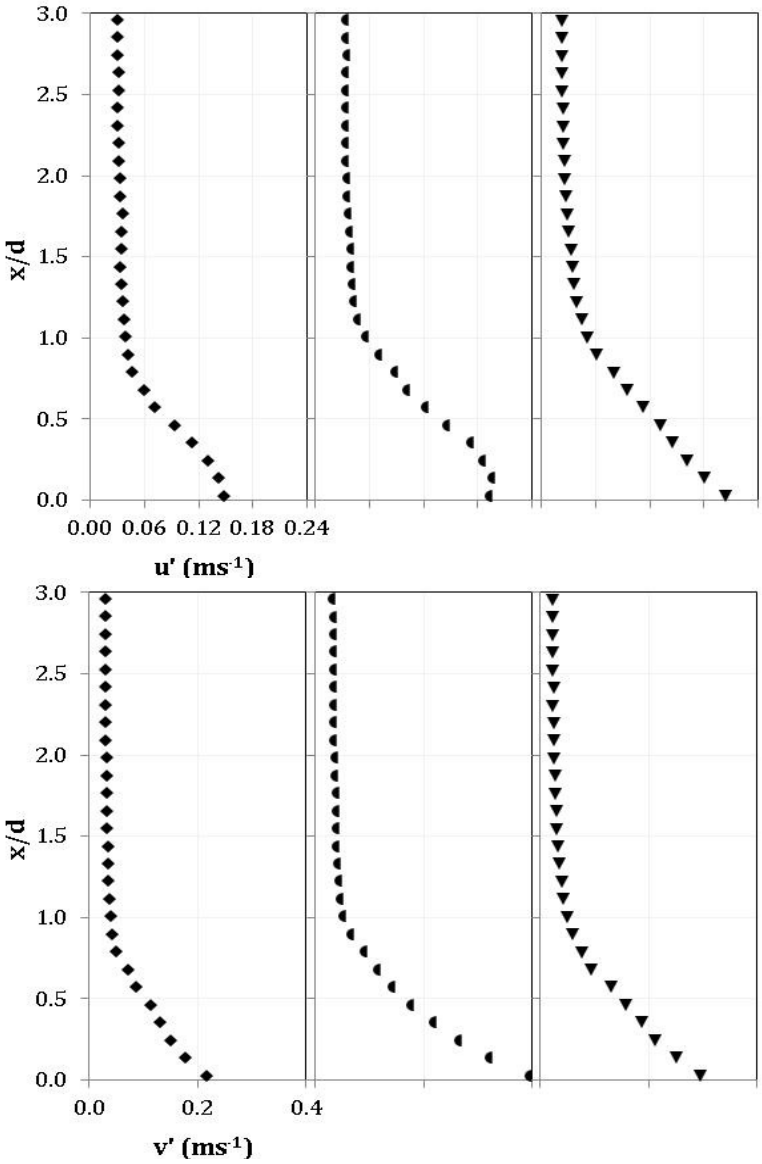

Figure 4-40 Jet height effect on axial and radial RMS fluctuating velocity data at 5d from the jet axis at h/d ratios of 2 (◆), 6 (◖) and 10 (▼)

The turbulent velocities within each of the three datasets do not change significantly from 2 to 5d away from the stagnation line. Figure 4-40 shows the axial and radial fluctuating velocities for each of the three jet separations taken 5d from the jet axis, and these are representative of the profiles within this near-field region. The axial turbulence increases within the wall jet with increasing r while the radial component increases between 2 and 6 h/d, falling again by 10 h/d.

4.4.3 Far-field radial wall jet region

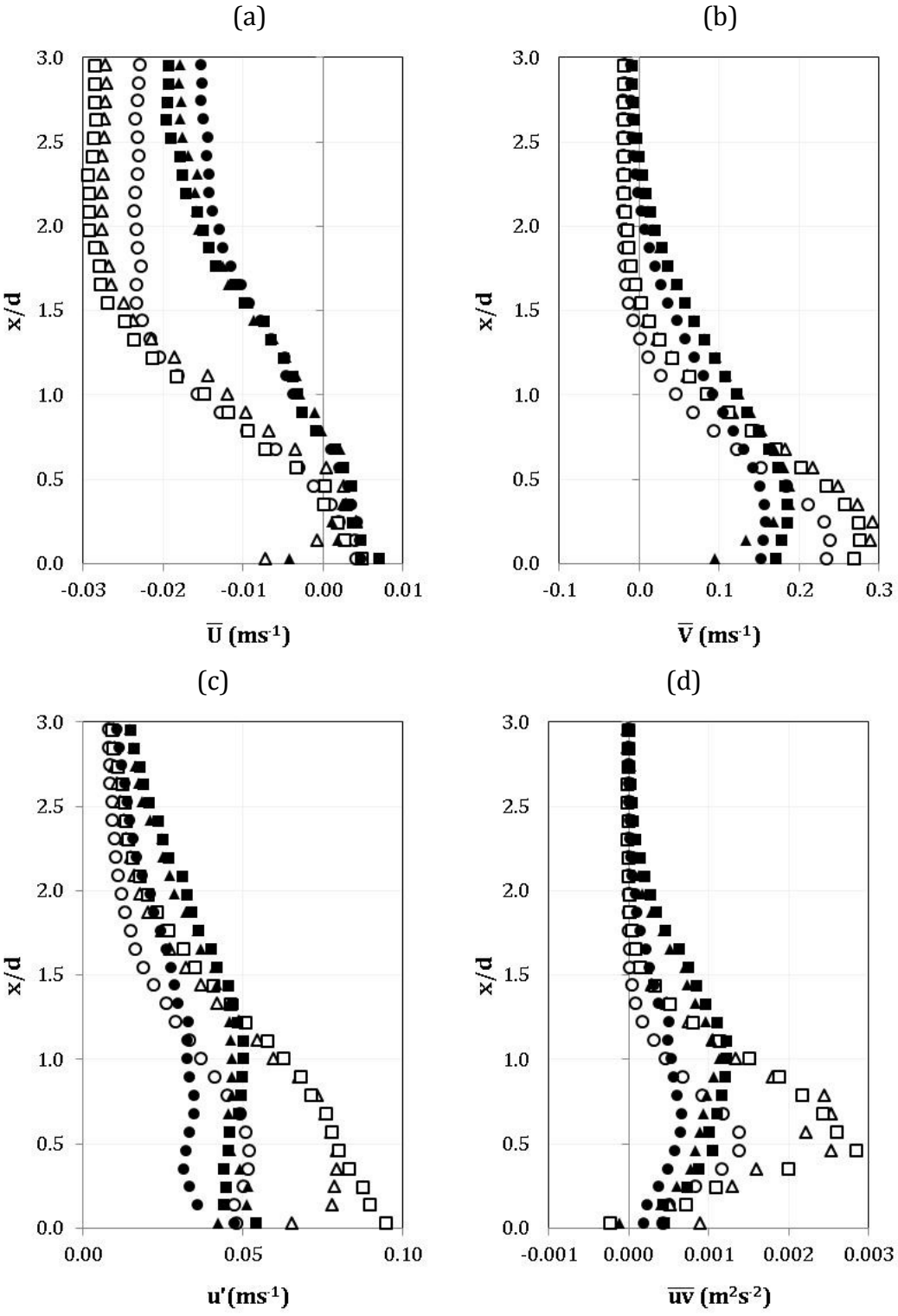

Figure 4-41 Effect of jet height on far-field radial wall jet turbulent properties (a) axial mean velocity, (b) radial mean velocity, (c) axial turbulent velocity, and (d) shear stress

Profile plots key: h/d ratios of 2 (circle), 6 (triangle) and 10 (square), radial location 10 r/d (open symbols) and 15 r/d (closed symbols)

Figure 4-41 shows mean velocities and turbulence data for 10 and 15d radial locations at each of the three jet heights tested. They show the 6 and 10 h/d profiles are very similar while the radial velocity is slightly lower for 2 h/d, as are the RMS axial velocity fluctuations and the shear stress. We can see there is little difference in the properties of the far-field radial wall jet between the jet heights tested here.

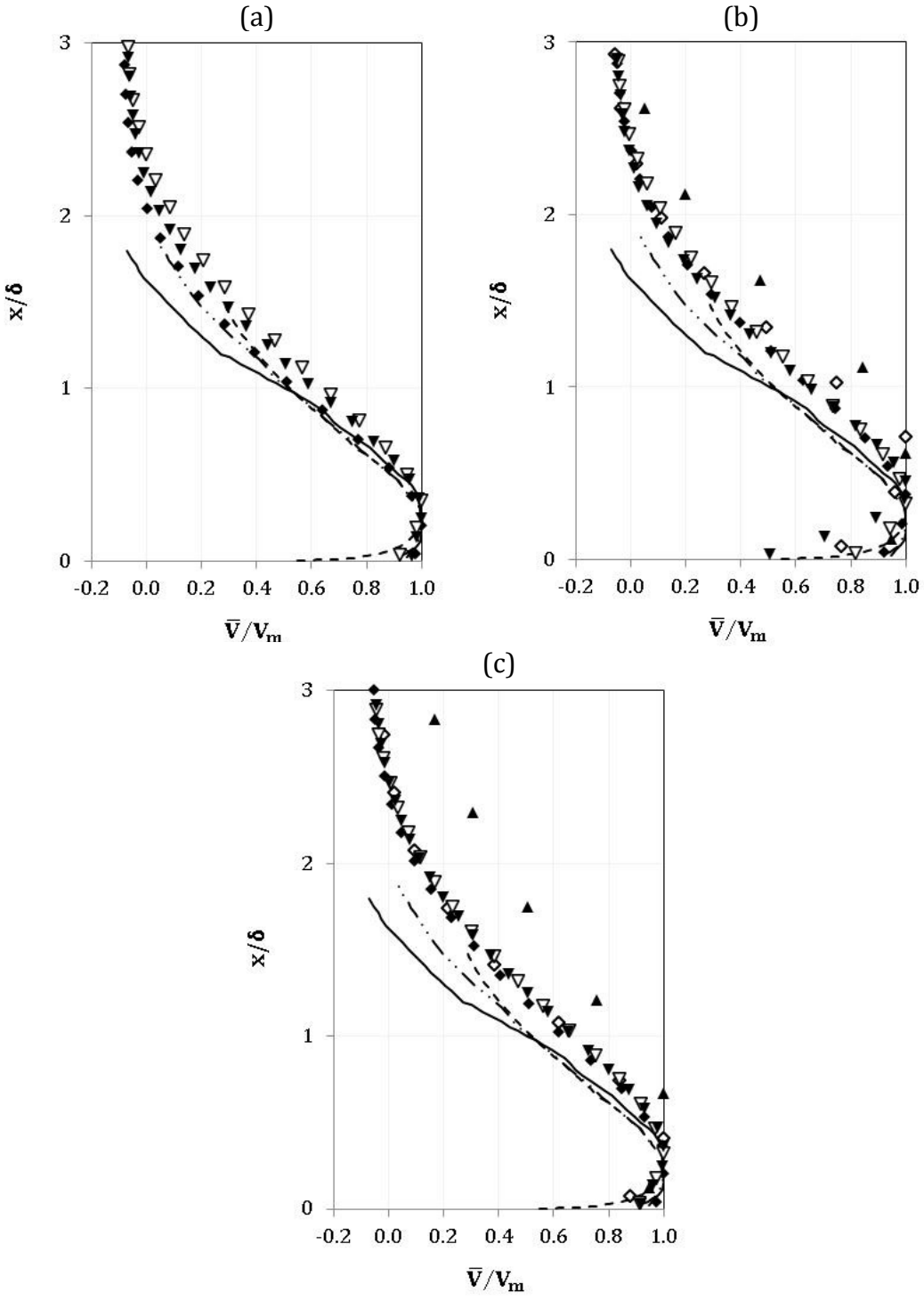

Figure 4-42 Normalised, single-phase, mean radial velocity in the far-field radial wall jet at h/d ratio of (a) 2, (b) 6 and (c) 10

Profiles taken at ▲ 2 r/d, ◇ 5 r/d, ◆ 10 r/d, ▽ 12 r/d and ▼ 15 r/d. And data from Poreh et al. 1967 (----) and Dianat et al. 1996 (— · · —), Fairweather and Hargrave 2002 (—).

To test for similarity within the radial wall jet, the data are normalised against the local maxima, V_m, and wall jet half-width, δ. The wall jet half-width is used to characterise the growth of the radial wall jet, defined as the distance from the local maxima to where the mean velocity within the upper shear layer equals half the local maxima. For the 2 h/d case, Figure 4-42(a), only the 3 profiles furthest from the jet axis presented a local maximum enabling estimation of the half-width. Each of these profiles collapses showing self-similarity. The presence of self-similarity of the radial wall jet within the far-field region as measured and reported within this thesis confirms the measurement area of the impinging jets up to 15 r/d (Figure 3-12, page 65) under study here are not influenced by the Jet Test Tank (JTT) walls which are 50d from the jet centreline (Figure 3-2, page 48). For the other jet heights we were also able to calculate the half-width at 5 and 2 r/d so these have been plotted also. From the 6 h/d data the radial wall jet has not become self-similar until 10 r/d whereas for the 10 h/d case self-similarity can be seen from 5 r/d with only the data for 2 r/d not collapsing as seen in Figure 4-42(c).

Agreement between the present water jet data (Figure 4-42) and the gas impinging jets of Poreh et al. (1967), Dianat et al. (1996) and Fairweather and Hargrave (2002) is in general good for the mean radial velocities ($\overline{V}/V_m$). The profile shapes are comparable and negative velocities are seen above the radial wall jet due to entrainment with exception of the hot-wire data of Poreh et al (1967) which tends to zero. Hot-wire anemometry is unable to discriminate between the different directional components of velocity. In the lower shear layer agreement is strong with only Poreh et al. (1967) showing a more rapid decrease nearest the impingement surface. The upper shear layer, above the local maxima (V_m), profiles diverge to some extent between the gas and liquid jet data due to the weaker entrainment field in the ambient surrounding liquid.

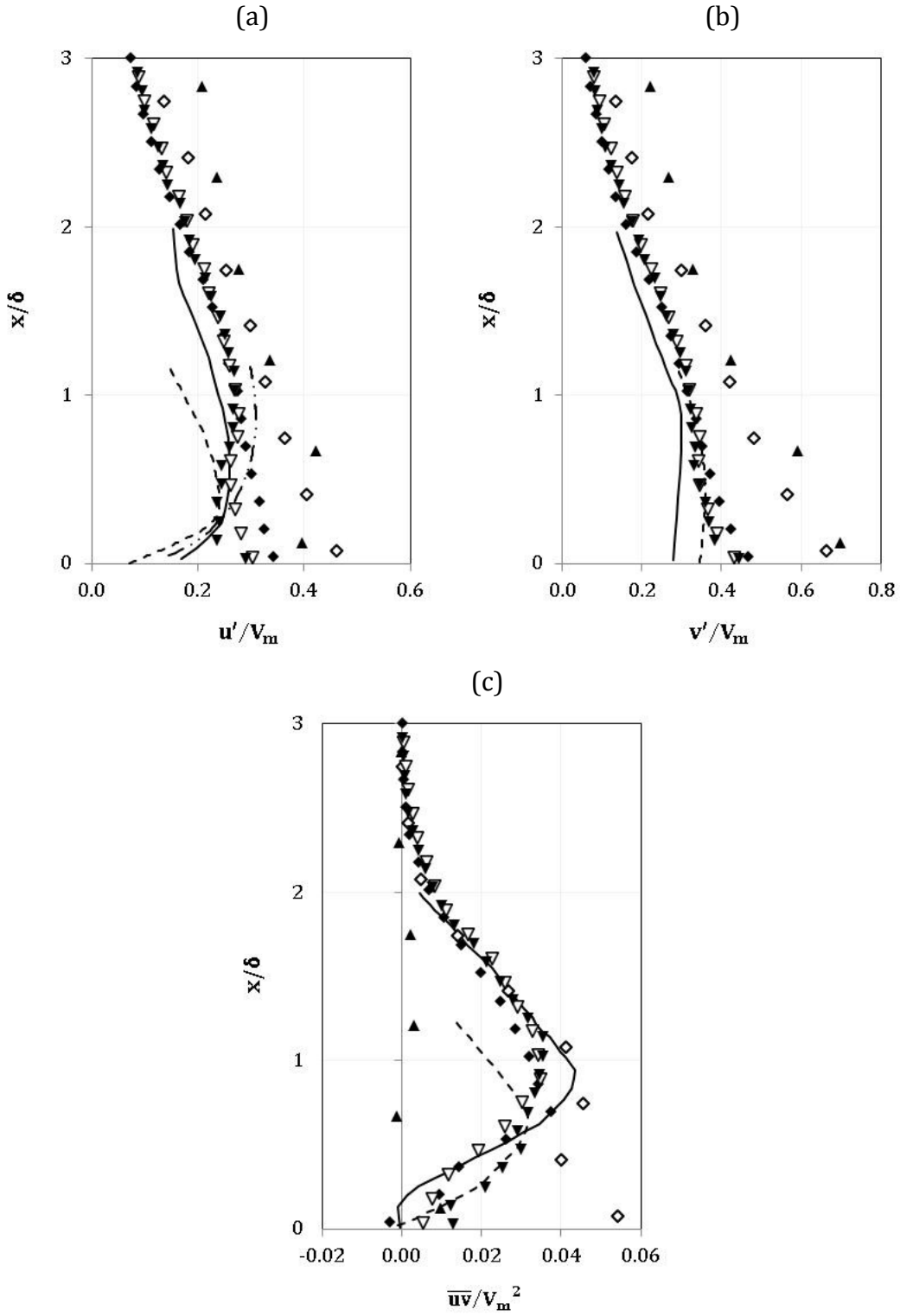

Figure 4-43 Normalised, single-phase, turbulence statistics in the far-field radial wall jet at h/d ratio of 10: (a) axial RMS fluctuating velocity, (b) radial fluctuating RMS velocity, and (c) shear stress

Profiles taken at ▲ 2 r/d, ◇ 5 r/d, ◆ 10 r/d, ▽ 12 r/d and ▼ 15 r/d. And data from Poreh 1967 (----) and Dianat 1996 (—··—), Fairweather 2002 (—).

Turbulence statistics obtained from the data at each jet height also agree very well, Figure 4-43. Again we can see that the data gathered at 2 and 5d from the jet axis do not collapse and therefore at these points self-similarity has not been reached. The profiles for 10, 12 and 15 r/d show a small amount of spread close to the impingement surface.

Agreement with air jet turbulence data is less convincing. Qualitatively, there are regions where the general profile shapes and magnitudes are not vastly dissimilar. Interestingly, the closest agreement for the turbulence data appears to be in the upper shear layer. Similarity between the jet heights explored struggles to achieve similarity until the furthest region of the radial wall jet studied here.

4.5 Chapter Conclusions

This chapter has presented two-dimensional measurement data of mean and fluctuating velocities, and shear stress for single-phase turbulent impinging jets at three strategic jet heights of 2, 6 and 10 h/d; the impingement surface positioned within the potential core, just outside the core, and within the fully developed free jet, respectively.

The first extensive exploration of the mean and turbulence characteristics of all three regions of an unconfined, axisymmetric liquid impinging jet (the developing jet and impingement region, through to the near- and far-field radial wall jet) has been completed and presented. The key conclusions drawn are outlined below:

- The experimental system (jet test rig and PIV) developed to enable the research activities presented within this thesis (detailed in Chapter 3) has been successfully tested against known flow structure of a single-phase impinging jet, and the small amount of data available (Poreh et al. 1967; Cooper et al. 1993; Fairweather and Hargrave, 2002; Rajaratnam et al. 2010). The mean velocity distributions ($\overline{U}$ and $\overline{V}$) near the jet outlet showed good symmetry, and the axial velocity distribution when normalised by the maximum jet centreline velocity, U_c ($\overline{U}/U_c$), correlates well with expected fully developed pipe conditions. Providing confidence in the experimental system as we move on to the multi-phase trials.
- The data sets presented have been used a benchmark for the particle-laden trials to follow in Chapters 5, 6 and 7.

Assessment of the jet height effect on the flow characteristics on an impinging liquid jet at all three regions of the flow have been presented and the key conclusions drawn are:

- All three jet heights initially begin with profiles where the mean axial velocity remains that of the pipe flow. Comparison to free liquid jet data at a comparable Reynolds number (Milanovic and Hammad, 2010) confirmed within the developing jet where the impingement surface is having no impact, the flow behaved as a free jet.
- As the jet height from the impingement surface increased, the more advanced the jet expansion, and centreline mean axial velocity decreased as the jet spread radially with increasing mean radial velocity.
- Within the impingement region, the centreline axial velocity is lower the greater the jet-to-plate separation, since the greater the jet height h, the more the developing jet has been able to expand radially before reaching

the wall, as expected. An increase in turbulence levels is seen from 2 to 6 h/d as the end of the potential core is exceeded, turbulence from the mixing layer penetrates to the centre. Followed by a decrease at 10 h/d as the jet continued to grow before impingement. Beltaos and Rajaratam (1974) and Rajaratnam et al. (2010) suggested for large jet heights (greater than 8.3 h/d), the influence of the wall is felt 0.86 x/h of the impingement surface. The data presented within this thesis for the larger jet height of 10 h/d agreed with this observation, but was not found to extend to the smaller jet heights of 6 and 2 h/d tested where the influence of the wall was felt at 1d above the impingement surface. The area of the stagnation region was found to be broader for 10 h/d as the developing jet has expanded radially to a greater extent.

- The development of the radial wall jet, particularly within the near-field region, was influenced by the differences in the turbulence evolution of the jet upstream of the stagnation point. The difference in the impinging jet width is seen in the near-field region. For the smallest jet height, and therefore the more narrow impinging jet, the growth of the wall jet is seen from just one diameter distance (r = 1d) parallel from the jet axis. The magnitudes of axial velocity within the wall jet for this region of the flow at 2 and 10 h/d are similar, while they are more negative at 6 h/d. At this middle jet height, the developing jet has evolved beyond the potential core and the turbulence will have penetrated through to the jet axis, but not evolved further where it will expand and lose momentum, hence the higher downward velocities. Simultaneously, the radial velocity grows as r increases, the local maxima seen for 6 and 10 h/d but not 2 h/d, likely due to the thickness of the lower shear layer and resolution of the experimental facility and methodology employed throughout the research undertaken within this thesis. The wall jet accelerated radially through the near-field wall jet, the onset of the far-field wall jet indicated by the largest jet height (10 h/d) by 5 r/d. The RMS fluctuating velocities in the very near-field wall jet (at 1 r/d) are their lowest values for 2 h/d, increasing through 6 to 10 h/d. Similar to the difference seen in the mean velocity data, the difference is due to how much (or little) the developing jet has evolved before impingement. The difference decreases with increasing r.
- By the far-field radial wall jet region, the mean velocities and turbulence data are similar for the two larger jet heights (6 and 10 h/d) with slightly lower values for the 2 h/d jet. The difference between the jet heights tested are significantly less in this region. Mean velocity and turbulence

data in this region, normalised against radial velocity local maxima values and wall jet half-width, were compared against the small amount of gas impinging jet data by Poreh et al. (1967), Dianat et al. (1996) and Fairweather and Hargrave (2002). The onset of the far-field radial wall jet was found to be from 10 r/d for the smaller two jet heights of 2 and 6 h/d, and 5 r/d for the 10 h/d jet.

Chapter 5
Results and Discussion – Particle-laden Turbulent Liquid Impinging Jets

The study of two-phase, solid-laden jets has been primarily focussed on computational modelling, although even here few papers have appeared in the literature to date. Particulate additives have been used previously to enhance heat transfer coefficients in the stagnation region due to turbulence production by particles in the viscous sub-layer. As such, some workers have studied the heat transfer effects of particle-laden flows (Shimizu et al., 1979; Hasegawa et al., 1986; Kurosaki et al., 1986; Yoshida et al., 1990); however very little physical modelling has been done which would enable validation of computational models (Yoshida et al., 1990; Ushijima et al., 2001; Longmire and Anderson, 2003). Only a few workers have published data in the developing region of a multi-phase free jet, although comparisons with that part of the impinging jet that can be considered as free have been made where possible. Tables summarising experimental free and impinging jet data sets can be found in the literature review (Chapter 2). For all other regions of the impinging jet little data exists at present.

This chapter presents the first of the particle-laden, turbulent impinging jet data acquired, and compares it with the single-phase data already discussed in Chapter 4 of this thesis. Performing this comparison demonstrates how the particulate phase behaves, in relation to an equivalent single phase, for an impinging jet at three jet-to-plate separation heights; viz. h/d ratios of 2, 6 and 10. The particle phase consists of silica particles of mean diameter 69.2μm with

a particle density of 2.45 g cm^{-3} and solids loading of 0.01 vol%. Selection of the test particles is discussed in Chapter 3.

Two components of the mean velocity, $\overline{U}$ and $\overline{V}$, as well as the root-mean-square (RMS) of the fluctuating velocities, u' ($= \sqrt{\overline{u^2}}$) and v' ($= \sqrt{\overline{v^2}}$), and shear stress ($\overline{uv}$) were calculated from the instantaneous velocity vector data acquired using PIV. Measurement results for the developing jet, impingement region, and the near- and far-field radial wall jet are presented. The origin (0,0) of the co-ordinate system is set to the stagnation point where the jet centreline crosses the impingement surface, as discussed in Chapter 1. Profile locations taken upstream of the stagnation point are reported as they decrease from the jet outlet towards the impingement surface (Figure 3-13, page 66), i.e., for the largest jet height of 10 h/d examined, 9 x/d is close to the jet outlet while 0.1 x/d is the profile taken closest to the impingement surface; the radial wall jet profiles increase radially from the jet axis, i.e., 1 r/d is in the near-field while 10 r/d is in the far-field.

The first section of this chapter, Section 5.1, maps a particle-laden turbulent impinging liquid jet set at six diameters (6d) above the impingement surface. Velocity measurements have been made for the particle phase of the jet using planar PIV, and the data compared with single-phase flow data acquired applying the same technique but with the use of neutrally-buoyant tracer particles.

Section 5.2 examines mean and turbulence properties of the particle-laden impinging jet at a range of jet separation heights; for h/d ratios of 2, 6 and 10. The flow phenomena in each region of the jet is considered, and the influence of changing the jet-to-plate separation distance explored.

5.1 Particle-laden Impinging Liquid Jet Data, h/d Ratio of 6

In the following, new measurement results are presented for a particle-laden impinging liquid jet located six diameters above an impingement surface (h/d ratio of 6). The developing jet and impingement region are mapped using horizontal profiles taken at different axial locations; and vertical profiles taken at radial locations from the jet axis to examine both the near- and far-field radial wall jet. A schematic representation of all profile locations can be found in Chapter 3 (Figure 3-13). Mean velocities $\overline{U}$ and $\overline{V}$ in the axial and radial directions of the jet, respectively, as well as the RMS of the turbulent fluctuating velocities (u' and v') and shear stress ($\overline{uv}$) are shown for all of these regions and discussed in turn. Particle flow behaviour is assessed in comparison to the single-phase data previously discussed in Chapter 4.

5.1.1 Mean Velocity Experimental Data

From instantaneous velocity vector data acquired using Particle Image Velocimetry (PIV), time-averaged axial and radial components of velocity, $\overline{U}$ and $\overline{V}$, respectively, were calculated and plotted.

The particle velocities of the multi-phase jet explored using test particles of diameter 69μm, show good flow symmetry about the jet axis in Figure 5-1.

The first aspect to note in terms of these results is that the particle phase centreline axial velocity, $\overline{U}$, starts to decay from 5 x/d, while the single-phase axial velocity data remained unchanged until around 1 x/d, as expected of the structure within the potential core. The particle phase is clearly not following the turbulent flow of the liquid jet of the issuing pipe line. A difference in the particle and single-phase axial mean velocity near the jet outlet is also seen in the case of some free jets. Tsuji et al. (1988) and Gillandt et al. (2001) both tested similar free jet configurations (Reynolds number of 5700) with slightly differently sized particles, 170 and 110μm at 0.5 and 0.04 vol%, respectively, and both found the particle phase mean axial velocity to be 17% less than the single-phase. The flow this close to the jet outlet for the present impinging jet is comparable to a free jet as the impingement surface is at a sufficient distance to not exert an influence on the flow in this region. One diameter from the jet outlet, at 5 x/d, the particle phase velocity is 0.37ms^{-1} lower than for the single-phase, a reduction of 20% in good agreement with the free jet data noted above. Flow close to the jet outlet is expected to retain the characteristics of that issuing from the source pipe, particularly within the potential core before turbulence has penetrated to the jet axis. The two-phase pipe flow data of Rizk

and Elghobashi (1989) show particle phase mean axial velocity to be lower than for the single-phase. For particles of diameter 45μm they report a centreline axial velocity 6% lower, from a normalised velocity ($\overline{U}_p/U_c$) of 1.0 for the single-phase, down to 0.96 for the particle-phase. While for larger particles of 136μm diameter the equivalent value was 24% lower, this time dropping to 0.76, the variation attributed to the difference in inter-phase surface area acted on by viscous drag. The present particles lie between these in size and the reported reductions.

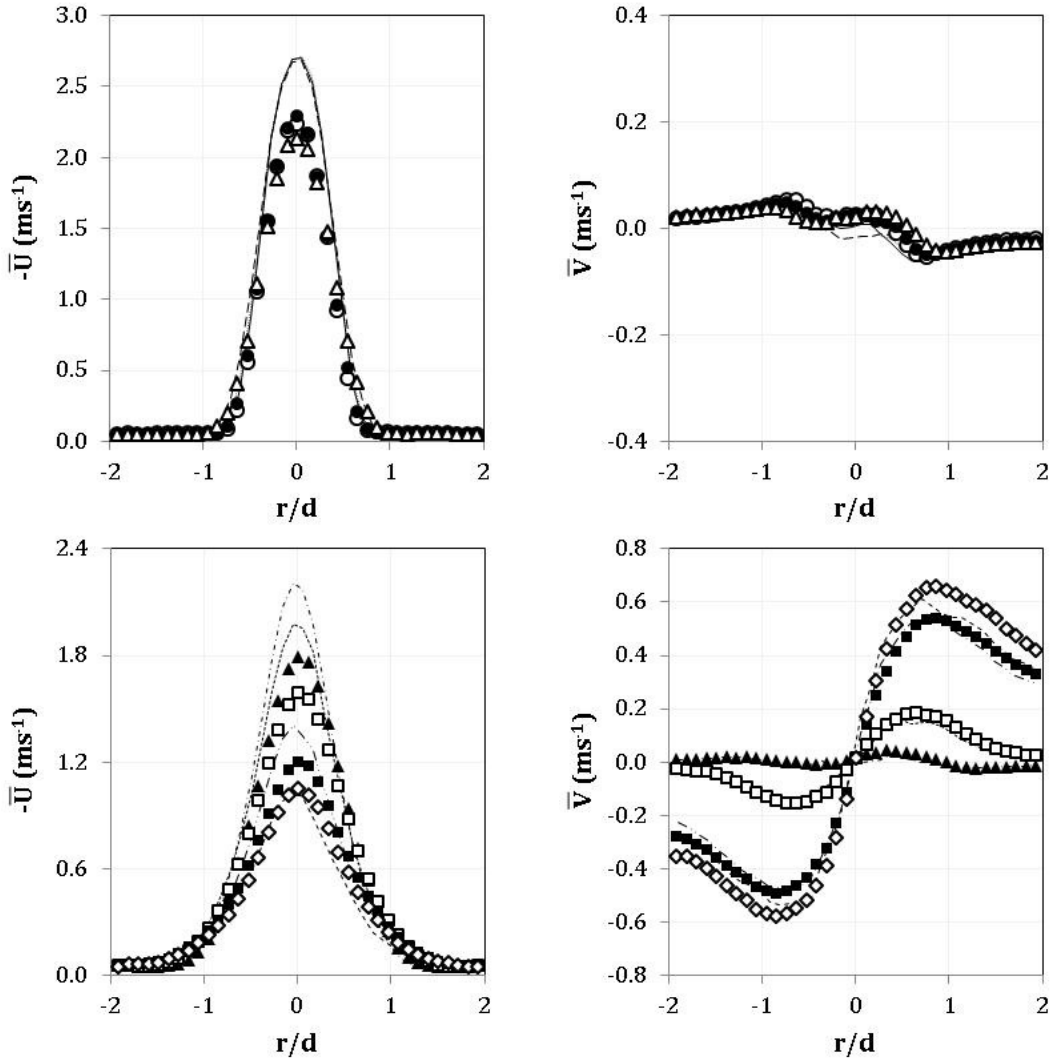

Figure 5-1 Particle and single-phase developing jet at h/d ratio = 6, axial and radial mean velocity data (multi phase data – symbols, single phase data – lines)

Transverse particle phase profiles taken at the following locations above the impingement surface: ○ 5.3 x/d, ● 5 x/d, △ 4 x/d, ▲ 1 x/d, □ 0.5 x/d, ■ 0.2 x/d and ◇ 0.1 x/d. Single-phase profiles at: — 5.3 x/d, ····· 5 x/d, —— 4 x/d, –·–·– 1 x/d, ---- 1.5 x/d, —··— 0.2 x/d, - - - 0.1 x/d.

The difference between the phases increases to 0.54ms^{-1} at 4 x/d. Both Tsuji et al. (1988) and Gillandt et al. (2001) found that as the potential core is eroded the values of the single- and particle phases equalise. The single-phase continued to decay while the particle phase decreased at a lower rate out to 20d from the jet outlet. The impinging jet in this test case has been prevented from continuing to develop to such large distances by the placement of the impingement surface.

A number of other workers have also performed measurements on particle-laden free jets (see Table 3-3 for list of data including experimental parameters), although the focus has primarily been on the fully developed regions beyond the potential core, and little attention has been given to the radial components of the mean velocity or turbulence properties. The data presented within this thesis that would be comparable to that of a free jet flow is to the downstream extent of the potential core (plus a few diameters further for the 10 h/d case only) so no direct comparisons can be made. However, these previous workers found for particle-laden free jets that: centreline axial mean velocity decay rates were smaller for the particle-laden flows, which is in agreement with the present data; and the spreading rate of the two-phase free jets were lower than their single-phase counterparts, not seen within the development jet data presented in this thesis. In the absence of comparable two-phase impinging jet data, confidence in the present multi-phase data can be gained by comparison instead to particle-laden free jet and pipe flow data.

In the present data, $\overline{U}$ continues to decay towards the impingement surface, most significantly within 1d of the wall. From 4 to 1 x/d, $\overline{U}$ decays by 0.34ms^{-1} followed by a greater deceleration of 0.74ms^{-1} over the smaller distance between 1 and 0.1 x/d. The particle phase $\overline{U}_p$ remains below that of the single-phase until the final profile taken 0.1d above the surface where the particle and single-phase velocities are aligned. In the stagnation region, while the single-phase axial velocity decreases rapidly as the wall is reached, the particle phase does not decelerate as rapidly due to inertia. The modification to the turbulence field within the stagnation region, due to the pressure gradient exerted by the wall, does not influence the particle phase as significantly as it does the single-phase: the particle inertia being sufficient to dominate until the wall is reached. The difference in deceleration rates between the phases under the effect of the wall reduces the single-phase velocity to match that of the particle phase.

Only two limited sets of earlier data for the jet stagnation line of particle-laden impinging jets could be found. A planar two-dimensional gas-solid impinging jet (Yoshida et al., 1990) at 8 nozzle widths above the impingement surface,

Reynolds number of 10,000 and particles of 48.9μm diameter, reported a similar reduced deceleration of the particle phase as the wall was approached. The other data available, by Ushijima et al. (2001) for a liquid-solid impinging jet at h/d ratio of 10, a Reynolds number of around 2000 and using particles of diameter 1050μm, also found a smaller rate of deceleration although a much smaller difference was seen between the phases.

In the region of the impinging jet where it can be regarded as a free jet, the width of the mean axial velocity distribution is marginally smaller for the particle flow than for the single phase. The particle responsiveness to the fluid flow is relatively small due to having large inertia, with their response time longer than the fluid timescale. This reduced particle phase spreading rate is in agreement with Gillandt et al. (2001) who undertook physical modelling of the developing region for multi-phase free jets. This trend is also seen to extend into the further regions of free jets (Popper et al., 1975; Sheen et al., 1994; Fan et al., 2010).

Contemporaneously, within the developing jet, the radial velocity, $\overline{V}$, remains around zero within 2d of the jet outlet where the flow is heavily dominated by the axial component of velocity, followed by a period of rapid increase as $\overline{U}$ is decreasing. Entrainment of the surrounding, otherwise stagnant, fluid is evident on the outer side of the turbulent/non-turbulent interface from the increase in $\overline{V}$ towards the issuing jet, i.e., small positive gradients seen ±0.8 r/d for x/d greater than or equal to 4. Approaching the impingement surface, $\overline{V}$ increases as the jet is deflected towards the radial wall jet, achieving a maximum for the profile taken closest to the impingement surface. The particle and single-phase data are in good agreement at all profile locations examined except at 0.1d above the impingement surface. From the jet axis out to the local maximum, V_m, both phases display a similar radial velocity evolution, in both the rate and magnitude of growth. The single-phase local maximum, $V_{m,l}$, is reached first, and the particle phase radial velocity continues to grow for another 0.2d achieving a greater local maximum, $V_{m,p}$. This difference between the phases close to the impingement plate, as the jet is deflected from the stagnation region towards the radial wall jet, is also evident in the vertical profile data at 2 r/d in Figure 5-2 (bottom left).

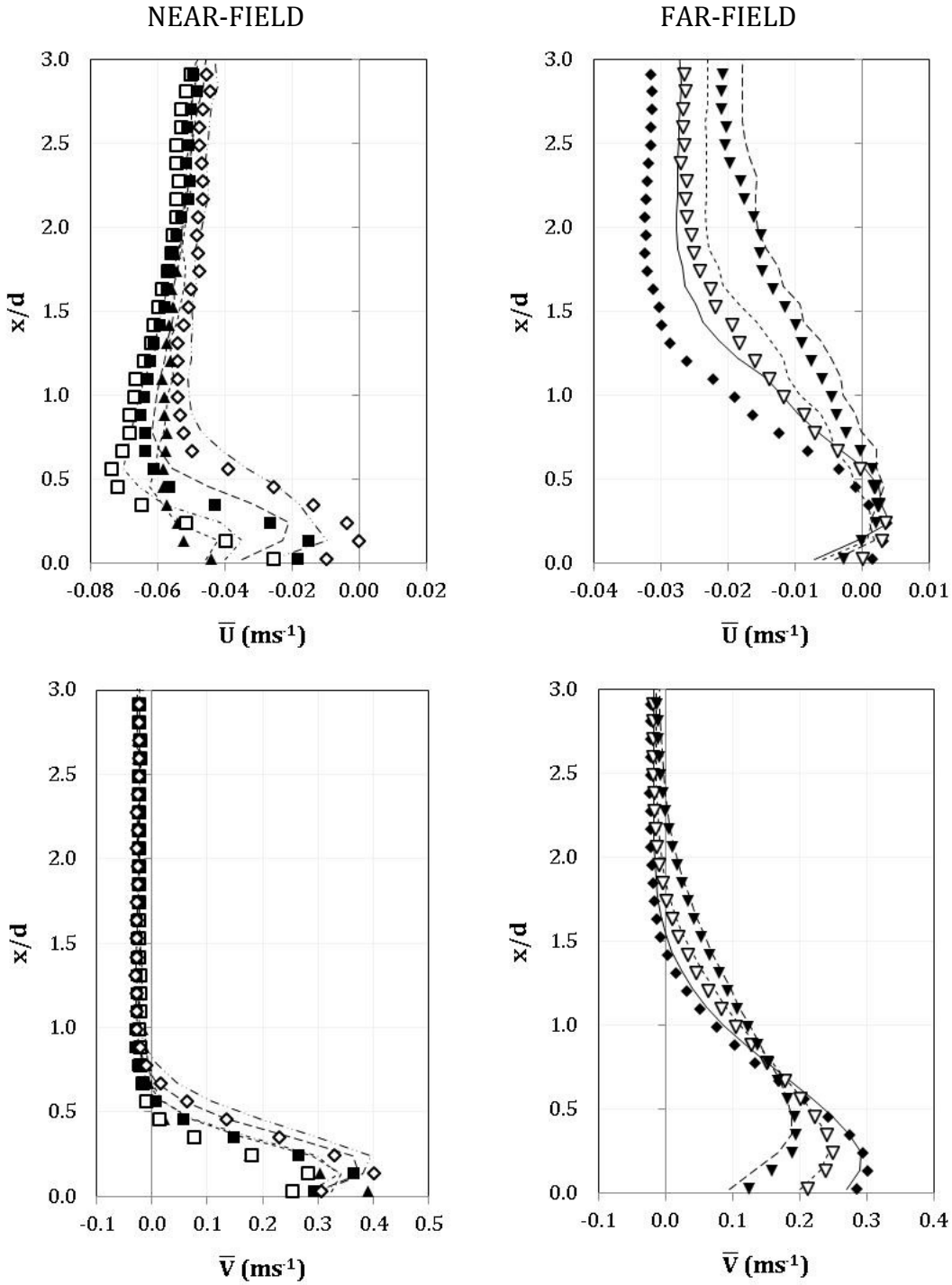

Figure 5-2 Particle and single-phase, near- and far-field radial wall jet at h/d ratio = 6; axial and radial mean velocity data (multi phase data – symbols, single phase data – lines)

Vertical particle phase profiles taken at: ▲ 2 r/d, □ 3 r/d, ■ 4 r/d, ◇ 5 r/d, ◆ 10 r/d, ▽ 12 r/d, and ▼ 15 r/d. Single-phase profiles at: - - - 2 r/d, –·–·– 3 r/d, — — 4 r/d, —··— 5 r/d, — 10 r/d, - - - 12 r/d, and — — 15 r/d.

The stagnation region deflects the impinging jet radially, first undergoing deflection and acceleration in the near-field, followed by radial spreading and deceleration in the far-field wall jet .

Examining the near-field region, from 2 to 5 r/d (Figure 5-2, left), the entrainment velocity grows as the upper boundary of the wall jet is approached from above (0.5d from the base at 2 r/d, and 0.8d at 5 r/d), with particle phase values marginally smaller than the single-phase case. This is true for both the axial and radial velocities, $\overline{U}$ and $\overline{V}$, although this is most clear on the axial plot due to the scale of the axis. Remember that the vertical velocity is reported away from the base so all entrainment velocities are negative, the larger the velocity magnitude, the faster the flow towards the base. As the wall jet boundary, the turbulent/non-turbulent interface, is crossed, the radial mean velocity ($\overline{V}$) becomes positive. Simultaneously the mean downwards velocity ($-\overline{U}$) reaches a maximum. The upper shear layer of the wall jet experiences an increase in radial velocity while the axial downward velocity decreases, as x/d becomes smaller. At 4 and 5 r/d, the axial velocity inflects near the wall followed by a small downwards increase, where the radial velocity also sees its local maximum (V_m). Only the profile taken at 5d from the jet axis sees the axial mean velocity reach zero.

The single-phase results display very similar profile shapes but with varying values within the near-field wall jet, with the difference between the phases more noticeable further from the jet centreline. The single-phase radial velocity $\overline{V}_l$ in the upper region of the wall jet is greater than that of the particle phase $\overline{V}_p$. The lower region of the wall jet shows more variation as the near-field develops. At 2 x/d, the particle phase overtakes the single-phase close to the wall. For 3 and 4 r/d the single-phase is faster, with the particle phase overtaking again at 5 r/d. The particle phase radial local maximum at 5 r/d being the only to exceed that of the single-phase. Yoshida et al. (1990) found the particle phase radial velocity to be smaller than the single-phase in the lower region of the wall jet, this was attributed to the particles initially having no momentum in the r direction. The radial velocities align in the upper region, close to the jet axis, diverging at 4 nozzle widths from the jet axis where the particle phase has a higher velocity. The axial component for the particle phase $\overline{U}_p$ is very similar to that of the single-phase at 2 r/d, overtaking the single-phase and remaining higher from 3 to 5 r/d within the wall jet. The entrainment region exhibits higher axial and radial single-phase velocities.

Axial and radial velocity profiles in the far-field region are of similar shape to the near-field but are stretched upwards as the wall jet expands. Again, the region of entrainment above the wall jet displays a small negative velocity, although in this region larger than for the single-phase, with the amount of turbulent fluid increasing as fluid is entrained. The downward velocity decays

through the upper shear layer, turning positive (showing some upward flow as the jet expands), before again becoming negative through the lower shear layer as the wall is approached. Within the lower shear layer of the wall jet, between the impingement surface and the position of the radial local maximum (V_m), the axial velocity data for the particle phase are more similar in magnitude to the single-phase than at greater vertical distances from the wall. Differences in axial velocity between the profiles taken at 10 to 15 r/d, or between the particle and single-phase are significantly reduced within the lower part of the radial wall jet. There is a gathering of all the profile plots around the location of the V_m. A slight separation is seen in the lower shear layer immediately above the base, the particle phase showing marginally higher values. Above this point, the axial velocity values begin to diverge; in contrast to the near-field, this time the single-phase has higher values of velocity.

The radial velocity, $\overline{V}$, parallel to the impingement surface for the particle phase is greater than is seen for the single-phase data in the lower region of the wall jet. The expansion of the radial wall jet is mapped by the falling magnitude and increasing vertical position of V_m. Again, there is a switch between the phases, within the lower part of the radial wall jet, the particle phase magnitude is greater, then as the outer boundary is approached the single-phase becomes more dominant.

So, the radial particle velocities are initially lower than for the single-phase in the near-field, but by the far-field they are of a greater velocity. Yoshida et al. (1990) found in the near-field of the wall jet, for a particle-laden impinging air jet at 8 h/d, the particle radial velocity ($\overline{V}_p$) near the wall was lower due to the particles initially having no momentum in the radial direction, with particles only partially responding to the turbulent fluctuations. This agrees with the near-field data presented here. By the far-field, the particle phase radial velocity exceeds that of the single-phase and the particles lose less momentum with increasing distance r from the jet axis.

5.1.2 RMS of the Fluctuating Velocity Data

Turbulent fluctuations are described by the root-mean-square (RMS) of the fluctuating velocity. The axial and radial components, u' ($= \sqrt{\overline{u^2}}$) and v' ($= \sqrt{\overline{v^2}}$) respectively, were calculated and plotted. Once again, each region of the impinging jet is discussed in turn.

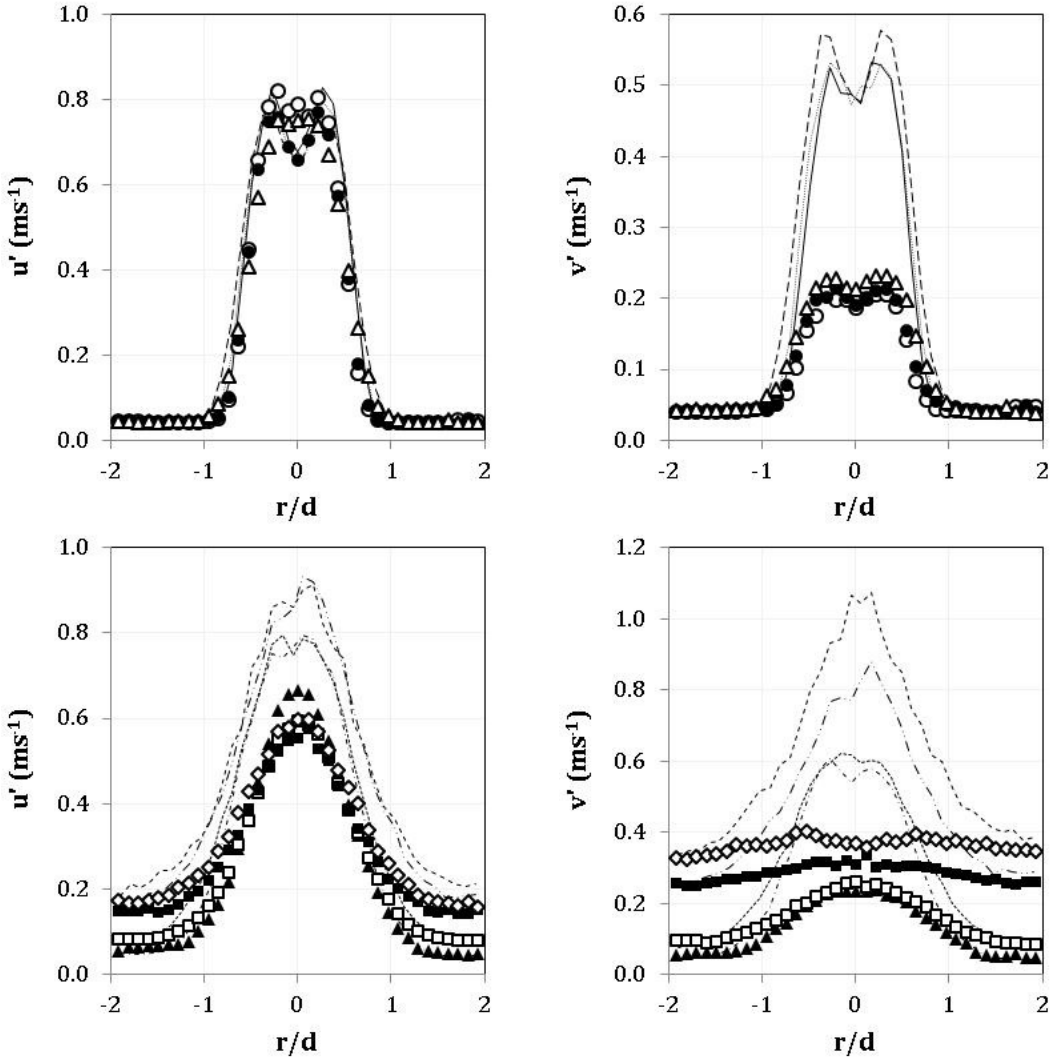

Figure 5-3 Particle and single-phase axial and radial RMS fluctuating turbulent velocity profiles upstream of stagnation point at h/d ratio = 6: particle phase data – symbols, single phase data – lines.

Particle phase profiles taken at ○ 5.3 x/d, ● 5 x/d, △ 4 x/d, ▲ 1 x/d, □ 0.5 x/d, ■ 0.2 x/d and ◇ 0.1 x/d. Single phase profiles at: — 5.3 x/d, ····· 5 x/d, —— 4 x/d, –·–·– 1 x/d, ---- 0.5 x/d, —··— 0.2 x/d, - - - 0.1 x/d.

Figure 5-3 presents the axial and radial RMS fluctuating velocities, also known as turbulent velocities, for the developing region of the impinging jet taken at a jet-to-plate separation of 6d. The particles in the flow exhibit considerably lower turbulence velocities relative to their single phase equivalents across the whole of the developing and impinging regions, with the exception of the axial

component near the jet outlet. Near the jet outlet, the two peaks seen at the outer edges of the jet, where velocity fluctuations are stronger than within the potential core and decrease towards the jet centreline, are less prominent than for the single-phase, but are located at the same distance from the jet centreline as would be anticipated. The location of the peaks is dictated by the development of the turbulent shear layer and can be considered to be at the centre of the shear layer.

The particle radial turbulent velocity (v_p') changes only marginally, a very slight reduction, within 2d of the jet outlet, beyond the influence of the pressure gradient exerted by the wall, then increases as the wall is approached and the jet deflected from the stagnation region to form the radial wall jet. The axial component (u'_p) is higher than its radial counterpart at all points, especially near the jet outlet. The pressure gradient exerted by the wall, attributed to the stagnation pressure created at impingement, influences the distribution of turbulence energy.

The difference between the particulate- and single-phase v' values are around $0.3ms^{-1}$ within 2d of the jet outlet, the difference between the phases growing as distance from the jet outlet increases, until a maximum difference of $0.7ms^{-1}$ at 0.1d above the wall. The 1 and 0.5d profiles have the same shape as the u' profiles in this region of the flow. Even closer to the wall, at 0.2 and 0.1 x/d, v' no longer falls as r increases above 1d as the radial wall jet is approached. This was also seen for the single-phase data, albeit at considerably higher magnitudes.

The rate of change as the impingement surface is approached is also different between the phases. The particle turbulent velocity, u'_p, decreases, while the single-phase turbulent velocity increases. The biggest difference is seen in the radial direction where, although both increase, the single-phase experiences a considerably greater rate of increase than the particle phase.

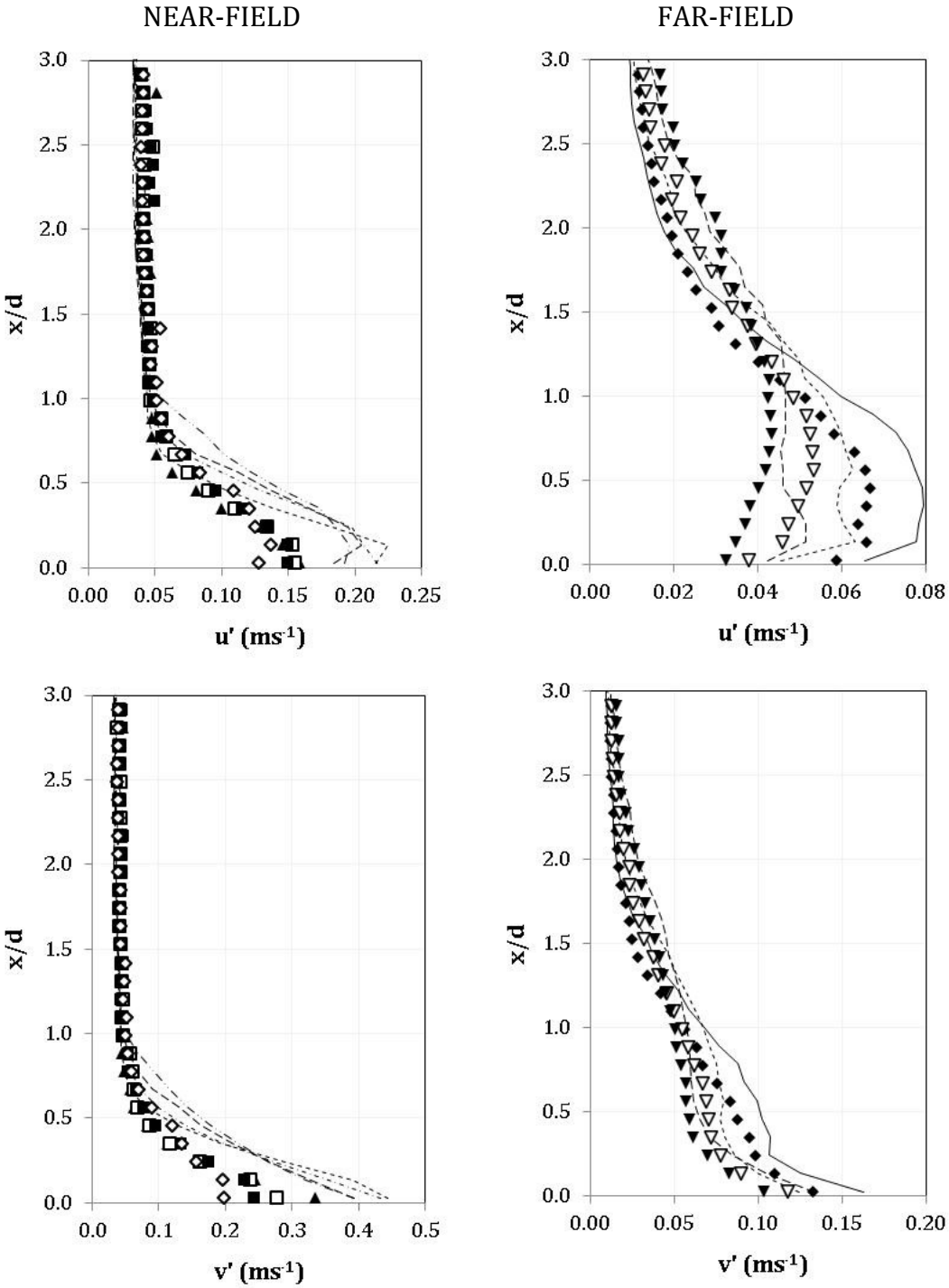

Figure 5-4 Particle and single-phase axial and radial RMS fluctuating velocity data, near- and far-field radial wall jet at h/d ratio = 6, (multi phase data – symbols, single phase data – lines)

Vertical particle phase profiles taken at: ▲ 2 r/d, □3 r/d, ■4 r/d, ◇5 r/d, ◆ 10 r/d, ▽ 12 r/d, and ▼ 15 r/d. Single-phase profiles at: - - - 2 r/d, –·–·– 3 r/d, — — 4 r/d, —··— 5 r/d, — 10 r/d, - - - 12 r/d, and — — 15 r/d.

Turbulent velocities of the particle phase continue to be smaller than the single-phase through the radial wall jet (Figure 5-4).

The particle axial RMS velocity, u'_p, decays by an order of magnitude from the jet outlet to the far-field of the wall jet (from ~0.8ms^{-1} to marginally more than 0.04ms^{-1} at 15d from the jet axis) after dropping by only 0.2ms^{-1} between the jet outlet and the impingement surface. Across the stagnation region, the turbulent velocity drops from a centreline value of around 0.57ms^{-1} at 0.1 x/d, to 0.27ms^{-1} at the same height 1d radially from the jet axis. The single-phase experiences a more significant drop in turbulent velocity across the same region.

Within the near-field of the wall jet, u'_p remains relatively unchanged within its lower region until 5 r/d when the flow begins to decelerate as the jet expands radially. The upper region sees a small variation, with values increasing from 2 to 5 r/d. The radial component exhibits a switch of dominance from the lower shear layer, where v'_p decreases with increasing distance from the jet axis, to the upper shear layer, where the reverse is seen. The single-phase jet showed the same behaviour but with larger differences in values. The radial turbulent velocity, v'_p, values increase within the near-field of the wall jet above that of the jet outlet but not as high as the radial fluctuating RMS velocity found close to the stagnation point. This is not seen in the single-phase data.

The far-field sees a consistent decay in turbulence as the distance from the jet axis increases. As with the developing jet region, the particle phase has lower turbulent velocities relative to the single-phase data, at all points of the impinging jet except the initial outlet region containing the potential core. The difference between the particle and single-phases decrease the further from the jet axis we travel, nearly the same at 15 r/d.

5.1.3 Reynolds Shear Stress Data

The Reynolds shear stress is another method of describing the turbulence of a flow and is taken as the averaged product of two fluctuating velocities.

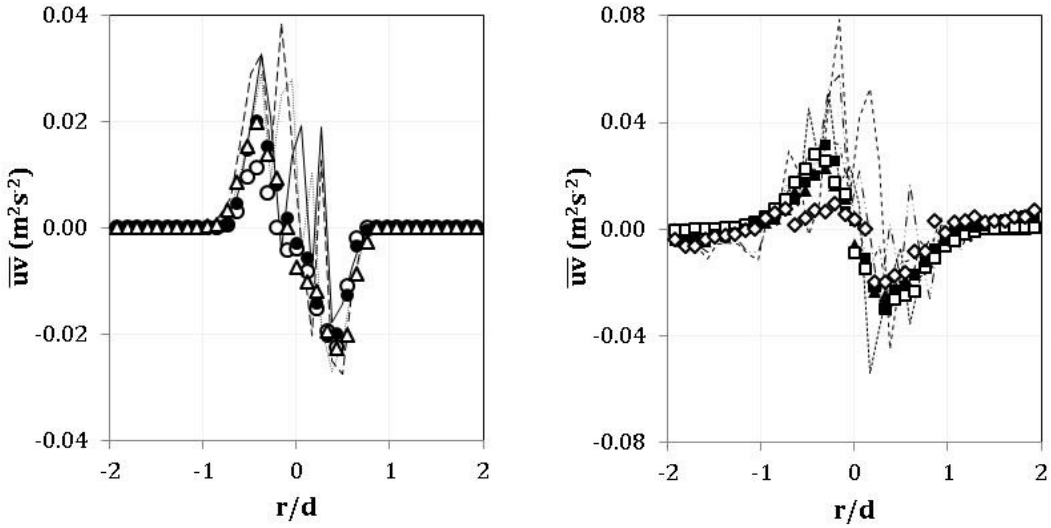

Figure 5-5 Particle and single-phase developing jet at h/d ratio = 6, shear stress data (multi phase data – symbols, single phase data – lines)

Multi-phase profiles taken at ○ 5.3 x/d, ● 5 x/d, △ 4 x/d, ▲ 1 x/d, □ 0.5 x/d, ■ 0.2 x/d and ◇ 0.1 x/d. Single phase profiles at: profiles: — 5.3 x/d, ····· 5 x/d, —— 4 x/d, –·–·– 1 x/d, ---- 0.5 x/d, —··— 0.2 x/d, - - - 0.1 x/d.

The particle phase shear stress within the developing jet increases as the wall is approached and the radial component of the flow grows. A clear difference between the particle and single-phase shear stress data in Figure 5-5 is that the particle shear stress data within the developing jet is considerably cleaner in appearance. The location and magnitudes of the local maxima are similar to the single-phase. Up to 5 diameters from the jet outlet, the apexes in the Reynolds shear stress coincide with the inflection locations of the radial mean velocities. Within the stagnation region, 1d of the impingement surface, there is no clear correlation to the locations of any of the local maxima. It should be noted that no smoothing has been applied to these datasets. All experimental trials were performed as similarly as possible and the same data processing and handling procedures applied.

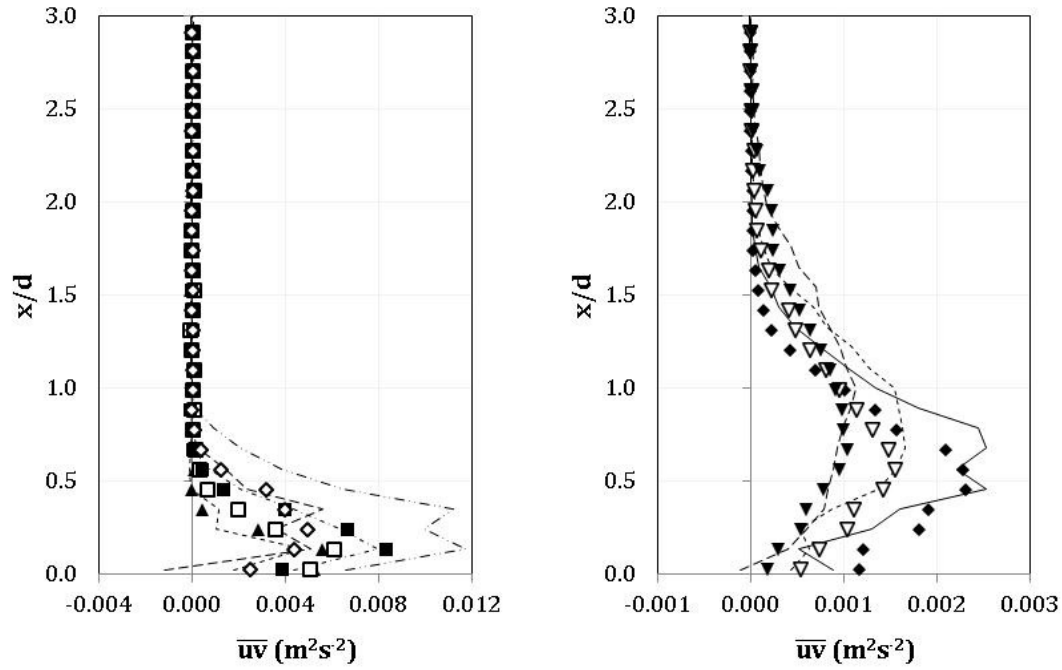

Figure 5-6 Particle and single-phase radial wall jet at h/d ratio = 6, shear stress data (multi phase data – symbols, single phase data – lines)

Vertical particle phase profiles taken at: ▲ 2 r/d, □ 3 r/d, ■ 4 r/d, ◇ 5 r/d, ◆ 10 r/d, ▽ 12 r/d, and ▼ 15 r/d. Single-phase profiles at: - - - 2 r/d, –·–·– 3 r/d, — — 4 r/d, —··— 5 r/d, — 10 r/d, - - - 12 r/d, and — — 15 r/d.

The Reynolds shear stress increases from the stagnation region where it is at its highest, out to 4 r/d and then decaying as the wall jet travels from the jet axis, Figure 5-6. Peak values are seen for all profiles examined in the radial wall jet.

The local maxima do not appear to coincide with peaks, troughs or where the velocity data (mean or turbulent) cross the axis (i.e., change sign). For the turbulent velocities in the near-field wall jet already discussed, a maximum near the impingement surface was only seen for the axial RMS velocity at 5 r/d. There is a shear stress maxima at 5 r/d at the same location. The far-field axial turbulent velocities have a local maxima which appears to be at s similar distance from the impingement surface as the shear stress local maxima. The highest shear stress in the radial wall jet is near the impingement surface, 4d from the jet axis. The single-phase impinging jet at 6 h/d had the highest shear stress at 5 r/d. Shear stress data profiles have the same general shape across the whole of the radial wall jet, and stretched or compressed depending on the expansion of the wall jet, and stretched upwards as r is increased. The difference in shear stress between the phases is at its greatest in the wall jet at 5 r/d.

5.1.4 Summary

A particle-laden impinging liquid jet with a jet-to-plate separation of 6 diameters has been mapped through all three regions of the flow; the developing jet and impingement region through to the near- and far-field of the radial wall jet. The particle phase does not follow the turbulent flow of the single-phase. In the developing jet where the pressure gradients of the wall are not yet felt, particle axial mean velocities are around 80% of those of the equivalent single-phase impinging jet. As the impingement surface is felt, the single-phase decelerates at a higher rate than the particles due to their inertia, until the profile taken just 0.1d above the impingement surface where the axial velocities of the two phases equalise. Radially a difference is only seen at the same profile closest to the wall where the particle phase exhibits a broader distribution with greater value and distance from the jet axis of the local maximum. RMS fluctuating velocities of the particles are significantly lower. The two peaks seen at the outer edges of the jet, where velocity fluctuations are stronger than in the potential core, are less prominent, particularly for the radial component. The difference between the phases increases as the wall is approached. The particle axial RMS velocity decreases while the single-phase increases. Simultaneously the particle radial component increases at a much smaller rate than the single-phase. The Reynolds shear stress increases as the impingement surface is approached as the radial flow grows. The particle phase velocity is considerably more stable. The local maxima are similar between the phases.

As the stagnation region deflects the impinging jet into the near-field of the radial wall jet, it undergoes deflection and acceleration. Tracking the vertical profiles from the entrainment region down towards the wall, entrainment velocities for the particle phase are marginally larger than for the single-phase case. Crossing the wall jet boundary layer, the turbulent/non-turbulent interface, both the axial mean velocity reaches a maximum (downward velocity) and begins to fall and radial velocities become positive (indicating upward flow). The upper shear layer of the wall jet experiences an increase in radial velocity while the axial downward velocity decreases, as x/d becomes smaller. A local maximum at the interface between the lower and upper shear layer is seen for the 4 and 5 x/d profiles. The single-phase trials display very similar profile shapes but with varying values within the near-field wall jet, the difference between the phases more noticeable further from the jet centreline. Generally within this region we see in the upper shear layer a higher single-phase radial velocity, while the lower shear layer exhibits the opposite. The

particle phase radial velocity overtakes from 5 diameters away from the jet centreline. Again the RMS fluctuating velocities are smaller for the particle phase, although the difference is less than upstream of this region. The single-phase drop in RMS velocities across the stagnation region is more extreme than for the particle phase. The radial RMS velocity increase within the near-field region was greater than the values seen near the outlet, but was not seen for the single-phase.

The profile shapes were the same as in the near-field but stretched upwards as the wall jet radially spread and decelerated in the far-field region of the wall jet. The radial growth of the wall jet is clearly seen from the position of the wall boundary moving further from the impingement surface as we move away from the jet centreline, and above this point the entrainment velocities are greater for the particle phase. Within the upper part of the wall jet, the axial velocity values converge as they gather at the local maximum common to both phases. A small divergence can be seen in the lower shear layer below the local maximum, this time the particle phase having slightly greater magnitude. Radially, from the impingement surface upwards, the particle phase is a little larger until a small distance above the local maximum where the single-phase becomes marginally more dominant. The local maxima of both the axial and radial mean velocities indicate the interface between the lower and upper shear layers within the wall jet. The far-field sees a consistent decay in turbulence as the distance from the jet axis increases. The particle phase still has lower turbulent velocities relative to the single-phase, the difference between the phases decreasing with distance from the jet axis and becoming nearly equal by 15 diameters.

The Reynolds shear stress is seen to increase from 2 to 4d away from the jet axis, and then begins to decay through to the furthest profile gathered within this work at 15d. The highest shear stress seen at 4d is more than twice the magnitude seen at any other part of the impingement region, including within the stagnation region. The profile shape is the same across the whole of the radial wall jet, expanding as distance from the jet centreline is increased. A peak in each of the shear stress profiles in the wall jet coincides with the radial RMS velocity maximum. For all profiles in the wall jet, the single-phase values are greater than for the particle phase.

5.2 Jet-to-plate Height Effect

Measurements of instantaneous velocity for the particle phase of an impinging jet at three jet-to-plate separations of 2, 6 and 10 h/d have been undertaken and results discussed here. The 6d case has already been discussed in detail earlier in this chapter (Section 5.1, page 150). In this section we compare the particle and single-phase data acquired at each of these heights: all variables, including solid loading and Reynolds number, were held constant to allow exploration of the effect of jet height on the particle and single-phase flows.

5.2.1 Flow Region Upstream of Stagnation Point

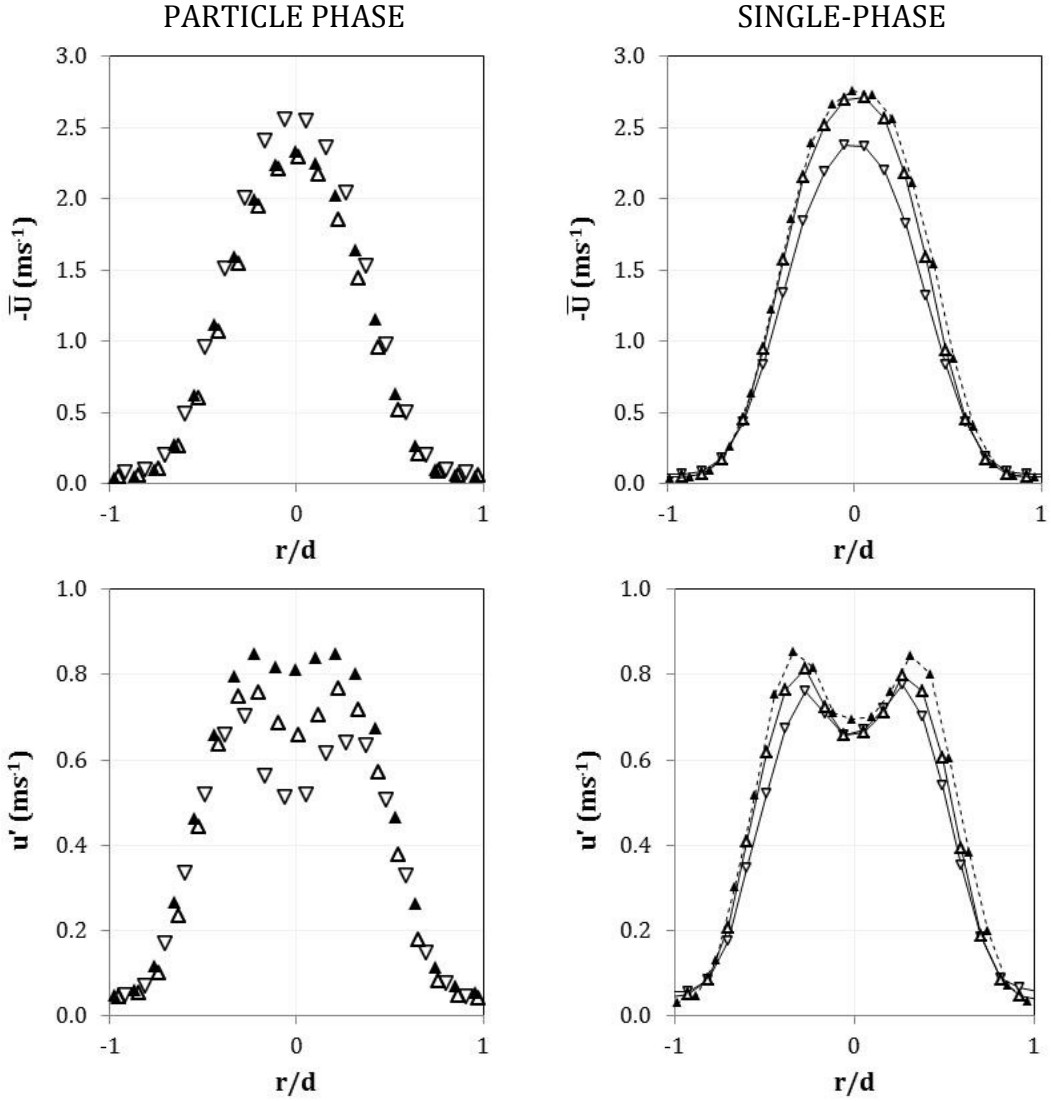

Figure 5-7 Axial mean and RMS fluctuating velocities for particle and single-phase impinging jets at each h/d ratio, 1d from jet outlet.

Data profiles at: 2 h/d (upside triangle), 6 h/d (open triangle) and 10 h/d (closed triangle). Particle phase are large symbols, single-phase are lines plus small symbols.

Axial mean ($\overline{U}$) and RMS fluctuating velocity (u') distributions at 1d from the jet outlet are presented for the particle and single phases (Figure 5-7). The particle mean velocity distribution for the lower jet at 2 h/d reaches a higher centreline velocity (U_m of 2.55ms^{-1}) than the 6 and 10 h/d jets (U_m of 2.30ms^{-1} and 2.33ms^{-1} respectively). For the 2 h/d jet the profile taken 1d from the outlet is also 1d from the impingement surface where the pressure gradient exerted by the wall will be felt. The impingement region was also seen to have an effect on the single-phase velocity distribution at 1 x/d for the 2 h/d jet, albeit the inverse. The difference in mean velocity between the phases for the 6 and 10 h/d jets are similar, with the particle phase 0.41 and 0.43ms^{-1} smaller than the single-phase, that is 17.8 and 18.4% reductions, respectively. Extending the comparison already made in the previous section for the 6d jet, the 10d is also in good agreement with the particle-laden free jet data of Tsuji et al. (1988) and Gillandt et al. (2001) who found the particle phase axial mean velocity to be 17% lower than the single-phase. In contrast, for the 2 h/d jet the particle mean velocity is 0.17ms^{-1} larger than the single-phase, confirming again that the impingement surface is having an influence at this profile location.

Particle turbulent velocities exhibit more of a spread in the centreline values between the jet heights. In ascending order, as h/d increases the centreline u' increases incrementally by ~0.15ms^{-1}. The magnitude of the twin peaks are similar although the peaks for the 10 h/d jet are less prominent, and hence the dip towards the centreline is also less prominent. The turbulent velocity distribution for the 6 h/d jet is very similar to all single-phase profiles; the lower jet exhibiting a dip in the centreline values while the higher jet turbulent velocity remains more constant across the jet potential core.

Further velocity profiles at 2 and 5d from the jet outlet have been taken for the impinging jets at h/d ratios of 6 and 10, Figure 5-8. No significant differences in mean velocities at each of the profile positions are seen. In the single phase trials, the 5d profile at 6 h/d was slighty lower than the same profile location at 10 h/d which suggested a wall effect at 1d above the impingement surface, although this wall effect is not evident in the particle data. Similar to the 1d profiles for the 6 and 10 h/d jets, the particle velocities are smaller than their single-phase equivalents.

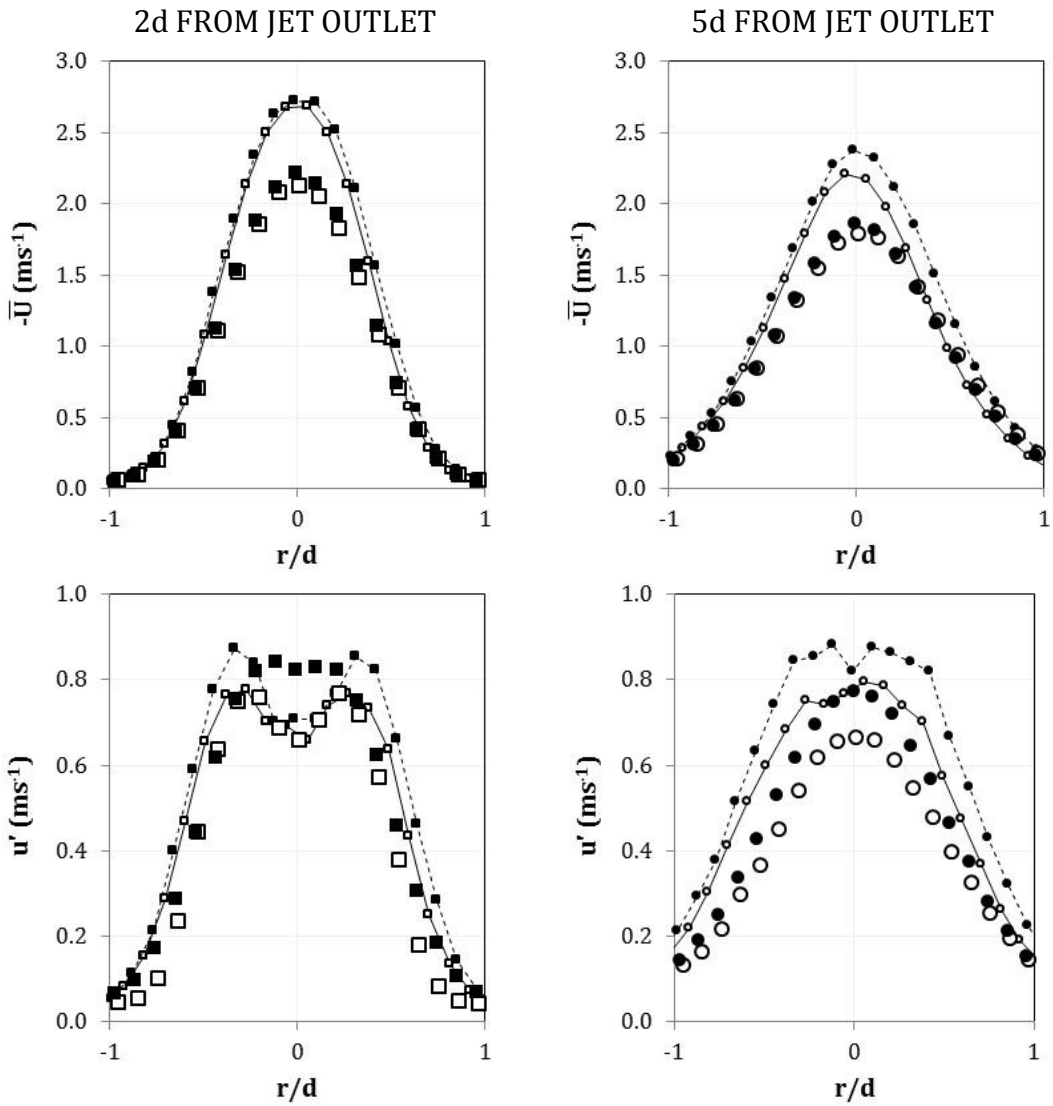

Figure 5-8 Axial mean and RMS fluctuating velocities for particle and single-phase impinging jets at each h/d ratio, 2 and 5d from jet outlet (squares and circles respectively)

Data profiles at: 6 h/d (open symbols) and 10 h/d (closed symbols). Particle phase are large symbols, single-phase are lines plus small symbols.

Although the variation in mean velocity was minimal, the turbulent velocities paint a different picture. Variation in the turbulent velocities is less clear at 2 and 5d in comparison to at 1d. At 2d from the jet outlet, with the exception of the absence of a dip towards the jet centreline in the particle data for the 10 h/d jet, the particle and single phases are similar. The magnitude of the peak turbulent velocities are marginally larger than for the 6 h/d jet, approximatley 0.09ms^{-1}. The region around the jet centreline that experiences a dip in turbulent velocity towards the axis is similar. Another 3 diameters from the jet outlet, at 5d, the turbulent velocities no longer have the double peak form. The difference between the phases, for both 6 and 10 h/d, is 0.11ms^{-1}.

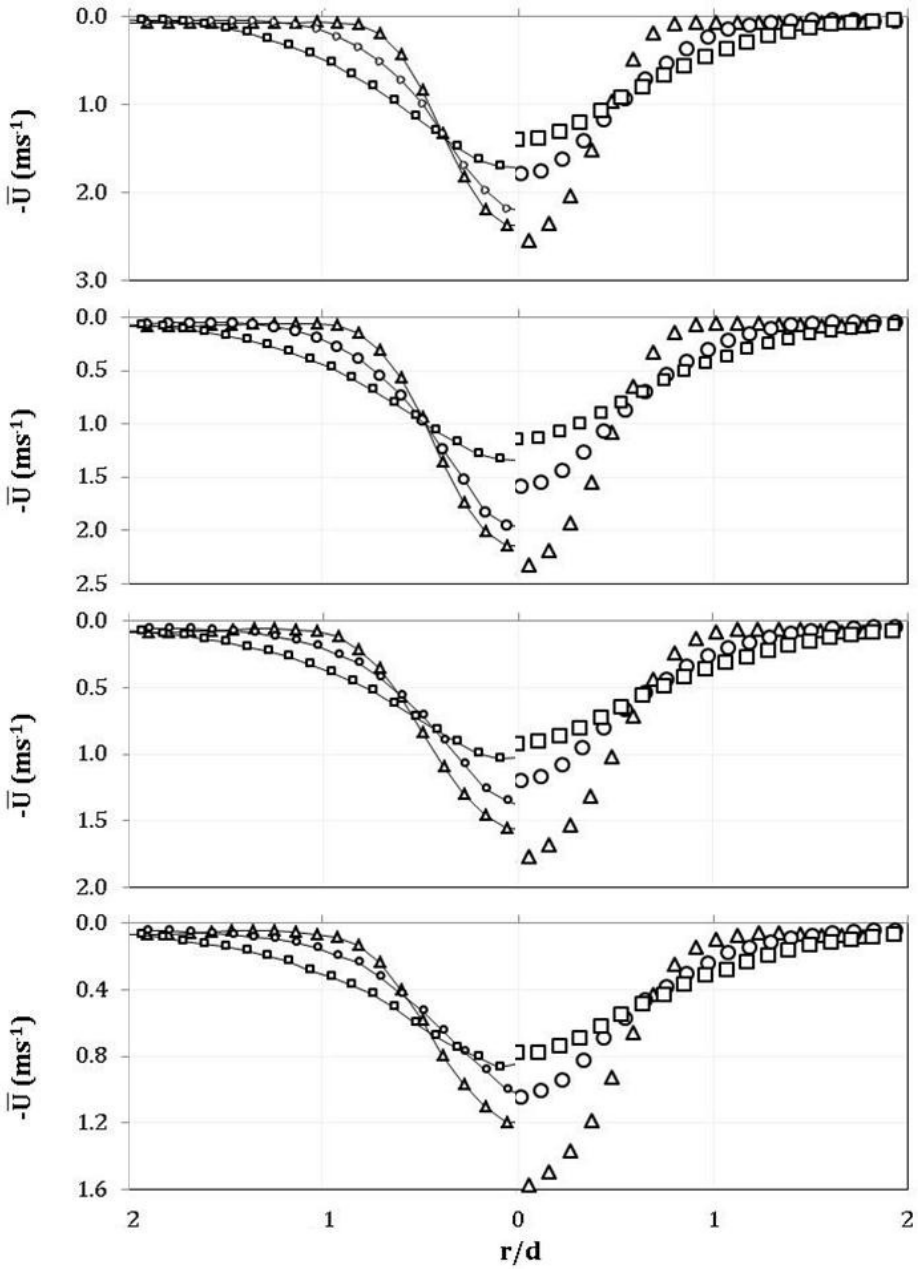

Figure 5-9 Particle and single-phase axial mean velocity within 1d of the impingement surface at h/d ratios of 2, 6 and 10

Transversal profiles taken at: 1, 0.5, 0.2 and 0.1d above impingement surface (top to bottom). Data at 2 h/d (△), 6 h/d (○) and 10 h/d (□): particle phase large symbol, single-phase line plus small symbol.

A visual comparison between the particle and single phase data within 1d of the impingement surface is presented in Figure 5-9 to Figure 5-13. Particle phase data is shown on the right of these graphs, with single phase data on the left in mirror form such that the x axis is positive either side of the jet centreline. Considerable effort was applied when performing the experimental trials to ensure the jet was well aligned to the base of the tank such that the developing

jet was symmetrical about the axis. Vertical data profiles one diameter either side of the jet centreline (1 and -1 r/d) were tested for symmetry; examples of such data checks are given in Figure 3-22. All comparisons are made using data from the jet axis radially outwards; the side of the jet selected is the same as that used in the radial wall jet measurements. Within each of these figures, the graphs represent different axial positions above the impingement surface; the top graph at 1d, the next 0.5d from the base followed by 0.2d and finally the bottom 0.1d above the base.

Particle and single phase velocities follow similar trends at all transverse locations; the mean axial velocity decays as the impingement surface is approached and the lower jet height (2 h/d) exhibits the highest axial mean velocity which becomes lower for the 6 and 10 h/d jets. The larger the jet height, the more advanced the jet development, resulting in lower centreline velocities. And as the jet development advances with increasing jet-to-plate separation, the jets expand more and this can be clearly seen in these data.

For the particle phase, the greatest difference between centreline velocities are seen between the 2 and 6 h/d jets, with a smaller drop between the 6 and 10 h/d cases. No apparent trend in how these differences develop as the wall is approached is evident; variations between 2 and 6 h/d ranging from 0.76ms^{-1} at 1d, up to 0.79ms^{-1} at 0.5d, and down again to 0.53ms^{-1} at 0.1d; and between 6 and 10 h/d ranging from 0.08ms^{-1} at 1d, 0.46 ms^{-1} at 0.5d, and finally down to 0.27ms^{-1} at 0.1d. The single phase data on the other hand show two fairly clear trends; from 2 to 6 h/d the difference remains fairly constant at 0.17ms^{-1} ±0.01ms^{-1}, for the 6 and 10 h/d jets the difference falls as the wall is approached. The two lower jet heights are either within the potential core, 2 h/d, or just outside it, 6 h/d, so the rate of decay in axial velocity is anticipated to be fairly similar, as seen in these data. The additional four diameters of jet evolution for the 10 h/d jet means the velocity entering the impingement region is lower, so a slower deceleration rate is necessary to reduce the velocity to zero at the stagnation point, compared to the large velocities of the other two jets. The particles do not follow this trend.

Within the impingement region, the particle phases have smaller axial mean velocities for the two larger jet heights, with the opposite seen for the lowest jet height (h/d ratio of 2). The velocity gradient between the particle and single-phases for the larger two jet heights reduces through the impingement region until becoming nearly equal at the 0.1d above the wall. This coming together of the velocities is not seen at 2 h/d. Instead the discrepancy between the phases

fluctuates from 0.17ms^{-1} at 1d, 0.25ms^{-1} at 0.5d, 0.21ms^{-1} at 0.2d, before increasing to a difference of 0.38ms^{-1} at 0.1d.

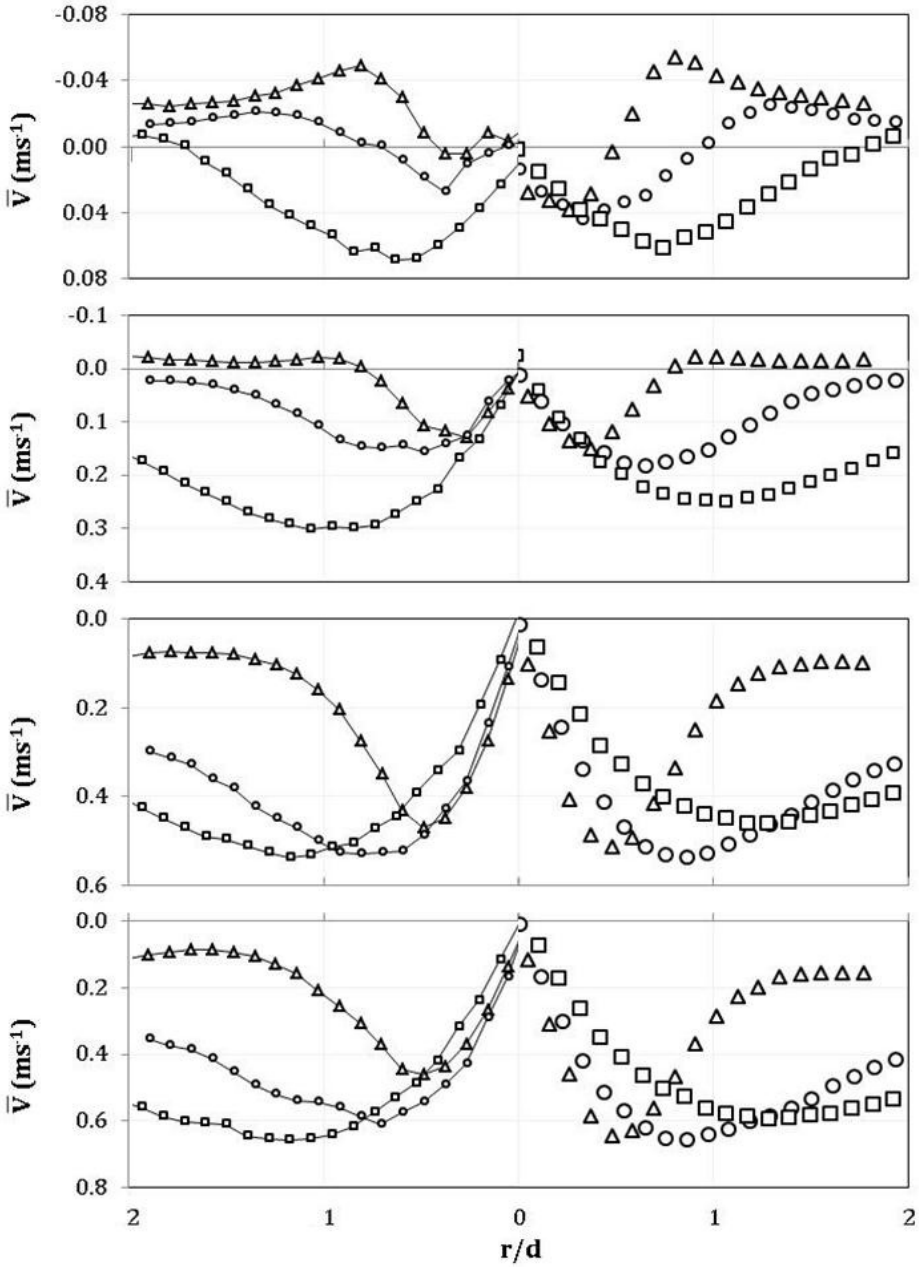

Figure 5-10 Particle and single-phase radial mean velocity within 1d of the impingement surface at h/d ratios of 2, 6 and 10

Transversal profiles taken at: 1, 0.5, 0.2 and 0.1d above impingement surface (top to bottom). Data at 2 h/d (△), 6 h/d (○) and 10 h/d (□): particle phase large symbols, single-phase line plus small symbol.

The particle and single-phase mean radial velocities, Figure 5-10, are similar at each profile location within 1d of the surface. All are zero at the jet centreline (0 r/d), increasing out from the jet axis until a local maximum (V_m) is reached. The

magnitude and radial position of V_m increases as the wall is approached due to deflection in the stagnation region.

For the 2 and 6 h/d jets, the particle V_m is a little larger than for the single phase and its location is marginally closer to the jet axis suggesting the spreading rate for the two-phase jet within the impingement region is lower than for the single phase. Hetsroni and Sokolov (1971), Popper et al. (1975), Sheen et al. (1994) and Fan et al. (2010) found the same for free jets beyond the developing region (x/d typically greater than 10). At 0.2 and 0.1d for the lowest jet, 2 h/d, the influence of the radial wall jet is evident; further from the impingement surface the radial velocity becomes negative outside the jet boundary where entrainment is occurring. The highest jet, 10 h/d, shows the reverse behaviour; the magnitude of the local maxima (V_m) is greater for the single phase, and the locations of these maxima from the centreline are approximately the same.

Turbulent fluctuating velocities for the particle phase are smaller than for the single phase within the impingement region, Figure 5-11. The magnitude of the axial turbulent velocity for the particles decrease the closer the impingement surface becomes; the larger the jet separation the smaller the centreline magnitude at all positions. The only profiles not to follow this trend are at 1 and 0.5d for the 2 h/d jet where the RMS turbulent velocity has the double peak shape complete with a dip towards the jet axis. However the magnitude of the peak fit this trend. The jet width grows as the jet line moves away from the wall, a trend similar to that seen in the single phase data, as expected.

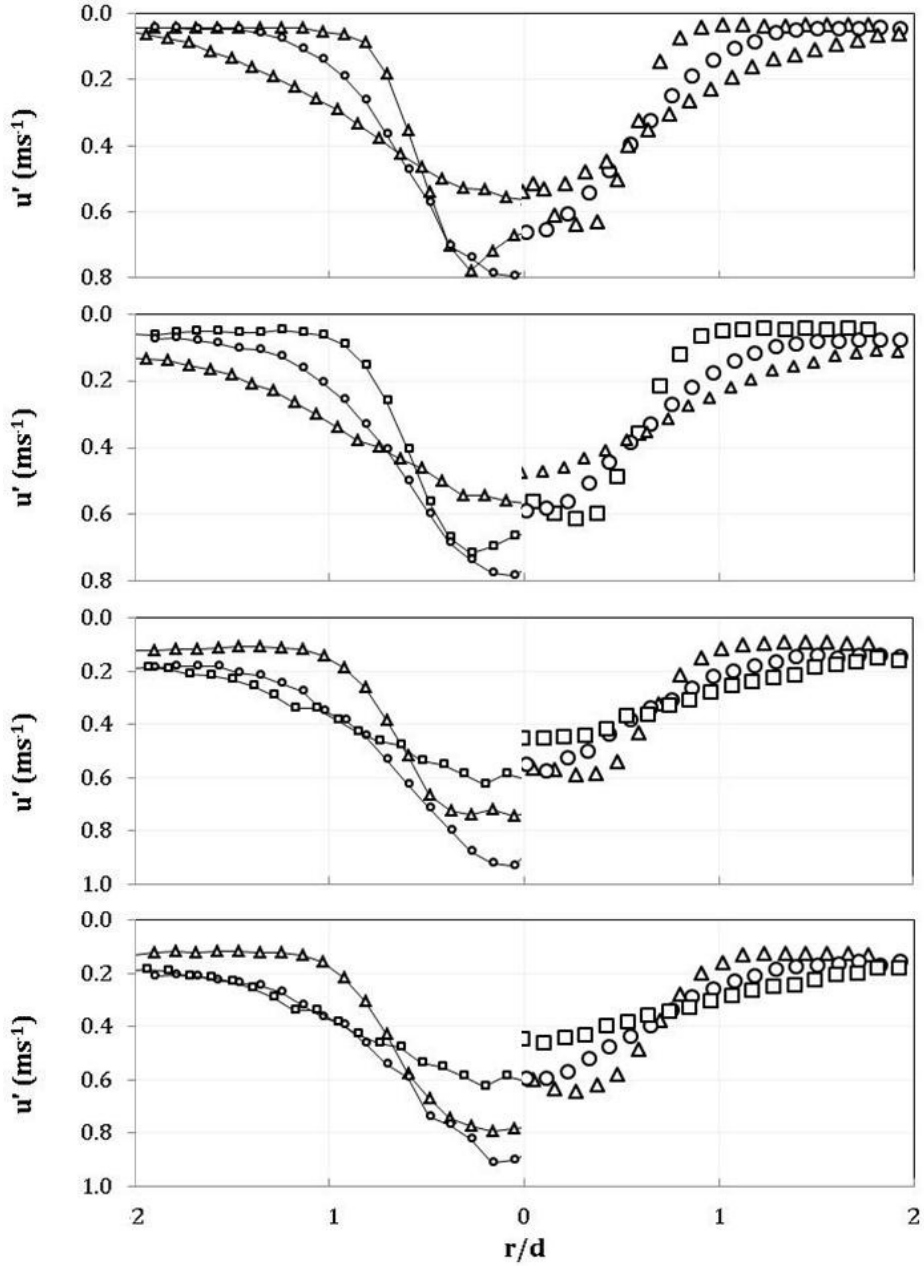

Figure 5-11 Particle and single-phase axial RMS fluctuating velocity within 1d of the impingement surface at h/d ratios of 2, 6 and 10

Transversal profiles taken at: 1, 0.5, 0.2 and 0.1d above impingement surface (top to bottom). Data at 2 h/d (△), 6 h/d (○) and 10 h/d (□): particle phase large symbols, single-phase line plus small symbol.

The variation of RMS radial velocities between the phases are more significant than for the axial component, Figure 5-12. There is less of a spread of values for the particle phase at each jet height tested compared to the single phase. Particle velocities for the 6 and 10 h/d jets are very similar, and at the final two profile positions do not show much variation across the width of the impingement region. A point of note is that for the 2 h/d jet the radial turbulent

velocity distributions develop the double peak shape as the wall is approached, the opposite to what has been seen previously.

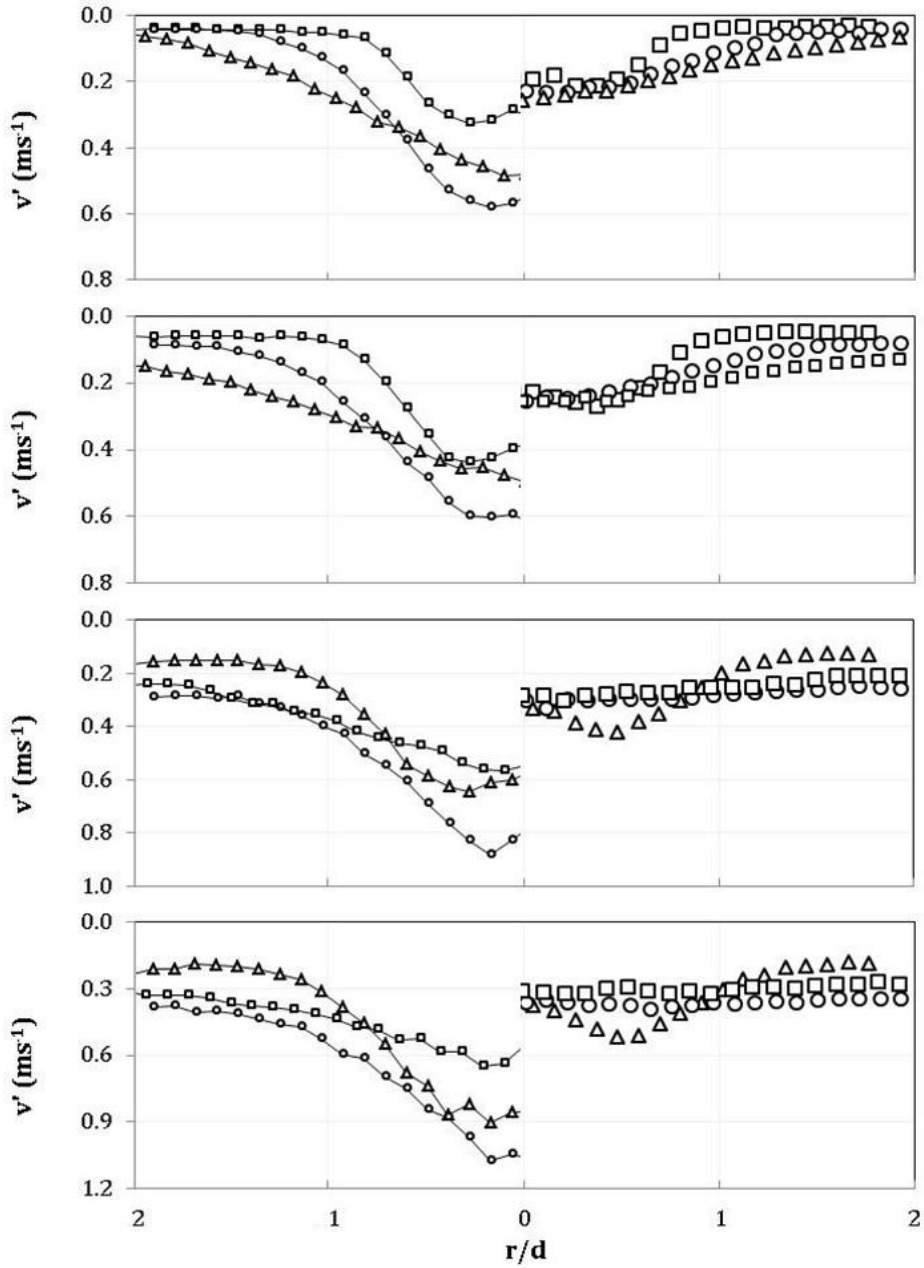

Figure 5-12 Particle and single-phase radial RMS fluctuating velocity within 1d of the impingement surface at h/d ratios of 2, 6 and 10

Transversal profiles taken at: 1, 0.5, 0.2 and 0.1d above impingement surface (top to bottom). Data at 2 h/d (△), 6 h/d (○) and 10 h/d (□): particle phase large symbols, single-phase line plus small symbol.

Little difference is seen in the magnitude of the shear stress between the particle and single phases within the impingement region, as seen in Figure 5-13. Particle shear stresses for the lowest jet height are smaller than for the other jets at 1d, with the middle height jet displaying the higher stress values. By 0.1d the particles have a similar distribution, and as the jet height increases, the shear stress this close to the wall decreases.

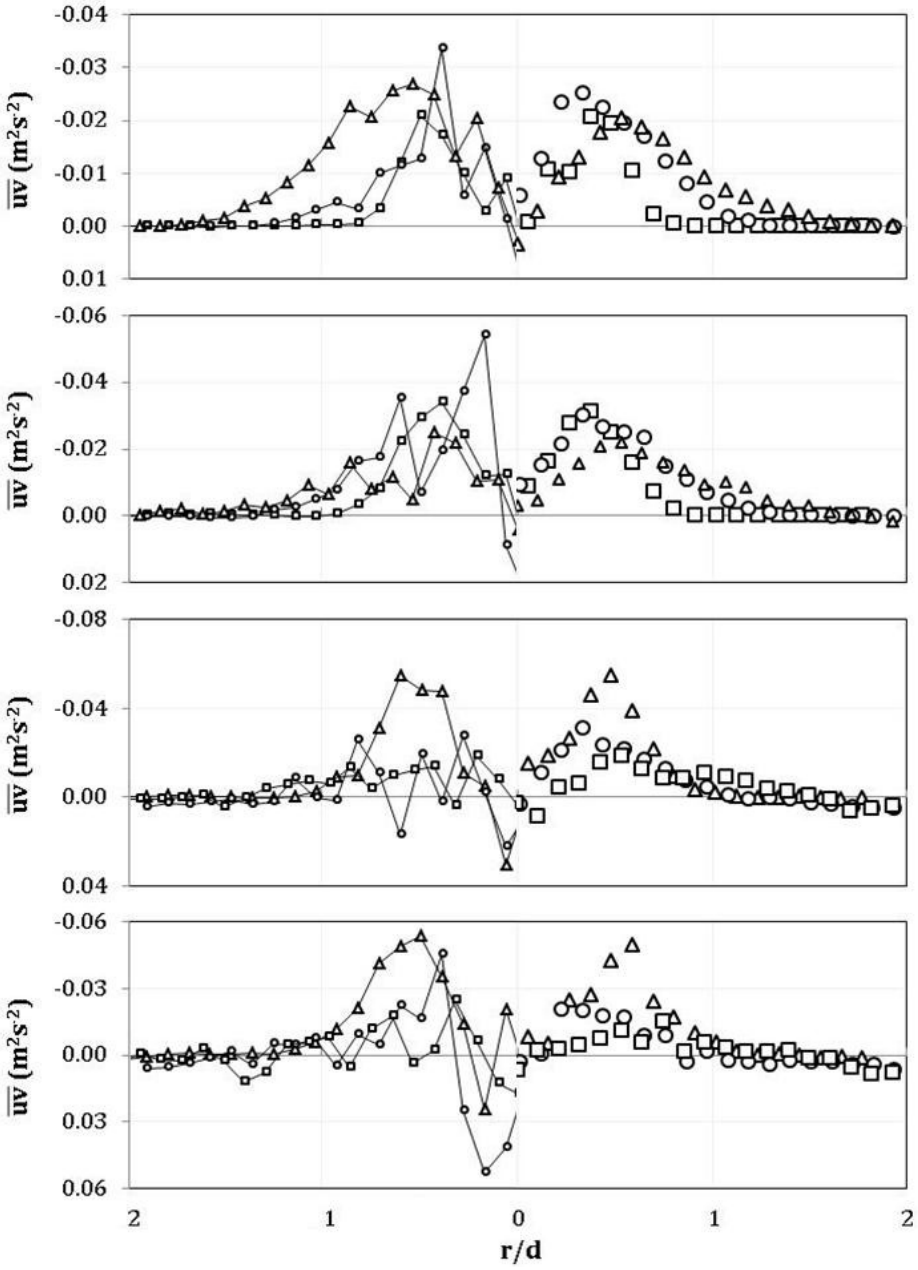

Figure 5-13 Particle and single-phase shear stress within 1d of the impingement surface at h/d ratios of 2, 6 and 10

Transversal profiles taken at: 1, 0.5, 0.2 and 0.1d above impingement surface (top to bottom). Data at 2 h/d (△), 6 h/d (○) and 10 h/d (□): particle phase large symbols, single-phase line plus small symbol.

5.2.2 Flow Region Downstream of Stagnation Point

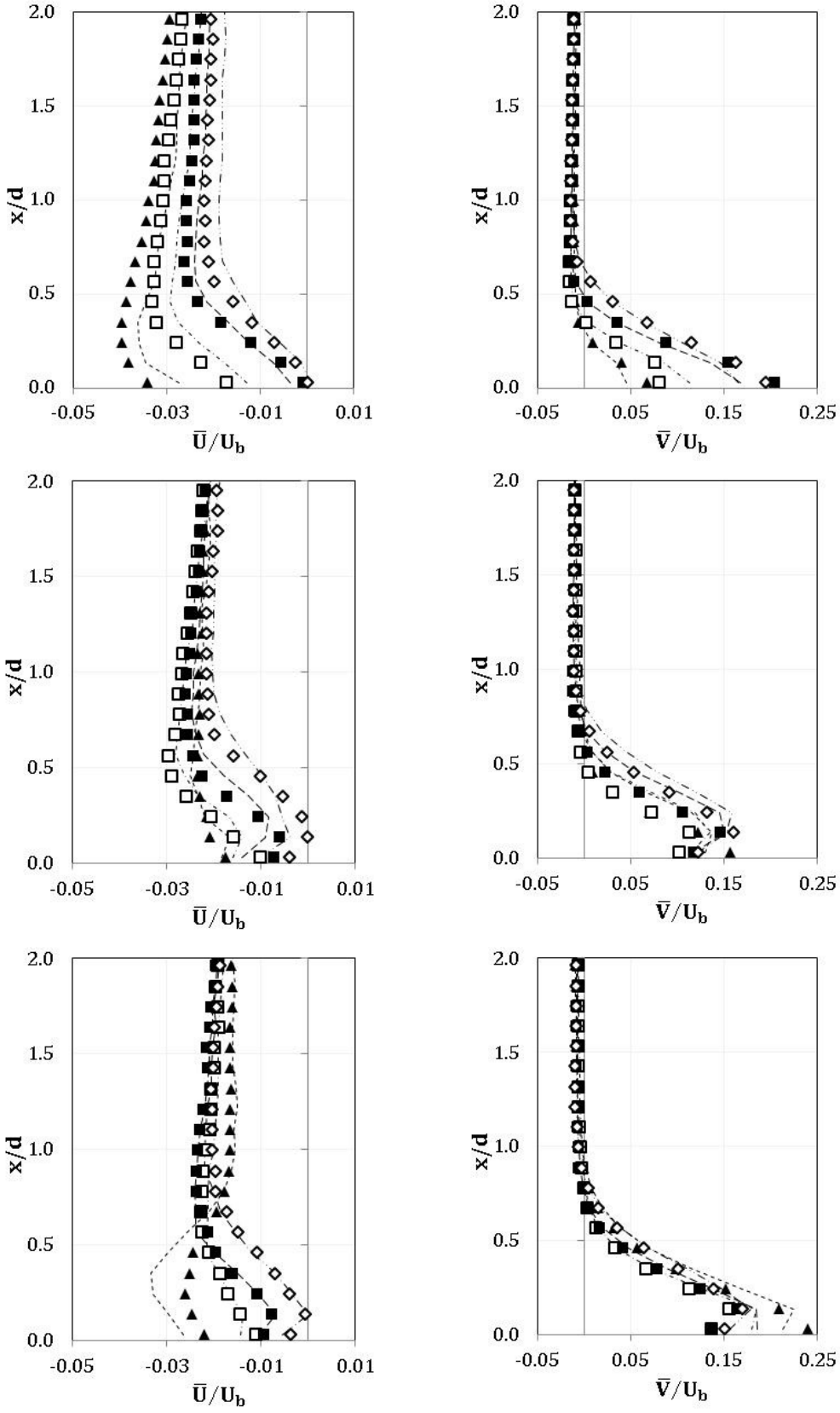

Figure 5-14 Normalised axial and radial mean velocity in the near-field region at h/d ratio of 2 (top), 6 (middle) and 10 (bottom); multi phase data – symbols; single phase data – lines

Vertical particle phase profiles taken at: ▲ 2 r/d, □3 r/d, ■4 r/d, and ◇5 r/d. Single-phase profiles at: - - - 2 r/d, –·–·– 3 r/d, — — 4 r/d, and —··— 5 r/d.

The axial and radial velocity, normalised by the bulk axial outlet velocity, evolution is clear for the smallest jet height (2 h/d), Figure 5-14, increasing as with distance away from the stagnation point. The point of inflection at the upper jet boundary moves further from the impingement surface while growing in magnitude. The particle phase axial velocities are smaller than their single phase equivalent, while little differences in the radial direction can also be seen. As the jet line is lifted away from the stagnation point, the width of the jet grows as seen from the developing jet above; this begins to be more visible in the radial wall jet profiles. The 2 r/d profile taken for the 6 h/d jet shows this where the radial velocity is greater than the next profile taken at 3 r/d, and the impingement region is wider in the radial direction due to the difference in jet height. Once the flow leaves this region is undergoes acceleration as it is deflected. The impingement region is wider still for the 10 h/d jet where the radial velocity is even greater at 2 h/d compared to 3 r/d.

At 6 h/d, the particle axial velocities are larger from 3 to 5 r/d in the lower part of the wall jet, and vice versa through the upper shear layer and into the entrainment region. A similar trend is seen in the radial direction, and acceleration of the radial wall jet from the impingement region can be seen from 3 r/d.

At 10 h/d, the particle and single phase velocities ($\overline{U}$ and $\overline{V}$) are very similar from 3 r/d. The lower shear layer at 3 and 4 r/d shows slightly higher radial velocities. The radial acceleration in the near-field is less significant than for the other jet heights. Again the impingement region can be seen at 2 r/d.

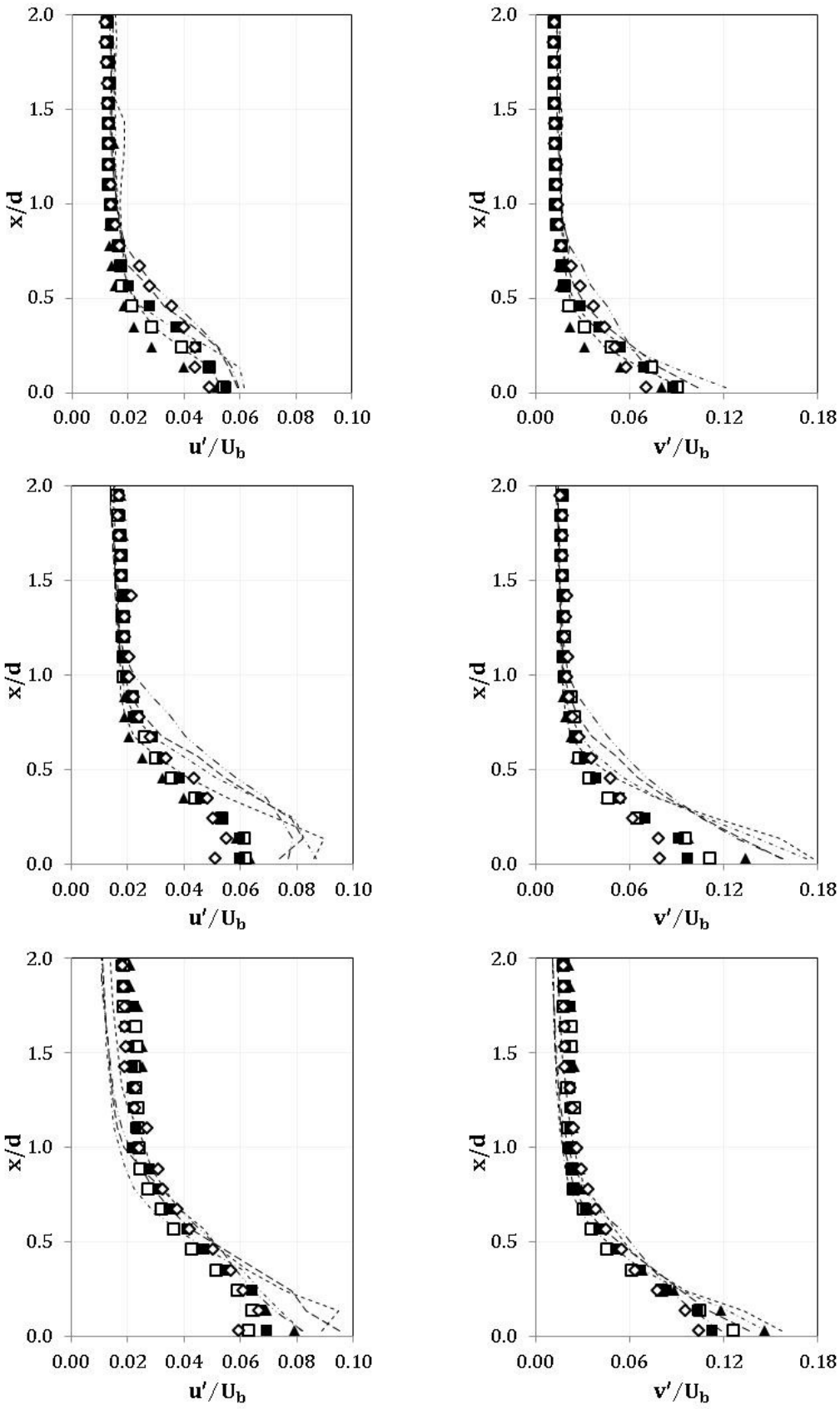

Figure 5-15 Normalised axial and radial RMS fluctuating velocity in the near-field region at h/d ratio of 2 (top), 6 (middle) and 10 (bottom); multi phase data – symbols; single phase data – lines

Vertical particle phase profiles taken at: ▲ 2 r/d, □3 r/d, ■4 r/d, and ◇5 r/d. Single-phase profiles at: - - - 2 r/d, –·–·– 3 r/d, — — 4 r/d, and —··— 5 r/d.

Turbulence intensities experienced by the particles in the near-field of the radial wall jet increase as the jet line moves away from the impingement surface, Figure 5-15. The radial component (v') is at its largest closer to the jet axis, and as the wall jet grows v' decays for all jet heights.

Across the width of the near-field of the wall jet, the 10 h/d jet shows the least variation, closely followed by the 6 h/d data. There is a spread in axial turbulence intensity values in the upper shear layer not seen in the lower shear layer. This spread is also evident in the radial data.

Comparing particle and single phase turbulence shows a greater difference for the middle jet height of 6 h/d where the particle magnitude is lower and does not come into agreement until the entrainment area. The other jets show the greatest variation in the lower region of the radial wall jet.

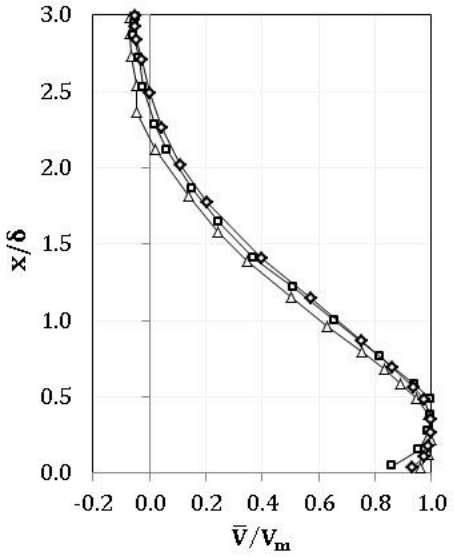

Figure 5-16 Best-fit profiles taken from the single-phase, self-similar radial wall jet at h/d ratios of 2 (△), 6 (□) and 10 (◇)

The single phase, far-field radial wall jet can be characterised by its self-similarity. We have already found this to be true from 5 or 10 r/d for the single phase data previously presented in Chapter 5. The same assessment has been applied using this new multi-phase data, comparing the results to other workers (Poreh et al., 1967; Dianat et al., 1996; Fairweather and Hargrave, 2002). Best-fit curves were taken from the self-similar profiles in the single phase far-field radial wall jet at each of the 3 h/d ratios examined and are shown in Figure 5-16. As can be seen, there is very little difference between these profiles suggesting that, for the range of jet-to-plate separations tested at a Reynolds number of 10,000, the resulting radial wall jets are self-similar.

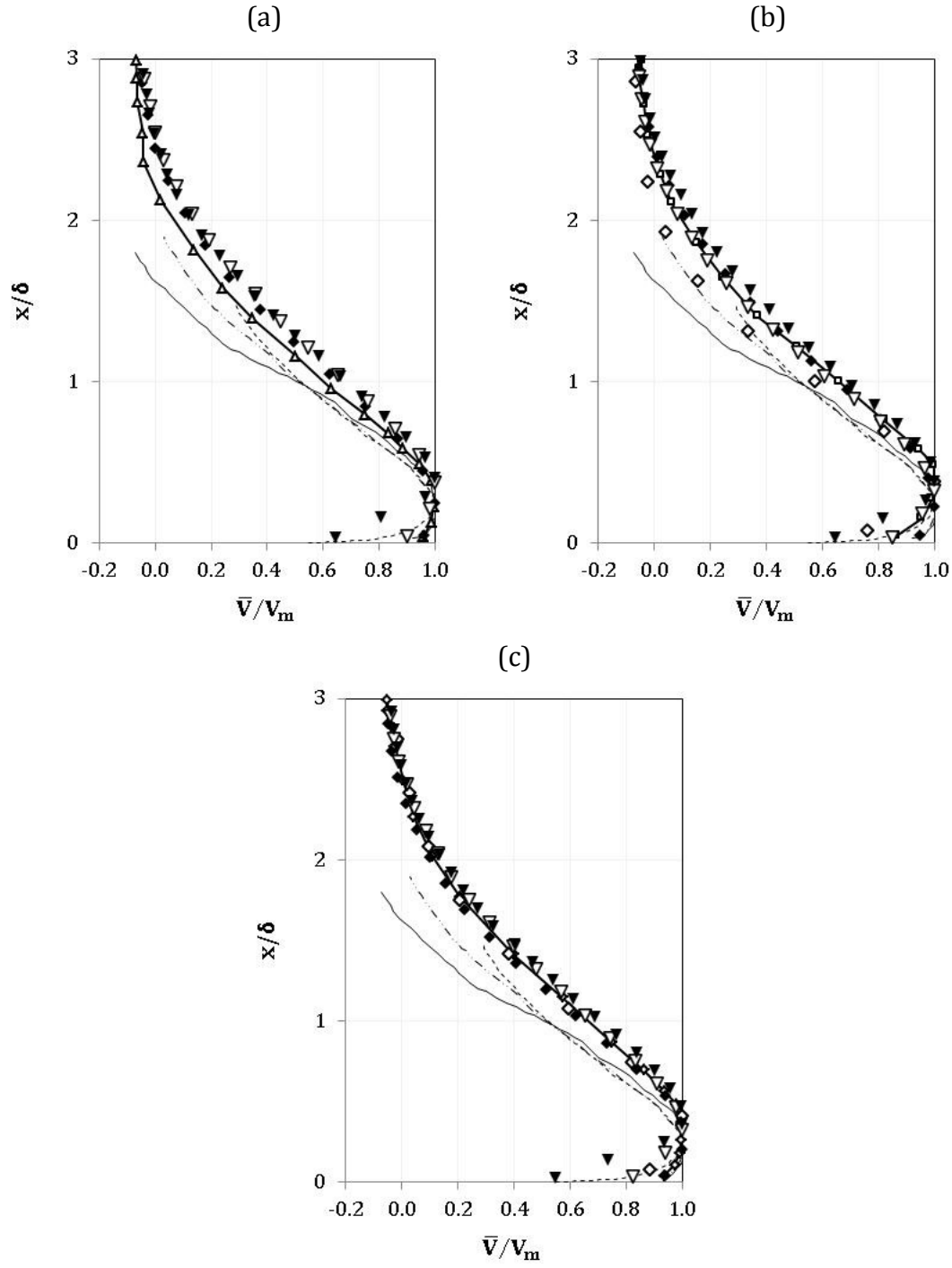

Figure 5-17 Normalised radial mean velocity in the self-similar, far-field region at h/d ratio of (a) 2, (b) 6 and (c) 10

Particle phase profiles taken at ◇ 5 r/d, ◆ 10 r/d, ▽ 12 r/d and ▼ 15 r/d. And data from single-phase trials (— and small symbol), Poreh et al., 1967 (----) and Dianat et al., 1996 (— · · —), Fairweather and Hargrave, 2002 (—).

Particle radial mean velocity data, normalised by the local maxima V_m is plotted against axial distance non-dimensionalised by the jet half-width to enable comparison with the single-phase radial wall jet data of Poreh et al. (1967),

Dianat et al. (1996) and Fairweather and Hargrave (2002), Figure 5-17. The mean particle velocities have been normalised against their local maxima, i.e., the particle velocity ($\overline{V}_p$) is normalised using the particle local maxima $V_{m,p}$. In order to estimate the jet half-width, the local maximum peak in the radial wall jet must be captured by the measurement. There are no data at 5 r/d for the 2 h/d jet as the local maximum peak was not measured so the half-width could not be established.

There is some variation in the particle velocity distributions for the three jet heights. The onset of self-similarity differs as the jet line is lowered towards the impingement surface. With the jet line at its greatest height above the wall (10 h/d) the radial velocity profiles are self-similar from 5 to 15 r/d, and in very good agreement with the single phase data. The other jets achieve self-similarity from 10 r/d. The particle velocities for the 2 h/d jet in the upper shear layer are marginally greater than for the single phase.

Agreement between the present data and earlier result obtained by Poreh et al. (1967), Dianat et al. (1996) and Fairweather and Hargrave (2002) is qualitatively good for all jet heights. Agreement in the lower part of the radial wall jets is particularly good. The non-dimensionalised data in the upper part of the wall jets are in reasonable agreement, although the present data lie above the air jet data of these other authors likely due to the weaker entrainment field of the liquid submerged jet.

In the lower part of the radial wall jet, very near the wall, the radial velocities at 15 r/d seem to dip rather than follow the same trend as the other far-field profiles. Some maintenance was performed on the jet test tank between the single phase trials and these particle-laden trials. On close inspection of the wall of the tank where the CCD camera was located, a small mark could be seen on the inside of the tank wall, just above the base accounting for the 2 or 3 data points nearest the base where the dip is seen. The other data points for the 15 r/d profiles were unaffected.

5.3 Chapter Conclusions

This chapter presents and examines the first particle-laden turbulent impinging jet velocity field datasets for all three regions of the impinging jet; viz. the free / developing jet region, the impingement / stagnation region, and the radial wall jet (Chapter 2). A high resolution of axial and radial profiles has been taken to provide as detailed a picture of the flow development of the impinging jet as was reasonably practicable taking into consideration the data processing and handling requirements of the PIV (Chapter 3). The datasets presented within this chapter also include jet outlet conditions essential to enable model validation and development of our understanding of such systems, often under-prescribed of previous workers. The effect of jet-to-plate separation was explored for jet heights of 2, 6 and 10 h/d, respectively.

The particle phase consisted of silica particles of mean diameter 69.2μm with a particle density of 2.45 g cm^{-3} and solids loading of 0.01 vol% (Chapter 3). Particle-phase turbulence statistics ($\overline{U}_p$, $\overline{V}_p$, u'_p, v'_p and $\overline{uv}_p$) were calculated from two-component instantaneous velocity vector data acquired using particle image velocimetry (PIV), and comparison made to the single-phase data already discussed in Chapter 4.

The key conclusions drawn within this results chapter are outlined below;

- The particle phase does not follow the liquid turbulent flow which is known to maintain the centreline velocity of the source pipe until the end of the potential core has been reached. Within the developing jet and impingement region, the particle phase velocities are generally smaller than their single-phase counterparts.

Free / developing jet region:

- The particle phase axial mean velocity is 82% of the single-phase value within the developing jet where the presence of the wall is not felt for the 6 and 10 h/d jets. In contrast, for the smallest jet height of 2 h/d, the particle phase axial mean velocity is 7.1% greater than for the single-phase. Particle RMS fluctuating velocities exhibit more of a spread in the centreline values between the jet heights. In ascending order, as h/d increases the centreline u'_p increases incrementally by $\sim 0.15 ms^{-1}$.

In the impingement region, within 1d of the impingement surface:

- Mean axial velocities decay as the wall is approached. The magnitude of axial velocity is directly related to the development of the free jet prior to impingement. The greater the jet height, the more advanced the jet

expansion, resulting in wider distributions and lower centreline velocities.

- The particle phase radial maximum velocity is marginally larger and closer to the jet axis than for the single-phase indicating that the particle phase spreading rate is lower, as seen for particle-laden free jets. As the let line moves away from the impingement surface, from 2 to 10 h/d, the local maxima move away from the jet axis. From 1 to 0.5d axial distance from the wall (0.5 to 1 x/d respectively) the magnitude of this maximum increases with increasing h/d ratio. However, within 0.2d of the surface the opposite is seen, albeit with the difference in magnitude being considerably less. Between the phases explored, the particle radial velocity is greater than the single-phase for the 2 and 6 h/d jets, but the reverse in seen for the 10 h/d jet.
- The particle phase exhibits considerably lower RMS turbulent velocities than the single-phase. There is also less variation between the jet heights explored. The magnitude of the particles decrease the closer the impingement surface gets; the larger the jet separation the smaller the centreline magnitude at all positions.

Radial wall jet:

- Comparison of the very near-field of the wall jet for each of the jet heights is difficult as the flow entering the wall jet from the impingement region is so different. It is not until around 5 r/d that results begin to align to some degree. For the smallest jet height, the near-field sees the deflection and acceleration to a greater extent than the other two jet heights.
- The radial mean velocity for the 2 h/d jet grows from 2 to 5d from the jet axis with no significant difference between the particle and single-phases, while the axial downward velocity decreases to zero at 5d, with the single-phase being smaller in magnitude, and with the difference between the phases decreasing. No peak within the wall jet is seen in this region.
- For the 6 h/d jet, the impingement region is seen in the 2 r/d profile, with acceleration following from 3 to 5d, and with radial local maxima present at these distances from the jet axis. For this case, the single-phase radial velocity is greater in the upper part of the wall jet, being overtaken by the particle phase in the lower part. Axially, local maxima are only seen at 4 and 5d with the particle phase exhibiting higher velocities than the single-phase.

- Finally, for the largest jet height at 10 h/d explored, radial mean velocity local maxima are seen in all profiles except at 2d. The upper region from the wall has similar values for both phases with some variation in the lower region; single-phase radial velocities at 3 and 4d are higher than for the particle phase, with the phases in good agreement at 5d. The axial velocity at 2d is dominant for the single-phase, becoming approximately equal between the phases from 3 to 5d.
- In the far-field of the radial wall jet, when the radial velocity is normalised by the local maximum and plotted against the jet half-width we would expect the profiles to be self-similar. This was seen for all three jet heights, with the onset of self-similarity changing as the jet line is lowered towards the impingement surface. The largest jet height, 10 h/d, achieves self-similarity from 5d whereas the other two jet heights achieve it from 10d, with all in good agreement with the single-phase results.
- Turbulence intensities experienced by the particles in the near-field radial wall jet increase as the jet line moves away from the impingement surface. The radial component (v') is at its largest closer to the jet axis, and as the wall jet grows v' decays for all jet heights. The particle turbulence is smaller than that of the single-phase, the greatest difference seen for the middle jet height of 6d.

Chapter 6
Results and Discussion – Particle Size Effect on Impinging Jet Flow

Multi-phase flow refers to any fluid flow consisting of more than one phase, i.e., a surrounding liquid or gas (the continuous or primary phase) laden with discrete solid, liquid or gas particles (the dispersed or secondary phase). Particulate multi-phase flows offer problems of far greater complexity than found in single-phase equivalents. The ability to predict the behaviour of such flows is central to the efficiency and effectiveness of any process where multi-phase flows are encountered, which is vast. As such, many workers have explored particle size effects on pipe (Rizk et al., 1989), channel (Kulick et al., 1994) and free jet multi-phase flows (Lilly, 1973; Levy and Lockwood, 1981; Sheen et al., 1994). However, to our knowledge, no such data for an impinging round jet has been published to date. The behaviour of solid particles in turbulent impinging liquid jets has broad applications across many industries including the nuclear applications introduced in Chapter 1, the focus of this work.

This chapter presents a sensitivity study for the particle size effect on a dilute particle-laden turbulent impinging liquid jet flow at a jet-to-plate separation of six diameters (6 h/d). Three particle sizes were tested; 20, 46 and 69μm; see Chapter 3 for full details on the particles used. The largest particle size was also used in Chapter 5. All variables, including solid loading (0.01 vol%) and Reynolds number (10,000), were held constant to allow exploration of the effect of particle size on the particle phase flow.

Two components of the mean velocity, $\overline{U}$ and $\overline{V}$, as well as the root-mean-square (RMS) of the fluctuating velocities, u' ($= \sqrt{\overline{u^2}}$) and v' ($= \sqrt{\overline{v^2}}$), and shear stress ($\overline{uv}$) were calculated from instantaneous velocity vector data acquired using PIV. Measurement results for the developing jet, impingement region, and the near- and far-field radial wall jet are presented. The origin (0,0) of the co-ordinate system is set to the stagnation point where the jet centreline crosses the impingement surface, as discussed in Chapter 1. Profile locations taken upstream of the stagnation point are reported to decrease from the jet outlet towards the impingement surface (Figure 3-13), i.e., the profile taken at 5 x/d is close to the jet outlet while 0.1 x/d is the profile taken closest to the impingement surface; the radial wall jet profiles increase radially from the jet axis, i.e., 1 r/d is in the near-field while 10 r/d is in the far-field. The liquid continuous-phase will be associated with the subscript "l", and subscript "p" will be used to refer to the particle dispersed-phase.

6.1 Particle Responsiveness to Turbulent Fluctuations

In fluid dynamics, the Stokes number (S_t) provides a measure of a particle's responsiveness to turbulent fluctuations within a flow. It is defined as the ratio of the particle response time to a characteristic fluid time scale,

$$S_t = \frac{\tau_p U_b}{d} \tag{6-1}$$

where U_b is the bulk exit velocity of the jet, d is the jet line diameter, and τ_p is the particle response time estimated using the following equation.

$$\tau_p = \frac{\rho_p {d_p}^2}{18\mu_l} \tag{6-2}$$

Particles typically fall into one of three categories. Particle motion coupled to the fluid motion, where particle inertia is small compared to the fluid turbulence scales, follows the fluid turbulent fluctuations and has small Stokes numbers, $S_t < 1$. In contrast, if the Stokes number is large, $S_t > 1$, particle inertia is also large and as such they are not influenced by the fluid, with their response time longer than the fluid timescale. Particle dispersion is at its greatest when the Stokes number is near unity, $S_t \approx 1$, where the particle motion is coupled to the large vortices, migrating to the margins of the eddies and dispersing further than the fluid (Hishida et al., 1992; Tang et al., 1992; Raju and Meiburg, 1995). A schematic representation of the three Stokes number classifications is shown in Figure 2-3.

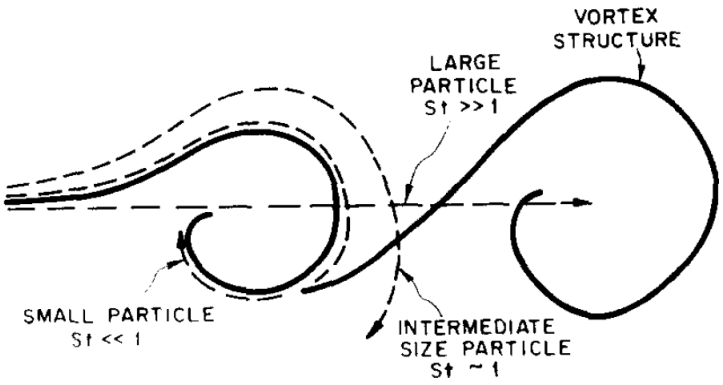

Figure 6-1 Pictorial representation of the effect of Stokes number on particle dispersion in large-scale turbulent structures (Crowe et al, 1988).

Particle Stokes numbers have been estimated, for the jet exit conditions used in this work, for all three particle sizes tested using equations(6-1) and (2-4), and are presented in Table 6-1. The Stokes numbers indicate the particles represent each of the particle dispersion categories' described. Particle 1 having S_t that is

less than 1 and hence would be expected to follow the flow fluctuations, while Particle 3 is larger than 1 and expected to not be influenced by the flow. The particles will detach from the flow, particularly if there is an abrupt deceleration as within the impingement region. Particle 2 has a Stokes number which is not significantly different from unity.

Table 6-1 Properties of test particles.

Test case	*Particle 1*	*Particle 2*	*Particle 3*
d_p (μm)	20	46	69
ρ_p (g.cm^{-3})	2.50	2.45	2.45
S_t	0.347	1.773	4.066
U_c (ms^{-1})	2.75	2.90	2.29

The mean axial jet outlet centreline velocity, U_c, supports the Stokes number assessment of the particles to some extent. Particle 1, which has St < 1, exhibits a centreline axial velocity similar to the single-phase U_c of 2.71ms^{-1}. However, although Particle 2 and Particle 3 are indeed different to the single-phase value, they would appear to either side of it. Particle 3 agrees with its Stokes number category, St > 1, and is not influenced by the fluid flow

Particle 2 however appears higher than the single-phase. Some workers (see Table 2-3 on page 26 for experimental parameters) have found for particle-laden free jets, the particle phase to exhibit higher axial velocities than the single-phase, $\overline{U}_p > \overline{U}$. This however has occurred in regions of deceleration where the particles do not decelerate as quickly, namely in the intermediate- to far- field regions of the free jet (Popper et al., 1974; Modarress et al., 1984a; Tsuji et al., 1988; Gillandt et al., 2001). The flow structure of the jet at the outlet correlates with fully developed turbulent pipe flow (Munson et al., 2002) and as such will not exhibit particle velocities larger than the single-phase.

No experimental measurement can be made without uncertainty, as is discussed in Section 3.4.6. An error of ± 5% is estimated for mean velocities in this region of the impinging jet flow and when applied to the centreline axial velocity, U_c, data in Table 6-1, the value for Particle 1 becomes 2.61 ms^{-1} and Particle 2 becomes 2.75 ms^{-1}, bringing them more in line with expectation.

6.2 Flow Region Upstream of Stagnation Point

In the following, measurement results for the developing jet and impingement region are presented for three particle-laden turbulent impinging liquid jets located six diameters above the impingement surface (h/d ratio of 6). In this section we compare the particle phase data acquired for three particle sizes; 20μm (Particle 1), 46μm (Particle 2), and 69μm (Particle 3), subscripts "1", "2" and "3" respectively.

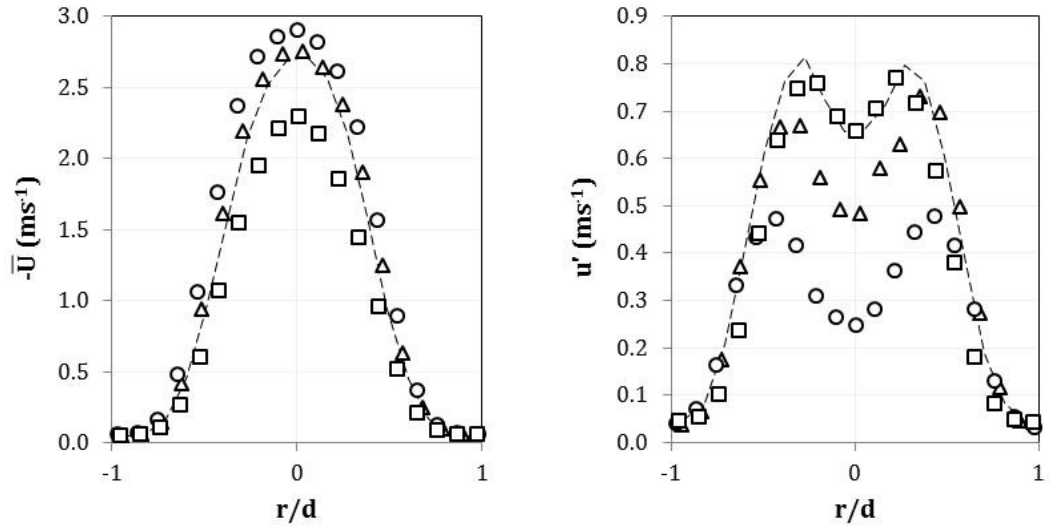

Figure 6-2 Particle size effect for turbulent impinging jet at h/d ratio of 6; axial mean and RMS fluctuating velocity 1d downstream of jet exit.

Dispersed particle phase profiles: △ Particle 1, ○ Particle 2, □ Particle 3. Plus single phase profile (- - -).

Axial mean ($\overline{U}$) and RMS fluctuating velocity (u') distributions at 1d from the jet outlet (5 x/d) are presented for the particle and single phases in Figure 6-2. The particle velocities of the multi-phase jet explored for each of the particles tested show good flow symmetry about the jet axis.

As predicted from the Stokes numbers given in Table 6-1, the axial mean velocity distribution for Particle 3 (S_t = 4.066) is lagging behind the single-phase, concurrent with the expectation of particles with larger Stokes numbers (S_t >1) having a relatively low responsiveness to the fluid flow. These particles were used in the acquisition of the data already discussed in Chapter 5; the particle phase velocity near the jet outlet was around 80% of the single-phase value, in agreement with the experimental work on free jets of Tsuji et al. (1988) and Gillandt et al. (2001). As the Stokes number increases from 1 to 10, particle dispersion decreases since the particles struggle to follow the fluid flow because of their large inertia. For St > 4, the particles move independently of

the turbulent motion of the carrier-phase (Hishida et al., 1992). The reduction in the spreading rate of the jet is attributed to momentum transfer from the particles to the continuous-phase, and turbulence modulation caused by the particles (Yoshida et al., 1990). The presence of particles also causes an increase in the dissipation rate of energy.

Taking into consideration the experimental uncertainty estimated for the system, the velocity distribution of Particle 2 (S_t = 1.773) appearing to be greater than the single-phase is within the experimental error of ± 5% as noted above. The broadened shape of the velocity profile is indicated by a Stokes numbers near unity, where the particles couple to the motion of the larger vortices, migrating to the margins of the eddies and dispersing further than the fluid (Figure 6-2, left).

The smallest particle size tested, Particle 1, has a velocity distribution similar to the single-phase, appearing marginally higher but is again within the experimental error of the system. According to the Stokes number (S_t < 1), these particles should follow the fluid flow, which they basically almost do. Hishida et al. (1992) found for 0.5 < S_t < 2.5, particles disperse more significantly than the fluid phase. The Stokes number for Particle 1 is 0.347 which is less than one but is also not far from the lower limit of the range described by Hishida et al. (1992).

The root-mean-square of the fluctuating velocities present the reverse order for the particle sizes from the mean axial velocity values. In ascending order; Particle 2 (46μm) exhibits the lowest turbulent velocity, followed by Particle 1 (20μm) and finally Particle 3 (69μm). Each distribution has the same shape, following the single-phase profile until each local maximum is reached where velocity fluctuations are stronger than within the potential core, hence the decrease towards the jet centreline. The location of the peaks is dictated by the development of the turbulent shear layer and can be considered to be located at the centre of the shear layer. Velocity gradients near the jet outlet are lower for particle-laden flows and therefore turbulence production in the shear layer is reduced.

Particle 2 exhibits the lowest turbulent velocities, with a centreline ($u'_{c,p2}$) magnitude 0.41ms^{-1} less than the single-phase centreline ($u'_{c,l}$) turbulent velocity. These particles are coupled to the motion of the larger, slower eddies as they are migrate further than the fluid. The centreline turbulent velocity of Particle 1 ($u'_{c,p1}$) is 0.18ms^{-1} greater than Particle 2, but still less than that of the single-phase. This is consistent with this particle size (20μm) sitting between two of the particle dispersion categories according to its Stokes

number; suggesting this particle size, near the jet exit, is partly following the fluid flow and partly coupling to the large vortices. And Particle 3 exhibits the greatest turbulent velocities which are similar to the single-phase.

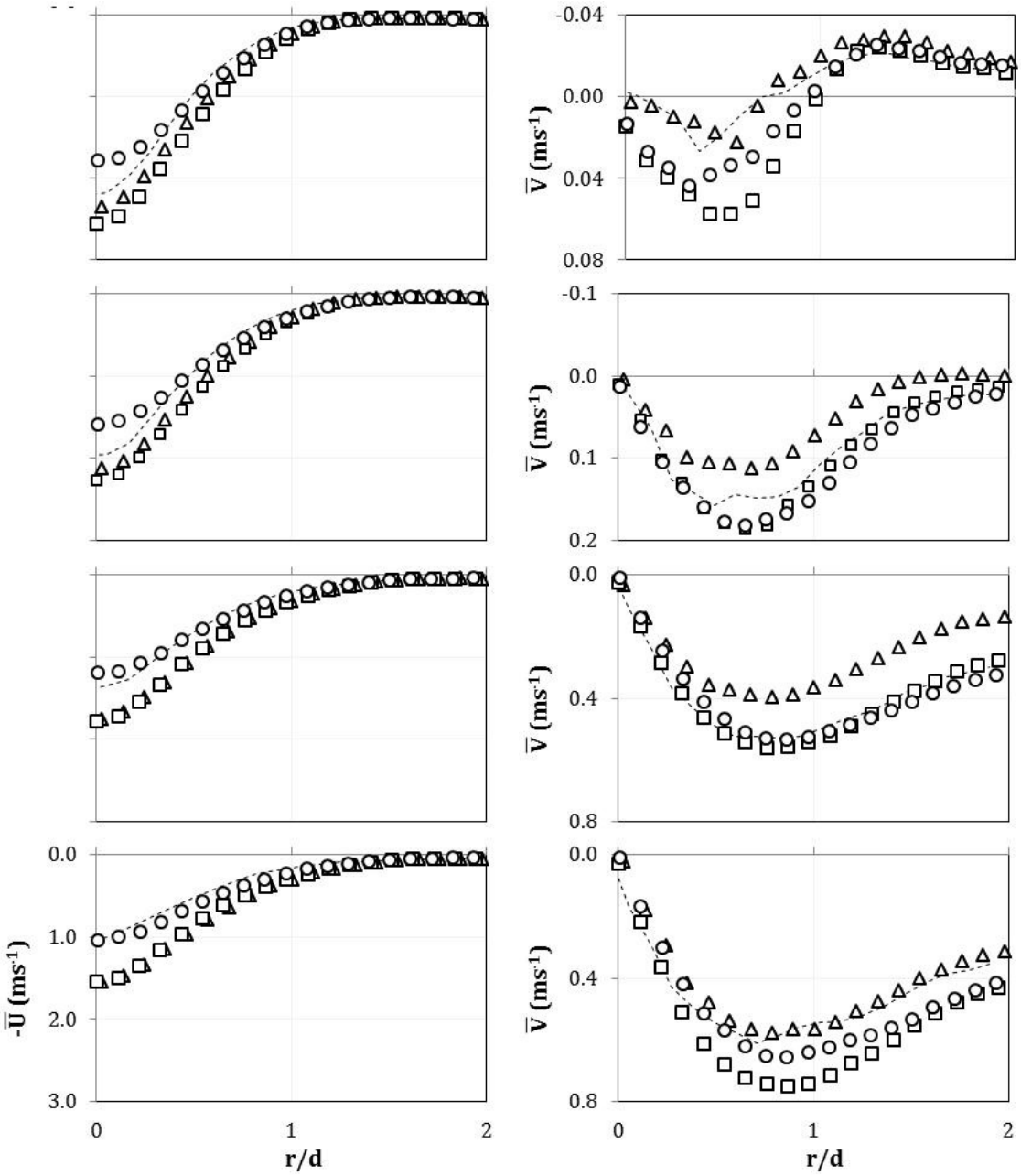

Figure 6-3 Particle size effect on turbulent impinging jet flow at h/d ratio of 6; axial and radial mean velocity within 1d of the impingement surface.

Dispersed particle phase profiles: △ Particle 1, ○ Particle 2, □ Particle 3. Plus single phase profile (- - -).

Particle phase mean velocities (Figure 6-3) follow similar trends at all transverse locations for each of the three particle sizes, i.e., the axial velocity

decays as the impingement surface is approached while the radial component grows.

There has been a change in the particle axial component of velocity, $\overline{U}_p$, from the profiles taken close to the jet outlet at 5 x/d, i.e., the order of magnitude has reversed. At 1 x/d (top plots), the axial velocity for each particle phase tested is now, in descending order: Particle 3 (69μm), Particle 1 (20μm) and then Particle 2 (46μm). The intermediate particle size, Particle 2, remains below the single-phase until the final transverse profile taken 0.1d from the impingement surface, where it marginally exceeds the single-phase. The smallest (Particle 1) and largest (Particle 3) particles remain at a higher velocity than Particle 2 and the single-phase as the wall is approached. Initially, Particle 3 is marginally higher than Particle 1 at 1 and 0.5 x/d, aligning at 0.2 and 0.1 x/d.

In the stagnation region, while the single-phase axial velocity decreases rapidly as the wall is reached, the particle phase typically does not decelerate as rapidly due to inertia. The modification to the turbulence field within the stagnation region, due to the pressure gradient exerted by the wall, does not influence the particle phase as significantly as it does the single-phase, with the particle momentum being sufficient to dominate until the wall is reached. This is true for the smallest and largest particle sizes tested here, Particle 1 and Particle 3 respectively. Particle 2, on the other hand, exhibits a lower axial velocity than both particles as well as the single-phase. In the jet outlet region this particle was coupling to the motion of the large vortices and dispersing further than the single-phase. The greater the dispersion of particles within the developing free jet, the more rapid the decay in centreline axial velocity as distance from the jet outlet (x) increases. When these particles reach the impingement region their velocity is already lower than the single-phase, as seen in Figure 6-3. Both Yoshida et al. (1990) and Longmire and Anderson (2003) found particles of 15 to 49μm in diameter to rebound up to 2.5d back upwards in to the oncoming approaching jet. This phenomenon would be difficult to detect using particle image velocimetry (PIV) as is employed within this work. The principle behind the PIV is not particle tracking but rather cross-correlates the cluster displacement of optimally six particles (Chapter 3). So individual particles rebounding off the impingement plate and travelling back up into the oncoming flow would be essentially lost in the measurement. Yoshida et a. (1990) used laser Doppler anemometry (LDA) which is a single-point measurement and would be capable of capturing this phenomenon. Although Longmire and Anderson (2003) used PIV they did not appear to use it in the same manner as undertaken within this work, rather they appear to have used it only for its

imaging capability rather than applying cross-correlations to attain velocity vector data.

Growth of the radial mean velocity shows a different trend. Instead of Particle 2, the intermediate particle size tested, having the lowest velocity, sits between the other particle sizes. As the particle size increases, the radial mean velocity local maximum ($V_{m,p}$) increases. As the impingement surface is approached, at 0.5 and 0.2 x/d the larger two particles', 46 and 69μm, $V_{m,p}$ values come together before diverging again close to the wall. Entrainment from the surrounding fluid can be seen as r increases from 1d in the radial velocity plot at 1 x/d (Figure 6-3, top left). And the initial radial wall jet development can be seen at the same distance from the jet axis at 0.1 and 0.2 x/d (the two bottom left plots).

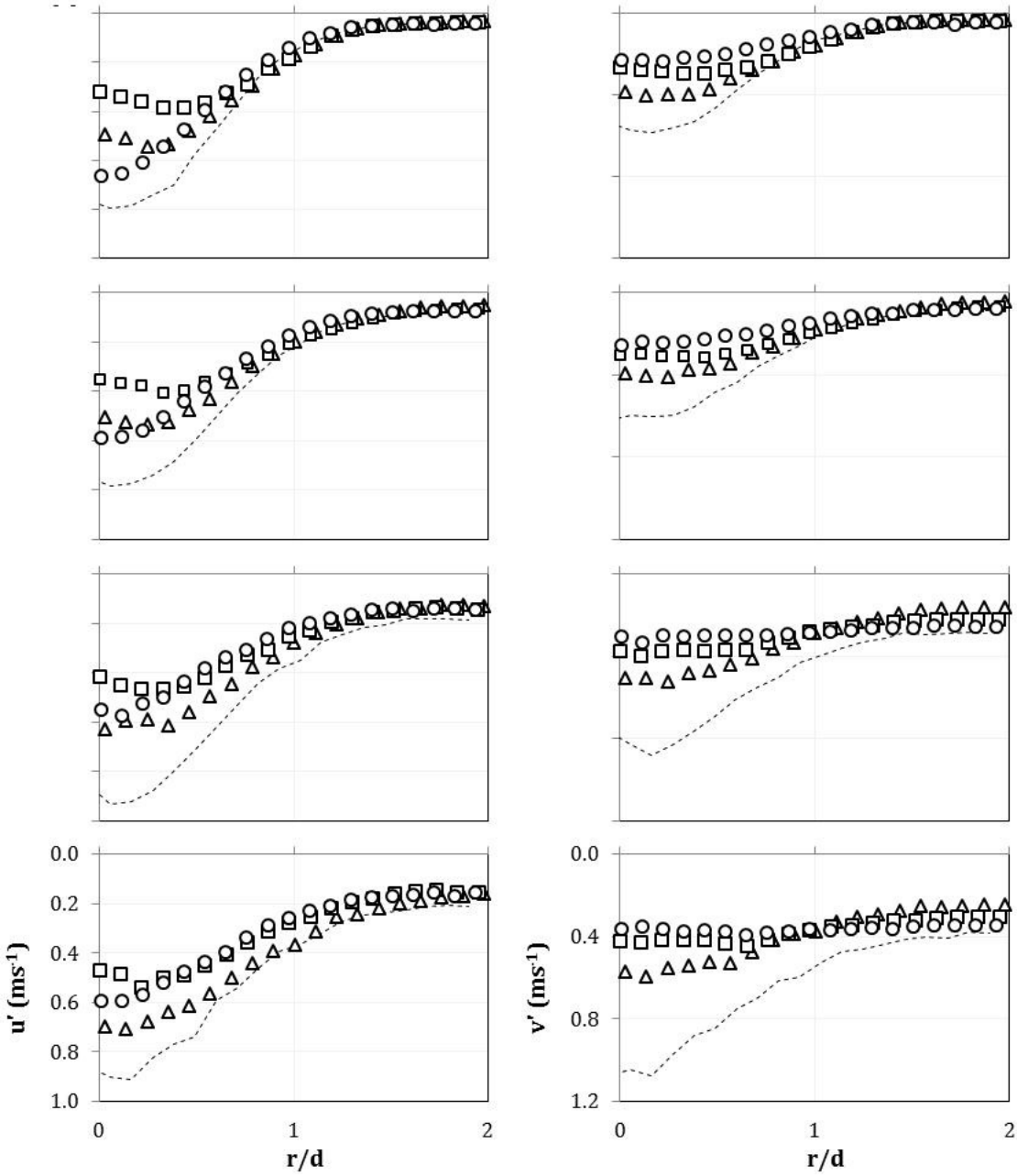

Figure 6-4 Particle size effect on turbulent impinging jet flow at h/d ratio of 6; axial and radial RMS fluctuating velocity within 1d of the impingement surface.

Dispersed particle phase profiles: △ Particle 1, ○ Particle 2, □ Particle 3. Plus single phase profile (- - -).

Axial and radial RMS fluctuating velocities have been calculated and are presented in Figure 6-4. All three particle phases exhibit considerably lower turbulent velocities relative to their single phase equivalent.

The axial turbulent velocity trend across the particle sizes at 1 and 0.5d from the impingement surface is the reverse of that seen near the jet outlet. Two of the particles, Particle 1 (20μm) and Particle 3 (69μm), still have a hint of the peak at the centre of the shear layer within the impingement region. The peak

persists for Particle 3 for all four profiles taken within 1d of the impingement surface up to and including 0.1 x/d, with the location of the peak moving towards the jet axis as the wall is approached. Only the Particle 2 position relative to Particle 1 and Particle 3 changes as the wall is approached. Within 1d of the impingement surface, the smallest axial turbulent velocity is exhibited by Particle 3, followed by Particle 1, and are both exceeded by Particle 2. Particle 1 remains larger than Particle 3 throughout this region. At 1 x/d, the turbulent velocity of Particle 2 is larger than the other particles and remains so at 0.5 x/d. At 0.2 and 0.1d from the wall it has reduced so it sits between the other two particles.

The centreline axial velocity $u'_{c,p3}$ and $u'_{c,p1}$ increases as r decreases, yet $u'_{c,p2}$ decreases as the wall is approached. The radial RMS fluctuating velocity varies between the three particles tested; Particle 2 (45μm) this time being the lowest, followed by Particle 3 (69μm) and then Particle 1 (20μm) exhibiting the largest. As the impingement surface is approached, the magnitude marginally increases for all particles, with the single-phase increasing more rapidly.

Reynolds shear stress data, Figure 6-5, goes through zero at the jet axis as expected, growing to a maximum value as it moves away from the jet axis. This is true for all profiles within 1d of the impingement surface except the one closest the wall at 0.1 x/d. The increase in disorder in these particle phase shear stress data may be due to increased anisotropy, amplified by the fluid-particle interactions near the wall, or lack of sample as discussed below. As the wall is approached, the shear stress data becomes increasing erratic. The level of disorder is least for Particle 2 which we have already deemed to have entered the impingement region with less momentum due to its greater dispersion within the developing region of the approaching jet. The largest particle, Particle 3, is approaching the impingement surface with the greatest inertia and it is likely that there may be particles rebounding from the wall, as seen by Yoshida et al. (1990) and Longmire and Anderson (2003).

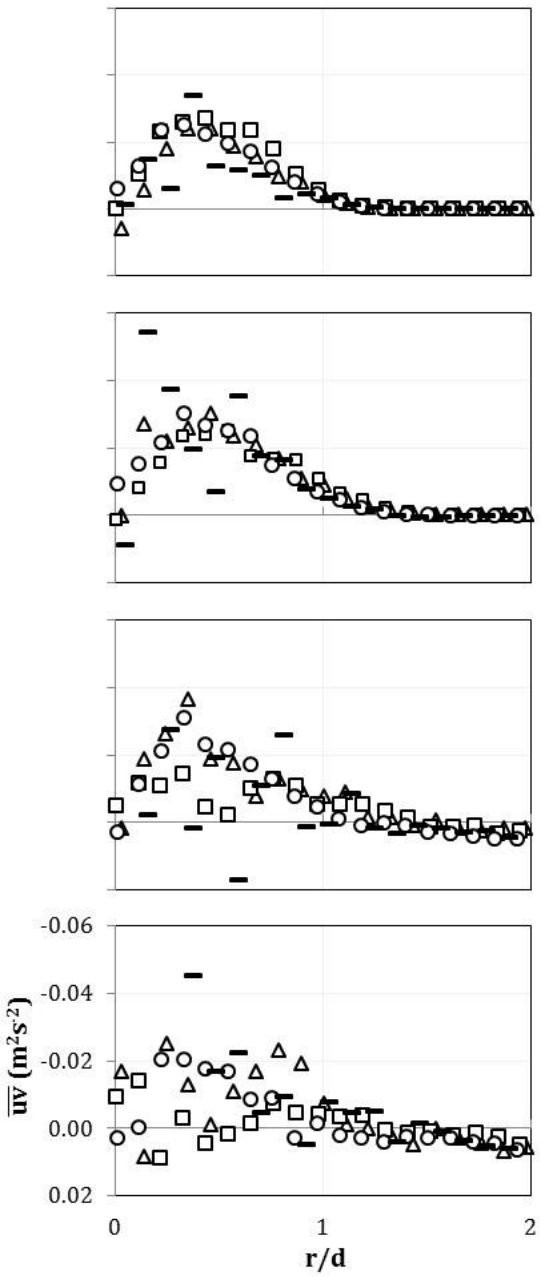

Figure 6-5 Particle size effect for turbulent impinging jet at h/d ratio of 6; Reynolds shear stress within 1d of the impingement surface.

Dispersed particle phase profiles: △ Particle 1, ○ Particle 2, □ Particle 3. Plus single phase profile (—).

The rebounding of particles has not been directly observed during the trials discussed here. The measurement approach of particle image velocimetry (PIV) determines the displacement of a number of particles within an interrogation area, IA. For a given time step a velocity vector is generated for that small measurement area, and individual particles are not tracked. So, for example, if four particles are detected within an IA, and three have displacements towards the impingement surface and the remaining one particle in the opposite direction (assuming displacements of the same magnitude), the resultant

velocity vector would be towards the impingement surface. Considering the different statistical treatments applied, the calculation of Reynolds shear stress would be most sensitive to variations in the data, more so than the arithmetic mean ($\overline{U}$ and $\overline{V}$) or root-mean-square calculation of the fluctuating component of velocity (u' and v').

Capturing the velocity gradients present in an impinging jet is experimentally very challenging, complicated further when attempting to measure multi-phase flow, hence why so little data is currently available in the literature (see Table 2-5 on page 34). The velocity range extends from the jet outlet axial centreline velocity (up to 2.75ms^{-1} for Particle 2 in this case) down to the stagnation point where the liquid-phase velocity is zero. This is an incredibly large range to measure, particularly with a single measurement technique. Particles tend to concentrate in zones of deceleration such as in the vicinity of the stagnation point, where the carrier phase is stagnant (Longmire and Anderson, 2003). Development work was undertaken to assess the appropriate number of time steps during data acquisition necessary in the experimental study of an impinging jet. The outcome of this development informed the selection of the number of time steps used throughout this programme of study. It is now considered that within the immediate vicinity of the impingement surface only, and in particular for the calculation of Reynolds shear stress from the instantaneous velocity vector data, a larger number of time steps may be advantageous in the estimation of the Reynolds shear stress near the impingement surface.

6.3 Flow Region Downstream of Stagnation Point

In the following, measurement results for the near- and far-field radial wall jet are presented for three particle-laden turbulent impinging liquid jets located six diameters above the impingement surface (h/d ratio of 6). The stagnation region deflects the impinging jet radially, first undergoing deflection and acceleration in the near-field, followed by radial spreading and deceleration in the far-field wall jet. In this section, we continue our comparison of the particle phase data acquired for three particle sizes; 20μm (Particle 1), 46μm (Particle 2), and 69μm (Particle 3), subscripts "1", "2" and "3" respectively.

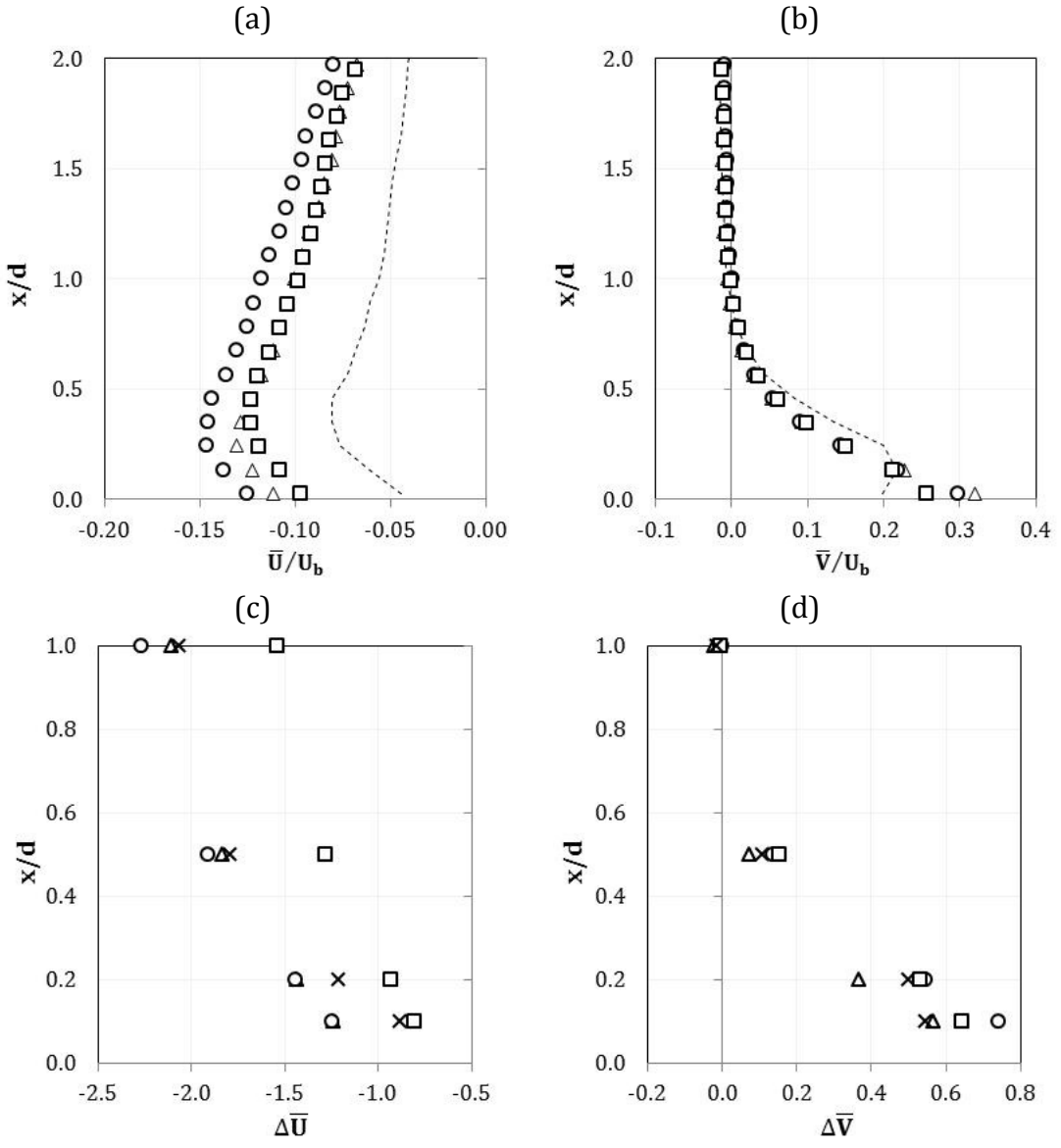

Figure 6-6 Profiles of normalised (a) axial and (b) radial mean velocity at r/d = 1, and difference in (c) axial and (d) radial mean velocity between 1 r/d and the jet centreline at 0 r/d; particle size effect.

Dispersed particle phase profiles: △ Particle 1, ○ Particle 2, □ Particle 3. Plus single phase profile (- - - or ×).

The axial and radial velocity evolution (normalised by the bulk axial outlet velocity, U_b) in the near-field wall jet for all three particles are presented in Figure 6-6 (and Figure 6-7 below). The impinging jet undergoes significant deceleration as it progresses through the impingement region, due to the pressure reflections normal to the wall modifying the distribution of turbulence energy in the vicinity of the impingement surface.

As discussed earlier in this thesis, the single-phase is more susceptible to the influence of the wall than the dispersed particles, the large inertia of the particles effectively limiting the influence of the wall, decelerating only due to drag interactions. Figure 6-6(c) and (d) show the drop in axial velocity and increase in radial velocity between 0 (the jet centreline) and 1 r/d (radial distance of one diameter from the jet centreline) within one diameter of the impingement surface, $\Delta\overline{U}$ and $\Delta\overline{V}$ respectively. There is a spread in $\Delta\overline{U}$ between the test particles, with the single-phase sitting between them. Close to the impingement surface at 0.1 x/d, the largest particle, Particle 3, exhibits the smallest $\Delta\overline{U}$ between these radial positions, as the flow moves one diameter downstream of the jet centreline. These larger particles, as we have already seen in Figure 6-2, are only weakly influenced by the fluid phase and are more resistant to losing momentum. Particles that rebound at the wall move upward into the oncoming flow and are turned downward again and accelerated outward (Longmire and Anderson, 2003), all test particles exceeding the single-phase mean axial velocity as seen in Figure 6-6(a). There is a small difference in the downward axial velocity between the test particles with Particle 2 (46μm) having a slightly larger magnitude than the other two cases. The position of the inflection, a little closer to the impingement surface than the radial wall jet boundary, is at the same location for all profiles, including the single-phase. With increasing distance from the impingement surface up to 1d, the spread in $\Delta\overline{U}$ between the particles grows as the magnitude of the velocity drop increases. The height of the radial wall jet at this radial station of 1 r/d is around 0.8d, above this position the $\Delta\overline{U}$ is large because the entrainment velocities are considerably smaller than within the radial wall jet, Figure 6-6(c).

For the radial mean velocity of the particle phase, $\overline{V}_p$, within the wall jet, with the exception of the two data points closest to the wall (Figure 6-6(b)), the particle velocities are lower than for the single-phase as particles initially have no momentum in the r-direction. The particle phase radial velocity profiles do not display the local maximum, V_m, seen for the single-phase. This is due to the liquid-phase being subject to the no-slip condition at the wall while the particle phase is not. The magnitude of $\overline{V}_p$ near the wall is larger than for the single-

phase, and this is in contrast to the findings of Yoshida et al. (1990). They found, in the lower region of the radial wall jet, that the particles lagged behind the gas-phase, while in the upper region the particle phase overtook the single phase with the difference increasing as radial distance from the jet axis grew to 4 r/d.

Within the developing radial wall jet, $\overline{V}_p$ for all of the test particles align except at the data point closest to the wall where they increase with decreasing particle size, Figure 6-6(b), i.e., Particle 1 has the largest radial velocity, then Particle 2, followed by Particle 3 which has the smallest. For a particle-laden pipe flow (Rizk and Elghobashi, 1989), as particle size increases, the mean velocity parallel to the wall decreases. This effect is attributed to the inter-phase surface area acted on by viscous drag. For the same solid loading ratio, as is the case for these trials, the surface area for Particle 1 (20μm) is nearly 2.5 times that of Particle 2 (46μm), which is in turn 1.5 times Particle 3 (69μm).

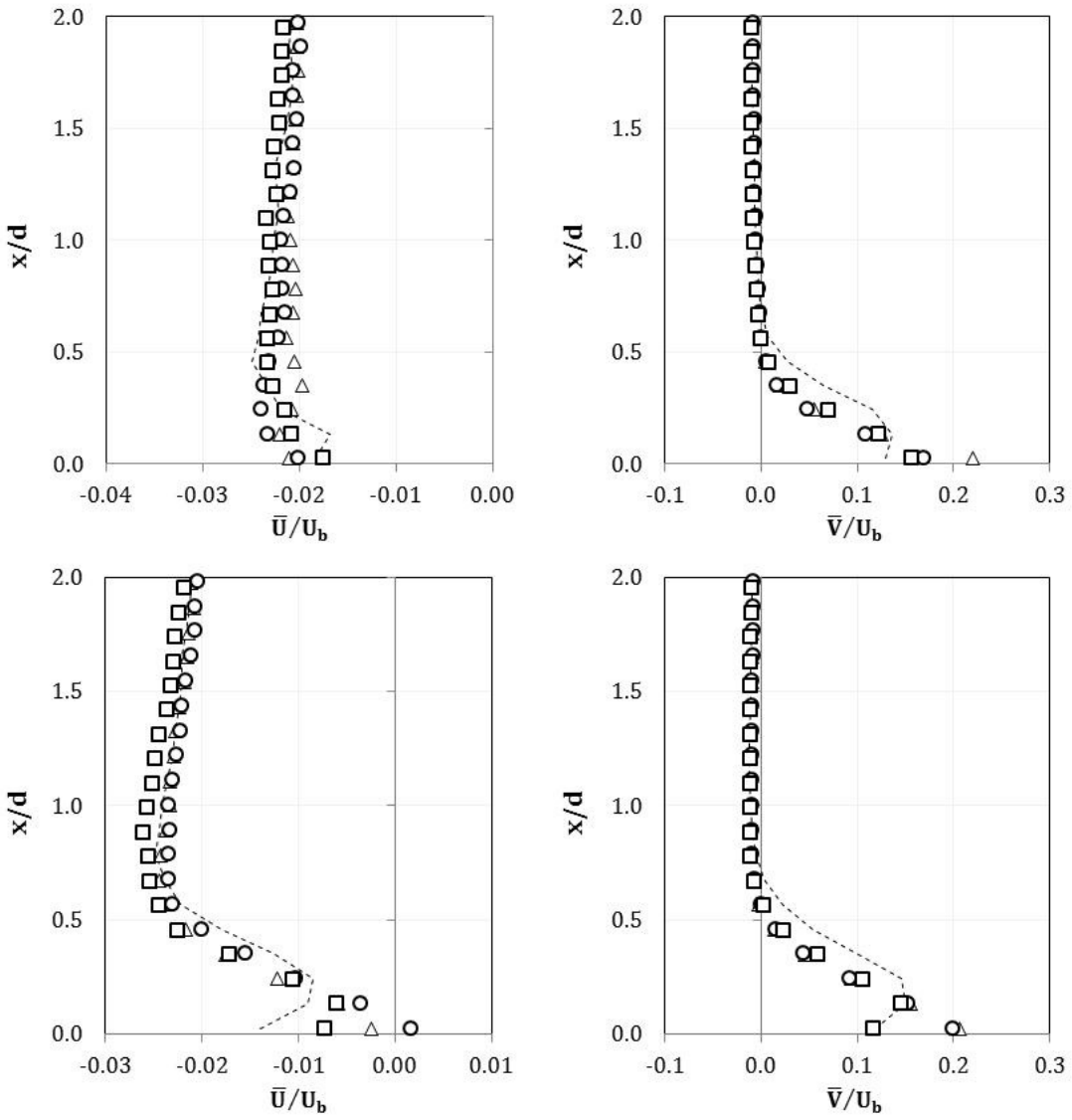

Figure 6-7 Profiles of normalised axial and radial mean velocity across the near-field radial wall jet at r/d = 2 (top), and 4 (bottom); particle size effect.

Dispersed particle phase profiles: △ Particle 1, ○ Particle 2, □ Particle 3. Plus single phase profile (- - -).

As the near-field radial wall jet progresses to two and four diameters from the jet centreline, the axial velocity drops quite considerably, Figure 6-7. At 2 r/d, there is little change in the axial velocity within 2d of the wall. The particle flow at this position only shows variation for the radial velocity which is very similar to the radial velocity at r = 1d with marginally smaller magnitude. The same small separation is seen for the data point closest to the impingement surface.

The radial velocity profile at 4rd is again similar as the rest of the near-field wall jet with a slight decrease in magnitude. The key difference in this case is that a local maximum (V_m) is seen for Particle 3, matching the value of the single-phase in the lower part of the wall jet attributed to the attenuation of the

liquid-solid interaction. The other particles continue to increase as the wall is reached. In the upper part of the wall jet, all three particles align and are lower than the single-phase, as earlier in the near-field. In the upper shear layer of the wall jet, the single-phase radial and axial velocity are marginally higher than for the particle phases. The particle axial velocities are larger than for the single-phase in the lower shear layer, again showing the same variation closest to the impingement surface, Particle 2 (46μm) showing the first indication of upwards expansion.

Overall, as the distance r from the jet axis increases there is a slight deceleration of the radial velocity component. moving from 1 to 4r/d, but less deceleration is seen for the single-phase.

The particle turbulent velocities in the wall jet (at 1, 2 and 4rd) are all lower than for the single-phase, except in the lower shear layer at 1rd for Particle 1 (u'_{p1}) at the wall, Figure 6-8. As the distance r increases from 1 to 2 diameters from the jet axis, u'_p undergoes a drop by up to half within the radial wall jet as it is no longer experiencing the residual effect of the approaching impinging jet. This is then followed by a small increase at 4 r/d as in the near-field.

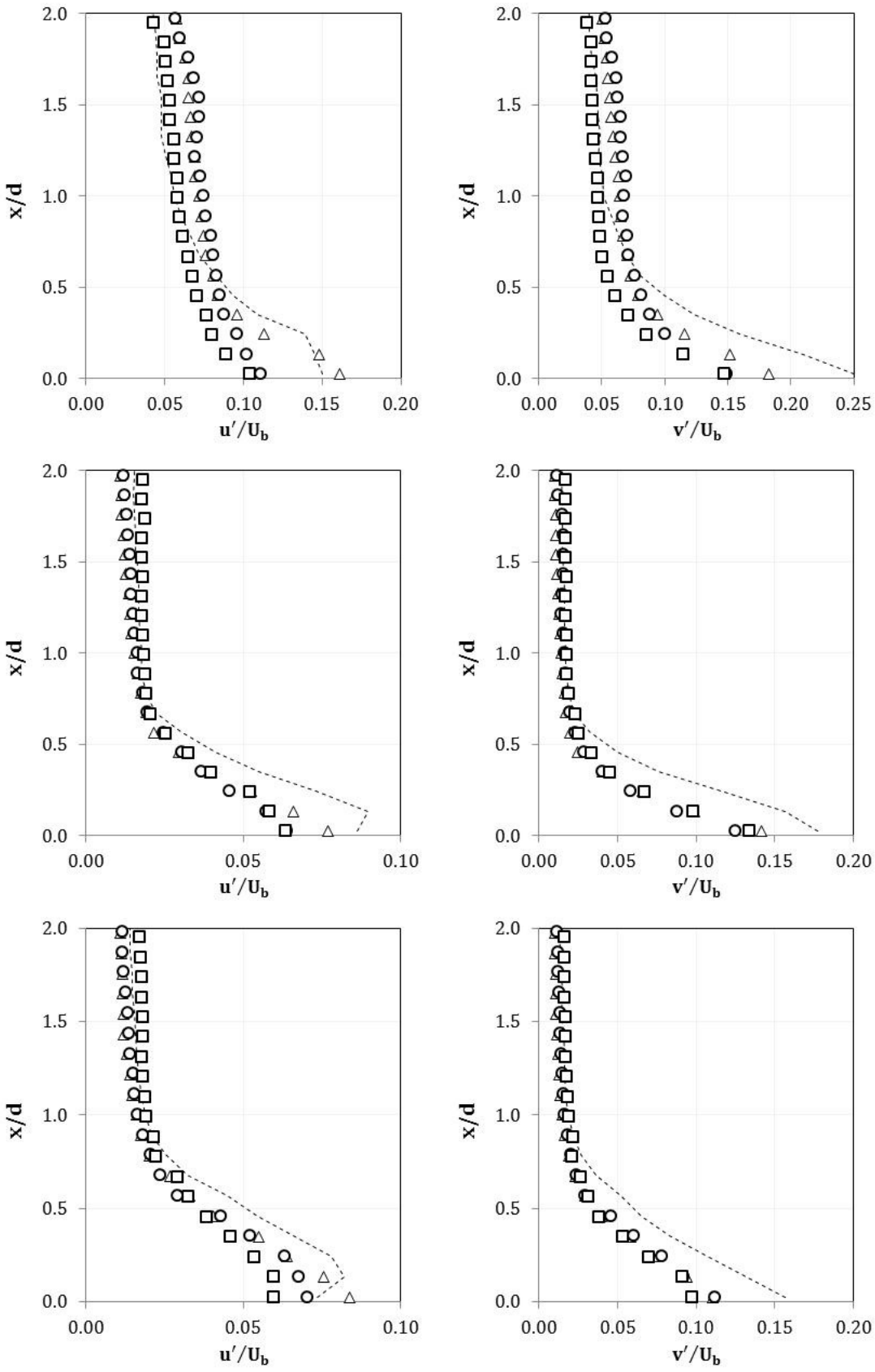

Figure 6-8 Profiles of normalised axial and radial RMS fluctuating velocity across the near-field radial wall jet at r/d = 1 (top), 2 (middle), and 4 (bottom); particle size effect.

Dispersed particle phase profiles: △ Particle 1, ○ Particle 2, □ Particle 3. Plus single phase profile (- - -).

The particle radial fluctuating velocities are greater than the axial components. The decay rate of v' increases as distance from the jet axis grows. There is little variation between the particles tested, the difference decreasing with increasing distance from the jet centreline. The greatest difference is seen in the entrainment region at 1r/d, where Particle 3 has a slightly lower turbulent velocity than the other 2 particles.

As we move away from the jet axis, in the entrainment region, the larger the particle the higher the entrainment turbulent velocity, both axial and radial.

This section of the thesis provides the RMS fluctuating velocity normal to the wall, u', which is important in the assessment of heat transfer. However, to date, no such data have been published by other workers, presumably due to measurement quality difficulties near the wall, as described by Yoshida et al. (1990) who reported poor quality LDA signals prevented the acquisition of such data for a particle-laden impinging plane jet.

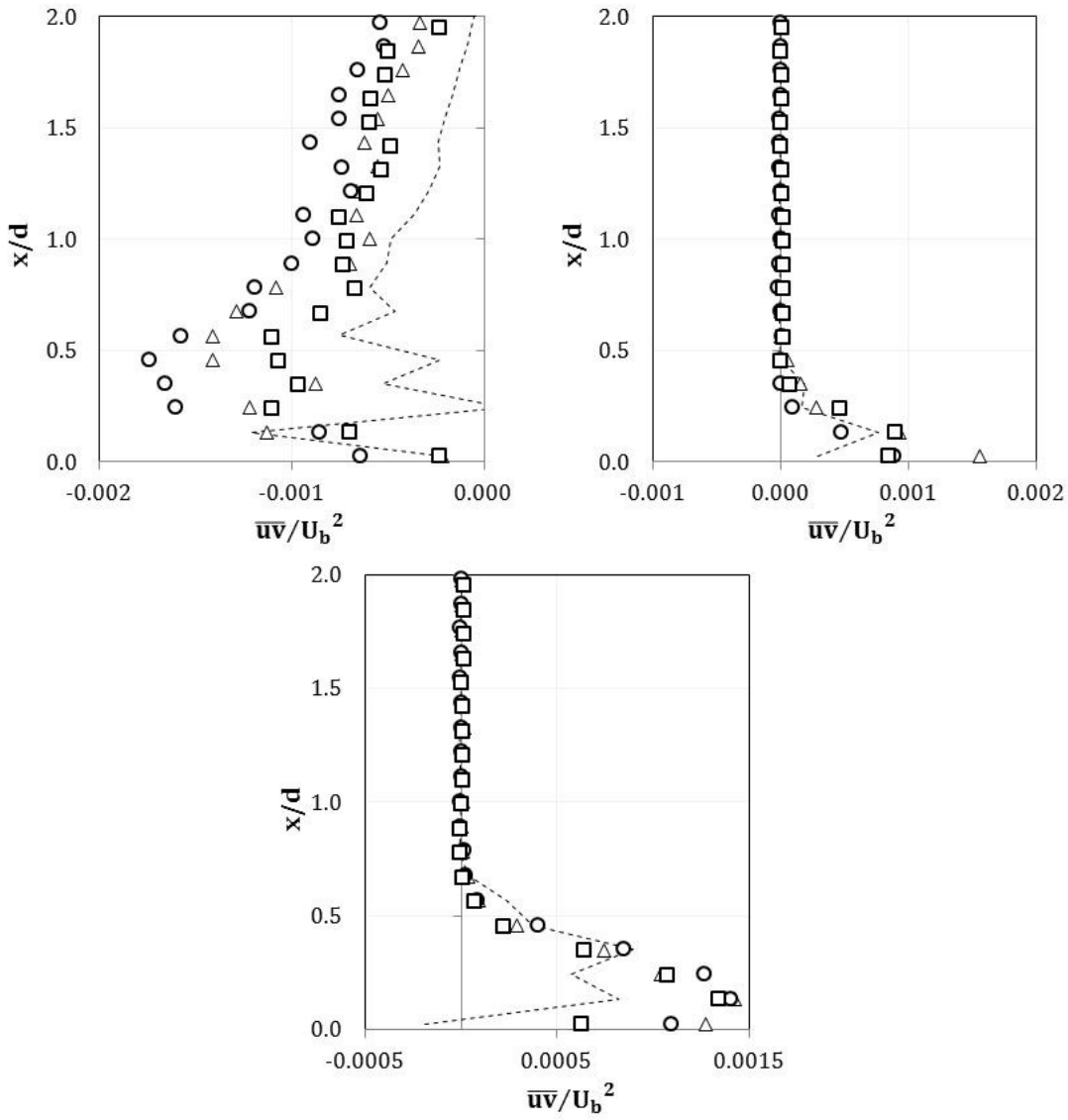

Figure 6-9 Profiles of normalised Reynolds shear stress across the near-field radial wall jet at r/d = 1 (top left), 2 (top right), and 4 (bottom); particle size effect.

Dispersed particle phase profiles: △ Particle 1, ○ Particle 2, □ Particle 3. Plus single phase profile (- - -).

As noted above, accurate measurement of the radial component of the instantaneous velocity has so far been unachievable (Yoshida et al., 1990), and the calculation of Reynolds shear stresses has not been performed. Here, we present particle Reynolds shear stress for all three test particles, Figure 6-9.

Shear stress increases from 1r/d to 2r/d, then decreases at 4r/d as the jet is radially spreading and decelerating. At 1r/d, we are likely capturing the inhomogeneous turbulent/non-turbulent interface which is continuously changing, considered to be accountable for the 'un-smooth' profile. The measurement of this interface is incredibly difficult because it is so changeable

and is why half-widths are typically reported as this can be more reliably measured (Westerweel et al., 2005).

The shear layers in the wall jet are much more evident for the particle phase data at 4r/d due to the scale of the phenomena and the resolution of the PIV measurements made, the local maximum coinciding with V_m.

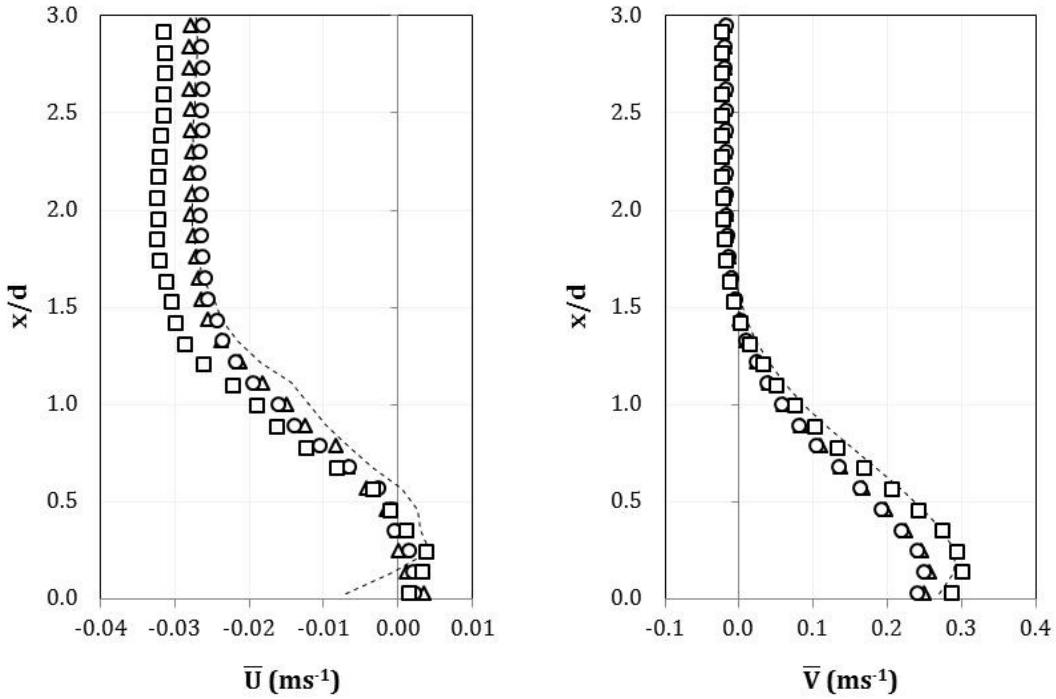

Figure 6-10 Axial and radial mean velocity within the far-field wall jet, r/d = 10; particle size effect.

Dispersed particle phase profiles: △ Particle 1, ○ Particle 2, □ Particle 3. Plus single phase profile (- - -).

Deceleration in the radial wall jet from the near- to far-field can be seen by comparing Figure 6-7 and Figure 6-10.

The axial velocity in the lower shear layer of the radial wall jet shows a small upward flow, due to wall jet expansion, Figure 6-10. The local maximum, U_m, seen for the single-phase case is not evident here as the particle phases are not subject to the no-slip condition at the wall, although at this vertical distance from the impingement surface the value of radial velocity for the three particle phases is the same as for the single-phase. Above this vertical position, the axial velocity is negative and increasing in magnitude through the upper shear layer, until the upper boundary is breached. The largest difference in the particle axial velocity, for the three test particles, is above the wall jet where for Particle 3 the downward entrainment velocity is largest.

Radially, Particle 3 follows the single-phase profile, while Particle 1 and Particle 2 are lower and are of the same magnitude, with each showing a local maximum and a small negative $\overline{V}$ above the wall jet. The vertical position of U_m and V_m are the same, as is the location of the upper boundary where both the axial and radial velocities asymptote to small non-zero values in the large scale re-circulation zone.

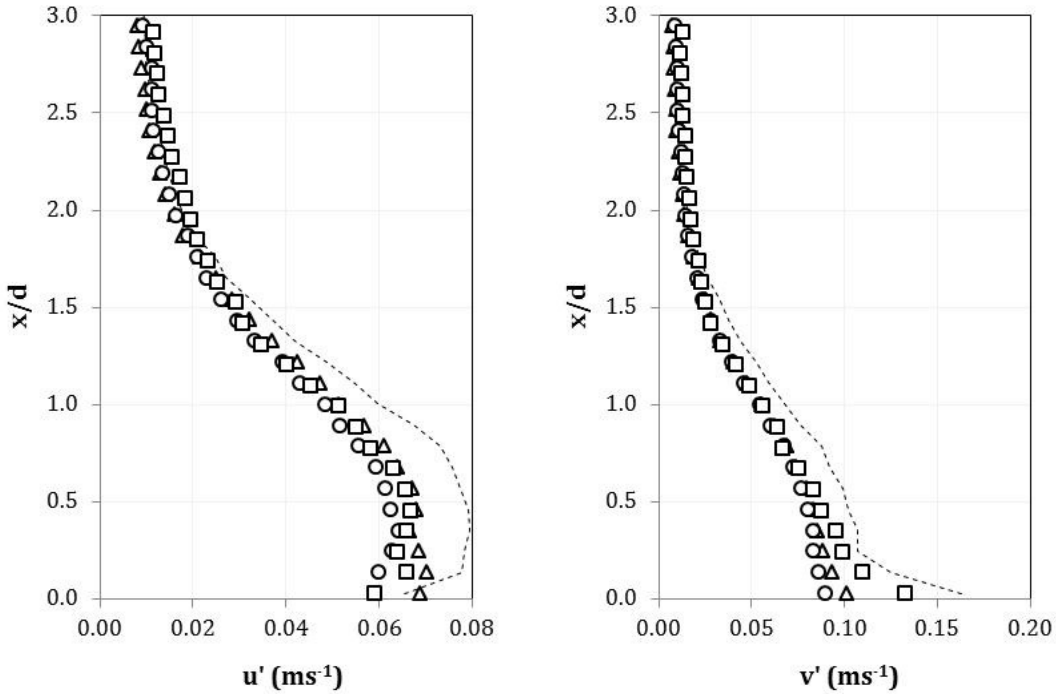

Figure 6-11 Axial and radial RMS fluctuating velocity within the far-field wall jet, r/d = 10; particle size effect.

Dispersed particle phase profiles: △ Particle 1, ○ Particle 2, □ Particle 3. Plus single phase profile (- - -).

The RMS of the fluctuating velocities in the far-field radial wall jet are lower than for the single-phase (Figure 6-11), as was also seen in the near-field. There is little difference between the test particles except in the lower shear layer of the wall jet. Again, Particle 1 has a marginally larger axial turbulent velocity than the other 2 particles, which are similar and parallel to the impingement surface, with Particle 3 exhibiting the largest radial turbulent velocity. It may be noted that the radial turbulent velocity is greater than the axial component.

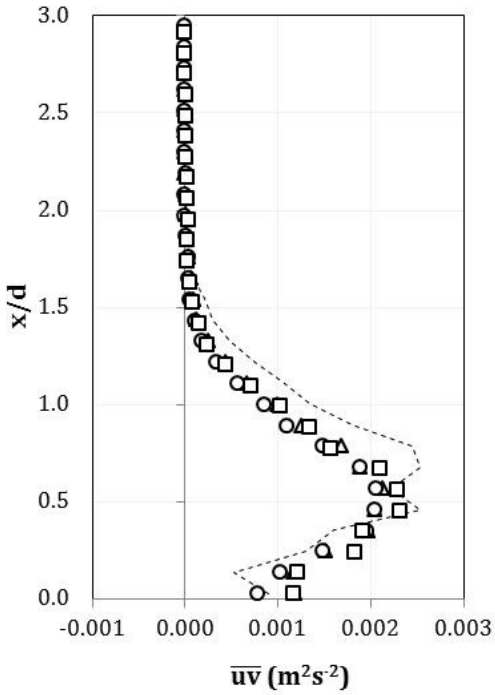

Figure 6-12 Reynolds shear stress within the far-field wall jet, r/d = 10; particle size effect.

Dispersed particle phase profiles: △ Particle 1, ○ Particle 2, □ Particle 3. Plus single phase profile (- - -).

Figure 6-12 presents the Reynolds shear stress in the far-field wall jet displaying little difference between the particles tested. There is good agreement with the single-phase, the local maximum seen at 0.5 x/d, for all three particles, coincides with u'_m; both are around 0.3d above the radial velocity peak (V_m).

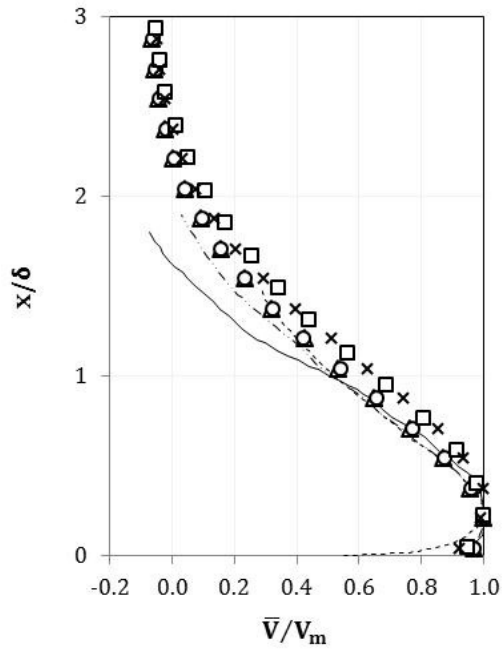

Figure 6-13 Normalised radial mean velocity in the self-similar, far-field region at h/d ratio of 6; particle size effect.

Dispersed particle phase profiles: △ Particle 1, ○ Particle 2, □ Particle 3. Liquid impinging jet data: × Present single-phase data (6 h/d). Plus gas impinging jet data: ---- Poreh et al. (1967), —·· — Dianat et al. (1996), and — Fairweather and Hargrave (2002).

In Figure 6-13, radial velocity data for the far-field wall jet at radial distances of r = 10d has been non-dimensionalised by the peak mean radial, V_m, and the velocity half-width, δ. All three particle sizes are presented and have each achieved self-similarity, and are in good qualitative agreement with the results of previous workers (Poreh et al., 1967; Dianat et al., 1996; Fairweather and Hargrave, 2002).

6.4 Chapter Conclusions

This chapter has presented a sensitivity study of the particle size effect on a particle-laden impinging liquid jet. Velocity field measurements were made using particle image velocimetry (PIV) to explore the turbulent flow characteristics of three particle sizes (mean diameters of 20, 46 and 69μm) at a jet-to-plate separation of 6d. The key conclusions drawn are outlined below.

Near the jet outlet, the mean axial velocity, $\overline{U}_p$, in the developing jet for each of the test particles support the Stokes number assessment to some extent;

- The largest particle, Particle 3 with a mean diameter of 69μm, was found to lag around behind the single-phase results, in line with the large Stokes number of 4.066. Particles with Stokes numbers greater than one (St >1) are said to have a relatively low responsivity to the fluid flow. The particle-phase velocity near the jet outlet was around 80% of the single-phase value, in good agreement with experimental work on free jets by Tsuji et al. (1988) and Gillandt et al. (2001).
- The velocity distribution profile of Particle 2 (St = 1.773) is broader than the single-phase, consistent with behaviour described by a Stokes number near unity (St ≈ 1), where the particles couple to the motion of the larger vortices, migrating to the margins of the eddies and dispersing further than the fluid.
- The smallest particle size tested, Particle 1, has a velocity distribution similar to the single-phase. According to the Stokes number (St < 1), these particles should follow the fluid flow, which they basically do. Hishida et al. (1992) found that for 0.5 < St < 2.5, particles disperse more significantly than the fluid phase. The Stokes number for Particle 1 is 0.347 which is of course less than one but also not far from the lower limit of the above range.

In the impingement region, within one diameter of the wall:

- The particle phase typically does not decelerate as rapidly as the single-phase due to particle inertia. The modification to the turbulence field within the stagnation region, due to the pressure reflections caused by the wall, does not influence the particle phase as significantly as it does the single-phase, with the particle momentum being sufficient to dominate until the wall is reached. This is true for the smallest and largest particle sizes tested here, Particle 1 (20μm) and Particle 3 (69μm) respectively. Particle 2 (46μm), on the other hand, exhibits a lower axial velocity than both particles as well as the single-phase. In the jet outlet

region this particle was coupling to the motion of the large vortices and dispersing further than the single-phase. The greater the dispersion of particles within the developing free jet, the more rapid the decay in centreline axial velocity as distance from the jet outlet (x) increases. When these particles reach the impingement region their velocity is already lower than the single-phase. The reduction in spreading rate in the developing jet is attributed to momentum transfer from the particles.

- The particle phases exhibit considerably lower RMS fluctuating velocities than the single-phase. The turbulent velocity normal to the impingement surface is larger than the radial component. As the impingement surface is approached, the magnitude marginally increases for all particles, although the single-phase increased more rapidly.

The impinging jet undergoes significant deceleration as it progresses through the impingement region. The near-field radial wall jet, from 1 to 4 r/d, sees a period of deflection and acceleration:

- There is a drop in axial velocity and increase in radial velocity between 0 (the jet centreline) and 1 r/d (radial distance of one diameter from the jet centreline) within one diameter of the impingement surface. Close to the impingement surface at 0.1 x/d, the largest particle is less influenced by the fluid phase and is more resistant to losing momentum. As the distance above the impingement surface increases up to 1d, the spread in axial mean velocity between the particles grows as the magnitude of the velocity drop increases.
- With the exception of the two data points closest to the wall, the particle velocities are lower than for the single-phase as particles initially have no momentum in the r-direction. The particle radial velocity profiles do not see a local maximum, V_m, until the largest particle at 4 r/d. This is due to the liquid-phase being subject to the no-slip condition at the wall while the particle phase is not. In the immediate vicinity of the impingement surface, the magnitude decreases with increasing particle size, attributed to the inter-phase surface area acted on by the viscous drag. For the same solid loading, the surface area of Particle 1 (20μm) is nearly 2.5 times that of Particle 2 (46μm), which is in turn 1.5 times Particle 3 (69μm). The magnitude of $V_{m,p3}$, the radial local maximum for Particle 3, aligns with the single-phase, attributed to the attenuation of the liquid-solid interaction. As the distance r from the jet axis increases there is a slight deceleration of the radial mean velocity, but at a slower rate that seen for the single-phase.

- The particle turbulent velocities are smaller than for the single-phase, except in the lower shear layer at 1 r/d for Particle 1 (u'_{p1}) at the wall. From 1 to 2 r/d, the axial turbulent velocities undergo a drop of up to 50% as the radial jet is no longer experiencing the residual effect of the approaching impinging jet, followed by a small increase at 4 r/d. The particle radial fluctuating velocities are greater than the axial components. The decay rate of v'_p increases as distance from the jet axis grows. There is little variation between the particles tested, the difference decreasing with increasing distance from the jet centreline. This thesis provides the first RMS fluctuating velocity data normal to the wall.
- Shear stress increases from 1r/d to 2r/d, then decreases at 4r/d as the jet is radially spreading and decelerating.

The radial wall jet which continues into the so-called far-field region (10 r/d), characterised by deceleration and radial expansion, shows;

- The mean velocity and turbulence data show little variation between the particle sizes tested. The lower shear layer sees a small upward flow due to wall jet expansion. The local maximum, U_m, seen for the single-phase case is not evident here as the particle phases are not subject to the no-slip condition at the wall. A difference in axial velocity between the particles is only really evident in the entrainment region, the velocity increasing with increasing particle size. The radial mean velocity profiles are of same shape as the single-phase, only the smaller two particles sizes showing slightly smaller, matching magnitudes.
- The axial and radial mean velocities asymptote to small non-zero values in the re-circulation zone above the radial wall jet.
- Similar to the near-field, the particle turbulent velocities are lower than for the single-phase. A difference between the particles is only seen in the lower shear layer of the wall jet, where the wall jet spread is small. Axially, the smallest particle has the largest turbulent velocity and the largest particle the smallest; the reverse is seen for the radial component. The Reynolds shear stress exhibits even less difference between the particles.
- Finally, the radial velocity data non-dimensionalised by the peak mean radial (V_m) and the velocity half-width (δ), shows all three particles have achieved self-similarity and are in reasonable qualitative agreement with the results of previous workers (Poreh et al., 1967; Dianat et al., 1996; Fairweather and Hargrave, 2002), variation believed to be due to

different experimental set-ups, measurement techniques and the weaker entrainment field of the liquid submerged impinging jets currently under study here.

Chapter 7
Turbulence Modulation due to Presence of Particle: Measurements using Fluorescent PIV

This chapter provides a preliminary exploration into the application of fluorescent particle image velocimetry (fPIV) for the study of turbulence modulation of a continuous liquid phase due to the presence of particles in a turbulent impinging jet flow.

Discrimination between the dispersed particles in the flow and the continuous fluid phase was achieved using Fluorescent PIV (fPIV). Measurement of the continuous phase was facilitated by the use of laser-induced fluorescing tracer particles, coupled with the application of an appropriate filter to the CCD camera allowing only the fluoresced light emitted from the tracers to be captured by the CCD camera. Comparisons between the continuous-, particle- and single-phase data provide a measure of turbulence modulation.

This chapter presents a particle-laden turbulent impinging liquid jet at a jet-to-plate separation of ten diameters. The largest particle size, Particle 3, has been used. All variables, including solid loading (0.01 vol%) and Reynolds number (10,000), were held constant to allow exploration of turbulence modulation alone. Comparison between the particle and single-phase data have previously been presented in Chapter 6. The fPIV technique is introduced in Section 7.1. A criterion for checking for the phase discriminated data is suggested in Section 7.2. And finally, an example of turbulence modulation data for a particle-laden

impinging liquid jet, for the near jet outlet and impingement regions, is given in Section 7.3 to demonstrate the capabilities of the technique. Within Sections 7.2 and 7.3 the terminology has been altered slightly to that used so far throughout this thesis to assist the reader. Previously the single-phase data acquired as presented in the previous results chapters will be referred to as “unladen liquid phase” as these trials were performed without the presence of dispersed particles. A new term for the continuous phase data acquired using fPIV and laser-induced fluorescing tracer particles is called the “laden liquid phase”, which is the carrier phase of the particle-laden impinging jet flow. And as previous the particle phase will continue to be referred to as the “particle phase”. Where appropriate, the following subscripts are used: unladen liquid phase - l,1ph, laden liquid phase – l,2ph, and particle phase – p.

7.1 Fluorescent Particle Image Velocimetry (fPIV)

Fluorescent particle image velocimetry (fPIV) enables discrimination between phases for the multi-phase trials by utilising laser-induced fluorescence. As previously for the single-phase trials, the fluid phase must be seeded otherwise the CCD camera is unable to capture the pure fluid flow. When investigating systems with more than one phase present, it is then necessary to discriminate between the tracers in the continuous phase (the laden liquid phase), and the dispersed phase particles (the particle phase).

Planar two-dimensional PIV uses a single camera to capture images of the measurement area of interest. For multi-phase trials utilising fluorescence to discriminate between the phases, it is necessary to run each experiment twice, once to capture the liquid phase through acquiring images of the tracers following the fluid flow, and a second time to capture the dispersed phase movement. This is achieved through the use of two optical filters. The dispersed particles will refract the laser light at the laser source wavelength of 532nm, as depicted in Figure 7-1 by the bright green vertical line. At the same time, the laser-induced fluorescing tracer particles are excited and emit light at the wavelengths shown by the solid black line. If no optical filter is used the camera will capture all light wavelengths present, from the laser sheet itself, light refracted by both particle species (tracers and dispersed particles), the fluoresced light emitted from the tracers, as well as any other reflections due to items in the measurement area, i.e., jet line and tank base. The camera at this point cannot discriminate between any of these sources and will capture images of all of them. By using optical filters we can restrict the wavelengths permitted to reach the camera.

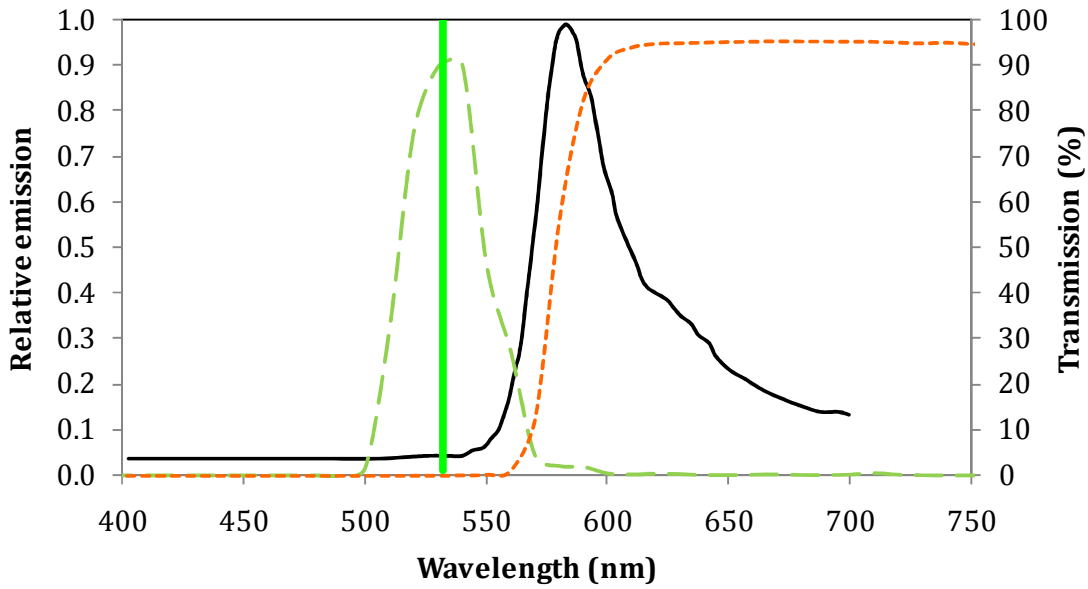

Figure 7-1 Wavelength spectra for fPIV measurements.

Emission (—) spectra of FPP-RhB-10 tracer particles for fPIV measurements, PIV laser sheet at 532nm (—), filter BN532 transmission spectra for dispersed phase measurements (– –), and filter LP580 transmission spectra for fluorescing tracer measurements (----).

To capture the dispersed phase particles, a narrow bandpass optical filter BN532 from Midwest Optical Systems was used. A bandpass filter selectively controls the wavelengths the camera will see. This filter only allows light of wavelengths around 532nm to be captured, as shown by the pale green long-dashed line in Figure 7-1. According to this plot there is a very small overlap of the wavelengths, around 560nm, permitted by this filter and wavelengths emitted (solid black line) by the tracers. The significant majority of the emitted wavelengths will be blocked and, with exception of the small portion of emitted light from the tracers, the camera in this configuration will effectively only measurement the motion of the turbulence modulating dispersed phase particles. The selection of this filter was informed by the necessity to minimise the emitted wavelengths to reach the camera.

To capture the fluorescing tracer particles, a longpass optical filter LP580 was used. The longpass type filter was used to allow transmission of the longer wavelengths only, while blocking the shorter wavelengths. For this application it has the advantage over the bandpass of allowing a broader range of wavelengths which is useful as it allows more of the emitted wavelengths, as can be seen from the orange short-dashed line in Figure 7-1. It is easily seen that this filter will capture a large portion of the wavelengths emitted (solid black line).

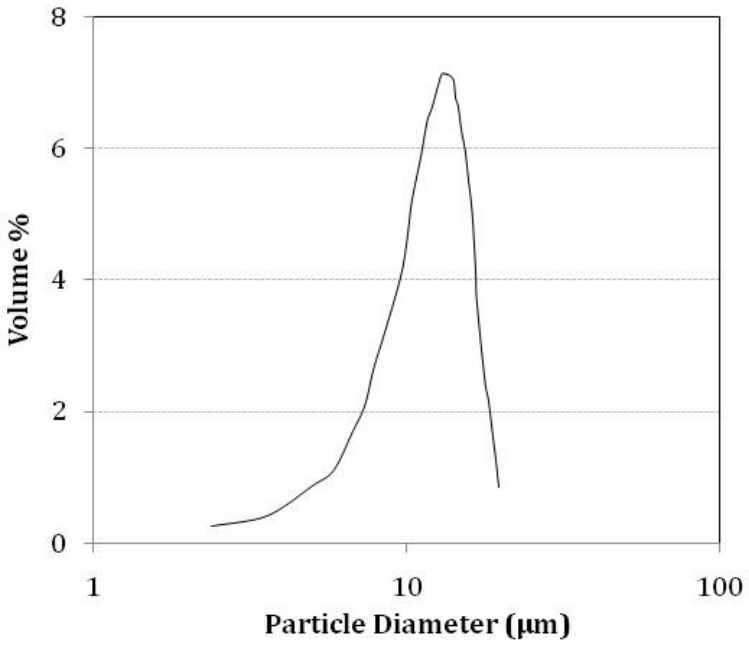

Figure 7-2 Particle size distribution of laser-induced fluorescing tracer particles.

The particle size distribution of the fluorescent tracer particles used for this preliminary exploration of this technique is shown in Figure 7-2. The particle Stokes number (St = 0.06) near the jet outlet indicated the particle motion was coupled to the fluid motion, where particle inertia is small compared to the fluid turbulence scales, following the fluid turbulent fluctuations.

The test particle used as the dispersed phase to acquire turbulence modulation information was the largest of the particles already used, Particle 3.

As per the description above regarding the use of two different optical filters to capture each of the phases, the jet test rig would be set-up and run with the addition of both the fluorescing tracers and the dispersed particles. The rig would be operated at steady state and the acquisition of data for these two phase wound have been undertaken in turn. The mean axial velocity distributions near the jet outlet generated, during the initial testing of the fPIV using this operational strategy, of the particle phase (●, solid circles in Figure 7-3) was seen to be similar to the liquid phases, both laden and unladen. From the study of jet height effect on particle-laden impinging jets presented in Chapter 6 we knew this not to be true. This was also in contradiction to particle-laden free jet and pipe flow work by Rizk et al (1989), Tsuji et al. (1998) and Gillandt et al. (2001), and as in the next thesis section. Measurements of the dispersed phase using the bandpass filter BN532 did indeed prevent the fluoresced wavelengths from the tracers reaching the CCD

camera, however light at the wavelength of the laser sheet were also scattered from the surface of these particles.

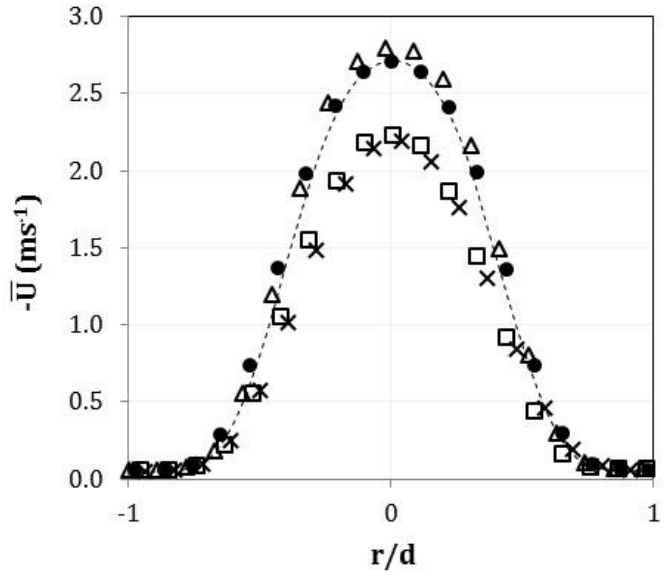

Figure 7-3 Mean axial velocity distribution for assessment of phase discrimination using fluorescent particle image velocimetry (fPIV).

Particle phases: ☐ Particle phase (from PIV), ● Particle phase (from fPIV), ✕ Particle phase, de-focussed lens (from fPIV).

Liquid phases: △ laden liquid phase, **----** unladen liquid phase.

A variation of light sheet intensity in PIV measurements have been found to cause images of particles in regions away from the centre to appear superficially smaller (Kadambi et al., 1998), while particles found away from the focal point appeared superficially large. Offsetting the negative effects of the variation in illumination and defocusing can create a more balanced PIV system which will then produce accurate particle sizes (Kadambi et al., 1998). Applying this logic in reverse, the CCD camera lens was defocused to effectively blur the particle images such that the larger particles (the dispersed phase) would appear superficially large, while rendering the tracer particles out of focus beyond the point of being detectable by the cross-correlation. The resultant mean axial velocity distribution near the jet outlet, the cross symbols in Figure 7-3, were then in good agreement with the Particle 3 data previously presented in Chapter 6.

Phase data comparisons made below for the purpose of assessing turbulence modulation were accomplished by the following data acquisition methods:

- Unladen liquid phase data were acquired using PIV and the addition of neutrally buoyant tracer particles with mean diameter of 20μm.

- Particle phase data were acquired using PIV, without the addition of tracer particles.
- Laden liquid phase data were acquired using fPIV coupled with longpass optical filter LP580, with the addition of laser-induced fluorescing particles (see Figure 7-2 for particle distribution).

7.2 Criterion for Checking Data

A method of checking phase discrimination data acquired near the jet outlet where the flow is comparable to free jets, for assessment of turbulence modulation of particle-laden impinging jets, is proposed.

The flow close to the jet outlet for the present impinging jet, at a jet height of 10 h/d, is comparable to a free jet as the impingement surface is at a sufficient distance to not exert an influence on the flow in this region. This allows comparison to turbulence modulation data available within the literature for free jets and pipe flow. Tsuji et al. (1998) tested axisymmetric air jets laden with particles ranging from 170 to 1400μm. For the smallest particle size, which is the closest to the particles used in the present study, they found the centreline axial mean velocity for the laden and unladen gas phase aligned, with the particle phase lagging behind at around 83% of the gas phase value. Gillandt et al. (2001) also tested an axisymmetric air jet but with slightly smaller particles of 110μm diameter. They also found the continuous axial velocities, both laden and unladen were aligned, with the particle phase 83% of the gas phase. Extending our comparison to include pipe flow, Rizk et al. (1989) tested two particle sizes, 45 and 136μm, and again found the gas phases (laden and unladen) aligned, with the particle phase falling behind. In this instance the particle phase was 94 and 76%, of the gas phase values. Channel flow data for particle sizes closer to those tested here (Kulick et al., 1994 tested particles of 50, 70 and 90μm) again found the gas phases, laden and unladen, centreline mean axial velocities were aligned.

7.3 Initial Impinging Jet Data, h/d Ratio of 10

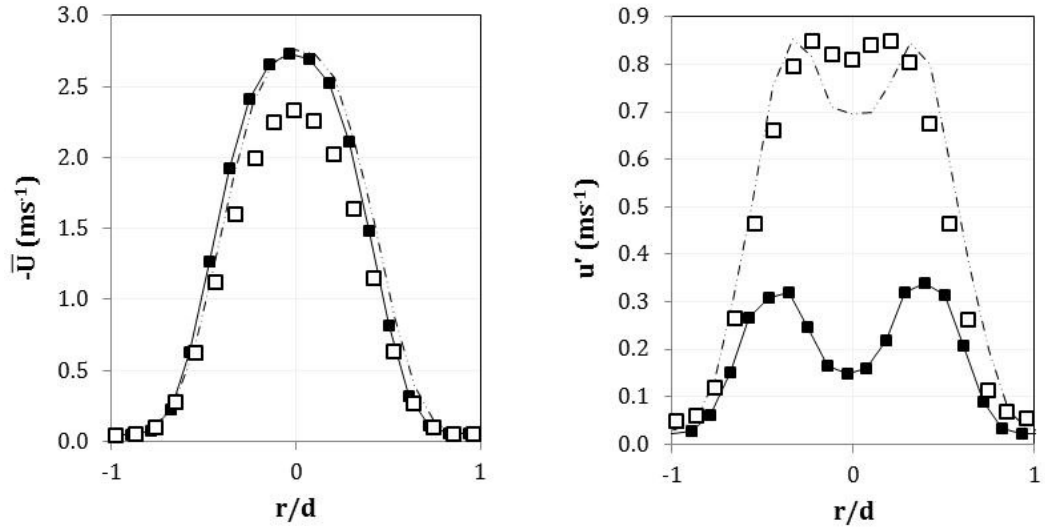

Figure 7-4 Turbulence modulation of axial mean and RMS fluctuating velocities at h/d ratio of 10, one diameter from the jet outlet (9 x/d).

☐ particle phase, ■ laden liquid-phase, —··— unladen liquid-phase.

The particle phase mean axial velocity, Figure 7-4, was around 80% of the laden and unladen liquid velocities, in good agreement the criterion proposed above. The % reduction is in very good agreement with Tsuji et al. (1998) and Gillandt et al. (2001) who both found the particle phase was 83% of the liquid phases. The particle size tested here, 69μm, was between the sizes tested by Rizk et al. (1989) and the reduction in particle phase mean axial velocity is between their values of 94 and 76%.

The particle Stokes number was calculated (Table 7-1), as previously discussed in Chapter 6, and was found to behave accordingly. Particles with larges Stokes numbers are not influenced by the fluid due to large inertia, and do not follow the fluid flow as seen on the mean velocity plot in Figure 7-4.

Table 7-1 Table of test particles employed in particle-laden trials.

Test case	*Particle 3*
Particle diameter (μm)	69
Particle density (g/cm^3)	2.45
d_p/l_e	0.173
Stokes number	4.066

The particle phase turbulent velocity distribution is similar to the unladen liquid phase. The two peaks seen at the outer edges of the jet, where velocity fluctuations are stronger than within the potential core and decrease towards the jet centreline, are less prominent for the particle phase, but is located at a similar distance from the jet centreline as would be anticipated. The particle phase distribution is marginally more narrow than the unladen liquid phase.

The laden liquid phase turbulent velocity was approximately 23% of the unladen liquid phase. Good agreement is seen with Tsuji et al. (1988) and Gillandt et al. (2001) who found the laden liquid phase turbulent velocity was reduced due to the presence of particles. Yoshida et al. (1990) found the particles generally caused a reduction in the gas turbulence.

These findings are in contradiction to the critical parameter for free jet and pipe flow proposed by Gore and Crowe (1989) for the current particle-laden impinging jet under investigation. The critical parameter proposed a simple approach at assess whether the turbulent intensity of the carrier phase will be enhanced or dampened due to the presence of particles; the ratio of the particle diameter to a turbulent length scale, d_p/l_e, where l_e is the integral length scale or the characteristic length of the most energetic eddy when only one phase is present. A demarcation of $d_p/l_e \approx 0.1$ is suggested, above this value the particles with enhance the turbulence of the carrier phase, below it will dampen it. For the region of flow near the jet outlet which is comparable to free jet flow, a value of 0.173 was calculated for Particle 3 indicating the particles will enhance turbulence intensity of the carrier phase. However, in this region of flow where the fluid flow may be considered as a free jet, the particles do not enhance the axial turbulence of the liquid (carrier) phase. In fact, the laden liquid phase centreline turbulent velocity is $0.54 ms^{-1}$ lower than the unladen liquid phase. The discrepancy may be due to this critical parameter not taking into account the density ratio between the continuous and dispersed phases, as also suggested by Kennedy and Moody (1998).

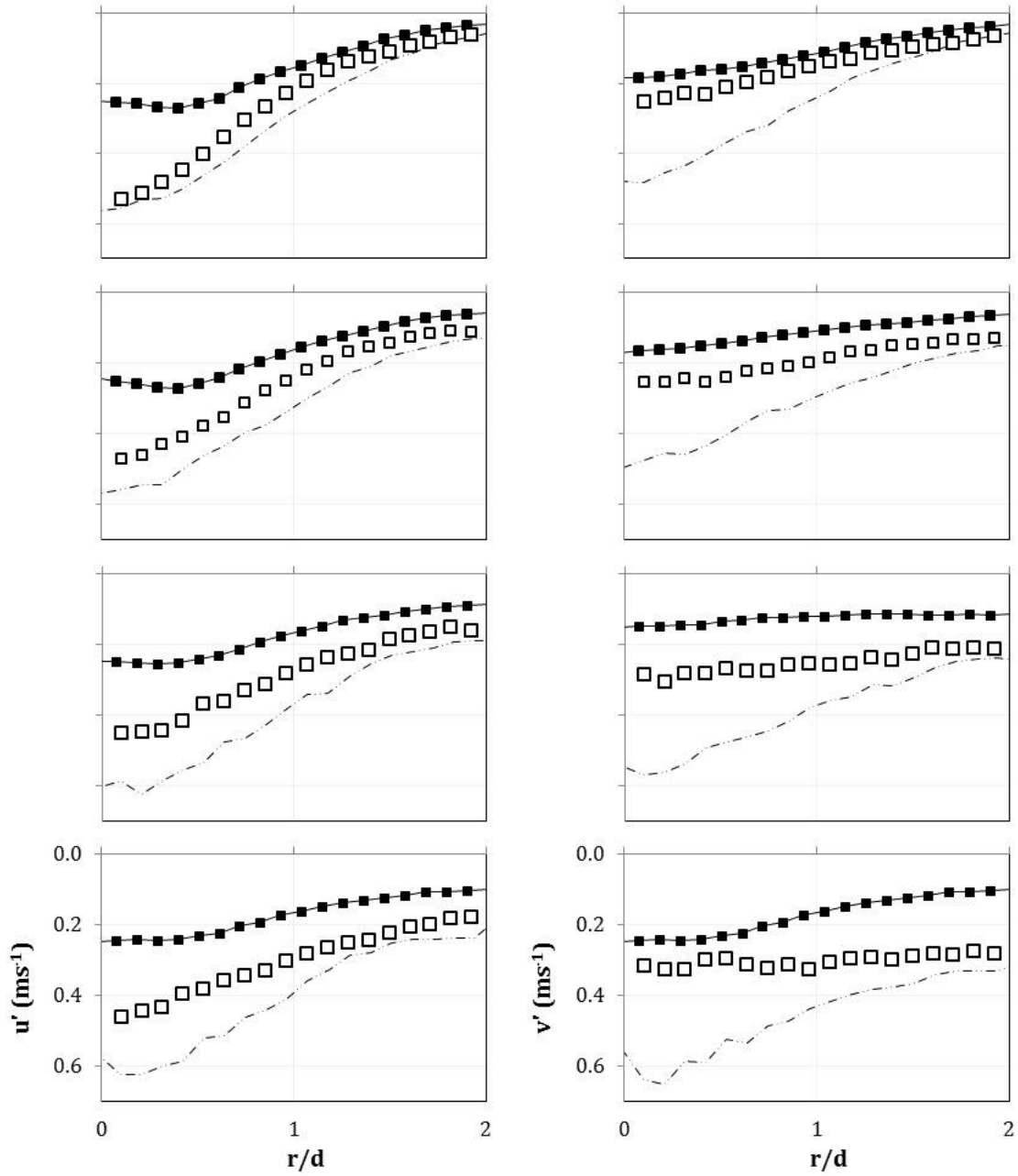

Figure 7-5 Profiles of axial and radial RMS fluctuating velocity within 1d of the impingement surface at h/d ratio of 10; turbulence modulation due to presence of particles.

Transversal profiles taken at: 1, 0.5, 0.2 and 0.1d above impingement surface (top to bottom).

☐ particle phase, ■ laden liquid phase, —··— unladen liquid phase.

Axial and radial RMS fluctuating velocity profiles within the impingement region are presented in Figure 7-5. A common trend between the phases is present for both directional components across all the profile locations shown.

The laden liquid phase exhibits smaller turbulent velocities followed by the particle phase. Within this region the difference between the phases are considerably less. The particle phase centreline axial turbulent velocity is

significantly lower than the profile taken near the jet outlet, from $u'_{p(c)}$ of 0.8 to around 0.5 ms^{-1}, reducing only slightly within the impingement region.

The laden and unladen liquid phase axial turbulent velocities are marginally lower than at the jet outlet region. The primary change to note is neither profile have the double peak structure as evident near the jet outlet.

Chapter 8
Conclusions and Recommendations for Future Work

8.1 Conclusions

The orthogonal impingement of a round turbulent jet onto a solid flat surface is an important class of turbulent free shear flow and is of considerable theoretical interest, as well as having extensive industrial applications. Heat transfer operations are a popular application of impinging jets due to very high convection coefficients, particularly within the impact zone. However the physical modelling of the turbulence of such systems have focussed on small regions of the impinging jet, primarily the stagnation and near-field radial wall jet close to the impingement surface. Particulate additives have been used previously to enhance heat transfer coefficients in the stagnation region due to turbulence production by particles in the viscous sub-layer. As such, some workers have studied the heat transfer effects of particle-laden flows; however very little physical modelling has been done which would enable validation of computational models. Only a few workers have published data in the developing region of a multi-phase free jet, for all other regions of the particle-laden impinging jet no data exists at present.

The programme of research discussed within this thesis has attempted to address this void by the exploration of process and material variables. This made possible only by the successful development of an experimental system for the acquisition of mean velocity and turbulence properties for solid-liquid

and liquid only turbulent impinging jets, to be used in the formulation and validation of computational models.

The first extensive exploration of all three regions of a liquid impinging jet, from jet outlet to impingement through to the far-field radial wall jet, at three strategic jet heights has been presented. The positioning of the impingement surface was at 2 (within the potential core), 6 (just outside the core) and 10 h/d (within the fully developed jet). The single-phase data was used for two additional purposes:

- To prove the experimental system developed by testing against known flow structure of a single-phase impinging jet, and the small amount of data available.
- And to provide a benchmark for the subsequent particle-laden impinging jet trials undertaken.

Comparison of the single-phase data between the different jet heights tested found that as the jet height from the impingement surface increased, the more advanced the jet expansion, and the centreline mean axial velocity decreased as the jet spread radially with increasing mean radial velocity. An increase in turbulence levels was seen from 2 to 6 h/d as the end of the potential core was exceeded where turbulence from the mixing layer penetrated to the centre, followed by a decrease at 10 h/d as the jet continued to grow before impingement. The area of the stagnation region was found to be broader for the largest jet height of 10 h/d as the developing jet had expanded radially to a greater extent. The near-field radial wall jet was influenced by the differences in the turbulence evolution of the jet upstream of the stagnation point. The magnitudes of the mean and turbulent axial velocities within the wall jet were greatest for the middle jet height (6 h/d); as the developing jet had evolved beyond the potential core where the turbulence in the mixing layer had penetrated to the jet axis, but not evolved further where it would expand and lose momentum as for the largest jet height of 10 h/d. The wall jet accelerated radially through the near-field region. The far-field radial wall jet was less affected by the differences in evolution prior to impingement than the near-field. Mean velocity and turbulence data normalised against radial mean velocity local maxima values and wall jet half-width compared well against the small amount of data in the literature (see Tables of data within the Literature Review, Chapter 2). The onset of the far-field radial wall jet was found to be from 10 r/d for the smaller jet heights of 2 and 6 h/d, and 5 r/d for the 10 h/d jet.

The turbulent flow characteristics of a liquid impinging jet laden with 69μm sized glass particles were explored at the three jet-to-plate separations, and comparison made to the single-phase trials. The particles were found to not follow the liquid turbulent flow. Within the developing jet and impingement region the particle velocities were generally smaller than their single-phase counterparts. Taking each region of the impinging jet in turn:

- Within one diameter of the jet outlet, the 6 and 10 h/d jets may be considered as free jet flow where the influence of the impingement surface is not yet felt, the particle phase axial velocity was 82% of the single-phase value, in good agreement with free jet data. For jet outlet conditions, these particles have low responsivity to the fluid flow and lag behind the single-phase, concurrent with the large particle Stokes number of 4.066. In contrast, the particle phase velocity for the smallest jet height of 2 h/d was 17% of the single-phase value. The approaching jet in this instance was under the influence of the wall, modification to the turbulence field within the stagnation region due to the pressure reflections at the wall causing the single-phase to decelerate while the particle phase was less affected due to large inertia of the particles.
- In the impingement region the particle phase radial velocity maxima were marginally larger, and closer to the jet axis, than the single-phase. The particle phase spreading rate was found to be lower than seen for particle-laden free jets. As the jet height increased, the local maxima moved away from the jet axis, similar to the broader stagnation region found from the single-phase trials. Approaching the impingement surface, from 1 to 0.5 x/d, the magnitude of the maxima increased with increasing h/d ratio. In the immediate vicinity of the impingement surface the difference between the phases, and between the jet heights, was considerably less. The particle axial velocity was greater than the single-phase for the smaller jet heights of 2 and 6 h/d, but the reverse was seen for the 10 h/d jet. The particles exhibited considerably lower turbulent velocities than the single-phase; variation between the jet heights were slight. The larger the jet separation, the smaller the centreline magnitude within the impingement region, decreasing as the impingement surface was approached.
- The near-field radial wall jet saw the deflection and acceleration to a greater extent for the smallest jet height (2 h/d) than the larger two (6 and 10 h/d). The particle phase axial mean velocities for the two smaller jet heights were larger than the single-phase, with the difference between the phase decreasing as distance from the jet axis increased. The

reverse was seen for the largest jet height at 2 r/d, with the phases aligning through the remainder of the near-field wall jet. Meanwhile, the radial velocity of the phases for the 2 h/d jet exhibited no significant difference. The middle jet height saw a larger single-phase radial velocity in the upper part of the wall jet, while the particle phase velocity was greatest in the lower part. And the largest jet height exhibited similar values at 2 r/d, with the single-phase marginally higher at 3 and 4 r/d, aligning at 5 r/d. Turbulence intensities exhibited by the particles in the near-field of the radial wall jet increased as the jet line moved away from the impingement surface. The particle turbulence was smaller than that of the single-phase, the greatest difference seen for the middle jet height of 6 h/d.

- The far-field radial wall jet saw little difference between the particle and single-phases, at each of the jet heights. The onset of self-similarity changed as the jet line was lowered towards the impingement surface. The largest jet height, 10 h/d, achieved self-similarity from 5 r/d whereas the other two jet heights achieved it from 10 r/d, all in good agreement with the single-phase results and the data fits established in literature.

A sensitivity study of the particle size effect on the flow characteristics of a particle-laden turbulent impinging liquid jet with jet-to-plate separation of six diameters (6 h/d) has also been undertaken. Three particles sizes were selected; 20, 46 and 69μm (referred to as Particle 1, Particle 2 and Particle 3 respectively). Near the jet outlet, the calculated particle Stokes' numbers found all three of the Stokes categories were represented. The largest particle, Particle 3 (which was used in the jet height assessment of Chapter 5) was found to lag behind the single-phase, in line with a large Stokes number of 4.066, as above. The velocity distribution of the middle sized particle, Particle 2, was coupled to the motion of the larger vortices, migrating to the margins of the eddies and dispersing further than the fluid consistent with the behaviour described by a Stokes number near unity. And the smallest particle size, Particle 1, had a velocity distribution similar to the single-phase, with values only marginally higher. With a particle Stokes number of 0.347, these particles nearly followed the fluid flow, sitting marginally above the single-phase distribution. Taking each region of the impinging jet in turn:

- Within the impingement region, the particles do not decelerate as rapidly as the single-phase. Particle 2 however exhibits a lower axial velocity than both of the other particles as well as the single-phase. In the jet

outlet region this particle was coupling to the motion of the large vortices and dispersing further than the single-phase. The greater the dispersion of the particles within the developing free jet, the more rapid the decay in centreline axial velocity. When these particles reach the impingement region their velocity was already lower than the single-phase. Turbulent velocities of the particle phases were considerably lower than the single-phase, the turbulent velocity normal to the impingement surface larger than the radial component. The increase in magnitude as the wall is approached is greatest for the single-phase.

- In the near-field radial wall jet, with the exception of the two data points closest to the impingement surface, the particle mean radial velocities are lower than the single-phase as particles initially have no momentum in the r-direction. No local maxima were seen, until the largest particle at 4 r/d, for the particle phases in this region due to the particles not being subject to the no-slip condition at the wall of the single-phase. The local maximum of Particle 3, at 4 r/d, aligns with the single-phase, attributed to the attenuation of the liquid-solid interaction. In the immediate vicinity of the impingement surface, the magnitude decreases with increasing particle size, attributed to the inter-phase surface area acted on by the viscous drag. As the distance r from the jet axis increases there is a slight deceleration of the radial mean velocity, but at a slower rate that seen for the single-phase. The particle turbulent velocities were generally smaller than the single-phase. Moving from 1 to 2 r/d, the axial turbulent velocities undergo a drop of up to 50% as the radial jet is no longer experiencing the residual effect of the approaching impinging jet, followed by a small increase at 4 r/d. Particle radial turbulent velocities were greater than the axial components, the rate of decay of the radial component increasing as distance from the jet axis increased. The variation between the particle sizes tested were small, with this difference decreasing further as the radial wall jet progressed. The shear stress increased from 1 to 2 r/d, then decreased at 4 r/d as the jet radially spread and decelerated.

In the far-field, variation in the mean and turbulent data between the particle sizes tested are minimal. A difference in axial velocity between the particles is only really evident in the entrainment region, the velocity increasing with increasing particle size. The radial mean velocity profiles are of same shape as the single-phase, only the smaller two particles sizes showing slightly smaller, matching magnitudes. All three test particles achieved self-similarity by 10 r/d, and again were in reasonable agreement with the results of previous workers.

The particle turbulent velocities, similar to the near-field, are lower than the single-phase. A difference between the particles is only seen in the lower shear layer of the wall jet, where the wall jet spread is small. Axially, the smallest particle has the largest turbulent velocity and the largest particle the smallest; the reverse is seen for the radial component. The Reynolds shear stress exhibits even less difference between the particles.

8.2 Recommendations for Future Work

The opportunities for further physical modelling work on particle-laden turbulent impinging jets are extensive due to the small amount of data currently available (see Tables of data within the Literature Review, Chapter 2). This opens up the opportunity to explore any of the variables introduced in Table 3-1 and 3-2 (pages 42 and 43 respectively), and more beyond. Thorough investigation of each of these variables noted in the above tables would require an enormous experimental programme extending over many years. A programme of this magnitude would also be excessively expensive. A number of key recommendations have been identified as a result of the research reported within this thesis, please note this list is not exhaustive.

Process variables

- The effect of Reynolds number on the flow characteristics of axisymmetric single-phase turbulent impinging jets has been studied (Cooper et al., 1993), as has particle-laden free jet flows (Tsuji et al., 1988; Longmire and Anderson, 2003), however no data for particle-laden impinging jets was found. The turbulence evolution of the developing jet is highly influenced by Reynolds number and would therefore be incredibly useful for the purposes of computational model validation.
- The exploration of non-steady state conditions, such as jet firing time as is the operational application of impinging jets currently employed in highly active storage tanks within the nuclear industry, notably the Highly Active Storage Tanks (HASTs) at the Sellafield site in the north-west of England, would be useful as they are more comparable to real-life applications of many impinging jets. To achieve this the experimental approach would require modification. The CCD camera currently has a memory capacity sufficient to allow each PIV run to acquire 62 image pairs. After acquisition, the images must be downloaded onto the PIV PC, typically taking 20-30 seconds.
- Developing an understanding of the mobilisation capability of settled sludge beds (of interest for the applications within the nuclear industry discussed in Chapter 1) by the use of turbulent impinging jets, it would be most useful to physically model different settling and consolidation times. Dependent on the physical properties and particle-particle interactions, varying the consolidation period can significantly change the bed structure and therefore have a direct impact on the capability of an impinging jet to re-suspend the particles.

Material variables

- The current experimental system does not allow for the successful acquisition of velocity data for particles of diameters larger than those reported within this thesis. Particles larger than around 100μm, and particle density of 2.5 g cm^{-3}, were found to settle and accumulate to an undesirable extent within the duration of the PIV data acquisition, rendering them unsuitable for the current programme of work. The measurement of particles of larger diameters (> 100μm), could be feasible with some modification to the feeding system of the jet test rig to maintain a suitable solids loadings of the jet line feed. Or alternatively, the test simulant could be engineered to reduce the settling velocities of larger particles, i.e., using particles of lower density, or altering the rheology of the carrier-phase could also have the same effect. Reducing the data acquisition duration would require significant investment, the current PIV CCD camera has a buffer capacity of only 62 image pairs requiring the images be downloaded between each run and a total of 50 PIV runs was employed within this work to achieve the necessary time-averaging as discussed in Chapter 3. Using the current data acquisition settings, the measurement duration was 3 minutes and 27 seconds without the time it takes to download the images from the camera. Flow characteristics of particle-laden flows can be highly influenced by the dispersed phase particle properties, the particle-phase being one of the two phases present. Extensive research has been undertaken into the particle size effect of free jet and pipe flows, however only a small number of isolated studies (Table 2-5, page 34) of particle-laden impinging jet can be found in the literature; Yoshida et al. (1990) studied particles of 48.9μm diameter issuing from a slot jet, Ushijima et al. (2001) used considerably larger particles of 1050μm diameter at a low Reynolds number of 2000, and Longmire and Anderson (2003) tested particles from 15 to 45μm with periodic forcing to generate vortices.
- Similar to particle size, much work has been done on the solids loading effect for free jet flow; only Longmire and Anderson (2003) attempted to study solids loading effect of an impinging jet, for solid loadings of 4 to 50%. The PIV measurement technique is a low solids concentration measurement (discussed in Chapter 4) and may be the reason why they appear to have utilised only the imaging capability of the PIV. Using the existing PIV on the current experimental facility will limit the solid loading.
- The controlled manipulation of colloidal properties such as zeta potential, pH, electrolyte species and concentration, would allow the investigator the

ability to alter the particle surface charge of colloidal particles enabling the study of stabilised or destabilised suspensions.

The work presented in this thesis is the first done using the new experimental system developed by the author as part of this work. In addition to the vast amount of further work introduced above, some modification to the application of the PIV could open-up the following opportunities for further work:

- Further explorative work is recommended in the immediate vicinity of the stagnation point. The flow phenomena in this region, i.e., the viscous sub-layer close to the impingement surface, is of a smaller scale (Cooper et al., 1993; Craft et al., 1993) than the current experimental set-up can accurately capture as previously discussed in Chapter 4. The focus of this thesis was to explore all three regions of the impinging jet using PIV, however the same measurement technique (with slight modification to the CCD camera) and experimental rig could be used to perform a 'zoomed-in' study of this area alone and is an area for further exploration. Consideration would need to be made regarding the upper particle size limit that could be applied. The study of a smaller measurement area may result in lowering the maximum particle size measureable due to the necessary displacement within an interrogation area (IA) required for the measurement technique. If particles are too large the PIV may not be able to detect discrete displacements within the IAs or indeed may fill or even be larger than the IA. When decreasing the observation field size and increasing the optical resolution of the investigation, the tracer particle diameters have to be decreased also.
- A preliminary assessment of the feasibility of studying turbulence modulation of the carrier-phase due to the presence of particles has been introduced in Chapter 7. The data were acquired by performing separate trials for each of the phases, applying a filter to the camera to isolate the laser-induced fluorescing tracers for measurement of the carrier-phase. However, phase discrimination may alternatively be achieved through the use of laser-induced fluorescing particles for the dispersed-phase also coupled with the use of an appropriate camera filter. These particles would be required to fluoresce at a different wavelength than the tracer particles so each could be isolated. Additionally, measurements could be made simultaneously through the addition of a second camera, one set-up with the filter for the tracers and the other set-up for the dispersed-phase particles.

List of References

Abramovich, G.N., Schindel, L., (2003) The theory of turbulent jets, Cambridge, Mass., M.I.T. Press.

Allen T., (1997) Particle size measurement, 5th edition, London: Chapman & Hall.

Ashford-Frost, S., Jambunathan, K., (1996) Effect of nozzle geometry and semi-confinement on the potential core of a turbulent axisymmetric free jet, Int. Comm. Heat Transfer, (23) 1333-1338.

Ball, C.G., Fellouah, H., Pollard, A., (2012) The flow field in turbulent round free jets, Prog. Aerospace Sci., (50) 1-26.

Baughn, J.W., Shimizu, S., (1989) Heat transfer measurements from a surface with uniform heat flux and an impinging jet, J. Heat Transfer (111) 1096-1098.

Beltaos S., Rajaratnam N., (1974) Impinging circular turbulent jets, J. Hydraulic Enging., ASCE, (100) 1313-1328.

Bergles AE., (1985) Techniques to augment heat transfer, Handbook of Heat Transfer Applications, 2nd Ed., McGraw-Hill.

Buchhave P., George WK., Lumley JL., (1979) The measurement of turbulence with the laser-Doppler anemometer, Ann. Rev. Fluid Mech., (11) 443-503.

Carlomagno, G.M., Ianiro, A., (2014) Thermo-fluid-dynamics of submerged jets impinging at short nozzle-to-plate distance: A review, Exp. Thermal Fluid Sci., (58) 15-35.

Cooper D., Jackson DC., Launder BE., Liao GX., (1993) Impinging jet studies for turbulence model assessment – I. Flow-field experiments, Int. J. Heat Mass Transfer, (36) 2675-2684.

Craft T.J., Graham L.W.G., Launder B.E., (1993) Impinging jet studies for turbulence model assessment – II. A comparison of the performance of four turbulence models, Int. J. Heat Mass Transfer, (36) 2685-2697.

Crowe C.T., Chung J.N., Troutt T.R., (1988) Particle mixing in free shear flows, Prog. Energy Combust. Sci., (14) 171-194.

Dianat M., Jones W.P., (1995) Predictions of the concentration field of an impacting turbulent jet, 10th symposium on turbulent shear flows 2, Pennsylvania State University.

Dianat M., Fairweather M., Jones W.P., (1996) Reynolds stress closure applied to axisymmetric, impinging turbulent jets, Theor. Comput. Fluid Dyn., (8) 435-447.

Dimotakis, P.E., (2000) The mixing transitions in turbulent flows, J. Fluid Mech., (409) 69-98.

Fairweather M., Hargrave G.K., (2002) Experimental investigation of an axisymmetric, impinging turbulent jet. 1. Velocity field, Experiments in Fluids, (33) 464-471.

Fan J., Xu S., Wang D., (2010) PDA measurements of two-phase flow structure and particle dispersion for a particle-laden jet in crossflow, J. Hydrodynamics, (1) 9-18.

Fellouah, H., Ball, C.G., Pollard, A., (2009) Reynolds number effects within the development region of a turbulent round free jet, Int. J. Heat Mass Transfer, (52) 3943-3954.

Fellouah H., Pollard A., (2009) The velocity spectra and turbulence length scale distributions in the near to intermediate regions of a round free turbulent jet, Phys. Fluids, (21) 115101.

Fitzgerald, J.A., Garimella, S.V., (1998) A study of the flow field of a confined and submerged impinging jet, Int. J. Heat Mass Transfer, (41), Nos. 8-9, 1025-1034.

Gauntner, J.W., Livingood, J.N.B., Hrycak, P., (1970) Survey of literature on flow characteristics of a single turbulent jet impinging on a flat plate, NASA Technical Note TN D-5652.

Geers L.F.G., Tunners M.J., Hanjalic K., (2004) Experimental investigation of impinging jet arrays, Experiments in Fluids, (36) 946-958.

Gillandt I., Fritsching U., Bauckhage K., (2001) Measurement of phase interaction in dispersed gas/particle two-phase flow, Int. J. Multiphase Flow, 1313-1332.

Glauert, M.B., (1956) The wall jet, J. Fluid Mechanics, (1) 625-643.

Goldstein R.J., Franchett M.E., (1988) Heat transfer from a flat surface to an oblique impinging jet, J. Heat Transfer, (100) 84-90.

Gore. R.A., Crowe, C.T., (1989) Effect of particle size on modulating turbulent intensity, Int. J. Multiphase Flow, (15), No. 2, 279-285.

Grant I., (1997) Particle image velocimetry: A review, Proc. Mech. Eng., Part C, (211) 55-76.

Hammad K.J., Milanovic I., (2011) Effect of Reynolds number on the turbulent flow structure in the near-wall region of an impinging round jet, Proc. ASME-JSME-KSME Fluids Eng. Conf., AJK2011-16010.

Hargrave G.K., Williams T.C., Anandarajah K., Halliwell N.A., (2006) The 3D velocity field of an impacting turbulent jet, J. of Phys.: Conf. Series, (45) 162-172.

Hasegawa S., Echigo R., Shimizu A., (1986) Convective and radiative heat transfer of flowing gaseous-solid suspensions, Handbook of Heat and Mass Transfer, (1) 523-557.

Hetsroni G., (1989) Particle-turbulent interaction, Int. J. Multi-phase Flow, (15) 735-746.

Hetsroni G., Sokolov M., (1971) Distribution of mass, velocity, intensity of turbulence in a two-phase turbulent jet, J. Appl. Mech., (38) 315-327.

Hinze, J.O., (1975) Turbulence, 2nd Edition, McGraw-Hill, New York.

Hishida, K., Ando, A., Maeda, M., (1992) Experiments on particle dispersion in a turbulent mixing layer, Int. J. Multiphase Flow. (18), No. 2, 181-194.

Hofmann H.M., Kind M., Martin H., (2007) Measurements on steady state heat transfer and flow structure and new correlations for heat and mass transfer in submerged impinging jets, Int. J. Heat Mass Transfer, (50) 3957-3965.

Jambunathan K., Lai E., Moss M.A., Button B.L., (1992) A review of heat transfer data for single circular jet impingements, Int. J. Heat Fluid Flow, (13) 106-115.

Jana B.D., Stack M.M., (2005) Modelling impact angle effects on erosion-corrosion of pure metals: Construction of materials performance maps, Wear, (259) 243-255.

Kadambi J.R., Martin W.T., Amirthaganesh S., Wernet M.P., (1998) Particle sizing using particle image velocimetry for two-phase flows, Powder Tech., (100) 251 - 259.

Kennedy I.M., Moody M.H., (1998) Particle dispersion in a turbulent round jet, Exp. Therm. Fluid Sci., (18) 11-26.

Kubacki S., Dick E., (2011) Hybrid RANS/LES of flow and heat transfer in round impinging jets, Int. J. Heat Fluid Flow, (32) 631-651.

Kulick J.D., Fessler J.R., Eaton J.K., (1994) Particle response and turbulence modification in fully developed channel flow, J. Fluid Mech., (277) 109-134.

Kurosaki Y., Murasaki T., Satoh I., Kashiwagi T., (1986) Study on heat transfer mechanism of a gas-solid suspension impinging jet: Effect of particle sizes and thermal properties, Heat Transfer 1986, (5) 2587-2592.

Lawson, B.E., Halliwell, N.A., Coupland, J.M., (1997) A generalised optimisation method for double pulsed particle image velocimetry, Optics Lasers Engrg., (27) 637-656.

Levy Y., Lockwood F.C, (1981) Velocity measurements in a particle laden turbulent free jet, Combustion Flame, (40) 333-339.

Lilly G.P., (1973) Effect of particle size on particle eddy diffusivity, Ind. Eng. Chem. Fundam., (12) 268-275.

Longmire E.K., Anderson S.L., (2003) Particle/vortex interactions in free and impinging air jets, Manipulation and control of jets in crossflow, Springer Wien New York, 212-222.

McArthur G.A.H., Tinsley T.P., McKendrick D., (2005) Development of a liquid jet sludge re-suspension model, in AIChE Annual Meeting.

Melling A., (1997) Tracer particle and seeding for particle image velocimetry, Measurement Science and Technology, (8) 1406-1416.

Milanovic I.M., Hammad K.J., (2010) PIV study of the near-field region of a turbulent round jet, Proc. ASME 3rd US-European Fluids Eng Summer Meeting, FEDSM-ICNMM2010-31139.

Modarress, D., Tan, H., Elghobashi, S., (1984a) Two-component LDA measurement in a two-phase turbulent jet, AIAA J., (22) No. 5, 624-630.

Modarress, D., Wuerer, J., Elghobashi, S., (1984b) An experimental study of a turbulence round two-phase jet, Chem. Engrg. Commun., (28) 341-354.

Munson, B. R., Young, D. F., Okiishi, T. H., (2002) Fundamentals of Fluid Mechanics, 4th Ed., New York: John Wiley and Sons, Inc,.

Neville A., McDougall B.A.B., (2002) Electrochemical assessment of erosion-corrosion of commercially pure titanium and a titanium alloy in slurry impingement, Proc. Mech. Engnrs., Part L, (216) 31-41.

Nishino K., Samada M., Kasuya K., Torii K., (1996) Turbulence statistics in the stagnation region of an axisymmetric impinging jet flow, Int. J. Heat Fluid Flow, (17) 193-201.

O'Donovan T.S., Murray D.B., (2007) Jet impingement heat transfer - Part I: Mean and root-square heat transfer and velocity distributions, Int. J. Heat Mass Transfer, (50) 3291-3301.

O'Donovan T.S., Murray D.B., (2007) Jet impingement heat transfer - Part II: A temporal investigation of heat transfer and local fluid velocities, Int. J. Heat Mass Transfer, (50) 3302-3314.

Parthasarathy, R.N., Faeth, G.M., (1987) Structure of particle-laden turbulent water jets in still water, Int. J. Multiphase Flow, (13) No. 5, 699-716.

Popper J., Abuaf N., Hetsroni G., (1975) Velocity measurements in a two phase turbulent jet, Int. J. Multiphase Flow, (1) 715-726.

Poreh M, Tsuei Y.G, Cermak J.E, (1967) Investigation of a turbulent radial wall jet, J. Appl. Mechanics, (34) 457-463.

Raffel M., Willert C., Wereley S., Kompenhams J., (2007) Particle image velocimetry: A practical guide, 2nd Edition, Springer Berlin.

Rajaratnam N., (1976) Turbulent jets, Elsevier Scientific Publishing Company.

Rajaratnam N., Zhu D.Z., Rai S.P., (2010) Turbulence measurements in the impinging region of a circular jet, Can. J. Civ. Eng., (37) 782-785.

Raju N., Meiburg E., (1995) The accumulation and dispersion of heavy particles in forced two-dimensional mixing layers. Part 2: The effect of gravity, Phys. Fluids, (6) 1241-1264.

Rizk M.A., Elghobashi S.E., (1989) A two-equation turbulence model for dispersed confined two-phase flows, Int. J. Multiphase Flow, (15) 119-133.

Shaw D.J., (1993) Colloid and surface chemistry, 4th edition, Butterworth-Heinemann Ltd.

Sheen H.J., Jou B.H., Lee Y.T., (1994) Effect of particle size on a two-phase turbulent jet, Exp. Thermal Fluid Science, (8) 315-327.

Shimizu A., Echigo R. Hasegawa S., (1979) Impinging jet heat transfer with gas-solid suspension medium, Adv. Enhanced Heat Transfer, Proc. 18th Heat Transfer Conf., 155-160.

Shinneeb A.M., Bugg J.D., Balachandar R., (2004) Variable threshold outlier identification in PIV data, Measurement Science and Technology, (15) 1722-1732.

Stanislas M., Monnier J.C., (1997) Practical aspects of image recording in particle image velocimetry, Measurement Science and Technology, (8) 1417-1426.

Tang L., Wen F., Yang Y., Crowe C.T., Chung J.N., (1992) Self-organizing particle dispersion mechanism in a plane wake, Phys. Fluids A, (10) 2244-2251.

Tsuji Y., Morikawa Y., Tanaka T., Karimine K., (1988) Measurement of an axisymmetric jet laden with coarse particles, Int. J. Multiphase Flow, (14) 565-574.

Unadkat H., Rielly C.D., Hargrave G.K., Nagy Z.K., (2009) Application of fluorescent PIV and digital image analysis to measure turbulence properties of solid-liquid stirred suspensions, Chem. Eng. Research Design, (87) 573-586.

Ushijima S., Nezu I., Hase N., (2001) Measurements on liquid-solids impinging jets laden with large particles using PIV and LDA, Paper no. 114, 6th Asian Symposium of Visualisation, PUEXCO, Pusan.

Warda H.A., Kassab S.Z., Elshorbagy K.A., Elsaadawy E.A., (1999) An experimental investigation of the near-field region of free turbulent round central and annular jets, Flow. Meas. Instrum., (10) 1-14.

Westerweel J., Scarano F., (2005) Universal outlier detection for PIV data, Exp. Fluids, (39) 1096-1100.

Westerweel J., Fukushima C., Pedersen J.M., Hunt J.C.R., (2005) Physical Review Letters, (95) 174501.

Wilson P.D., (1996) The nuclear fuel cycle: From ore to wastes, Oxford University Press, 344.

Wolf D.H., Incropera F.P., Viskanta R., (1993) Jet impingement boiling, Adv. Heat Transfer, (23) 1-132.

Yoon H.S., Sharp K.V, Hill D.F., Adrian R.J., Balachandar S., Ha M.Y., Kar K., (2001) Integrated experimental and computational approach to simulation of flow in a stirred tank, Chem. Eng. Science, (56) 6635-6649.

Yoshida H., Suenaga K., Echigo R., (1990) Turbulence structure and heat transfer of a two-dimensional impinging jet with gas-solid suspensions, Int. J. Heat Mass Transfer, (33) 859-867.

Zheng Y.G., Yao Z.M., Ke W., (2000) Erosion-corrosion resistant alloy development for aggressive slurry flows, Materials Letters, (46) 362-368.

Zhou D.W, Lee S.J, (2007) Forced convective heat transfer with impinging rectangular jets, Int. J. Heat Mass Transfer, (50) 1916-1926.